# Onshore sandbar migration

## Processing PIV measurements to analyse wave driven sediment transport in the nearshore

Inge van den Ende

Delft University of Technology

TU Delft

# Onshore sandbar migration

## Processing PIV measurements to analyse wave driven sediment transport in the nearshore

by

Inge van den Ende

Master thesis
Master Hydraulic Engineering
Specialisations Coastal Engineering & Environmental Fluid Mechanics

February 7, 2017

| | | |
|---|---|---|
| Thesis committee: | Prof.dr.ir. A.J.H.M. Reniers, | TU Delft |
| | Ir. M. Henriquez, | TU Delft |
| | Dr.ir. M.F.S. Tissier, | TU Delft |
| | Dr.ir. M. van Koningsveld, | Van Oord |
| | Ir. M. Wengrove | University of New Hampshire |

An electronic version of this thesis is available at `http://repository.tudelft.nl/`.

TU Delft

# Abstract

This study investigates wave driven onshore sandbar migration. Observations show that sandbars move onshore during mild wave conditions [Aubrey, 1979]. Literature describes different potential sediment mechanisms that cause this onshore migration, but the dominant cause is still under debate. The goal of the present study is to determine the dominant sediment mechanism in wave driven onshore sandbar migration.

The study uses data collected in a mobile-bed wave flume. The study consists of two parts: (1) calculating sediment transport based on PIV data and (2) analysing wave driven sediment transport in the wave bottom boundary layer. The analysis distinguishes three transport mechanisms: current related, long wave related and short wave related sediment transport. The study further distinguishes wave properties corresponding to different intra-wave processes within the short wave related sediment transport.

The findings show that short wave related sediment transport is dominant. The wave shape changes towards the bottom: asymmetry is transformed into skewness, which results in strongly skewed and backward pitched waves close to the bottom. Additionally, the results seem to indicate that the short wave related sediment transport mainly depends on near-bed skewness and not or slightly on the asymmetric pressure gradient. The implication is that sediment transport calculations should focus on short wave related transport, near-bed skewness and should include the wave shape development in the wave bottom boundary layer.

In addition, the study shows that PIV data have potential to determine sediment transport without additional concentration measurements. Three essential steps in the method are: (1) placement of the PIV laser in front of the wave flume instead of the common position on top to illuminate both the flow and bottom sediment, (2) calibrate the intensity and concentration based on the mean bed and mean water intensity and (3) multiply the PIV sediment velocities with the concentration to obtain sediment transport.

The results of this study contribute to improve the accuracy of coastal morphology predictions and the efficiency of beach nourishments and other coastal protection measures.

# Acknowledgements

This Master Thesis has been written as part of the Master of Science program Hydraulic Engineering of the faculty of Civil Engineering and Geosciences of the Delft University of Technology. I would like to thank my committee for your enthusiasm and interest in the subject. In fruitful discussions, everyone helped with thinking of new ways to look at the data during one of the many challenges in this study. Thank you, Ad, for your analytical comments and great knowledge of everything about waves. Martijn, for all the elaborate explanations about the details of wave driven sediment transport close to the bottom. Marion, for your comments of a great wave expert. Meagan, for your many helpful suggestions and support. Our biking and ice-skating trips were great. Mark and Gerben, thanks for your very structured data analysis methods, which guided me in building the data analysis model.

Next, I would to thank my family for teaching me curiosity and wonder from the first day, and for always supporting me so greatly. Your enthusiasm about my research topic was very encouraging.

# Contents

# General

## Symbols & units

| | | |
|---|---|---|
| $a$ | wave amplitude | [m] |
| $A$ | orbital amplitude just above the wbbl ($A = \hat{u}/T_p$) | [m] |
| $As$ | wave asymmetry | [-] |
| $As^*$ | not normalised wave asymmetry | [$m^3/s^3$] |
| $c$ | volumetric concentration | [$m^3/m^3$] |
| $c_w$ | wave celerity (phase speed) | [m/s] |
| $D$ | grain diameter | [m] |
| $D_{50}$ | median grain diameter | [m] |
| $E$ | wave energy | [J] = [kg $m^2$ / $s^2$] |
| $g$ | gravitational acceleration ($g \approx 9.81$) | [$m/s^2$] |
| $H$ | wave height ($H = 2a$) | [m] |
| $h_{block}$ | the block thickness in pug flow | [m] |
| $I$ | Image intensity or brightness | [Counts] |
| $k$ | wave number ($k = 2\pi/L$) | [rad/m] |
| $K$ | coefficient of friction | |
| $k_s$ | hydraulic roughness | [m] |
| $k_N$ | Nikuradse roughness ($k_N = 30z_0$) | [m] |
| $L$ | wave length | [m] |
| $M$ | mass transport | [kg/s] |
| $m$ | mass | [kg] |
| $n$ | ratio between group velocity and phase velocity or ratio between prototype value and model value of the index parameter | [-] |
| $l$ | horizontal lenght | [m] |
| $P$ | energy transport (power) | [J m/s] |
| $Q_i$ | discharge in direction i | [kg m/s] |
| $S$ | sediment transport volume including pores | [$m^3/s$] |
| $S^*$ | sediment transport volume excluding pores | [$m^3/s$] |
| $\overline{S}$ | wave-averaged sediment transport volume | [$m^3/s$] |
| $S_i$ | sediment transport volume in direction i | [$m^3/s$] |
| $S_{ij}$ | radiation stress (transport of momentum): momentum in direction i, transport in direction j | [J] |
| $Sk$ | wave skewness | [-] |
| $Sk^*$ | not normalised wave skewness | [$m^3/s^3$] |
| $T$ | wave period | [s] |
| $t$ | time | [s] |
| $u$ | horizontal orbital flow velocity | [m/s] |
| $u_{LW}$ | long wave horizontal orbital flow velocity | [m/s] |
| $u_{SW}$ | short wave horizontal orbital flow velocity | [m/s] |
| $\hat{u}$ | amplitude of horizontal orbital velocity | [m/s] |
| $\hat{u}_\infty$ | amplitude of horizontal orbital velocity at the top of the wbbl | [m/s] |
| $u_{rms}$ | root-mean-square velocity ($u_{rms} = \hat{u}/\sqrt{2}$) | [m/s] |
| $u_*$ | shear velocity ($u_* = \sqrt{\tau_b/\rho}$) | [m/s] |

| | | |
|---|---|---|
| $v$ | flow velocity parallel to wave crest | [m/s] |
| $w$ | vertical orbital flow velocity | [m/s] |
| $\hat{w}$ | amplitude of vertical orbital velocity | [m/s] |
| $w_s$ | settling velocity | [m/s] |
| $z$ | vertical coordinate: 0 at average water surface and positive upwards | [m] |
| $z_0$ | depth were orbital velocity is zero | [m] |
| $z_b$ | bottom height | [m] |
| $z_\delta$ | top of wbbl | [m] |

Greek symbols

| | | |
|---|---|---|
| $\beta$ | bottom slope | [degrees] |
| $\gamma$ | submerged unit weight of sediment $\gamma = (\rho_s - \rho)g$ | [N] |
| $\delta$ | boundary layer thickness | [m] |
| $\eta$ | water level | [m] |
| $\eta_S$ | approximation error in S | [-] |
| $\theta$ | Shields parameter | [-] |
| $\kappa$ | Von Kármán constant ($\kappa \approx 0.4$) | [-] |
| $\lambda$ | typical length | [m] |
| $\mu$ | sediment packing factor (volume of sediment/total volume) | [-] |
| $\nu$ | kinematic viscosity | [$m^2/s$] |
| $\nu_t$ | turbulent viscosity | [$m^2/s$] |
| $\xi$ | Iribarren number | [-] |
| $\rho$ | water density | [$kg/m^3$] |
| $\rho_s$ | sediment density | [$kg/m^3$] |
| $\tau$ | shear stress | [$N/m^2$] |
| $\tau_b$ | bottom shear stress | [$N/m^2$] |
| $\omega$ | wave frequency ($\omega = 2\pi/T$) | [rad/s] |
| $\phi$ | wave phase | [-] |
| $\phi_{b,n}$ | bottom phase shift of the $n^{th}$ frequency | [-] |
| $\Phi_n$ | waveform parameter | [-] |

## Signs on parameters

| | | |
|---|---|---|
| $\overline{x}$ | over line | Average over time |
| $\tilde{x}$ | tilde | Wave related component |

## Abbreviations

| | |
|---|---|
| BP | Bottom profile |
| PIV | Particle image velocimetry |
| WG | Wave gauge |

## Definitions

| | |
|---|---|
| Nearshore processes | Wave transformation processes that occur when approaching the shore, e.g. shoaling, breaking, diffraction, refraction. |
| (Intra-)wave processes | Processes that occur when a wave passes, e.g. Stokes drift, Longuet-Higgins streaming, skewness, asymmetry, vortex tubes. |
| Wave properties | Properties that can be measured from each wave, e.g. wave height, orbital amplitude, skewness, asymmetry. |
| Sediment transport mechanisms | Causes of sediment transport, e.g. current related sediment transport, wave related sediment transport. |

## Directions & wave phase

The positive directions are shown in Figure 1a. In this study, the x-direction is the cross-shore direction and the y-direction is the longshore direction. Figure 1b shows the wave phases.

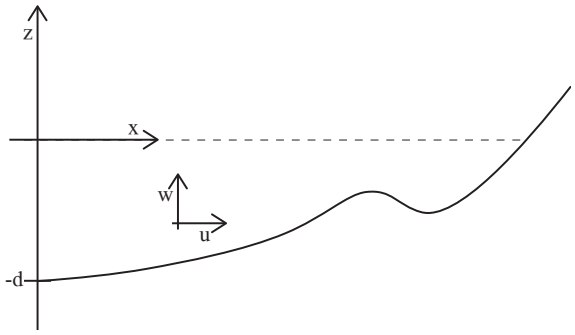


(a) Positive directions

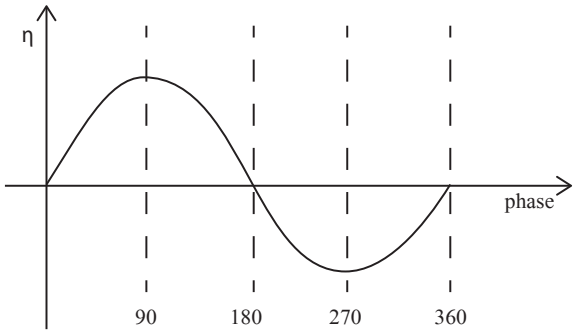


(b) Wave phases

Figure 1: Defined directions and wave phases

# 1 Introduction

## 1.1. Project description

This study investigates onshore sandbar migration and wave driven onshore sediment transport. To predict future coastline changes, it is important to understand and model wave driven sediment transport. Understanding onshore sandbar migration will improve coastal prediction models. Better prediction models enable a more effective and efficient design of nourishments and other coastal protection measures.

Longshore-aligned sandbars occur at many coasts in the nearshore. Sandbars affect the cross-shore wave transformation and profile evolution. During storms these bars act as natural breakwaters [Carter and Balsillie, 1983]. When the waves break on the bar, like during storms, the sandbar moves offshore (Figure 1.1a) [Gallagher et al., 1998, Thornton and Humiston, 1996]. During mild conditions, when the waves do not break on the bar, observations indicate an onshore migration of the bar (Figure 1.1b) [Aubrey, 1979, Wright and Short, 1984].

When assuming longshore uniformity, the onshore and offshore movement of the bar is caused by a gradient in the cross-shore sediment transport. For offshore migration a stronger undertow on top of the bar causes this gradient. For onshore bar migration the spatially varying process responsible for this gradient remains unclear, even though it is known that onshore wave-driven sediment transport is the primary mechanism in restoring the beach after storm erosion [Roelvink and Reniers, 2011]. The present study aims to determine the dominant wave processes that cause onshore bar migration by analysing the intra-wave sediment transport in the wave bottom boundary layer for non-breaking waves. The sediment velocities and sediment transport are studied to give insight in the driving mechanisms.

Sediment transport processes causing onshore bar migration are evaluated using data collected in the TU Delft hydraulic laboratory free surface wave flume over a mobile bed [Henriquez, 2016]. This data set shows onshore bar migration with the detail of individual suspension events. Particle Image Velocimetry (PIV) measurements of an onshore bar migration capture the hydrodynamics and bed level change on an intra-wave time scale close to the bed. The sampling locations are offshore, on top of, and onshore of the migrating bar, which corresponds to erosion, no bottom change, and sedimentation (Figure 1.1c). In addition to PIV measurements, the bottom profile was measured after each test, and the wave height was measured at several locations using wave gauges.

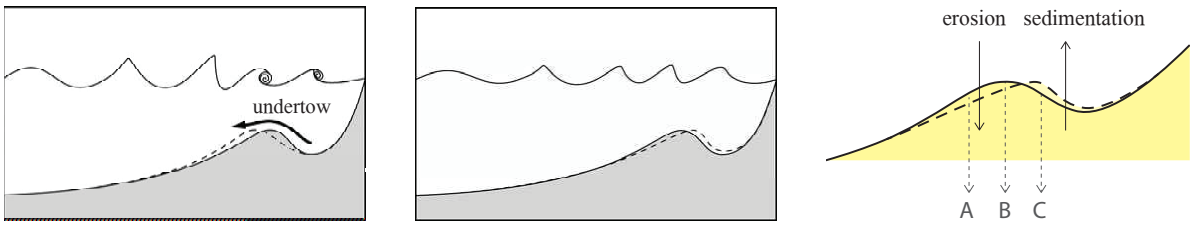


(a) Offshore bar migration (b) Onshore bar migration (c) Location of PIV measurements

Figure 1.1: Bar migration

## 1.2. Research questions

Multiple wave mechanisms affect cross-shore sediment transport. The present study uses PIV analysis to gain further understanding of *the dominant intra-wave process that causes onshore sandbar migration.*

This approach assumes a decomposition of sediment transport into current related sediment transport ($\overline{u} \cdot \overline{c}$), time-averaged long wave related sediment transport ($\overline{\tilde{u}_{LW} \cdot \tilde{c}}$) and time-averaged short wave related sediment transport ($\overline{\tilde{u}_{SW} \cdot \tilde{c}}$) (Equation 1.1, section 2.4). Current related sediment transport is caused by a mean velocity $\overline{u}$. Both wave related sediment mechanisms have a mean velocity of zero ($\overline{\tilde{u}} = 0$) and are due to the alignment of oscillatory velocity ($\tilde{u}$) and the oscillatory concentration ($\tilde{c}$) (section **??**).

According to the three sediment mechanisms, the different intra-wave processes (Table 1.1, section 2.4) can be divided in three groups: time-averaged processes, long periodic processes and short periodic processes. Time-averaged processes are visible in the mean velocity profile, while the mean velocity of periodic processes is zero.

$$\overline{S} = \overline{u \cdot c} = \overline{u} \cdot \overline{c} + \overline{\tilde{u}_{LW} \cdot \tilde{c}_{LW}} + \overline{\tilde{u}_{SW} \cdot \tilde{c}_{SW}} \tag{1.1}$$

The research topic can be divided in two main parts: (1) determining sediment transport based on PIV data and (2) the wave driven sediment transport analysis in the wave bottom boundary layer (Figure 1.2).

First, the sediment transport has to be determined based on the PIV data and has to be validated (research question I). This is especially important since it is innovative to calculate the sediment transport from PIV measurements. To validate this method, the sediment transport based on the PIV measurements is compared to the sediment transport based on the bottom measurements. The sediment transport calculated from the PIV measurements will further be referred to as PIV sediment transport.

Second, the PIV sediment transport can be analysed to understand the dominant mechanism of onshore sediment transport. First the most influential sediment mechanism will be determined. Therefore the current related transport is compared to the long wave related and short wave related sediment transport (research question II). Next, the dominant sediment mechanism found in research question II, namely time-averaged short wave related transport, will be studied in more detail in research question III. The focus of the short wave analysis is on the two intra-wave processes skewness and asymmetry. Because skewness and asymmetry can easily be determined at the free surface, an improved understanding of the two intra-wave processes can directly contribute to improving sediment transport predictions.

This leads to the following research questions:

*PIV sediment transport validation*

I. Can the bottom profile development be predicted from the results of the PIV analysis?
   a. How does the bottom profile develop over time?
   b. How can sediment transport be quantified from the PIV data? Most importantly, is it possible to quantify concentration from PIV data without additional concentration measurements?
   c. What is the difference between the calculated sediment transport from the bottom measurements and from the PIV analysis?

*Analysis of PIV sediment transport: sediment transport mechanisms*

II. What contributes most to the time-averaged sediment transport: the current related, the time-averaged long wave related or the time-averaged short wave related sediment transport?

*Time-averaged short wave related sediment transport*

III. When comparing skewness and asymmetry, which periodic short wave mechanism is the dominant cause of onshore bar migration?
   a. How does the development over depth of the wave properties relate to the sediment transport?
   b. How do the wave properties relate to the sediment transport in cross-shore direction (offshore, on top of, and onshore of bar, Figure 1.1c)?
   c. What is the relation between the wave shape of the velocity, concentration and sediment transport?
   d. What is the relation between the net sediment transport per wave and the wave properties?

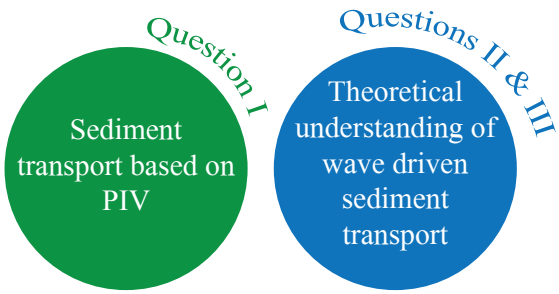


Figure 1.2: Story lines

Table 1.1: Overview of the intra-wave processes that affect the cross-shore sediment transport. This study focusses on the intra-wave processes skewness and asymmetry. The complete overview of all intra-wave processes is given as help to clearly understand wave driven onshore sediment transport. An elaborated explanation is given is section 2.4.

| | |
|---|---|
| *Current related sediment transport* | |
| 1. Stokes drift | Sinusoidal waves have a second order mean current, which can transport sediment [Stokes, 1847] (onshore). |
| 2. Longuet-Higgins streaming (Progressive wave streaming) | In the wbbl the vertical and horizontal velocity components are not 90 degrees out of phase. This causes a mean near-bed mean flow [Longuet-Higgins, 1953] (onshore). |
| 3. Wave-shape streaming | Skewness or asymmetry in the wbbl causes a fluctuating amount of turbulence in different wave phases. Because turbulence increases the shear stress, this results in a net turbulent shear stress [Kranenburg et al., 2013] (offshore). |
| *Time-averaged long wave related sediment transport* | |
| 4. Bound long waves | Because the large waves of the waves group stir up more sediment, bound long waves cause an offshore sediment transport (offshore). |
| *Time-averaged short wave related sediment transport* | |
| 5. Skewed wave: Velocity skewness | Skewed waves with higher crests than troughs suspend more sediment during the onshore orbital velocities, which causes onshore sediment transport [Henderson et al., 2004] (onshore). |
| 6. Asymmetrical wave: Acceleration skewness (Horizontal pressure gradient) | The different pressure gradients under the steep front and gentle back of asymmetric waves can cause sediment transport [Foster et al., 2006, Hoefel, 2003, Sleath, 1999] (onshore). |
| 7. Vortex tubes | Turbulent instabilities generated at a shear inflection point in the flow (Kelvin-Helmholtz instabilities) can cause sediment suspension (offshore). |
| 8. Vertical sediment advection | Net sediment transport due to the timing of the vertical velocities, similar to Stokes drift for mass transport (onshore). |
| 9. Horizontal sediment advection | Horizontal advection causes a increased concentration in front of the wave crest, which is taken towards the shore when the wave crest passes (onshore). |
| 10. Sediment phase lag | Slow response of the sediment can decrease the sediment transport and even transport it in opposite direction [Dohmen-Janssen, 1999]. |

# 2

# Literature study

*In this chapter the theoretical background is given for wave driven onshore sandbar migration.*

## 2.1. Bar migration in the nearshore

At many coasts longshore-aligned sandbars occur in the nearshore (Figure 2.1). Most swimmers have experienced the surprise of suddenly being able to stand far from the coast. These sandbars migrate constantly in cross-shore direction. During storms the bars act as natural breakwaters and the waves break above the bar. The sandbars move offshore during storm conditions (Section 2.1.1) [Hoefel, 2003]. During mild conditions observations indicate an onshore migration of the bar (Section 2.1.2) [Aubrey, 1979, Wright and Short, 1984].

The sandbar migrates towards a new equilibrium position around the breaking zone with every new wave climate [Pape et al., 2010]. Since the wave climate constantly changes on natural beaches, the bar is constantly relocating. In a two-dimensional situation this bar movement is caused by a gradient in the cross-shore sediment transport according to the Exner equation (Equation 2.1 & 2.2). The sediment balance in equation 2.1 is the classic Exner equation with sediment transport excluding pores. This equation is modified to equation 2.2 to calculate sediment transport including pores.

For this analysis, an assumption is made that bar migration is purely two-dimensional, i.e. an alongshore uniform coastline with perpendicular waves and no (longshore or tidal) currents. Since the cross-shore gradient in sediment transport drives bar migration, wave processes that cause sediment transport and have a maximum or minimum on top of the bar are studied.

$$\frac{\partial z_b}{\partial t} + \frac{1}{\epsilon_0}\frac{\partial S_x^*}{\partial x} = 0 \tag{2.1}$$

$$\frac{\partial z_b}{\partial t} + \frac{\partial S_x}{\partial x} = 0 \tag{2.2}$$

### 2.1.1. Offshore bar migration

The dominant cause of offshore bar migration is undertow. The undertow is the result of an imbalance over the vertical between set-up and wave force due to wave breaking. Wave breaking is the dominant wave process of offshore bar migration and drives the change in horizontal wave momentum, also called radiation

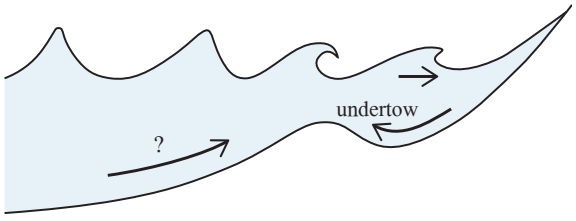


Figure 2.1: Bar migration by undertow and unknown mechanism

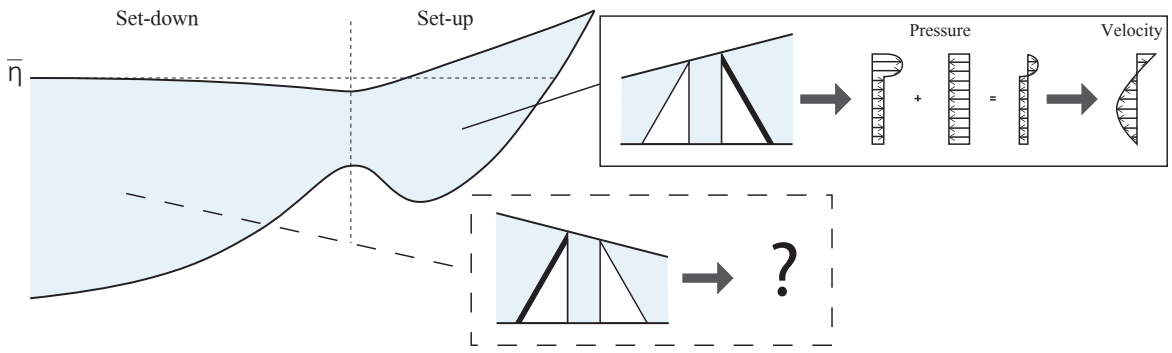


Figure 2.2: Set-down and set-up with the pressure balance

stress (Appendix B.3.3). Integrated over the vertical these forces are equal (Equation 2.3), but the forces have a different distribution over the vertical (Figure 3.2). This imbalance causes a circulation that is directed offshore close to the bottom (Figure 3.2). The bottom current, the undertow, drags sediment along causing offshore sediment transport. The strong undertow overrules streaming velocities close to the bed [Bosboom and Stive, 2015, p.184]. Undertow has a maximum on top of the bar.

$$\frac{\partial}{\partial x}[S_{xx}] = \frac{\partial}{\partial x}[\overline{\int_{z_b}^{\eta} \rho \tilde{u}^2 \, dz} + \overline{\int_{z_b}^{\eta} p_{wave} \, dz}] = -\frac{\partial \eta}{\partial x} \tag{2.3}$$

### 2.1.2. Onshore bar migration

For onshore bar migration there is no clear dominant wave process, like wave breaking for offshore bar migration. Without a closed boundary or dominant wave process, the driving mechanism of onshore bar migration remains unknown. Therefore the possible intra-wave processes driving onshore sediment transport is studied further in section 2.4.

## 2.2. Waves in the nearshore

Many people see a wave as a forward traveling surface elevation, while the water particles below the surface actually only move back and forward. Only the pressure disturbance travels forward, which can transport momentum and energy [Holthuijsen, 2007]. Where sound waves (Figure 2.3a) have a one dimensional motion, water waves (Figure 2.3b, 2.4a) have a two dimensional orbital motion due to the free surface. Due to the asymmetric boundaries, the free-surface versus the bottom, the orbital velocities decrease over the vertical and the waves can cause a mass transport. Mass, momentum and energy transport by waves is explained in Appendix A. In this analysis wave refers to water wave (surface gravity wave).

To describe the particle motion in surface gravity waves in equations, the wave is divided in an upper an lower part: the free-stream motion and the wave bottom boundary layer (Figure 2.4b). This division is based on the assumption that the rotation generated by the bottom friction stays close to the bottom in the wave bottom boundary layer (wbbl). In overview:

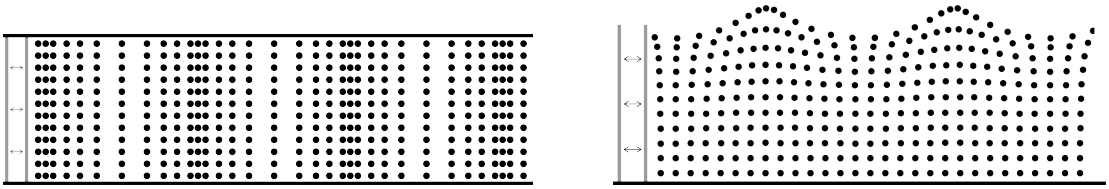

(a) Sound wave

(b) Surface wave

Figure 2.3: Waves

| | | |
|---|---|---|
| 1. | Free-stream orbital motion | Assumed frictionless and rotation free, linear wave theory (Equation 2.4 & 2.5, Appendix B.1). |
| 2. | Wave bottom boundary layer (wbbl) | Rotation not negligible, linear wave theory not valid. Phase lead and change in wave shape (phase shift). |

With high sediment concentrations near the bed, the largest part of the sediment transport occurs in the wbbl. Therefore the wbbl is the most important in sediment transport calculations. First the orbital velocities at the top of the wbbl can be calculated with linear wave theory ($\hat{u}_\infty$, Equation 2.6) [e.g. van Rijn, 1990, p.260]. Second the velocity transformation in the wbbl has to be calculated.

The velocity transformation in the wbbl is more complex due to the variation in wbbl thickness and bottom influence on the velocity signal. The wbbl is only a few millimeters to centimeters thick [Nielsen, 1992]. The thickness increases with wave period, since the wbbl has more time to develop. The thickness also increases with increasing viscosity and bed roughness. Different definitions of the wbbl thickness are given in Appendix C.4.3.

In the wbbl, drag induced from the bottom friction decelerates the fluid and rotation is not negligible. The vertical velocities become smaller, giving a flat elliptical motion. The smaller velocities in the wbbl have less inertia and can therefore react quicker to a varying pressure gradient. This results in a phase lead of the wbbl velocities to the free-stream velocity.

$$u = \hat{u} \cdot cos(\omega t - kx), \qquad \hat{u} = \frac{\omega a \cdot \cosh(k(z - z_b))}{\sinh(-z_b \cdot k)} \tag{2.4}$$

$$w = \hat{w} \cdot \sinh(\omega t - kx), \qquad \hat{w} = \frac{-\omega a \cdot \sinh(k(z - z_b))}{\sinh(-z_b \cdot k)} \tag{2.5}$$

$$\hat{u}_\infty = \frac{\omega a}{\sinh(-z_b \cdot k)} \tag{2.6}$$

### 2.2.1. Approaching the sandbar

When waves enter the nearshore and approach the sandbar, four important processes occur: shoaling, obtaining the skewed shape (triad interactions), wave breaking and bound long waves. All processes are due to the dependence of the wave speed on the water depth in the nearshore. With the decreasing water depth towards the shore, the wave speed decreases. The decreasing celerity towards the shore causes a wave congestion: the wave group celerity decreases and the wave energy transport remains constant, so the wave energy and with that the wave height go up towards the shore (Appendix A.4). This is called shoaling. Even shallower the wave celerity of the crest becomes higher than that of the trough: the waves start to pitch forward and finally break.

When approaching the sand bar, the waves cause a set-down. Larger waves cause a larger set-down. Therefore the approaching wave groups cause bound long waves, which have the crest at the moment of small waves and the through at the moment of large waves.

These nearshore processes affect the *wave shape*. In the shoaling area the waves get a skewed shape due to non-linear interaction and in the surfzone the waves have an asymmetric shape. Figure 2.6a shows this nearshore change of the wave shape. The changes in orbital motion influence the mass, momentum and energy transfer of the waves.

Wave skewness causes skewed orbital velocities and asymmetric accelerations, while wave asymmetry causes asymmetric velocities and skewed accelerations (Figure 2.8). Therefore the skewness parameter is

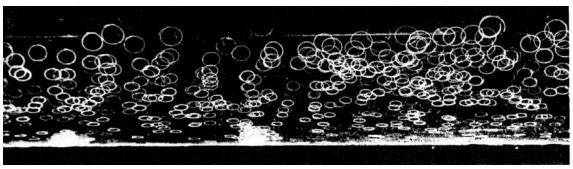

(a) Orbital motion by particle tracking [Wallet and Ruellan, 1950]

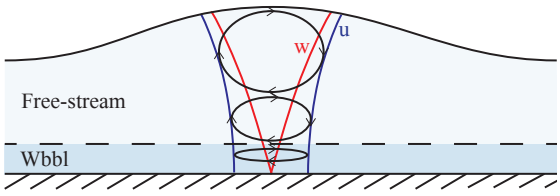


(b) Orbital motion by linear wave theory

Figure 2.4: Orbital motion

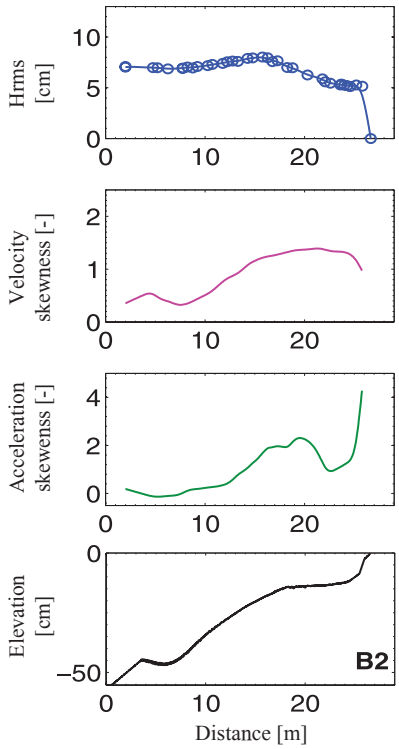


Figure 2.5: Wave properties at an accreting beach profile. Case B2 starts with a very wide sandbar, which start moving onshore as a dune propagation and develops a asymmetry shape with a steep shoreward slope. Hence this situation is comparable to onshore sandbar migration. [Grasso et al., 2009] (fig. 12)

based on the peak trough ratio of the velocity signal (Equation 2.7) [Ribberink and Al-Salem, 1994] and the asymmetry parameter on the peak trough ratio of the acceleration signal (Equation 2.8) [Watanabe and Sato, 2004]. Equations 2.9 and 2.10 give the skewness and asymmetry [Ruessink et al., 2012], in which $i\Gamma$ is the Hilbert transformation. Normalised, the properties ($Sk$, $As$) express the wave shape. When non- normalised, the properties ($Sk^*$ and $As^*$) can be used to calculate sediment transport (section 2.4).

$$R_u = \frac{u_{max}}{u_{max} - u_{min}} \tag{2.7}$$

$$R_a = \frac{a_{max}}{a_{max} - a_{min}} \tag{2.8}$$

$$Sk = \frac{\overline{\tilde{u}^3}}{\sigma_{\tilde{u}}^3} = \frac{\overline{\tilde{u}^3}}{(\overline{\tilde{u}^2})^{1.5}}, \qquad Sk^* = \overline{\tilde{u}^3} \tag{2.9}$$

$$As = \frac{\overline{i\Gamma(\tilde{u})^3}}{(\overline{\tilde{u}^2})^{1.5}}, \qquad As^* = \overline{i\Gamma(\tilde{u})^3} \tag{2.10}$$

Mathematically the wave shape is a summation of waves with different frequencies ($f1$, $f2$, $f3$, $f4$, $f5$, etc.) (Figure 2.6b). In deep water the wave speed depends on the wave length. Hence the different frequencies are separate waves, all travelling with their own speed through each other and the wave shape changes constantly. In shallow water the wave speeds depends on the depth. When all frequencies have the same speed, the different frequencies are bound together as one wave. Hence the wave shape is fixed and the higher harmonic frequencies determine the wave shape (Figure 2.7a). Equation 2.11 describes a wave, in which $\Phi_n$ is the waveform parameter. More energy in these higher frequencies gives more skewness and/or asymmetry. Hence in shallow water these higher harmonic frequencies become more pronounced in the wave spectrum (Figure 2.6b).

Because the *wave shape in the wbbl* influences the wave driven sediment transport, it is important to realise that the wave shape in the wbbl is different from the wave shape in the free-stream orbital motion.

The wave shape visible on the water surface is equal to the wave shape of the free-stream orbital motion. This wave shape is a summation of waves with different frequencies ($f1$, $f2$, $f3$, $f4$, $f5$, etc.). This wave shape will change in the wave bottom boundary layer, because the harmonic frequencies will relocate due to the near-bed phase lead. This is also referred to as *phase shift*. There are different possible methods to predict the near-bed velocity wave shape: a constant phase lead (frequency-independent phase lead), a frequency dependent phase lead and the method of Nielsen and Callaghan [2003] [Roelvink and Reniers, 2011]. Terrile et al. [2009] proposed to improve the the method of Drake and Calantoni [2001] based on the waveform parameter, $\Phi_n$ (Equations 2.11, 2.12). Abreu et al. [2010] further developed this concept.

When assuming a frequency-independent phase lead, all wave harmonics have the same phase shift. Since the harmonics have different wave lengths, this results in different time shifts. As a result of these different time shifts the wave harmonics relocate relative to each other and the wave shape changes. After deciding on a phase shift method, Equation 2.12 describes the wave shape in the wbbl, in which $\phi_{b,n}$ is the phase shift per frequency [Abreu et al., 2010, Drake and Calantoni, 2001]. The phase lead gradually changes over depth in the wbbl, so at each height in the wbbl the wave will have an unique wave shape.

For a laminar flow the phase lead is $45^o$ and constant for all harmonic frequencies (1/8 of their period). Therefore in laminar flow, the wave shape in the wbbl can be calculated analytically with linear wave theory by summing all harmonic frequencies to get the wbbl wave shape [Henderson et al., 2004]. For turbulent flow, the the phase leads depends on the amount of turbulence (Figure 2.7b) [Carstensen et al., 2010a, Dohmen-Janssen, 1999, p.10] and does not have to be constant for all harmonic frequencies. With a numerical analysis Henderson et al. [2004] find $25^o$ for coastal waters based on the assumption that all harmonic frequencies have the same phase shift (relative to their specific wave period).

$$u = \sum_{n=1}^{N} \hat{u}_n \cdot \cos(\omega_n t + \Phi_n) \tag{2.11}$$

$$u_b = \sum_{n=1}^{N} \hat{u}_{b,n} \cdot \cos\left(\omega_n t + \Phi_n + \phi_{b,n}\right) \tag{2.12}$$

### 2.2.2. Passing the sandbar

If the wave don't break on the bar, the skewed and asymmetric waves approach deeper water. In deeper water the frequency becomes relatively more important for the phase speed. The bound harmonics of the skewed and asymmetric waves release in deepening water (down-slope) [Beji and Battjes, 1993]. This phenomenon of harmonic decoupling changes the wave shape.

Next to that the bound long waves become free long waves. Because the large waves break first, there are no fixed wave groups any more. This releases the long waves. Hence in the breaking zone only free long waves occur. Because the largest breakers give the largest set-up, the free long waves have the crest at the moment of largest waves and though at the moment of smallest waves.

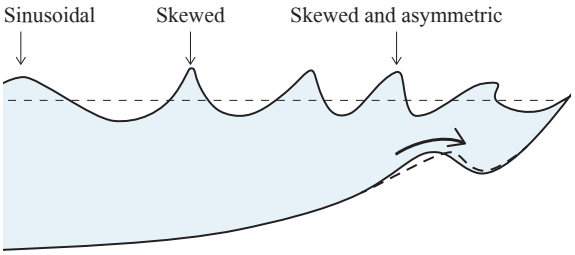


(a) Wave shape during onshore bar migration [Henriquez, 2016]

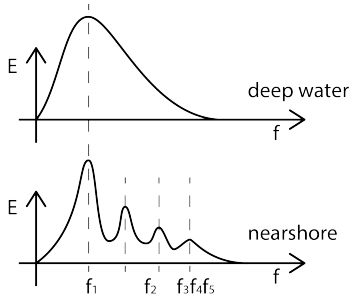


(b) Sketch of deep water and nearshore wave spectrum

Figure 2.6: Wave shape in the nearshore

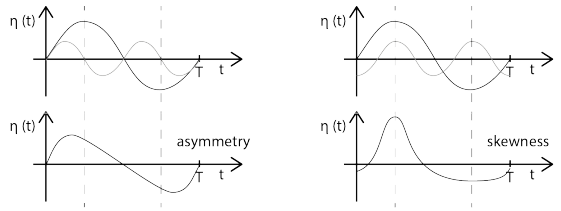


(a) Skewness and asymmetry based two frequencies. If the higher harmonic is $90^o$ out of phase the wave is asymmetric. If the higher harmonic is in phase, the wave is skewed.

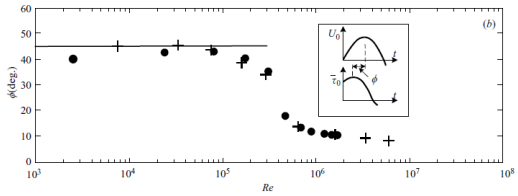


(b) Relation between Reynolds number and phase lead [Carstensen et al., 2010a] (fig.21).

Figure 2.7: Schematisation of non-linear waves and the relation between turbulence and phase lead.

## 2.3. Sediment transport

Sediment transport can be calculated by multiplying the sediment velocities and the concentration (Equation 2.13). Most sediment transport occurs in the direction of the near-bed currents, because the concentrations close to the bottom are high.

$$S_x = \int_{z_b}^{\eta} c \cdot u_{sediment}\ dz \tag{2.13}$$

Sediment velocity is caused by flow velocities and accelerations (Equation 2.14). *Drag* is the shear stress between the flow velocity and the sediment grains and is expressed with the Shields parameter (Appendix C.3). *Pressure differences* cause flow acceleration and sediment acceleration. Sediment acceleration due to a pressure difference is expressed with the Sleath parameter (Appendix C.3). Friction between the grains decreases the sediment movement.

On larger scale *drag* is called bottom shear stress. Empirical formulas use bottom shear stress as measure of sediment suspension and describe a quadratic relation between bottom shear stress and the horizontal velocities (Appendix C.4). This relation is quadratic, because the horizontal velocities not only move sediment through drag but also decrease the necessary shear stress (*grain interaction*) by decreasing the normal force with lift forces.

$$Horizontal\ force = drag + pressure + grain\ interaction \tag{2.14}$$

In this research the sediment velocities are assumed equal to the flow velocities (Equation 2.15). Particles with little inertia (fines) follow the orbital motion, larger particles with more inertia do not fully follow the orbital motion due to gravity. Hence this assumption is only valid with light particles.

$$u = u_{flow} \approx u_{sediment} \tag{2.15}$$

Sediment transport can be divided in two types: bed load transport and suspended load transport (Figure **??**). *Bed load transport* is instantaneous sediment transport close to the bottom. Hence the sediment is picked

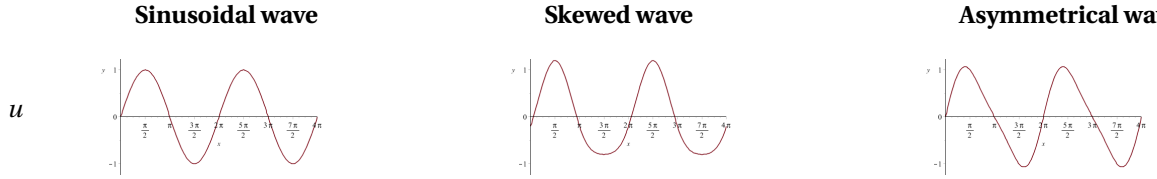


(a) Symmetric velocity (b) Skewed velocity (c) Asymmetrical velocity

(d) Symmetric acceleration (e) Asymmetrical acceleration (f) Skewed acceleration

Figure 2.8: Orbital velocity and acceleration of different wave types with a maximum orbital velocity of 1.

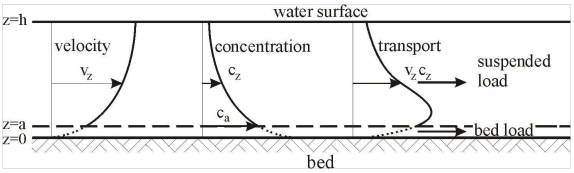


Figure 2.9: Sediment transport [Graaff, 2009] (p.78)

up and transported simultaneously. A specific type of bed load transport is *sheet flow* : at high shear stresses (large Shields parameter) the particles start to move in multiple layers close to the bed, a continuous 'sheet' of approximately 10 ~ 60 grains thick [Dohmen-Janssen, 1999]. *Suspended load transport* occurs higher in the water column and therefore sediment needs time to be picked up and settle. Due to this suspension and settling time, the sediment is not simultaneously picked up and transported. This separates suspension causing velocities and transporting velocities.

Often turbulence or waves suspend the sediment and currents transport it [Nielsen, 1992, p.2]. In the results of Dohmen-Janssen [1999] (Figure 2.10) it is clearly visible that the sediment is moved upwards by the orbital velocities. For unbroken waves the friction of the orbital flow and thus sheet flow is dominant and for broken waves the turbulence and thus suspended load is dominant [Henriquez, 2016]. Hence in case of unbroken waves the sediment transport can be assumed instantaneous.

## 2.4. Wave driven sediment transport in the nearshore

Onshore bar migration is caused by a gradient in the cross-shore sediment transport by a maximum in onshore transport or minimum in offshore transport. To find the dominant cause of onshore bar migration, this section will explain the possible wave driven sediment transport mechanisms. The largest part of wave driven sediment transport by short surface waves occurs in the sheet flow layer (80-90 % Dohmen-Janssen [1999, p.205]). Hence the focus will be on the effect of wave mechanisms close to the bottom.

When neglecting diffusion, sediment transport can be calculated with concentration multiplied by velocity (Equation 2.16). Under the assumption that the sediment moves with the fluid velocity this becomes concentration multiplied by fluid velocity.

$$S_x = c \cdot u_{sediment} \approx c \cdot u \tag{2.16}$$

In wave dominant environments, the oscillatory motion of waves mostly moves sediment forwards and backwards, but only the net (mean) sediment transport affects bed level change. Therefore the sediment transport will be averaged over time (Equation 2.17). The difference between large gross transport and small net transport makes accurate predictions difficult. On the long term these small net transports can have important impact [Ruessink et al., 2007]. Onshore wave-driven sediment transport is the primary mechanism in restoring the beach after storm erosion [Roelvink and Reniers, 2011].

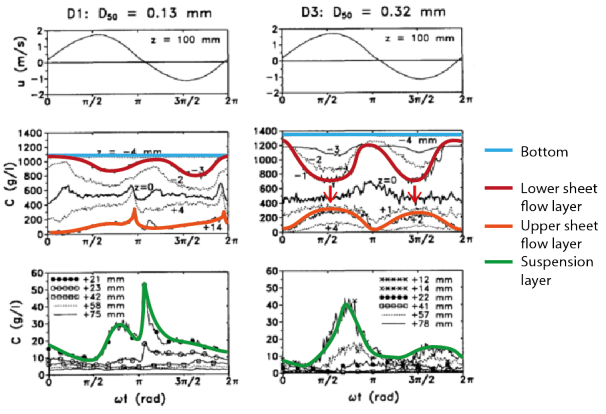


Figure 2.10: Results of Dohmen-Janssen [1999, p.117]: free-stream velocities (top), concentrations in sheet flow layer (middle) and suspension layer (bottom) for fine (left) and coarse (right) sediment

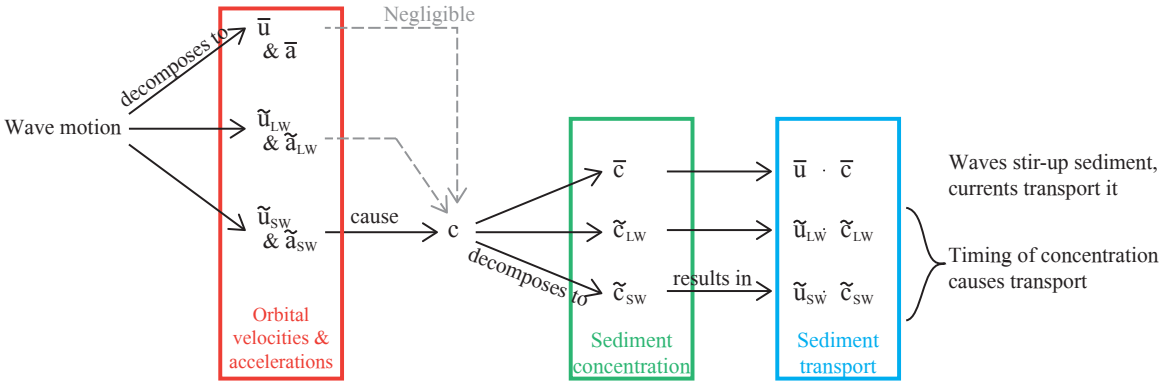


Figure 2.11: Overview of the wave driven sediment transport mechanisms

$$\overline{S_x} = \overline{c \cdot u} \tag{2.17}$$

To have a more detailed look at sediment transport, the orbital motion will be decomposed in a mean and oscillatory velocity component (Equation 2.18). There are two important wave types that influence the sediment transport: long waves (infragravity waves) and short waves (wind waves). Hence the oscillatory component can be further subdivided in a long wave component and a short wave component (Equation 2.19).

Next tot that the orbital motion causes the sediment suspension in wave driven sediment transport. With high velocities close to the bottom, the short waves cause most sediment suspension [Roelvink and Stive, 1989] (Figure 2.11). Therefore the effect of the mean and long wave components will be neglected. Because only multiples/cross-terms of the same frequency give a non-zero result when time averaging, the sediment concentration will be divided in the same components as the orbital velocity: mean concentration, long wave oscillatory concentration and short wave oscillatory concentration (Equation 2.20).

When first multiplying the decomposed velocity and concentration and second time-averaging, three sediment transport components remain: the current related sediment transport ($\overline{u} \cdot \overline{c}$), the time-averaged long wave related sediment transport ($\overline{\tilde{u}_{LW} \cdot \tilde{c}_{LW}}$) and the time-averaged wave related sediment transport ($\overline{\tilde{u}_{SW} \cdot \tilde{c}_{SW}}$) (Equation 2.21).

The other cross-terms are zero, because only the cross-terms with the same frequency are non-zero when time averaging. Without decomposing the concentration, the sediment transport can also be divided in the same three transport component (Equation 2.22).

$$u = \overline{u} + \tilde{u}, \qquad \overline{\tilde{u}} = 0 \tag{2.18}$$

$$u = \overline{u} + \tilde{u}_{LW} + \tilde{u}_{SW} \tag{2.19}$$

$$c = \overline{c} + \tilde{c}_{LW} + \tilde{c}_{SW} \tag{2.20}$$

$$\overline{S} = \overline{u \cdot c} = \overline{u} \cdot \overline{c} + \overline{\tilde{u}_{LW} \cdot \tilde{c}_{LW}} + \overline{\tilde{u}_{SW} \cdot \tilde{c}_{SW}} \tag{2.21}$$

$$\overline{S} = \overline{u \cdot c} = \overline{u} \cdot \overline{c} + \overline{\tilde{u}_{LW} \cdot c} + \overline{\tilde{u}_{SW} \cdot c} \tag{2.22}$$

For the current related transport ($\overline{u} \cdot \overline{c}$) the oscillatory velocities stir-up the sediment and te wave current transports it. On natural beaches, tidal and longshore currents will add to the wave current ($\overline{u}$) and contribute to the transporting the sediment. Often waves stir-up the sediment and currents transport it. Therefore it is important to model the effect of waves on the mean concentration ($\overline{c}$) correctly.

For wave related transport (short and long waves) timing of concentration causes the sediment transport. In other words,the sediment transport depends on the alignment of concentration with the velocity. If there is more sediment in suspension during a certain orbital velocity, this causes a mean sediment transport. In purely wave driven sediment transport, the short wave related transport is important.

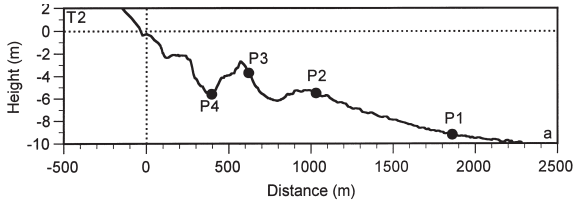


(a) Location of measurement

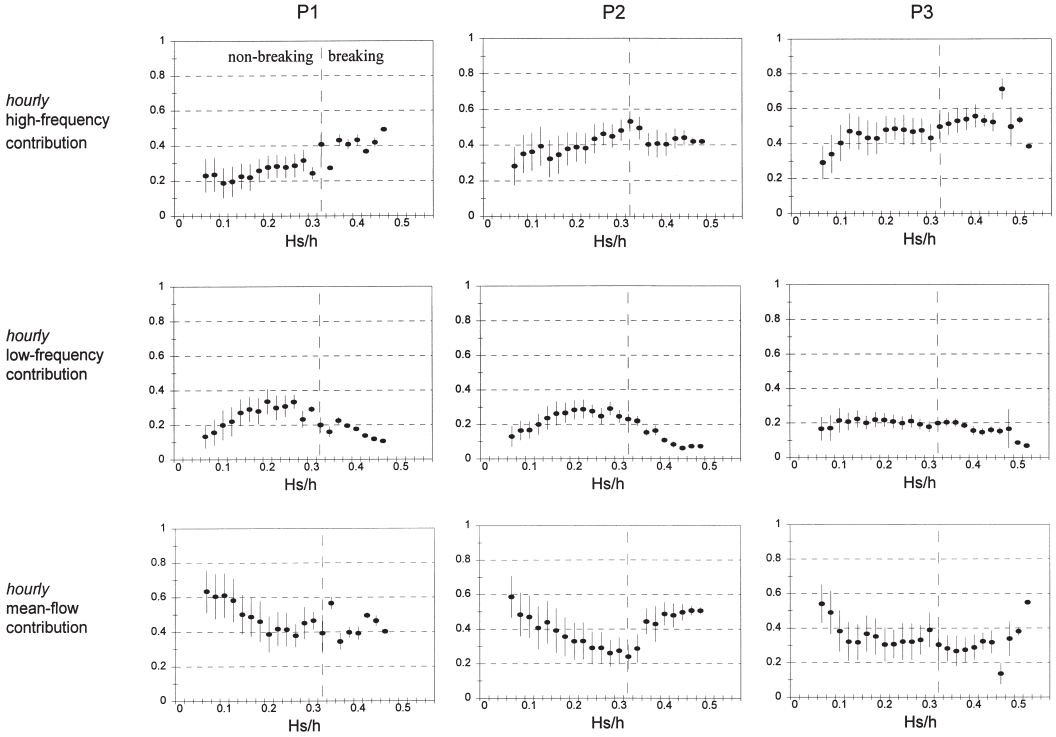


(b) Ratio between mechanisms on an hourly scale during low-energy, non breaking conditions (onshore bar movement)

Figure 2.12: Results of field observations of Ruessink et al. [1999] showing the ratio between the three sediment mechanisms.

Yu et al. [2010] compares the relative importance of non-linear wave shape (skewness, asymmetry) and streaming in a two-phase model. Yu et al. [2010] found that for skewed waves non-linear wave shape is the dominant onshore transport mechanism and streaming only causes an additional 36 %. Ruessink et al. [1999]: The influence of non-breaking high-frequency waves increases towards the shore (Figure 2.12) and found for non-breaking waves close to the shore during low-energetic conditions on average a ratio of around 40 % high frequency, 20 % low frequency and 30-40 % current related transport. In the following sections the velocity and concentration components will be explained. The components can be further separated in intra-wave processes that affect sediment transport.

This study will focus on the intra-wave processes skewness and asymmetry, but in this section all intra-wave processes are explained to give a complete overview as help to clearly understand wave driven onshore sediment transport. Table 2.1 gives an overview of all intra-wave processes. Most onshore processes increase towards the top of the bar (Stokes drift [Henderson et al., 2004], LH-streaming [Trowbridge and Young, 1989], asymmetry [Elgar et al., 2001] and with that near bed skewness [Henderson et al., 2004]), which makes it difficult to determine the dominant wave mechanism that causes onshore bar migration by comparing the different locations.

### 2.4.1. Mean velocity

Surface gravity waves have a mean mass transport due to the asymmetry over the vertical (section 2.2, Appendix A.2). This mean current will transport sediment. The mean current is divided in three processes: Stokes drift (section 2.4.1.1), Longuet-Higgins streaming (section 2.4.1.2) and wave shape streaming (section

Table 2.1: Intra-wave processes that affect the cross-shore sediment transport

| | |
|---|---|
| *Current related sediment transport* | |
| 1. Stokes drift | Sinusoidal waves have a second order mean current, which can transport sediment [Stokes, 1847] (onshore). |
| 2. Longuet-Higgins streaming (Progressive wave streaming) | In the wbbl the vertical and horizontal velocity components are not 90 degrees out of phase. This causes a mean near-bed mean flow [Longuet-Higgins, 1953] (onshore). |
| 3. Wave-shape streaming | Skewness or asymmetry in the wbbl causes a fluctuating amount of turbulence in different wave phases. Because turbulence increases the shear stress, this results in a net turbulent shear stress [Kranenburg et al., 2013] (offshore). |
| *Time-averaged long wave related sediment transport* | |
| 4. Bound long waves | Because the large waves of the waves group stir up more sediment, bound long waves cause an offshore sediment transport (offshore). |
| *Time-averaged short wave related sediment transport* | |
| 5. Skewed wave: Velocity skewness | Skewed waves with higher crests than troughs suspend more sediment during the onshore orbital velocities, which causes onshore sediment transport [Henderson et al., 2004] (onshore). |
| 6. Asymmetrical wave: Acceleration skewness (Horizontal pressure gradient) | The different pressure gradients under the steep front and gentle back of asymmetric waves can cause sediment transport [Foster et al., 2006, Hoefel, 2003, Sleath, 1999] (onshore). |
| 7. Vortex tubes | Turbulent instabilities generated at a shear inflection point in the flow (Kelvin-Helmholtz instabilities) can cause sediment suspension (offshore). |
| 8. Vertical sediment advection | Net sediment transport due to the timing of the vertical velocities, similar to Stokes drift for mass transport (onshore). |
| 9. Horizontal sediment advection | Horizontal advection causes a increased concentration in front of the wave crest, which is taken towards the shore when the wave crest passes (onshore). |
| 10. Sediment phase lag | Slow response of the sediment can decrease the sediment transport and even transport it in opposite direction [Dohmen-Janssen, 1999]. |

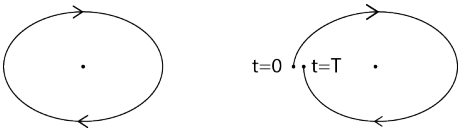


Figure 2.13: Linear orbital motion (closed orbit) versus non-linear orbital motion (non-closed orbit) [van Rijn, 1990, p.245]

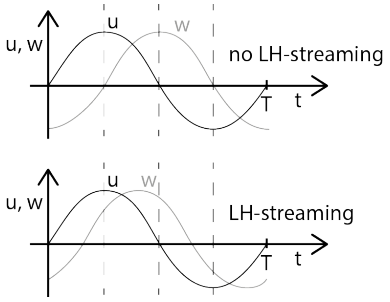


Figure 2.14: Phase difference between horizontal and vertical velocities and LH-streaming

2.4.1.3). Stokes drift and boundary layer streaming have the same order of magnitude [Henderson et al., 2004, p.2]. An overview of the moment of occurrence of the different processes is given in Table **??**.

#### 2.4.1.1 Stokes drift

Stokes drift occurs because the horizontal orbital velocities decrease with depth (Figure 2.13, Appendix A.2, term 2.23). Stokes drift can cause sediment transport by carrying entrained sediment. In numerical models the Stokes drift is simulated by the (non-linear) advection terms.

Henderson et al. [2004] showed the importance of the Stokes drift by failing to predict onshore bar migration without the non-linear advection terms. Removal of the advection terms from the momentum equation (Stokes drift) or the sediment conservation equation had around the same impact [Henderson et al., 2004, p.12].

$$\frac{\partial \tilde{u}}{\partial z} \tag{2.23}$$

#### 2.4.1.2 Longuet-Higgins streaming

LH-streaming is an onshore directed wbbl current caused by the vertical transport of horizontal momentum, because $\tilde{u}$ and $\tilde{w}$ are not $90^o$ out of phase in the wbbl (Appendix A.2, term 2.24). Longuet-Higgins streaming occurs in the wbbl, where the sediment concentration is relatively high. The streaming velocities increase with an increasing wave height $H$ and wave period $T$ [Longuet-Higgins, 1953] and decrease with increasing wave length $L$ and wave asymmetry [Naqshban et al., 2009]. Time and depth variation of eddy viscosity has a positive contribution to the streaming velocities [Naqshban et al., 2009].

Bosboom and Klopman [2001] found that LH-streaming contributed 40 % to the total sediment transport by comparing a propagating wave to a wave tunnel in a numerical model that solves intra-wave oscillatory motion and sediment concentration.

Since LH-streaming is caused by the asymmetrical overlap of horizontal and vertical orbital velocities (Figure 2.14), the important wave phases will be between $65^o$ ($90^o$ -$25^o$) and $155^o$ ($180^o$ - $25^o$).

$$\frac{\partial \overline{\tilde{u}\tilde{w}}}{\partial z} \tag{2.24}$$

#### 2.4.1.3 Wave shape streaming

In the nearshore, due to the changes in wave shape an extra form of streaming occurs in the wbbl: wave shape streaming, also called turbulent wbbl current. Where LH-streaming is caused by the orbital velocities ($\tilde{u}$, $\tilde{w}$), wave shape streaming is caused by the turbulent velocities ($u'$, $w'$, term 2.25). The shape of the orbital motion in the wbbl in combination with the covariance between eddy viscosity and shear stress causes an offshore wbbl current. This offshore streaming is measured in wave tunnels, where there are no vertical velocities and hence no LH-streaming (section A.2.2). For moderately energetic waves, Trowbridge and Madsen [1984]

showed that wave shape streaming can decrease or even reverse LH-streaming, since in coastal waters the turbulent stresses are larger than viscous stresses due to orbital velocities [Bosboom and Stive, 2015, p.182].

Positive skewness in the wbbl causes larger and shorter onshore velocities. These larger velocities cause more turbulence. More turbulence means a higher shear stress, since mixing increases the velocity gradient close the bottom. With a fixed bottom, the bottom does not start moving with this higher shear stress. According to Newton's third law, action is reaction. So the flow will be pushed backwards. It is like pushing against a tree, while standing on ice-skates: you will slide backwards just like the flow field. For a mobile bed, the effect decreases, since the velocity gradient close to the bottom decreases. But the effect remains the same: if you stand on ice-skates and you throw a ball, you will still slide backwards.

Because the amount of turbulence increases with velocity, the shear stress is not linearly related to velocity (section 2.3). The wave-averaged turbulent shear stress is larger for onshore velocities, resulting in a net offshore flow [Dohmen-Janssen, 1999, p.14].

$$\frac{\partial \overline{u'w'}}{\partial z} \tag{2.25}$$

### 2.4.2. Long wave oscillatory velocity

Long waves occur because waves travel in wave groups. In a wave group the large waves and small waves are clustered together. Because large waves have a larger mean wave current (section 2.4.1), the mean velocity varies on the wave group scale. This relatively long scale variation in near-bead velocities is the long wave component of the velocity signal. Hence, long wave influence close to the bed is the variation in mean current during the wave group.

### 2.4.3. Short wave oscillatory velocity

Short waves have relatively quickly varying orbital velocities. Because the time for the wave bottom boundary layer to develop is very limited, the wbbl stays relatively thin and the orbital velocities are high close to the bed. Theory describes that short waves stir up the sediment due to these high orbital velocities close to bottom. Since the mean oscillatory velocity is zero, sediment transport depends on the timing of suspension and only occurs with an oscillatory concentration that is in phase with the oscillatory velocity (section 2.4.6).

### 2.4.4. Mean concentration

Sediment can be stirred up by velocities through shear stress and by a pressure force (Appendix C.3). Hence all velocities (mean, oscillatory and turbulent) and corresponding pressure gradients can stir up sediment.

Measurements of concentration profiles in the sheetflow layer suggest a nearly linear concentration curve (Figure 2.15). O'Donoghue and Wright [2004a] shows that the time-averaged concentration profile is well characterised with Equation 2.26, which is similar to the Rouse profile. In this equation is $\overline{c}$ the concentration normalised by the concentration in the bed, $\overline{c}_a$ the normalised reference concentration at reference height $z = z_a$, $z$ the elevation above the still bed, $\delta_e$ the instantaneous erosion depth and $\alpha$ is a shape parameter of the concentration profile. The parameters $\overline{c}_a$, $\delta_e$ and $\alpha$ are time dependent.

$$\overline{c} = \frac{(z_a + \delta_e)^\alpha}{(z_a + \delta_e)^\alpha + \left[\frac{1}{\overline{c}_a} - 1\right](z + \delta_e)^\alpha} \tag{2.26}$$

### 2.4.5. Long wave oscillatory concentration

Bound long waves have their crest during the small waves of the wave group and their through during the large waves of the wave group. Because these large waves stir up more sediment, the sediment concentration is higher during the offshore orbital velocities of the long wave (Figure 4.11). This results in offshore sediment transport. In other words, the long waves cause sediment transport because their is a correlation between the frequency of orbital velocities of the long wave ($\tilde{u}_{LW}$) and frequency of concentration variation due to short waves. Hence the sediment transport is fully caused by the timing of high concentration. In this study, the concentration variation at the group time scale is referred to with the long wave oscillatory velocity ($\tilde{c}_{LW}$).

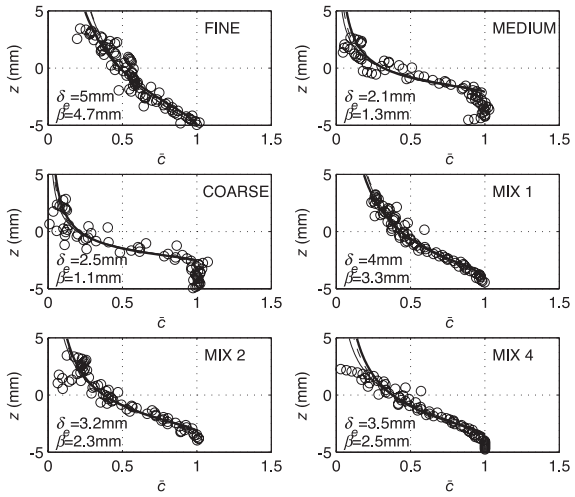


(a) Concentration measurements in sheetflow at maximum onshore velocity and three fits O'Donoghue and Wright [2004a].

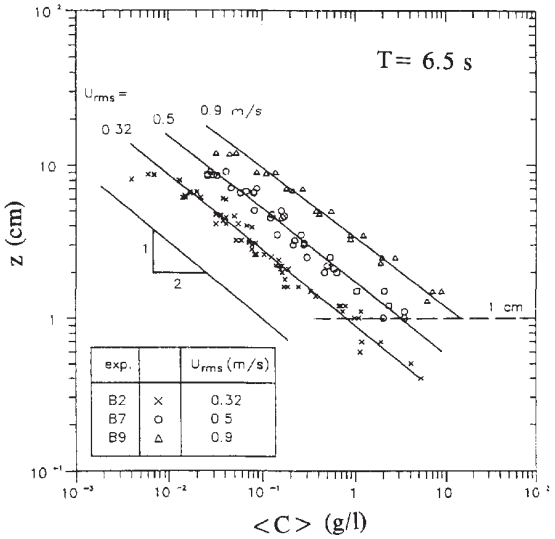


(b) Velocity influence ($u_{rms}$) on sediment concentration [Al-Salem, 1993] (fig 8.9).

Figure 2.15: Observed concentration profile in the sheetflow layer.

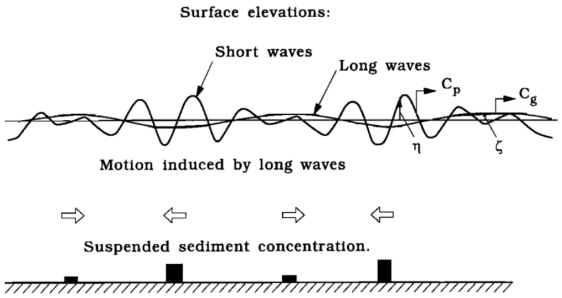


Figure 2.16: Visual explanation of offshore sediment transport due to bound long waves [Deigaard et al., 1999, fig.1]. Because the large waves in the wave group stir-up more sediment and simultaneously cause the through of the long wave, the net long wave related transport is directed offshore.

### 2.4.6. Short wave oscillatory concentration

Because the mean short wave oscillatory velocity is zero, the short wave related sediment transport fully depends on the timing of sediment concentration. Therefore this section describes multiple wave mechanisms cause a concentration increase at a specific wave phase (Table 2.1). The amount of sediment transport depends on the alignment between the concentration peak and the maximum velocity. More sediment transport occurs with a larger alignment between the concentration peak and the maximum velocity.

#### 2.4.6.1 Skewness

With velocity skewness onshore velocities are larger and of shorter duration than offshore velocities (Figure 2.8b). Because these higher velocities suspend more sediment and transport the sediment faster, the sediment transport is non-linearly related to the orbital velocities. Since the shear stress, which causes the suspension, is already non-linearly related to the velocity (section 2.3, Equation 2.27), the sediment transport is related to the velocity with a power 3 or higher as found in classical sediment transport formulas (Equation 2.29, often $m = 3$). Due to this higher power the wave-averaged sediment transport is non-zero for a skewed wave, while the wave-averaged velocity is zero. The analytical solution for the non-zero terms in the sediment transport is given in Appendix D.3.

In this approach concentration is assumed proportional to the shear stress (Equation 2.28), however without direction. This assumption implies instantaneous response. The possible influence of a sediment phase-lag is explained in section 2.4.6.6.

$$\tau \propto u|u| \tag{2.27}$$

$$c \propto u^2 \tag{2.28}$$

$$S \propto u^m \tag{2.29}$$

Henderson et al. [2004] finds that the sediment transport does not depend on the free-stream velocity, but the near-bed velocity (Figure 2.17a, Equation 2.30). Due to the phase lead of the near-bed velocities, the near-bed skewness depends on the free-stream asymmetry and free-stream skewness. The larger the free-stream asymmetry, the stronger the skewness increase (Figure 2.17) [Henriquez, 2016, p.66]. So, free-stream asymmetry is transformed to near-bed skewness. Berni et al. [2013] formulated an equation for the skewness at the bed (Equation 2.31), based on the work of Henderson et al. [2004] and the assumption that all harmonic frequencies have the same phase shift (relative to their own wave period). Horikawa et al. [1982] finds that the phase of the concentration is almost equal to the phase of the velocity in vicinity of the bed, which indicates the importance of near-bed skewness for sediment transport.

In a numerical model for skewed waves over a flat bottom Kranenburg et al. [2013] found that velocity skewness causes 60 % of the sediment transport. The other 40 % was caused by streaming (section 2.4.1.2). O'Donoghue and Wright [2004b] measured the effect of velocity skewness in a wave tunnel and found that the sediment transport is mainly onshore for coarse grains and decreases with decreasing grain size due to the phase lag (section 2.4.6.6). Foster et al. [1999] derives an analytical solution for the wbbl assuming linearised equations (Appendix B.2) and an eddy viscosity that is separable in space and time. With this solution Foster finds that the maximum onshore sediment transport is caused by purely skewed waves. Purely asymmetric waves give a small offshore transport.

$$S \propto u^3_{nearbed} \tag{2.30}$$

$$\frac{Sk_b}{Sk_\infty} = \cos\phi_b - \sin\phi_b \frac{As_\infty}{Sk_\infty} \tag{2.31}$$

Berni et al. [2013] found that the waveform in laminar oscillatory flow as measured by 'Batchelor (2000)' is described with Equation 2.32.

$$\frac{Sk_b}{Sk_\infty} = 1 - \frac{As_\infty}{Sk_\infty} \tag{2.32}$$

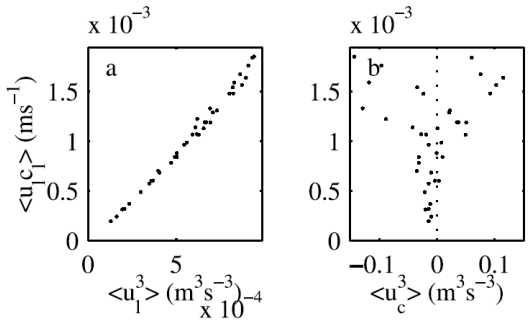


(a) Near-bed shoreward sediment flux on the bar crest versus third moment of near-bed velocity (left) and free-stream velocity (right) [Henderson et al., 2004] (p.10)

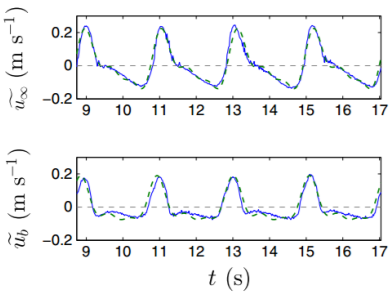


(b) Wave shape in free-stream and near bed [Berni et al., 2013] (fig.16)

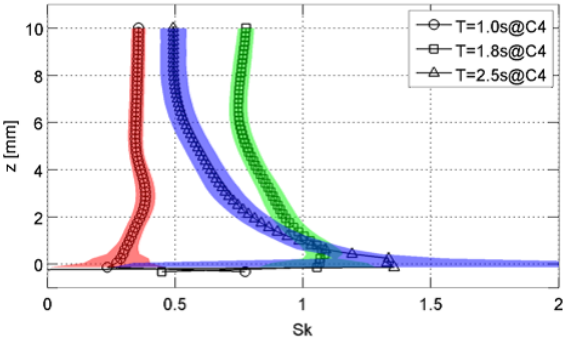


(c) Development of skewness towards the bottom for a fixed bed [Henriquez, 2016] (fig.5.9)

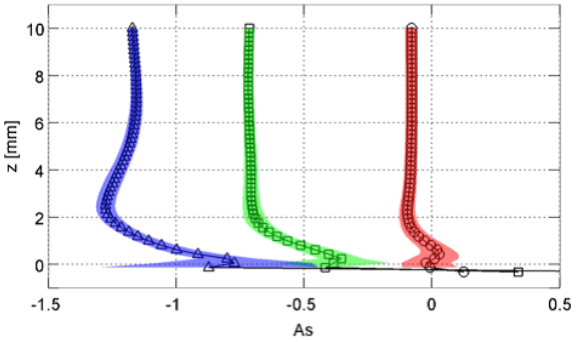


(d) Development of asymmetry towards the bottom for a fixed bed [Henriquez, 2016] (fig.5.9)

Figure 2.17: Influence of the transformed near-bed wave shape.

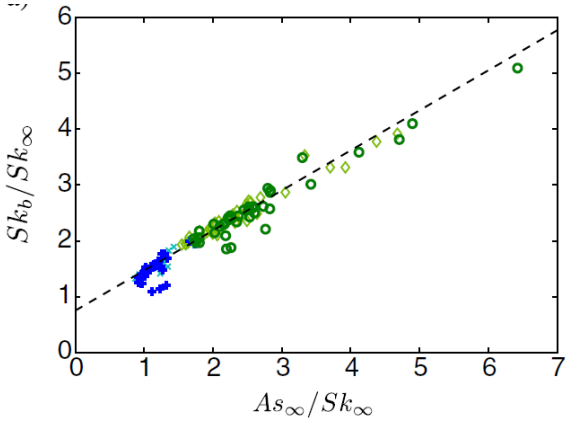


(a) The relation between free-stream asymmetry and skewness to near-bed skewness of [Berni et al., 2013] (fig.14)

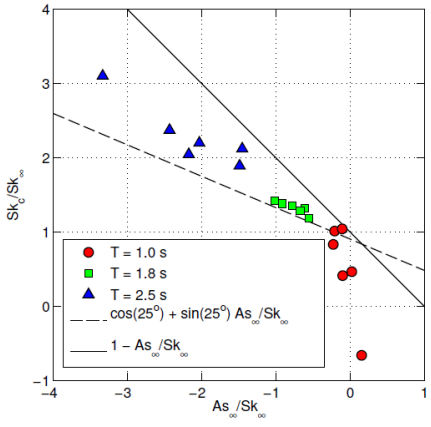


(b) The relation between free-stream asymmetry and skewness to near-bed skewness [Henriquez, 2016] (fig.5.10)

Figure 2.18: Influence of the transformed near-bed wave shape.

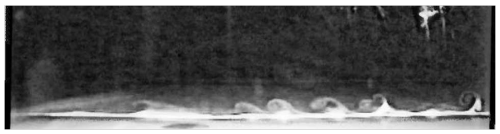

(a) Vortex tubes observed in the fixed-bed wave tunnel measurements of Carstensen et al. [2010b] for a free-stream flow from left to right ($U_{0m}$ = 43.9 cm/s, $T$ = 9.2 s, $Re = 2.8 \cdot 10^5$, $\omega * t$ = 37 to 131$^o$)

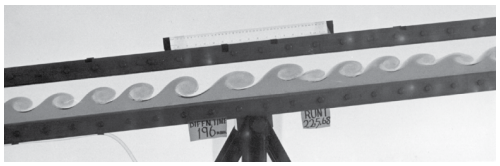

(b) KH-instabilities in a tilting tank with stratified flow [Thorpe, 1971]

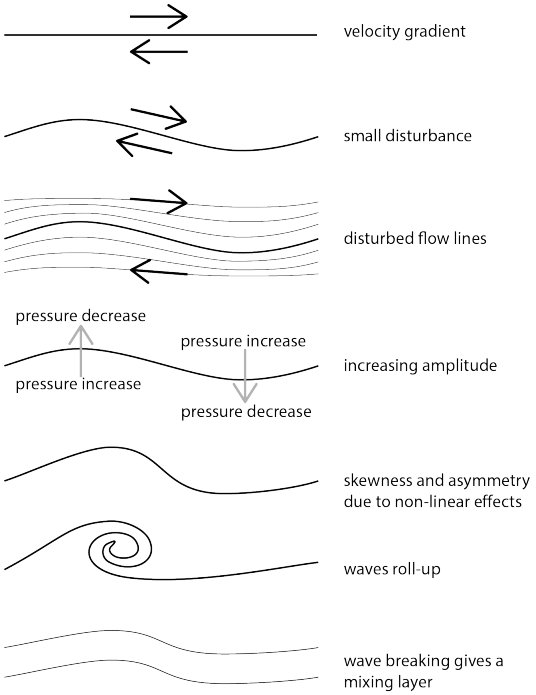


(c) Development of KH-instabilities [Pietrzak, 2015]

Figure 2.19: Kelvin-Helmholtz instabilities

#### 2.4.6.2 Asymmetry

The horizontal pressure gradient not only accelerates the fluid, but also the sediment grains. The pressure gradient can move the sediment as block (plug flow) [Foster et al., 2006], while the orbital velocities move the upper grains first. For asymmetrical waves the steep front of the wave has a larger pressure gradient with a shorter duration than the gentle back of the wave. Hence an asymmetrical wave has skewed accelerations (figure 2.8). This difference in acceleration can cause a net onshore sediment transport.

When including acceleration-based transport in numerical energetics models, the performance in onshore migration increases significantly [Hoefel, 2003]. Without acceleration-based transport this performance is low [Gallagher et al., 1998]. This would indicate that the difference in horizontal pressure gradient (acceleration skewness) is an important mechanism in onshore sediment transport. However, Henderson et al. [2004] excluded the horizontal pressure force on the sediment particles in his model and successfully predicted a onshore bar migration.

In the measurements of Ribberink and Al-Salem [1995] asymmetric waves cause a onshore sediment transport in the sheet flow layer and a small offshore sediment transport in the suspension layer. This difference can possibly be due to the sediment phase lag (section 2.4.6.6).

Foster et al. [2006] observes that the thickness of the mobile-bed layer increases with several centimetres at the moment of large accelerations at flow reversal from offshore to onshore flow (moment of rising water level, positive acceleration). The bed settles rapidly during the deceleration that follows the wave crest [Foster et al., 2006]. This suggest that incipient motion depends on the combination of bed shear and pressure gradient. Therefore Foster suggest that plug flow, depends on a combination of the Shields and Sleath parameter (Appendix C.3). Equation 2.33 gives the force balance on a block of sediment, in which $\alpha$ is a coefficient [Foster et al., 2006]. This suggests that the shear and pressure gradient terms together have to exceed a threshold value of incipient motion. So the two terms may oppose each other to stabilize the bed.

$$\left| \theta(t) \frac{D_{50}}{h_{block}} + S(t) \right| > \mu K (1 + \alpha) \tag{2.33}$$

#### 2.4.6.3 Vortex tubes

In oscillation flows vortex tubes can develop in the wbbl. Carstensen et al. [2010b] observed vortex tubes in an oscillating non-stratified laminar flow (Figure 2.19a). Vortex tubes are a type of internal wave and quite con-

stant in longitudinal direction. Carstensen et al. [2010a] found that vortex tubes are a result of the inflection point shear instability.

These vortex tubes are similar to Kelvin-Helmholtz instabilities (K-H instabilities). K-H instabilities are wave-like structures that occur at an interface with a horizontal velocity gradient (Figure 2.19b, 2.19c). Usually these instabilities are found in stratified flows ($Ri > 1/4$) [Pietrzak, 2015], because stratification dampens turbulence. In non-stratified turbulent flows the velocity gradient can not get large enough for KH-instabilities. Carstensen et al. [2010b] found the vortex tubes in laminar flow, which also allows velocity gradients.

Wave driven sheet flow is a stratified oscillation flow, so relatively large horizontal velocity gradients can occur. Due to the phase lead of the wbbl, an inflection point exists in the velocity profile. Vortex tubes probably occur when the gradient in horizontal velocity exceeds a critical limit. The gradient depends on the variation in maximum orbital velocities over height and the phase lead. The critical limit depends on the stratification and Reynolds number.

In the bed shear stress the vortex tubes are clearly visible with first a strong decrease in magnitude (A) followed by a strong increase (B) (Figure 2.20b). Moment A is in between two vortex tubes and moment B is during a vortex [Carstensen et al., 2010b, p.216]. In the measurements each wave gives a similar graph. This implies that vortex tubes start at the same wave phase, travel with the same speed and have the same lifespan. The vortex (moment B) occurred at $94.5^o$ ($Re = 2.0 \cdot 10^5$), $100^o$ ($Re = 2.7 \cdot 10^5$) or $90.5^o$ ($Re = 3.1 \cdot 10^5$) [Carstensen et al., 2010b, p.217]. Hence the timing varies slightly with Reynolds number. Next to vortex tubes, turbulence spots were measured. Turbulent spots shortly increase the velocity close the bottom and caused the spikes in figure 2.20c. Turbulent spots are three-dimensional isolated areas close to the bed in the otherwise laminar boundary layer [Carstensen et al., 2010a].

The results of Dohmen-Janssen [1999] (Figure 2.10) show concentration peaks at flow reversal. It could be that these suspension events are vortex tubes. The same holds for the observed mobile-bed thickness increase of several centimetres at the moment of large accelerations at flow reversal from offshore to onshore flow by Foster et al. [2006] (section 2.4.6.2). Since fine sediment results in a larger stratification at the same orbital velocities, it sounds logical that the vortex tubes occur sooner with fine sediments. Dohmen-Janssen [1999, p.18] mentions that Inman et al. [1985], King [1991] found a sudden increase of the sheet flow layer around large flow velocities, they called the regime in which this occurs the bursting regime. They observed that bursting is restricted to fine sediments.

$$Ri = \frac{-g\dfrac{\partial \rho}{\partial z}}{\rho\left(\dfrac{\partial u}{\partial z}\right)^2} \tag{2.34}$$

The swirling strength visualises vortices with the imaginary part of the complex eigenvalues of the velocity gradient tensor. The swirling strength is described with equations 2.35 and 2.36.

$$\lambda = \frac{1}{2}\left(\frac{\partial u}{\partial x} + \frac{\partial w}{\partial z}\right) + \sqrt{4\frac{\partial u}{\partial z}\frac{\partial w}{\partial x} + \left(\frac{\partial u}{\partial x} - \frac{\partial w}{\partial z}\right)^2} \tag{2.35}$$

$$\lambda_{ci} = \sqrt{\mathrm{Im}(\lambda)^2} \tag{2.36}$$

#### 2.4.6.4 Vertical sediment advection

Due to sediment advection, the timing of vertical velocities can cause a net sediment transport (term 2.37). The upward velocities bring more sediment in suspension and are followed by onshore velocities. The downward velocities will settle the sediment and are followed by offshore velocities. Hence the correlation between sediment concentration and orbital velocities causes a net sediment transport. This process is similar to Stokes drift. Where Stokes drift is due to the vertical transport of water mass, this advection sediment transport is due to the vertical transport of sediment.

This shoreward transport is mostly concentrated in the wbbl, where the sediment concentrations are highest [Henderson et al., 2004, p.13]. More precisely: because the sediment is located higher in the wbbl during onshore velocities and lower in the wbbl during offshore velocities, there is an onshore sediment flux higher in the wbbl and an offshore flux lower in the wbbl [Kranenburg et al., 2013, p.133]. This becomes relevant at heights were $\tilde{w}$ is on the order of $w_s$ .

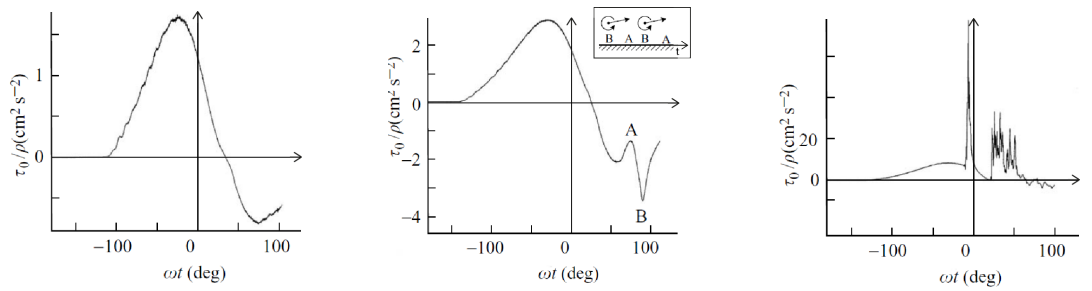


(a) Laminar
for $Re < 2 \cdot 10^5$

(b) Laminar with vortex tubes
for $2 \cdot 10^5 < Re < 5 \cdot 10^5$

(c) Transition to turbulent
for $Re > 5 \cdot 10^5$

Figure 2.20: Bed shear stress in different flow regimes in a wave tunnel [Carstensen et al., 2010b, p.214]

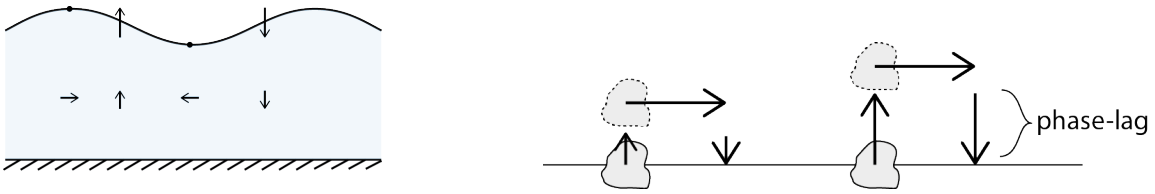


(a) Instanteneous orbital velocities

(b) Sediment phase lag

Figure 2.21: Sediment-wave interaction

$$\overline{(\tilde{w} - w_s)\frac{\partial c}{\partial z}} \tag{2.37}$$

#### 2.4.6.5 Horizontal sediment advection

The correlation between sediment concentration and horizontal velocities can also cause a net sediment transport (term 2.38). Due to horizontal advection, the concentration becomes higher in front of the wave crest. The instantaneous orbital velocities in Figure 2.21a show that all horizontal velocities are directed towards the front of the wave crest. This increases the water level in front of the wave crest: the wave passes. These horizontal velocities also take along sediment that, when the crest of the wave passes, will be transported onshore. In other words, because the horizontal velocities are correlated with a higher concentration in front of the crest when compared to behind the crest, horizontal advection causes a net onshore flow [Kranenburg et al., 2013, p.133].

$$\overline{\tilde{u}\frac{\partial c}{\partial x}} \tag{2.38}$$

#### 2.4.6.6 Sediment phase-lag

The sediment phase-lag is the reaction time of the sediment, in other words the time to suspend or settle (figure 2.21b). Phase-lag effects are important for large orbital velocities (higher suspension), fine sands (slower settling) and small wave periods (relatively slow suspension and settling compared to change in velocity direction) [Dohmen-Janssen, 1999, p.22]. If the phase lag decreases the time-averaged wave related sediment transport and can even make it negative. The phase lag has little effect on the current related transport. With an increasing phase lag, the current related sediment transport becomes relatively more important [Kranenburg, 2013, p.82].

The phase-lag influences the time-averaged wave related sediment transport because suspended sediment that is not settled before flow reversal will be transported the opposite way. In combination with oscillating motion, a longer settling time first increases the sediment transport, but decreases the transport when the sediment start to be transported in the opposite direction (Figure 2.22b). For purely sinusoidal waves the phase-lag will be equal for positive and negative velocities, but in case of velocity skewness the higher onshore velocities will entrain the sediment higher into the water column. Increasing velocities [Dohmen-Janssen, 1999, p.21] or decreasing grain size [O'Donoghue and Wright, 2004b] can therefore decrease the

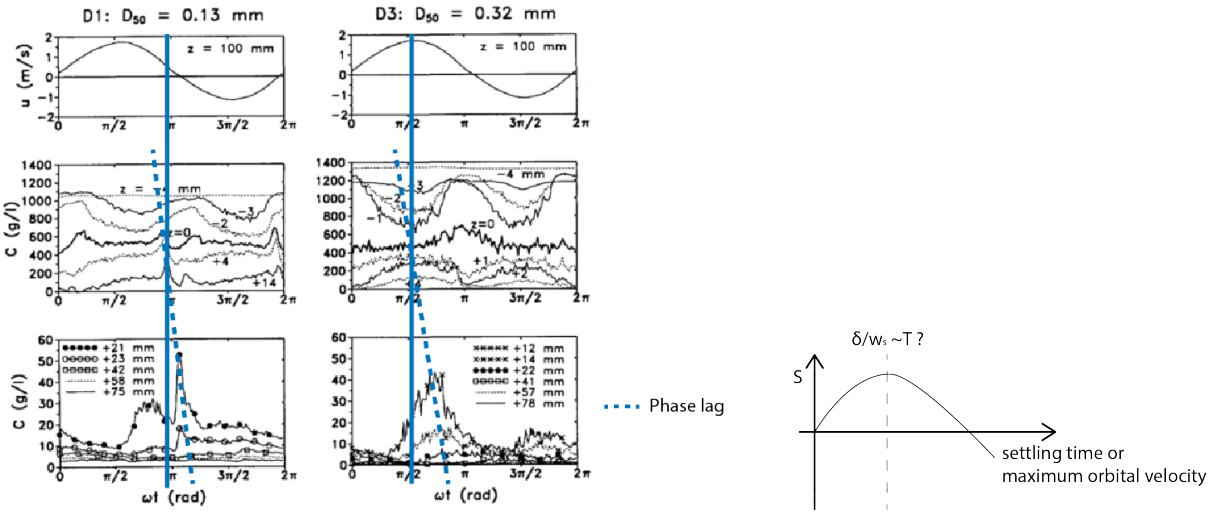


(a) Phase lag in the results of Dohmen-Janssen [1999](p.117)

(b) Impression of the sediment-phase lag relation

Figure 2.22: Effect of the phase lag on the sediment concentration and transport

sediment transport and even give a negative transport.

The phase-lag parameter (Equation 2.39) is the required settling time over available settling time [Dohmen-Janssen, 1999, p.22]. This divides the velocities that stir up the sediment through shear stress and the velocities that transport the sediment. The closer the sediment stays to the bed, the smaller the phase-lag (figure 2.22a). Therefore instantaneous response is often valid close to the bed [Dohmen-Janssen, 1999, p.35].

$$\frac{\delta / w_s}{T} = \frac{\delta}{w_s T} \tag{2.39}$$

## 2.5. Methodology: Measuring sediment transport with PIV

Sediment transport can be measured with a photographic technique. When taking pictures from the side, the moving sediment grains are captured in the image. Figure 2.23a gives an example of a measurement set-up with two light sources: one on each side of the camera [Ahmed and Sato, 2001, Liu and Sato, 2005]. This set-up measures the flow close to the wall. So, there will be side-wall effects: both on the velocity and the sediment transport. According to Dohmen-Janssen [1999] the side-wall effects on the water flow at the bottom are small and can be neglected, but the sediment transport can be decreased by 20 % by the side-wall.

The sediment transport can either be determined from the images with particle tracking [Liu and Sato, 2005, Tapia, 2006] or by multiplying the velocity with the intensity [Ahmed and Sato, 2001, Horikawa et al., 1982]. For the latter the velocities are determined with Particle Image Velocimetry (PIV) and the concentration is based on the image brightness.

Image intensity can be used as a measure of concentration, because particles reflect more light than water. Horikawa et al. [1982] measured the concentration with two techniques: electro-resistance concentration meter (Concentration Conductivity Meter, CCM) and a photographic technique (Figure 2.24). This resulted in an exponential relation between image intensity and concentration (Figure 2.23b and Equation 2.40, in which b is brightness). The concentration calculation of Ahmed and Sato [2001] is based on this same calibration relationship. It is expected that particles close to the wall reflect more light than far particles. Dudley [2007] shows that this is effect has a threshold. For a small distance close to the wall, all particles have full illumination. Passed this threshold the intensity decays.

However brightness or image intensity depends on more factors than concentration. Therefore Liu and Sato [2005] decided to abandon this relation and to only analyse the erosion depth and the velocities. This is the main reason why sediment transport calculations based on an image analysis are found very little in literature.

$$c = 0.0003 \cdot e^{0.1644 \cdot b} \tag{2.40}$$

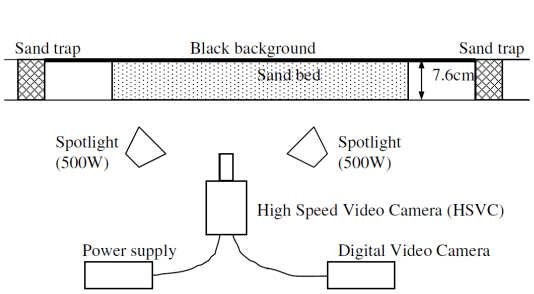


(a) Set-up of Ahmed and Sato [2001] and Liu and Sato [2005]

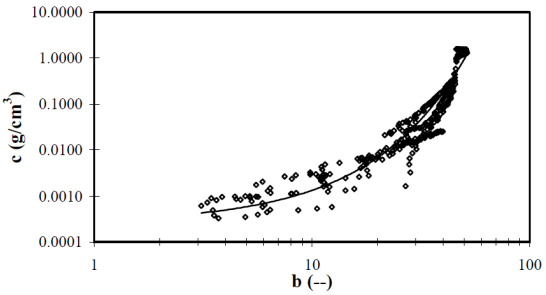


(b) Calibration between brightness and concentration Horikawa et al. [1982]

Figure 2.23: PIV technique to measure sediment transport

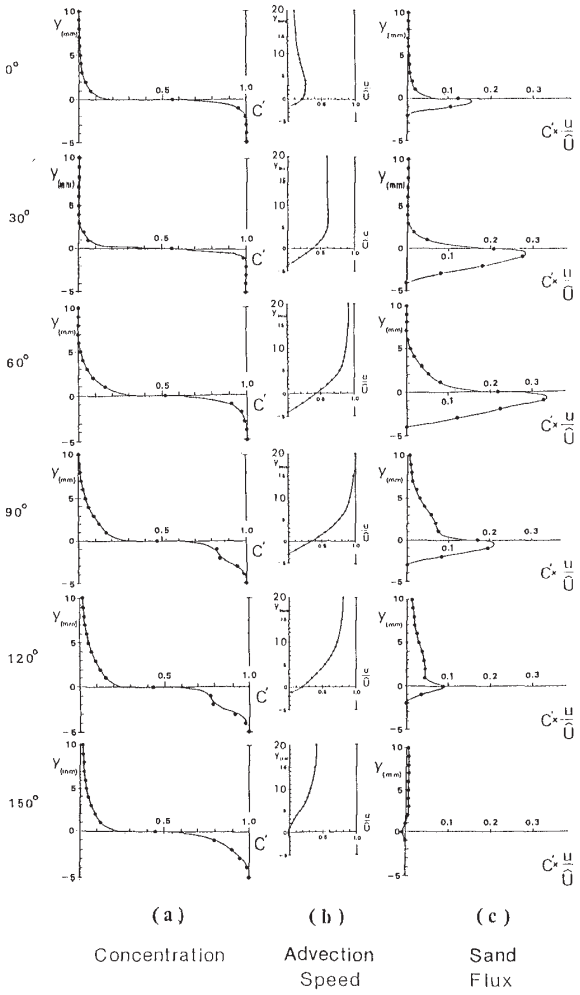


Figure 2.24: Concentration, velocity measurements and resulting sediment flux in the sheetflow at different wave phases [Horikawa et al., 1982]

## 2.6. Practical implications: Modelling onshore wave driven sediment transport

Often onshore wave driven transport is calculated with the shear stress based on the free-stream velocity on top of the wave bottom boundary layer [Roelvink and Reniers, 2011, Eq.4.28] (Equation 2.41). With this the wave shape change in the wbbl is neglected. The onshore wave related transport is maximum for skewed waves (Stokes waves) and negligible for asymmetric waves [Roelvink and Reniers, 2011]. When taking the wave shape change in the wbbl into account (section 2.4), this result will change. The remaining questions in literature are: at which height above the bed is the wave shape the most representative for the sediment transport? And, does numerical models need to include sediment transport caused by the velocity skewness or sediment transport caused by the pressure gradient under asymmetric waves? Note that for situations with strong tidal or longshore currents, it is especially important to model the mean concentration ($\overline{c}$) due to short waves correctly.

$$\tau \sim C u_{\infty}^2 \tag{2.41}$$

When including the wave shape development in the wave bottom boundary layers, models can use several methods to determine the near-bed phase shifts: constant, frequency dependent, or of Nielsen and Callaghan 2003 [Roelvink and Reniers, 2011, p.99]. These types of phase shift result in different wave shapes in the wbbl and thus different sediment transport. A more elaborate explanation of the phase shift is given in section 2.2.2.

# 3

# Methods

*This chapter describes the method of this research to analyse sediment transport in the wave bottom boundary layer. The first step is the empirical data collection with a wave flume experiment (section 3.1), the second step is the data processing and validation (section 3.2) and the third step the data analysis and interpretation (section 3.3).*

## 3.1. Empirical data collection: wave flume experiment

To analyse onshore sediment transport, Henriquez measured onshore bar migrations in a wave flume (Appendix E) [Henriquez, 2016]. The measurements contained fixed-bed and mobile-bed experiments. In this master thesis the mobile-bed experiments are analysed. Most important to note in this chapter is the inventive PIV set-up, which enables sediment transport calculation from PIV measurements (Figure 3.2, Section 3.1.2).

### 3.1.1. Overview tests

Figure 3.1 spreads out the test plan. There were three measurement locations (A,B and C) and since there was only one PIV camera, *three test series* were done to measure at each location. Per test series *three bar migrations* were measured and per onshore bar migration *three tests* of each 15 minutes were executed. Three test series with three bar migrations with each three tests results in total in 27 tests. Appendix G gives an overview of the measurements in a table.

### 3.1.2. Set-up

The experiments were done at the Delft University of Technology (DUT) in a mobile-bed wave flume. In this wave flume onshore bar migration was measured during multiple tests of 15 minutes. PIV photos were taken at three locations of the sand bar: offshore, on top and onshore of the bar. During each test PIV and wave

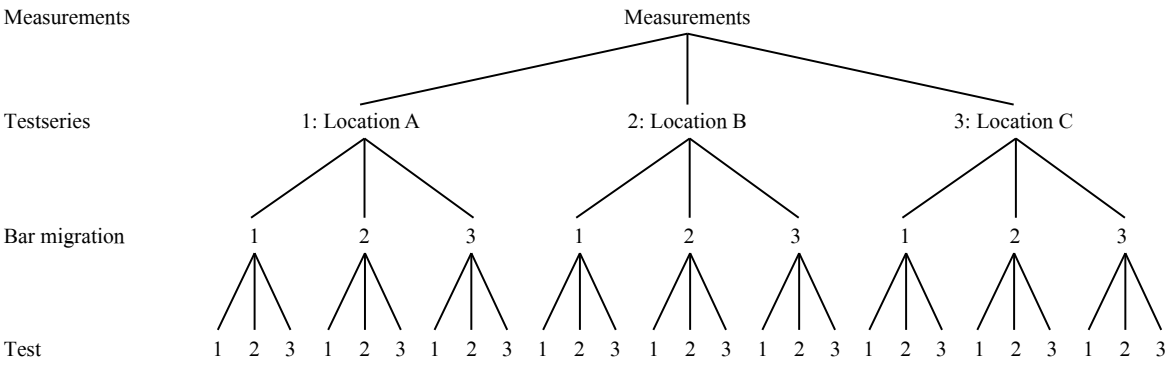


Figure 3.1: Measurement structure

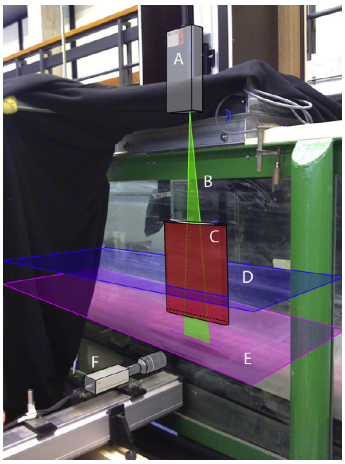


(a) Common PIV set-up with laser on top

(b) Current PIV set-up with laser on front

Figure 3.2: The position of the laser in the experimental set-up: A = laser, F = camera

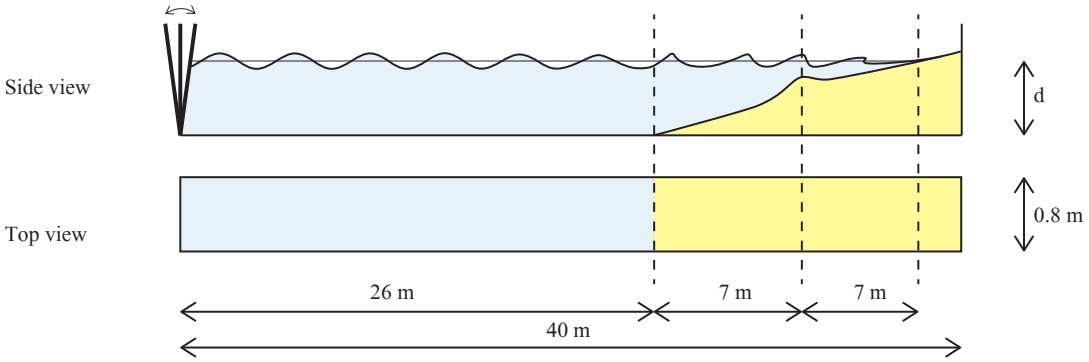


(a) Measurements of the flume

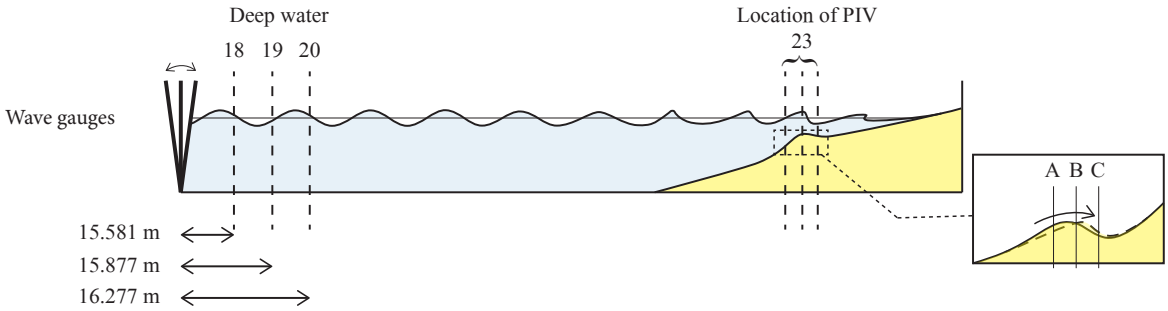


(b) Wave gauges and PIV location


(c) Bottom profile

Figure 3.3: Measurements of the flume and measure locations (number 18,19,20 and 23 are the identification of the wave gauges)

gauge measurements were executed. Between the different tests the bottom profile was measured. The wave flume was 40 meter long and 0.8 meter wide (Figure 3.3a). The water depth was 0.50 meter and the bottom profile had a slope of around 1:15.

With Particle Image Velocimetry (PIV) the velocities on and around the bar were measured (Location A,B and C, Figure 3.3b). PIV is an optical method for flow visualization that measures velocity fields by taking two photos shortly after each other. The velocity was calculated by the travel distance of individual particles between these two photos. The frequency within a photo pair is 500 Hz and the frequency between the photo pairs 14 Hz. The PIV frame size is 40 by 60 mm and the resolution 29.76 pixels/mm.

During the PIV measurement the flow was illuminated with a laser, while the camera took high frequency photos. Henriquez [2016] uses an inventive PIV set-up. Usually the laser is placed on top of the flume to create a two dimensional laser sheet in the flume (Figure 3.2a). With this method the light does not penetrate in the bottom. To be able to calculate the sediment transport from the PIV photos, the laser was placed in front of the wave flume to illuminate the flow and the bed (Figure 3.2b). To be able to take photos from outside the flume, the wall has to transparent and clear. So, with this method both the bottom and flow were illuminated. Since grains reflect more light than water, the photo intensity can now be used as measure of concentration. To avoid light from entering the experiment beside the laser, the whole experiment was covered. The drawbacks of the frontal placement and the use of intensity will be discussed in the Discussion (Chapter 5).

Wave gauges measured the wave height during each test at various locations (Figure 3.3b). The frequency of wave gauges was 2000 Hz. The bottom profile was measured in between the tests by an echo sounder on a measurement car at two sections (Section (a) and (b) in Figure 3.3c). The bottom height was measured at each 10 mm. The results of profile (a) were gave less accurate results, therefore only the results of profile (b) will be used.

### 3.1.3. Wave conditions

Two wave climates were used in the experiment (Appendix E.1.3). For each bar migration first a single bar cross-shore profile was created by running a more energetic wave climate. After that, tests were done with a mild wave climate to measure onshore bar migration. In other words, a mild wave climate during the onshore bar migration measurements and a more energetic wave climate in between two onshore bar migrations to reset the bottom profile to its original position. The wave conditions and coastal profile were inspired by the Duck94 experiments in North Carolina (US), where natural onshore bar migration was observed.

During the mobile bed experiment only irregular waves were used, generated with a standard JONSWAP spectrum. The peak period $T_p$ was 1.8 seconds and the significant wave height $H_{m0}$ of the mild wave climate was 0.085 meters.

### 3.1.4. Sediment properties

For scaling reasons, light weight polyester granular sediment was used (Appendix E.1.2). The sediment density, $\rho_s$, was 1200 $kg/m^3$ and the median diameter, $d_{50}$ was 0.52 mm. For light weight sediment, the sediment velocities can be assumed equal to the fluid velocities.

The scaling is based on a constant Reynolds number, Shields number and relative settling velocity, but this results in a scaling mismatch for the Sleath parameter (Appendix F) [Henriquez et al., 2009]. The scaling results in a relatively larger grain diameter and relatively smaller sediment density in the model than on the simulated natural beach. Due to incorrect scaling of relative density, the mobility of the sediment can be larger than predicted [Henriquez et al., 2009].

## 3.2. Data processing and validation

This research analyses the information of the PIV photos by determining the sediment velocities and sediment transport. The data processing results in the sediment transport, after which the data analysis can start (section 3.3). The following sections explain how the sediment transport is obtained from the PIV data. Next, the sediment transport based on the PIV data will have to be validated. Therefore the sediment transport is determined based on the bottom profile measurements. Figure **??** gives an visual overview of the validation strategy.

The data model is built entirely for this research, except for the velocity calculation. The velocity calculation is done with DaVis software, but the main part of the model is built in MATLAB. In this research data correction will be avoided to keep the analysis as clear as possible. Small corrections can be added in future research if necessary. Appendix G gives an overview of all analysed tests. Technical information about the

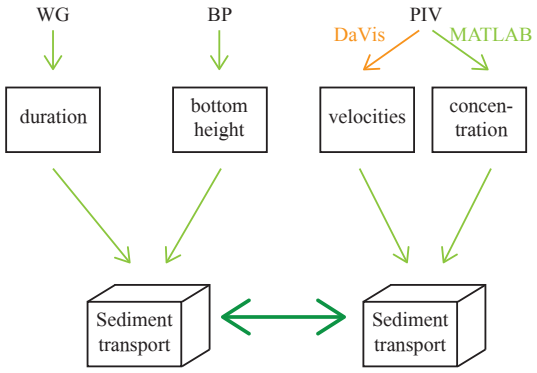


Figure 3.4: Data analysis process overview: the comparison between the PIV data and bottom data.

data analysis is given in Appendix H.

### 3.2.1. Data processing: Sediment velocities and transport from PIV measurements

During the whole test the wbbl sediment is captured in PIV photos. From these images the sediment transport can be calculated by multiplying the sediment velocities and concentration at each data point. Under the assumptions that all sediment transport occurs in the PIV frame (between $z_{PIV,bottom}$ and $z_{PIV,top}$), the total sediment transport is calculated by integrating over height (Equation 3.1). Without observed sediment suspension through the top boundary this seems a valid assumption.

$$S_x = \int_{z_{PIV,bottom}}^{z_{PIV,top}} u \cdot c \; dz \tag{3.1}$$

The sediment *velocity* is calculated trough a PIV analysis in Davis (Figure 3.5a & 3.5b, Appendix H.2). This PIV analysis starts at the start of the first wave. The velocity is determined by the maximum correlation between two images. There are no tracers added during the experiment. Hence the correlation is based on the location of particles: both dust and sediment particles. Since sediment particles are much larger, those will strongly influence the correlation. Hence: if sediment grains are present the sediment velocity is determined and if there are no sediment grains present the flow velocity (dust velocity) is determined. For the calculation the flow velocity and sediment velocity are assumed equal. The effect of this assumption will be discussed in Chapter 5 "Discussion", section 5.2. Note that, because the sediment velocities are based on both dust and sediment grains, the definition of sediment velocity in this study is "velocity that sediment has if there are sediment grains present".

Next to that, the *concentration* has to be determined from the PIV photos. The frontal placement of the laser facilitates using the intensity of the image to determine the sediment concentration. Since sediment reflects more light than water, a higher intensity means a higher concentration (Figure 3.5c). This is a rough method, because the image intensity depends on more factors than only sediment concentration. The concentration is calculated from the intensity in the following steps:

1. Resize intensity to the same resolution as the velocity to get the concentration at the same location as the velocity (Figure 3.5c & 3.5d). To calculate the sediment transport at a location the velocity and concentration are both needed at the same location. Because the velocity is determined in DaVis and the concentration in MATLAB, the grid alignment between the velocity and concentration has to be constructed carefully. If the alignment is not fully correct, this can strongly influence the result because the concentration will be slightly too low or too high at every grid point.

2. Divide the data set into calibration sets with comparable light exposure. The calibration can be done with different amounts of data: per location, per test or per image. With more data a calibration is more reliable. However the mean image intensity variation over time is an argument to keep the calibration time-frame as short as possible. In this study it is decided to divide the data in calibration sets with comparable light exposure. With a new camera set-up at every location, each measurement location will be a new calibration set.

3. Determine a calibration curve between intensity and concentration (Figure 3.6b).

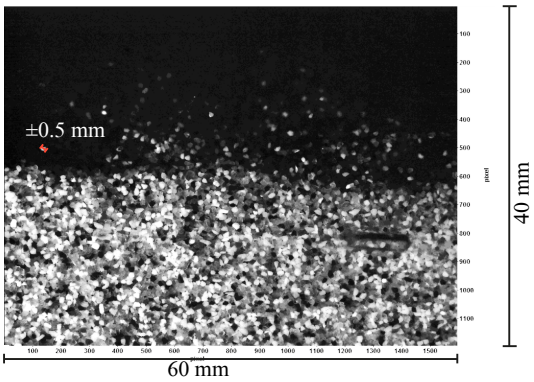


(a) Instantaneous PIV image

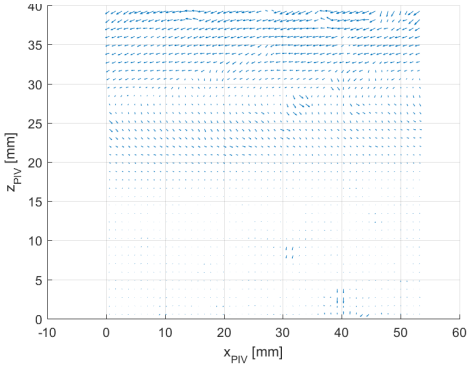


(b) Velocity 2D

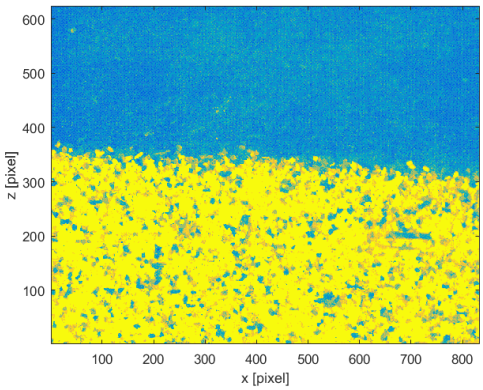


(c) Instantaneous image intensity

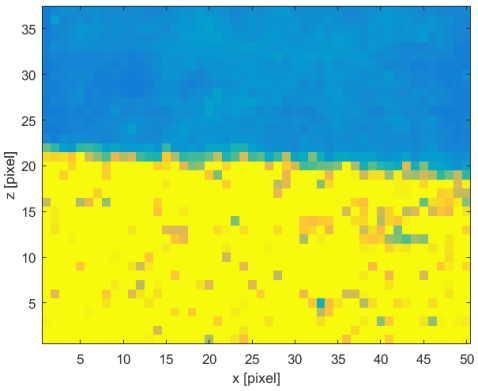


(d) Image intensity after resizing to 37 x 50 grid points.

Figure 3.5: Based on the PIV images (3.5a) the velocities and sediment concentration will be determined. The velocities (3.5b) will be calculated based on the correlation between two PIV images. The image intensity grid (3.5c) is resized to obtain the same grid size as the velocities (3.5d). This resized intensity can be used to calculate the concentration.

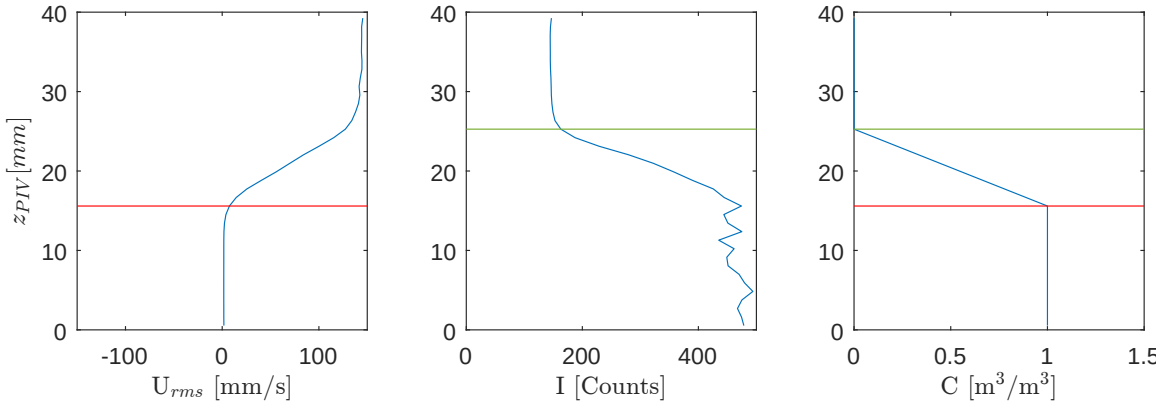


(a) Determining the boundaries of the sheet flow layer for the calibration. The red line shows the lower boundary and the green line the upper boundary. The boundaries are used to determine the mean bed and water intensities, next the boundaries are used to determine the linear part of the concentration profile. Example of test 1.1.1.

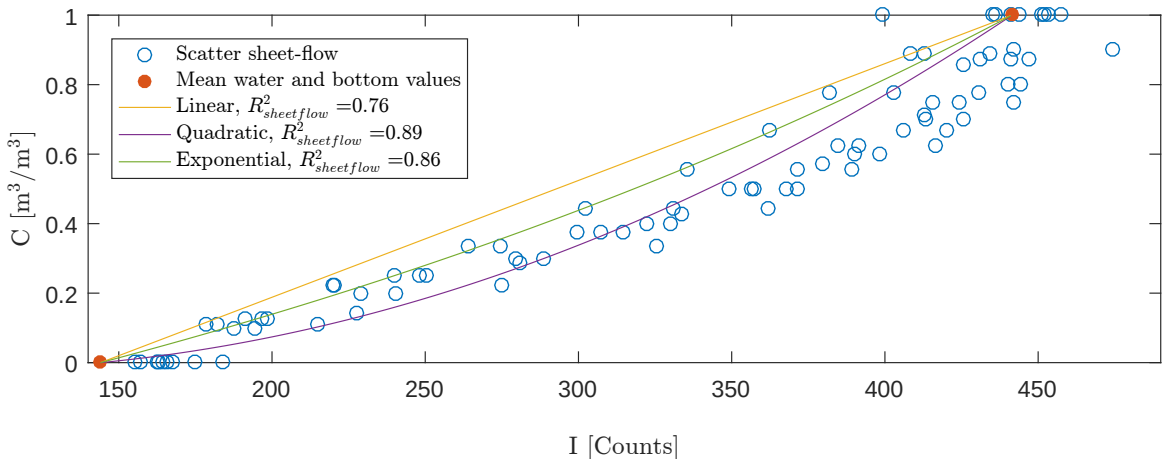


(b) Example of the calibration methods. The linear calibration is based on the mean water and bed intensity. The quadratic and exponential equilibration methods adapt to the measured intensities in the sheet flow layer.

Figure 3.6: The calibration process between intensity and concentration. The image intensities are compared to a linear concentration profile (3.6a). Different calibration methods can be applied to this comparison (3.6b).

4. Calculate the concentration with the calibration equation.

5. Since concentration cannot be negative, apply the condition that all negative values are zero.

Step 3, the calibration between intensity and concentration is the most sensitive step of the calculation. The mean bed and water intensity result in two fixed points in the calibration. Each trend line through this two points is a calibration curve (Figure 3.6b). The linear curve is purely based on these two fixed points, the quadratic and exponential curve adjust to the data in the sheet flow layer.

To determine the two fixed points of the calibration curve, the volumetric bottom concentration is set at 1 $m^3/m^3$ (concentration including pores) and the water concentration at 0 $m^3/m^3$. The mean bottom intensity has to be equal to the bottom concentration and the mean water intensity to the water concentration. The bed is defined as the area where the root-mean-square velocity ($u_{rms}$) is zero. Water is defined as the area with a minimum intensity.

As a starting point the concentration is assumed to increase linearly in the sheet flow layer (section 2.4.4, Figure 3.6a). Comparing the intensities in the sheet flow layer to a linear concentration profile can give a non-linear calibration. A linear, quadratic and exponential calibration are fitted through the data set (Figure 3.6b). Appendix I shows the method to determine the calibration curves mathematically. Based on the best fit and the sediment transport results the most suitable calibration method will be selected (section 4.1).

With the velocities and concentration the *sediment transport* can be calculated at each grid point (Equation 3.2, Figure 3.7). To determine the total sediment transport the transport will be averaged in cross-shore direction and integrated over image height (Equation 3.3, in which $\Delta x_{PIV,width}$ is the width of PIV image).

$$S_x(x,z,t) = u(x,z,t) \cdot c(x,z,t) \tag{3.2}$$

$$S_x = \int_{z_{PIV,bottom}}^{z_{PIV,top}} \left[ \int_{x_{PIV,left}}^{x_{PIV,rigth}} \frac{u \cdot c}{\Delta x_{PIV,width}} \, dx \right] dz \tag{3.3}$$

Next, based on the sediment transport per location the gradient between locations can be determined. To calculate the sediment gradient first the sediment transport at each location is calculated and next the gradient between the measurement locations (Equation 3.4, Figure 3.8). For comparison the relative sediment gradient is used. The relative sediment gradient is the sediment gradient divided by the total sediment transport at the most offshore location (Equation 3.5). Since the PIV measurements are collected at one location at a time, the gradient is in space and time (Equation 3.6). However since the measurements are done during different onshore bar migrations, no time interval can be determined. In the comparison the time interval can be neglected, because it would be the same for both measurements techniques.

$$\Delta S_{12}/\Delta x_{12} = \frac{S_2 - S_1}{x_2 - x_1} \tag{3.4}$$

$$\Delta S_{12,relative} = \frac{S_2 - S_1}{(x_2 - x_1) \cdot S_1} \tag{3.5}$$

$$\Delta S_{12}/(\Delta x_{12} \Delta t_{12}) = \frac{S_2 - S_1}{(x_2 - x_1)(t_2 - t_1)} \tag{3.6}$$

The PIV frame is 6 centimetres wide. Within this frame the sediment gradient can be calculated. The sediment gradient within the PIV frame gives the local gradient, while the sediment gradient between the measurement locations gives a more global gradient. Both gradients can be compared to the bottom profile data. With this, it is possible to validate the trend in the PIV sediment transport on both small scale and large scale. The gradient within the PIV frame is determined by comparing the sediment transport in the left and the right half of the frame. After calculating the mean sediment transport of the left and right half of the PIV window (Equation 3.7), the difference between the two sides is divided by half the image width to get the sediment gradient (Equation 3.8).

Next to that, the bottom change can be determined by comparing the still bed level in the first minute of the test to the still bed level in the last minute of the test. The still bed level is the elevation of the non-moving bed. Because the still bed level varies during each wave, the bed elevation is based on the mean value of one minute to average out the intra-wave bed level fluctuations. The still bed level is the highest elevation where the root-mean-square velocity ($u_{rms}$) is zero. Note that the non-moving bed level of the PIV measurements

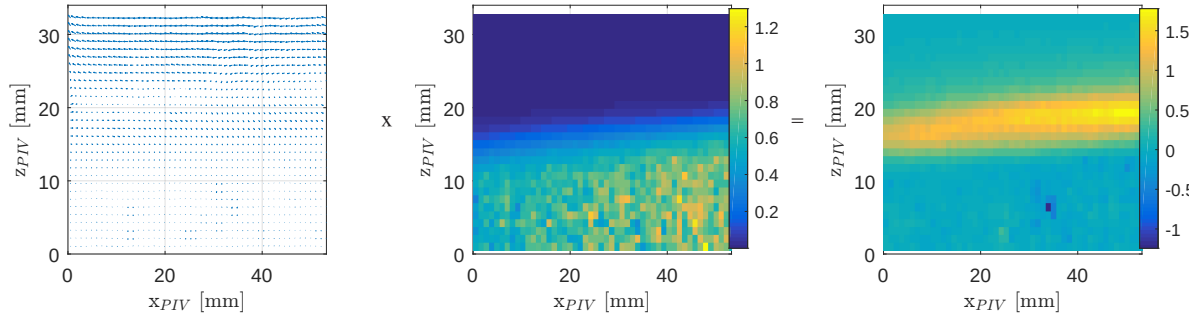


(a) Velocity 2D (b) Concentration 2D (c) Sediment transport 2D

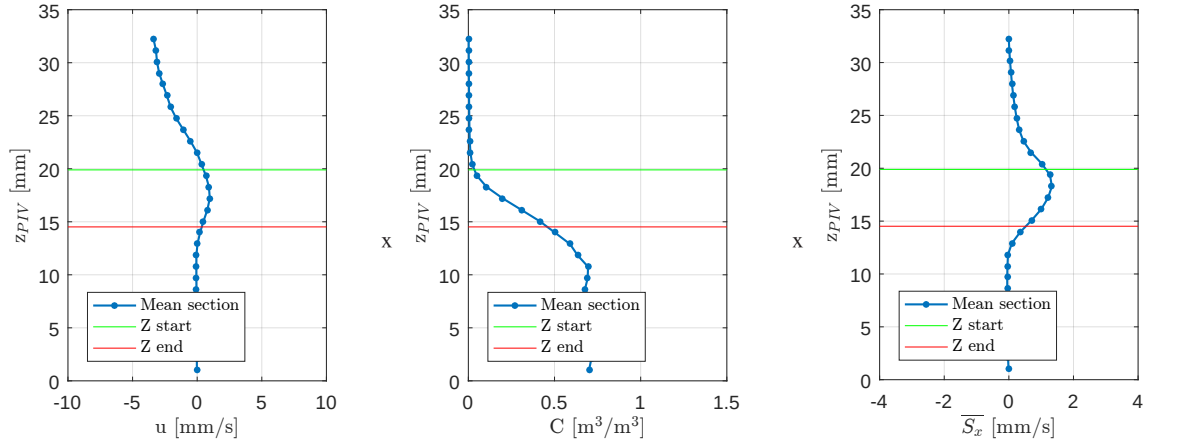


(d) Horizontal velocity (e) Concentration (f) Sediment transport

Figure 3.7: The sediment transport (3.7c & 3.7f) is calculated by multiplying the sediment velocities (3.7a & 3.7d) with the sediment concentration (3.7b & 3.7e).

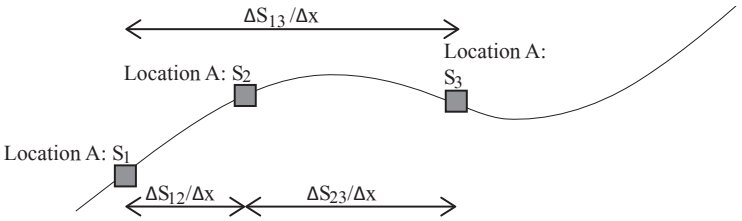


Figure 3.8: Sediment location and gradient

is determined during wave action, while the bed level of the bottom profile measurements is determined during still water. The still bed level during wave action is a different bed level than the bottom height with still water, because part of the sediment will be moving.

$$S_{x,right} = \frac{\int_{x_{PIV,left}}^{x_{PIV,middle}} \int_{z_{PIV,bottom}}^{z_{PIV,top}} u \cdot c \; dz \; dx}{\frac{1}{2}\Delta x_{PIV,width}} \tag{3.7}$$

$$\frac{dS_x}{dx} = \frac{S_{x,right} - S_{x,left}}{\frac{1}{2}\Delta x_{PIV,width}} \tag{3.8}$$

### 3.2.2. Data validation: Sediment transport from bottom profile measurements

To validate the PIV measurements, the PIV sediment transport will be compared to the observed bottom change. Before and after each test the bottom profile is measured. The sediment transport can be calculated from the bottom profile measurements in the following steps:

1. Calibrate the bottom height of the measurements. Between measurements the height of the echo sounder can slightly vary. With this calibration the wave flume bottom is set to exactly -500 mm.

2. Calculate the bottom change by subtraction of the bottom height before each test from the bottom height after the test (Figure 3.9, from the top figure to the middle figure). Equation 3.9 describes this step, in which $D_{test}$ is the test duration.

$$\frac{\partial z_b}{\partial t} = \frac{z_{b,end} - z_{b,start}}{D_{test}} \tag{3.9}$$

3. Calculate the sediment transport by integrating the sediment gradient with the Exner (Equation 3.10, Figure 3.9, from the middle figure to the bottom figure), in which $\partial t$ is the test duration. The integration is from the start of the flume, $x_{start}$, to the end of the flume, $x_{end}$. The boundary condition is zero sediment transport at the edge of the flume.

$$S_x = \int_{x_{start}}^{x_{end}} \frac{\partial z_b}{\partial t} dx = 0 \tag{3.10}$$

4. Select the sediment transport at the PIV locations. The sediment gradient and sediment transport at the PIV locations can be compared with the sediment transport calculated with the PIV data.

## 3.3. Data analysis and interpretation

After processing the PIV data into the sediment transport data set in space and time, a detailed analysis of the sediment transport development in the wave bottom boundary layer is performed. This is done in two parts: analysis of the different sediment transport mechanisms and analysis per wave of the wave related sediment transport. The two parts of the analysis are explained in the following sections.

### 3.3.1. Part 1: Sediment transport mechanisms

As described in literature, the sediment transport can be divided in three mechanisms: the current related transport, the time-averaged long wave related transport and the time-averaged short wave related sediment transport (section 2.4). Equation 3.11 gives a recap of the sediment transport mechanisms described in literature. All of these three types can be determined based on the PIV data.

First total time-averaged sediment transport ($\overline{S_x}$) is calculated by first multiplying the instantaneous horizontal velocity with the instantaneous concentration and second time-averaging.

Second the current related transport is calculated. The current related sediment transport ($\overline{u} \cdot \overline{c}$) is calculated by first time-averaging the horizontal velocity and the concentration and then multiplying the two mean properties.

Third, both wave related transport mechanisms will be determined. The oscillatory velocity can be determined by subtracting the mean velocity from each instantaneous velocity (Equation 3.12). Next the division

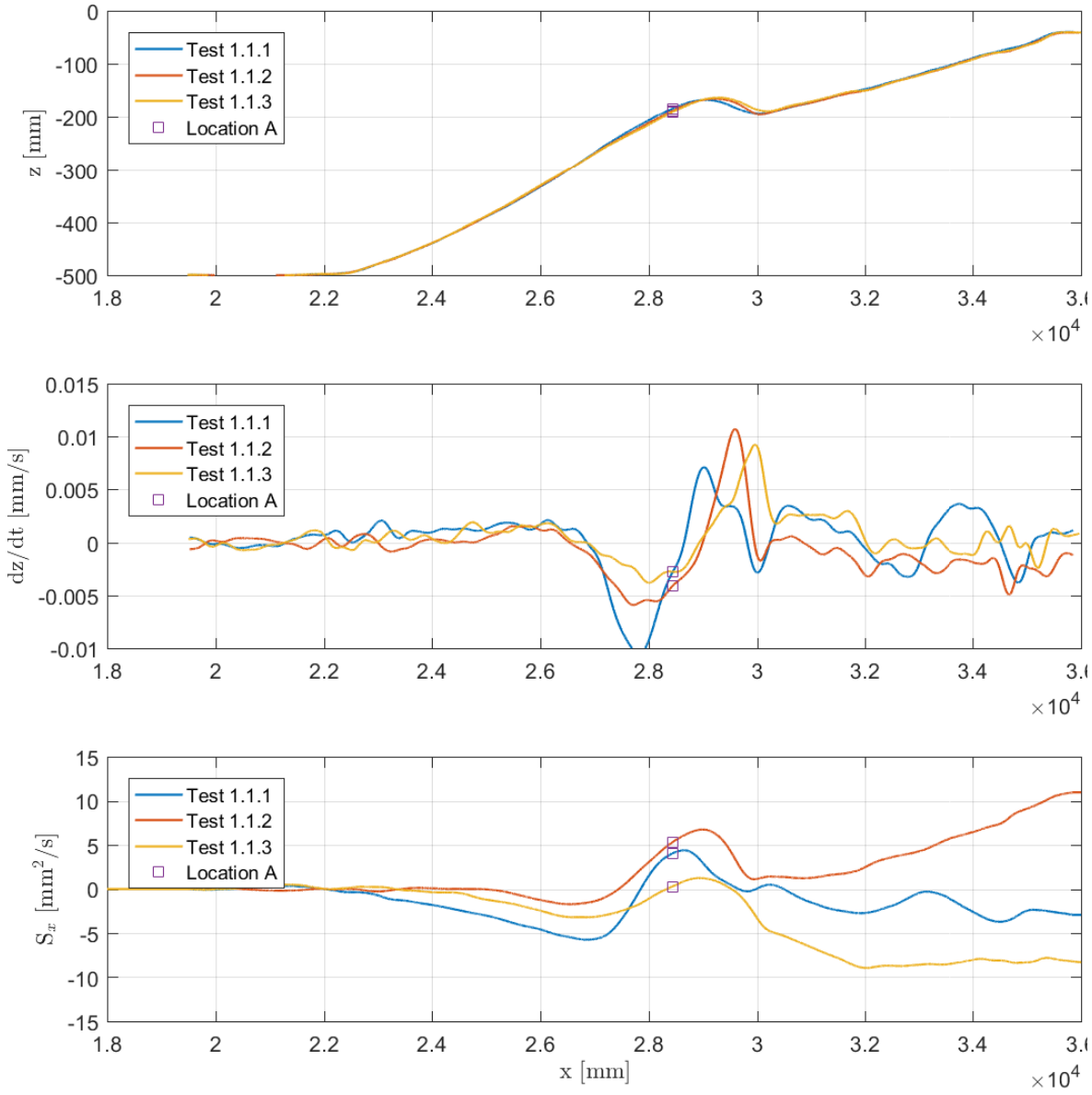


Figure 3.9: Example of sediment transport calculation based on the bottom measurements.

between short and long wave related transport is made. The oscillatory velocity has to be divided in a long and short wave component (Equation 3.13). This division will be made based on the wave spectrum. With a Fourier analysis the long wave influence on the current is removed. The short and the long waves will be separated at two times the peak period. In the results, it will be checked or a division at two times the peak period correctly separates the two peaks. Last, both the long and the short wave oscillatory velocity are multiplied with the concentration and finally time-averaged ($\overline{\tilde{u}_{LW} \cdot c}$, $\overline{\tilde{u}_{SW} \cdot c}$).

$$\overline{S_x} = \overline{u \cdot c} = \overline{u} \cdot \overline{c} + \overline{\tilde{u}_{LW} \cdot c} + \overline{\tilde{u}_{SW} \cdot c} \tag{3.11}$$

$$\tilde{u} = u - \overline{u} \tag{3.12}$$

$$\tilde{u} = \tilde{u}_{LW} + \tilde{u}_{SW} \tag{3.13}$$

The ratio between the sediment transport mechanisms, the change in ratio over the sandbar and the vertical distribution of the sediment transport mechanisms are compared to the ratios and mechanism description in literature (section 2.4).

### 3.3.2. Part 2: Short wave related transport

In this part the short wave related sediment transport is analysed. Because all intra-wave processes occur simultaneously it is difficult to extract individual processes from the data. This analysis focuses on two important intra-wave processes: skewness and asymmetry. An improved understanding of these two intra-wave processes can directly contribute to numerical model improvements, because these properties can easily be determined at the free surface. There are different ways to study the relation between these wave properties and the short wave related transport in the wave bottom boundary layer. This section will describe the method to study the influence of the intra-wave processes skewness and asymmetry (section 2.4).

There are different types of analyses possible: mean, instantaneous, per wave and phase-averaged. In a mean analysis the mean properties related to intra-wave processes are studied based on location. In the instantaneous analysis the values at each time step and each location (ea. $u(x_1, z_1, t_1)$) are compared to the sediment transport at the same time step and location ($S(x_1, z_1, t_1)$). In the analysis per wave the wave properties per wave are determined and related to the total sediment transport of that specific wave. In the phase-averaged analyses analysis the average wave is constructed through phase averaging. This research restricts to the mean analysis and the analysis per wave.

In a mean analysis the wave properties can be analysed in cross-shore direction, in vertical direction or in a cross-spectral analysis. This research will do the first two. In a mean analysis the mean properties related to intra-wave processes are studied based on location. The locations are both the development over the bar in cross-shore direction and the development over height in the wave bottom boundary layer. Skewness and asymmetry are calculated with equation 2.9 and 2.10. It is important to realise that the velocities are the sediment velocities and thus the skewness and asymmetry are based on the sediment velocity and not the orbital velocity. However in this study the sediment velocities are assumed equal to the orbital velocities.

To be able to compare the wave properties over height and in cross-shore direction, the wave properties will be selected at three *characteristic elevations*. The three characteristic elevations are: free-stream, elevation of maximum sediment transport and near-bed (Figure 3.10). The free-stream elevation is the elevation where the root-mean-square velocity is constant over height (Equation 3.14), because the root-mean-square velocity starts decreasing in the wbbl due to the influence of bottom friction and rotation. The elevation of maximum sediment transport are the five grid points around the maximum short wave related sediment transport (Equation 3.15). The near-bed elevation are the five grid points above the still bed level. The still bed level is determined at the highest elevation where the root-mean-square velocity is zero (Equation 3.16).

$$\overline{\frac{du_{rms}}{dz}} = 0 \tag{3.14}$$

$$\overline{\tilde{u}_{SW} \cdot c} = \left[\overline{\tilde{u}_{SW} \cdot c}\right]_{max} \tag{3.15}$$

$$\overline{u_{rms}} = 0 \tag{3.16}$$

In the *mean analysis* in cross-shore direction, the development of the wave properties over the bar can be compared to theory. A large gradient in cross-shore direction indicates an important effect on the sediment transport gradient and thus the bar migration.

In the mean analysis over height, an increase of the wave property towards the elevation of maximum sediment transport indicates that the corresponding wave process is more important than expected from surface elevation measurements. A decrease indicates the opposite. Next to that the phase lead, $\phi_b$, can be calculated with the equation of Berni et al. [2013] (Equation 2.31) and plotted over height. This shows the wave shape change in the wave bottom boundary layer and relates to the state-of-the-art research [Berni et al., 2013, Foster et al., 2006, Henderson et al., 2004, Henriquez, 2016] (section 2.4.6.1, 2.4.6.2). Since skewness and asymmetry are two important drivers of sediment transport, the wave shape development in the wbbl is an important indicator of the dominant intra-wave process.

For an *analysis per wave* the individual waves are separated at the downward zero crossings of the periodic velocity. Each individual wave has its own set of wave properties: wave period, orbital amplitude, skewness, asymmetry, mean velocity and sediment transport. These properties are calculated per wave and vary over height. In the analysis per wave the skewness and asymmetry are calculated with the skewness and asymmetry parameter (Equation 2.7, 2.8). The skewness and asymmetry parameter are always positive, values smaller than 0.5 correspond to negative skewness and asymmetry and values larger than 0.5 correspond to positive skewness and asymmetry.

The wave properties at the three characteristic heights will be related to the total short wave related sediment transport per test. The relation between the different wave properties and the total sediment transport per wave shows the importance of the wave properties. Next to that, this analysis shows at which elevation above the bed the properties are strongest related to sediment transport. In numerical modelling the properties at this characteristic height can be used to calculate sediment transport.

The wave separation is based on the velocities at the elevation of maximum sediment transport to minimize the influence of phase lead on the resulting total sediment transport per wave. Due to irregular variations close to zero there will some 'spurious' waves from the separation process. Therefore only waves with a wave period between 1.3 seconds (0.8 Hz) and 2.5 seconds (0.4 Hz) will be taken into account in the analysis. In the wave spectrum it can be seen that the spectrum peak (Figure 4.10) occurs between 0.4 Hz and 0.8 Hz.

In the analysis per wave, it is decided to have fixed elevations based on the mean profile per test. Another possibility is to adapt the calculation for varying bottom height and determine the elevations on the sediment profile per wave. But because the sediment profile per wave is very capricious, the accuracy of the elevations will be low. It is decided that it is preferable to have a clear elevation that does not account for the bottom change, but because the fixed elevation is the mean elevation the uncertainty due to the bottom variation will average out. The bottom change will widen the scatter, but not change the mean trend. Of the uncertainty that occurs when adapting the elevations to the instantaneous still bed level it is not know or it influences the mean. To avoid a result that can be partly based on calculation errors, the fixed elevation is used, which probably results in a wide scatter.

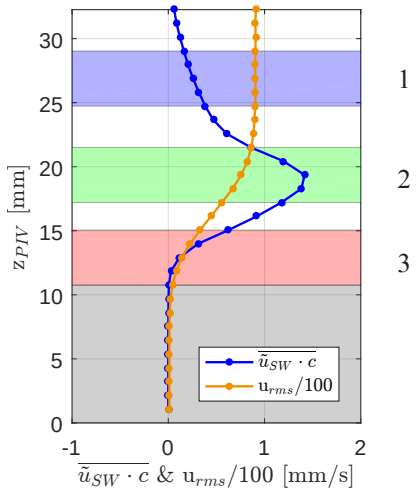


Figure 3.10: The characteristic elevation is this study: (1) free-stream elevation, (2) elevation of maximum short wave related sediment transport and (3) near-bed elevation.

# 4

# Results

*This chapter will present and explain the results of the data analysis. The results are presented in the sequence of the three research questions: (1) sediment transport estimation and data validation (section 4.1), (2) analysis of the sediment transport mechanisms (section 4.2) and (3) the wave related transport analysis (section 4.3).*

## 4.1. Sediment transport estimation and data validation

To validate the sediment transport based on PIV measurements, the transport, sediment gradient and bed level change based on the PIV measurements and based on the bottom profile measurements are compared. In this section three abbreviations are used frequently: WG = Wave gauge, BP = Bottom profile and PIV = Particle image velocimetry. Appendix J shows the results per test.

*Sediment transport*

Figure 4.1 compares the sediment transport from different calibration methods to the sediment transport based on bottom change. The quadratic calibration gives the best calibration fit (Figure 4.2, 4.3) and the best result (Figure 4.1). Therefore the quadratic calibration will be used in this research. Figure 4.4 compares the transport results based on the quadratic relation to the bottom profile measurements including uncertainty. Because the sediment transport of the bottom data is based on a zero sediment transport boundary condition at offshore side of the flume, the uncertainty increases towards the shore. The sediment transport of the PIV measurement is significantly larger (Figure 4.4, Table 4.1) than the sediment transport from the bottom measurements and outside the uncertainty interval. To understand this difference the calibration is explained more elaborate in the following paragraphs and will be further discussed in Chapter 5.

Where this research finds a quadratic calibration, Horikawa et al. [1982] found an exponential relation between intensity and concentration (section 2.5). Because in this research the calibration is fixed in two points, the exponential trend line curves less than the quadratic trend line and results in more sediment transport (Figures 4.2 and 4.3). The two fixed points, namely mean bed and mean water intensity, limit the effect of the calibration, but a calibration without the fixed points would be physically incorrect. That both studies find a non-linear relation, can be explained by the effect of concentration on image intensity. With a lower concentration it is possible to see deeper into the flow. I.e. particles further away from the camera become visible. Therefore the intensity/concentration-ratio increases with a decreasing concentration, which results in a curved intensity profile in the sheet flow layer (Figure 4.5a, 4.5b). In this research the concentration in the sheet flow layers is assumed linear. A non-linear calibration changes the curved intensity profile to a linear concentration profile (Figure 4.5c), which will decrease the sediment transport in the sheet flow layer.

Next to that, the calibration can be affected by variation in the mean image brightness. Figure 4.6a shows that the bottom concentration varies over time during the measurement. The cause of this intensity variation over time is laser reflection. Because the flume is covered, the only light source is the laser. The change in reflection of the laser light, can cause this variation over time. The large term variation (Figure 4.6a) is due to a changing reflection on the bottom profile. The short term variation (Figure 4.6b) is due to a change reflection on the water surface. Hence the variation is correlated to the wave phase. Figure 4.6b shows that the period of the fluctuation is in the same order of magnitude as the wave period. Hence this can influence the intra-wave sediment transport.

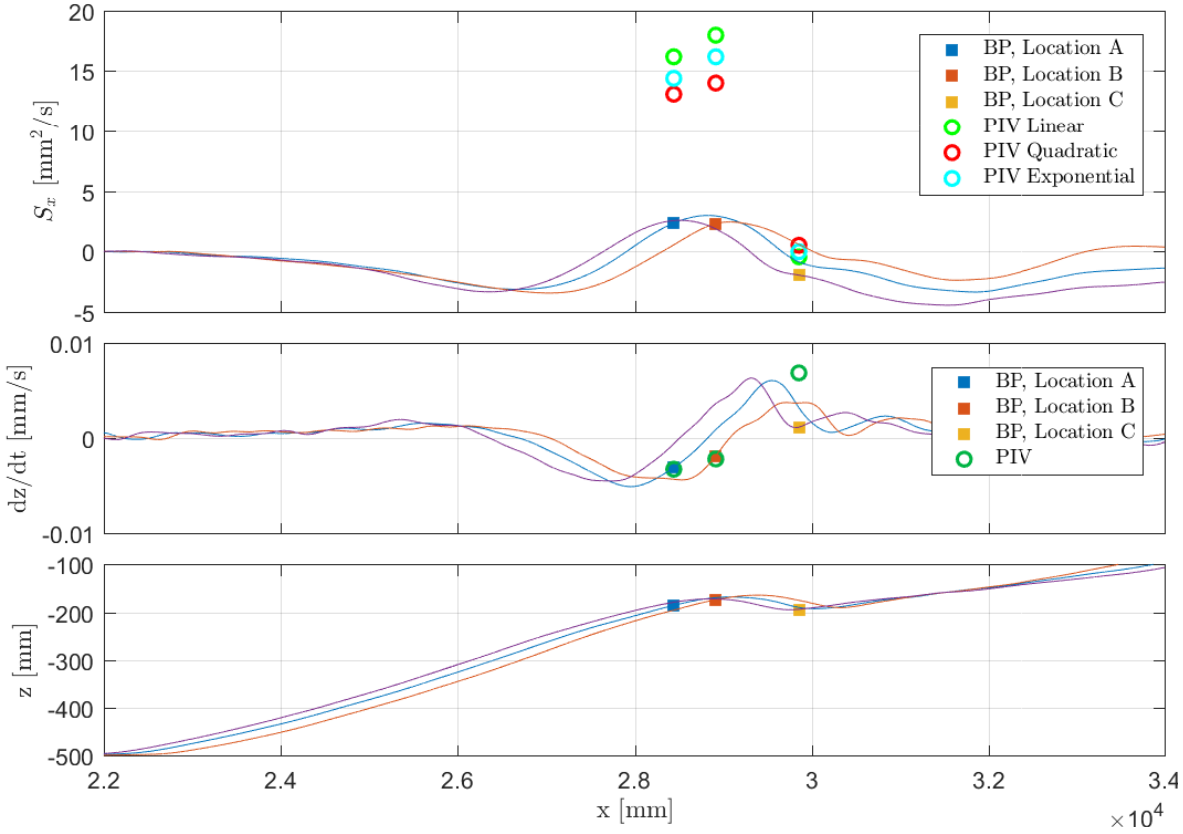


Figure 4.1: Comparison of sediment transport based on different calibration methods: a linear, quadratic and exponential calibration.

*Sediment gradient between measurement locations*

With a maximum in onshore transport on top of the sandbar, the sediment transport based on the PIV measurements is in line with theory and the sediment transport based on the bottom profile development (Figure 4.1). Hence based on this qualitative comparison the PIV transport looks valid, although the PIV sediment transport is larger than the bottom profile sediment transport.

The sediment curve based on the bottom profile measurements shows a maximum on top of the bar. The PIV sediment transport confirms this expectation with the maximum transport at top of the bar (Location B) and the minimum transport onshore of the bar (Location C). In other words, the relative sediment gradients between the different measurement locations are compared. Table 4.1 shows the comparison. Because the transport follows a correct pattern over the bar, the relative sediment transport gradient ($\Delta S_{12}/S_1$) gives better results in the comparison than the total sediment transport ($S_1$). Only the ratio between location A and B is very different. Location A and B are both located slightly in front of the bar (Figure 3.6). Because these two locations are close together, a small inaccuracy in sediment transport has a strong impact on the relative sediment gradient. It is more important to notice that the PIV sediment transport has the maximum on top of the bar like the transport curves suggest.

*Sediment gradient within the PIV frame*

Next to the gradient between locations the gradient within the PIV frame can be used as validation measure. By comparing the sediment transport on the left to the transport on the right side, the sediment gradient within the PIV frame can be calculated. When looking at the bottom and water intensity in cross-shore direction, it is found that the PIV images do not have a uniform brightness (Figure 4.7a). The mean bed intensity varies up to 40 % within the PIV frame, while the mean bed and water intensity should be constant in cross-shore direction. Because the calibration is based on the intensity profile averaged in cross shore direction, the gradient is persistent through the calibrated concentration. This image brightness gradient results in a sediment gradient that is more than 10 times larger than the sediment gradient value. Since the intensity gradient can have a different kind of directions and shapes (Figure 4.7b), it is difficult to have a high precision when applying a gradient correction. Next to that the concentration in the sheet flow is unknown and therefore the

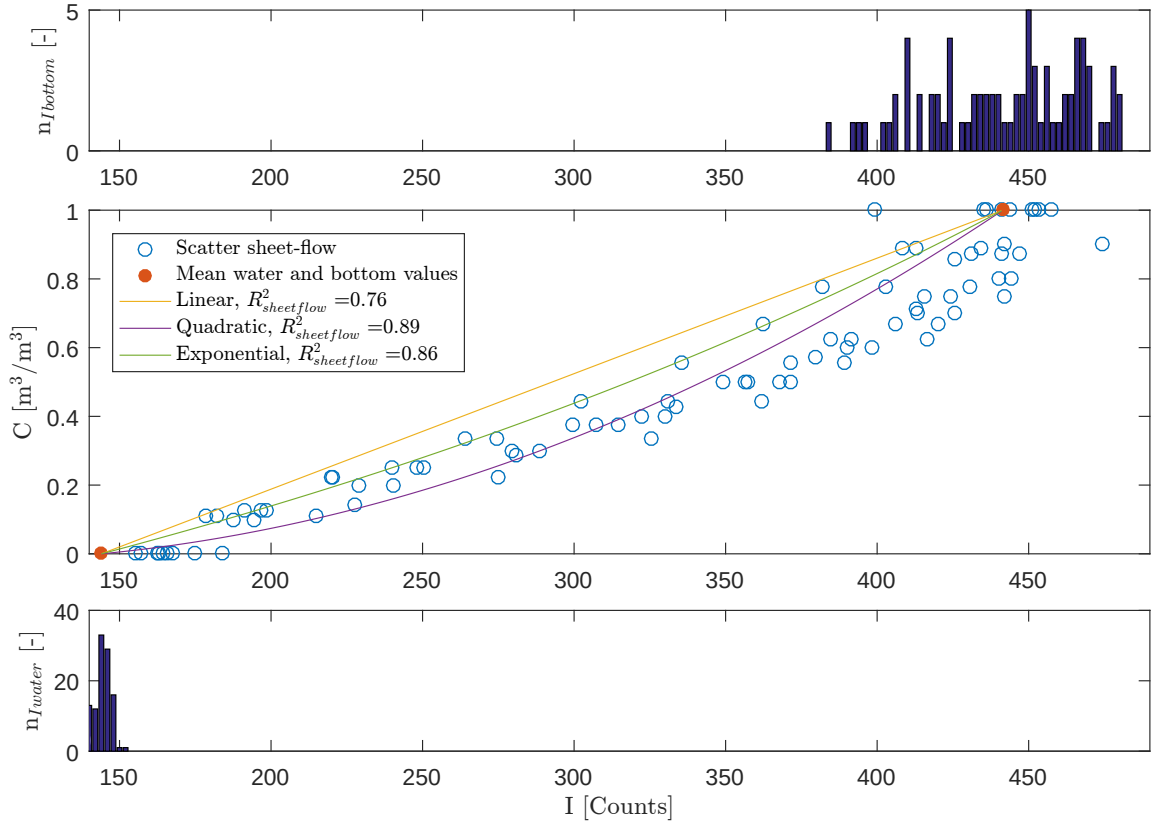


(a) Calibration set 1: offshore of the sandbar (Testseries 1, Location A)

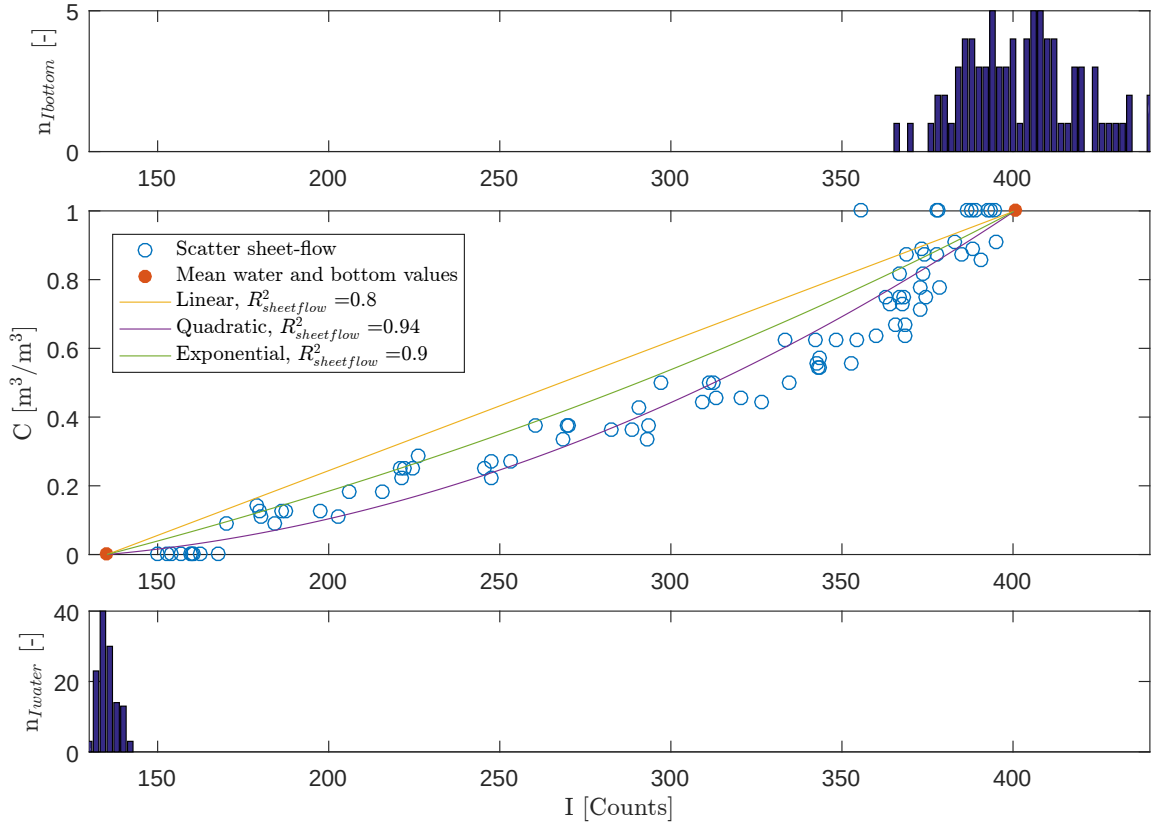


(b) Calibration set 2: on top of the sandbar (Testseries 2, Location B)

Figure 4.2: Calibration trend line per calibration set. The sub-figure in the middle displays the trend lines of the three different calibration methods: linear, quadratic and exponential. The orange dots are the fixed points based on the mean water and bottom intensity. The blue dots are the data points in the sheet flow layer. The top and bottom sub-figures show the distribution in bed and water intensity. In this study the data is divided into four calibration sets: one for each measurement location, but two for the location onshore of the bar because the light exposure at this location changed between the test. The coefficient of determination, $R^2$, shows the fit between the trend line and the sheet flow data. So, the coefficient of determination does not include the fixed points.

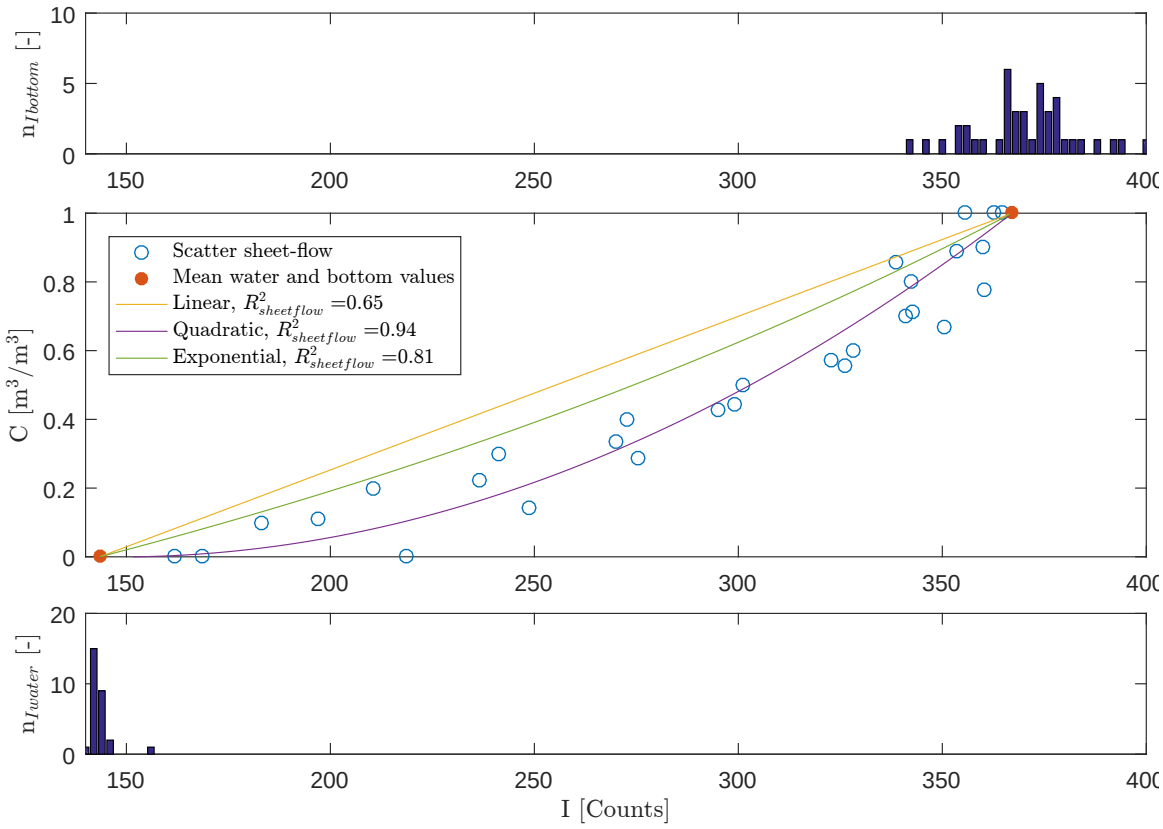


(a) Calibration set 3: the first set onshore of the sandbar (Bar migration 1.1 and 1.2, Location C)

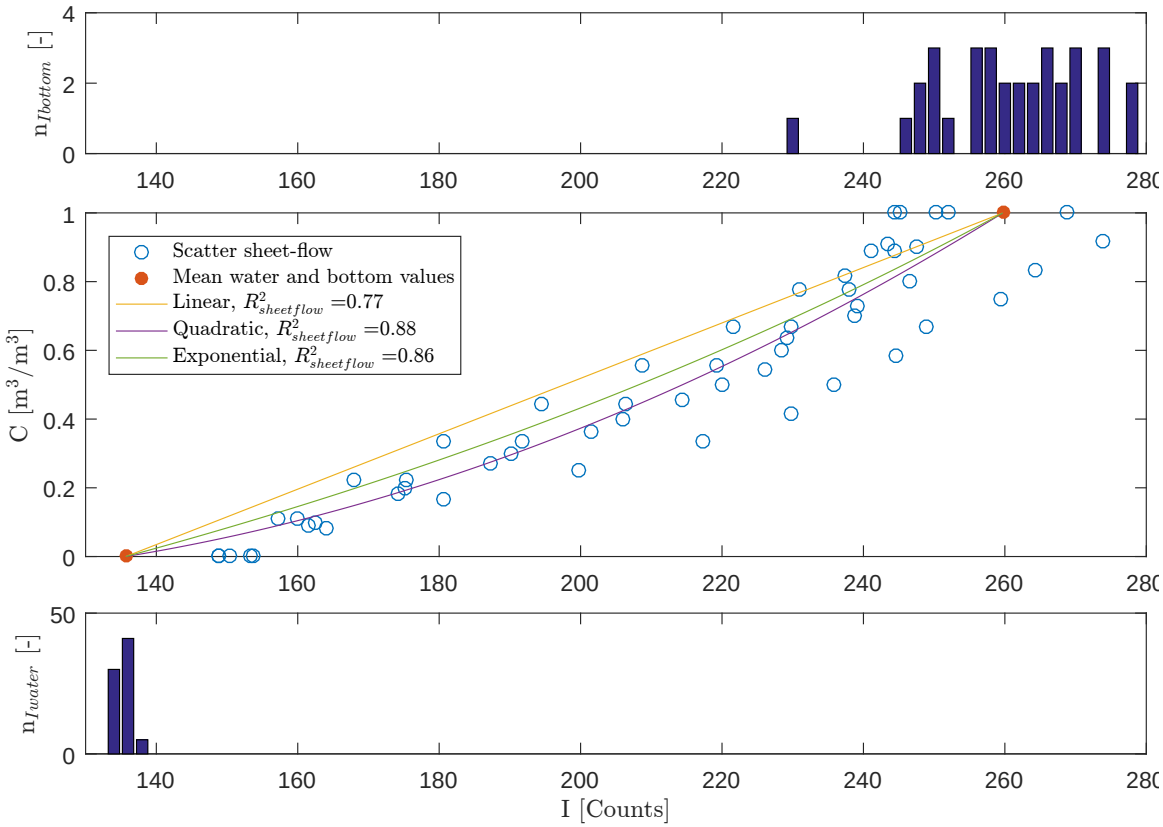


(b) Calibration set 4: the second set onshore of the sandbar (Bar migration 1.3, Location C)

Figure 4.3: Continuation of Figure 4.2

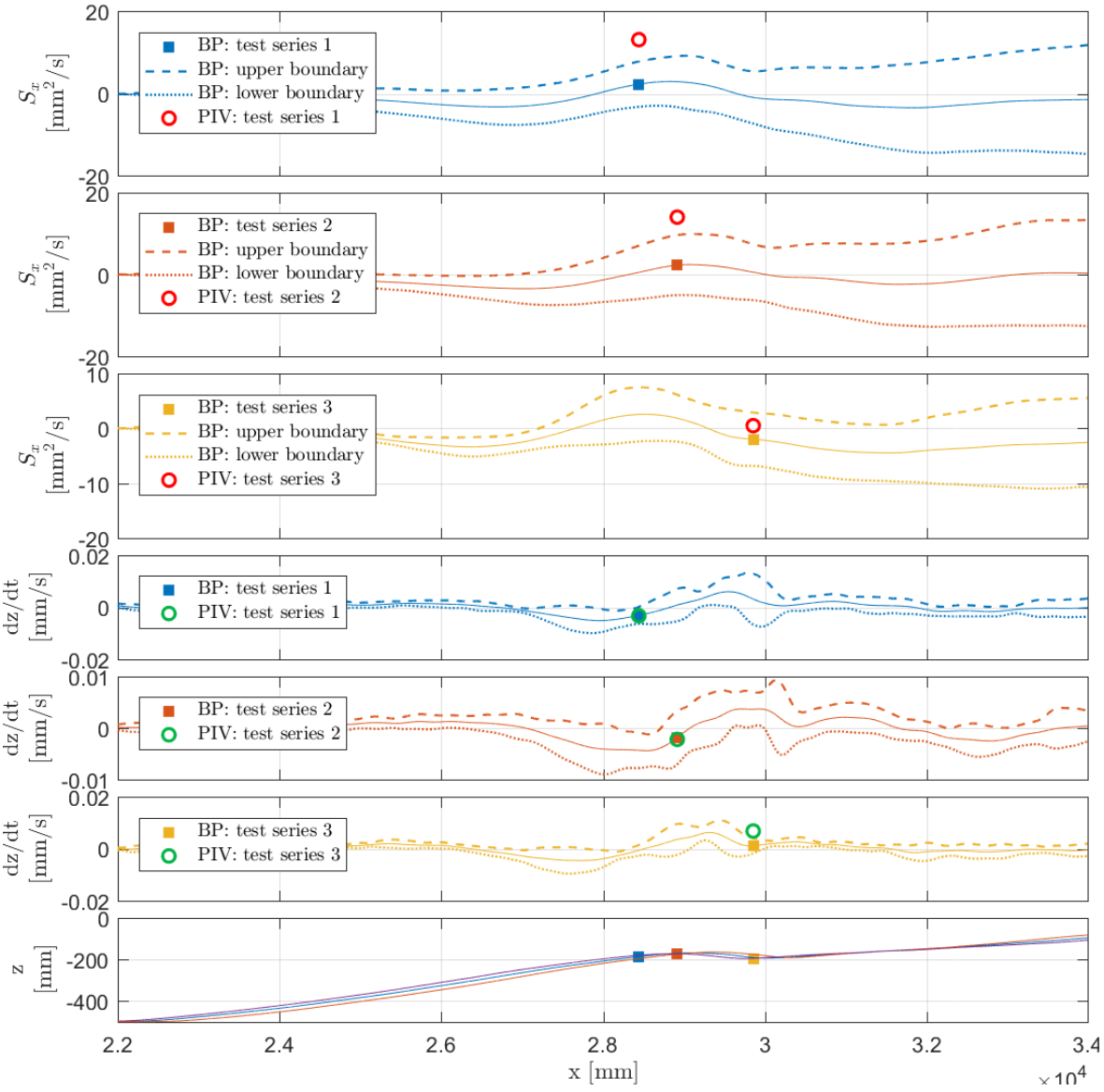


Figure 4.4: Sediment transport comparison between BP and quadratic PIV results. The dashed and dotted line show the upper and lower limit of the 95 % confidence interval. Hence the lower boundary is at 2.5 % of the results and the upper boundary is at 97.5 %. Only the PIV measurement at location C is within the uncertainty range. The first plot shows the total sediment transport of test series 1 (location A), the second plot of test series 2 (location B) and the third plot of test series 3 (location C). The fourth to sixths plot show the comparison in bed level change for the same locations. The sevenths plot shows the mean bottom height for all test series.

Table 4.1: Comparison between sediment transport and gradient of different locations. Figure 3.8 gives shows the location of the calculated gradients.

| **Property** | **BP** | **PIV** | *Ratio: PIV/BP* |
|---|---|---|---|
| $S_1$ [mm$^2$/s] | 2.3 | 14.1 | *6.1* |
| $S_2$ [mm$^2$/s] | 2.3 | 15.2 | *6.6* |
| $S_3$ [mm$^2$/s] | -2.0 | 0.17 | *-0.085* |
| $\Delta S_{12}/\Delta x_{12}$ [mm/s] | $-0.1 \cdot 10^{-3}$ | $25 \cdot 10^{-3}$ | - |
| $\Delta S_{23}/\Delta x_{23}$ [mm/s] | $-4.6 \cdot 10^{-3}$ | $-16 \cdot 10^{-3}$ | *3.5* |
| $\Delta S_{13}/\Delta x_{13}$ [mm/s] | $-3.1 \cdot 10^{-3}$ | $-10 \cdot 10^{-3}$ | *3.2* |
| $\frac{\Delta S_{12}}{S_1}$ [-] | -0.019 | 0.078 | - |
| $\frac{\Delta S_{23}}{S_2}$ [-] | -1.9 | -1.0 | *0.5* |
| $\frac{\Delta S_{13}}{S_1}$ [-] | -1.9 | -1.0 | *0.5* |

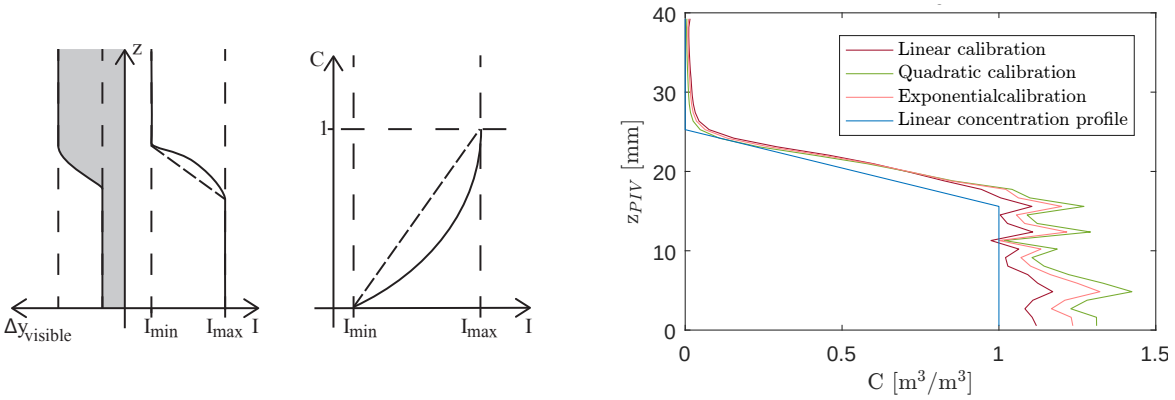


(a) Effect of visible distance into the flow on intensity

(b) Non-linear calibration relation

(c) Effect of the calibration method on the concentration profile. Due to the fixed points in the calibration (Figures 4.2 and 4.3) the influence of the calibration method is small. Example of test 1.1.1.

Figure 4.5: Non-linear relation between intensity and concentration. The effect of the visible distance on image intensity (a) is visible in the calibration relation (b). A non-linear calibration affects the shape of the concentration profile in the sheet flow layer (c).

effect of the correction on the sheet flow intensity can not be checked. With an error of ten times the value, a complex correction and no validation for the most important intensities, an image brightness correction is not advisable. The sediment gradient within the PIV frame will not be studied further. This brightness gradient will have none or at most a small effect on the sediment transport calculation, because the sediment transport is based on the mean in cross-shore direction and the sediment transport within the PIV frame is relatively constant. The intensity gradient in cross-shore direction would only have an influence on the mean sediment transport if the sediment transport would strongly vary in cross-shore direction within the PIV frame. Since the width of the frame is only 6 centimetres, the sediment gradient in cross-shore direction remains small.

*Bed level change*

Because the PIV images contain the still bed level, the bed level change per test can be determined from the PIV measurements. Figure 4.4 shows the comparison in bed level change between the PIV measurements and bottom profile measurements per location. At the locations offshore of the sandbar and on the bar crest the mean bed level change the bottom change is accurately the same. Onshore of the sandbar the bed level change of the PIV is larger than the bed level change of the bottom measurements and just outside the confi-

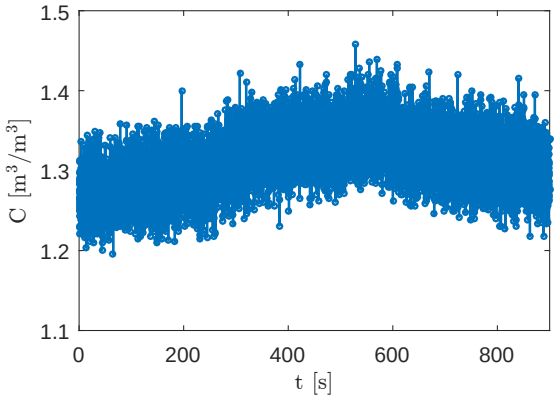


(a) Variation in mean bed concentration on long time scale. Example of test 1.1.1.

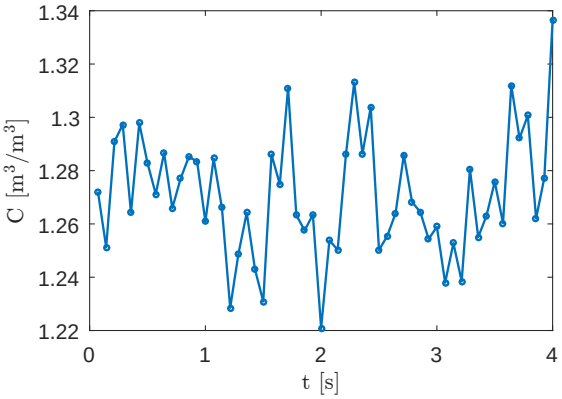


(b) Variation in mean bed concentration on short time scale. The variation is on the scale of the wave period. The peak period is 1.8 seconds. Example of test 1.1.1.

Figure 4.6: Variation in mean bed concentration over time.

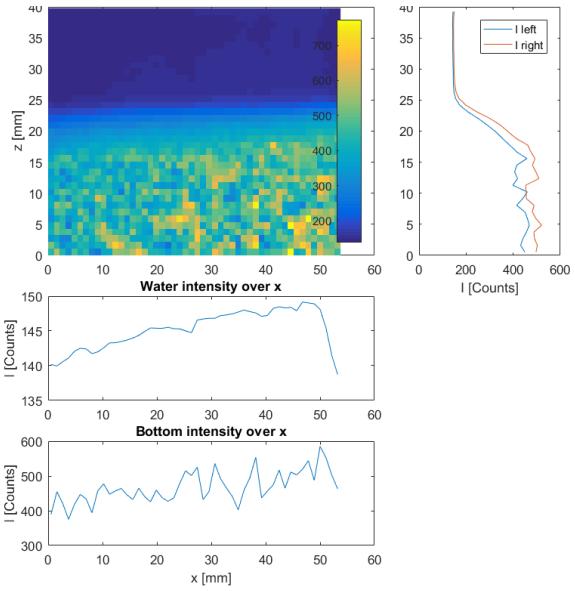


(a) Intensity gradient: both the mean bottom intensity and mean water intensity vary in cross-shore direction. The intensity gradient between left and right (subplot on the right) strongly influences the sediment gradient.

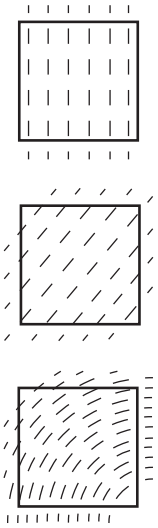

(b) Types of gradients: horizontal, diagonal and curved.

Figure 4.7: Uneven image brightness

dence interval of the bottom measurements. Hence in general the

Note that this is the non-moving bed level during wave action, while the bottom measurements determine the bed level during still water. Because part of the sediment is moving during wave action, the PIV still bed level is lower than the bed level of the bottom measurements. Under the assumption that the amount of moving sediment remains constant, the bed level change of the measurements can be compared. Based on the results of the comparison, the two properties seem well comparable.

Based on the positive results of the bed level change comparison, the validity of both results is confirmed. Since the bed level change is the base of the sediment transport calculation for the bottom measurements, this sediment transport of the bottom measurements seem more reliable than the sediment transport based the PIV measurements. In the PIV calculation bottom change and sediment transport are two independent properties, because sediment transport is calculated with the velocity times concentration.

### 4.1.1. Preliminary conclusion

Concluding, with a maximum transport on top of the bar, the PIV results qualitatively confirm the expectation. However quantitatively the PIV data does not match the bottom data. The sediment transport from the PIV data is significantly larger than the sediment transport of the bottom change.

Because the goal of this research is to determine the dominant cause of onshore bar migration, the analysis in the following sections (sections 4.2 and 4.3) will compare ratios. Because the results are valid in a qualitative manner, it is assumed that a sediment transport analysis will give realistic ratios. Therefore the results are assumed valid for further analysis. However when interpreting and drawing conclusions regarding sediment transport using PIV concentrations, the caveat of limitations regarding this type of analysis must be considered.

## 4.2. Analysis of the sediment transport mechanisms

The total sediment transport shows a maximum on top of the bar, as expected for onshore bar migration (Figure 4.8). To understand the cause of this maximum on top of the bar the sediment transport is analysed in more detail. Three mechanisms for sediment transport are considered. These mechanisms are current related transport, time-averaged long wave related transport and time-averaged short wave related sediment transport (section 2.4, Equation 2.22).

Figure 4.9 shows the mean *ratio* between the transport mechanisms. To distinguish the different sediment mechanisms, the short waves and long waves are separated at a cut-off frequency of half the peak frequency (Figures 4.10, 4.11). At the locations with onshore sediment transport (offshore of the bar and on top of the bar) the time-averaged short wave related transport is the largest in size and onshore directed. The second mechanism in size is long wave related transport, which is offshore directed. The current related transport is the smallest in size and directed onshore. At the location offshore of the bar the long wave related transport is the largest in size and offshore directed. The offshore long wave related transport balances with the combination of onshore short wave related and onshore current related transport. This results in an almost zero total transport.

The *sediment gradients* of the different types of sediment transport differ over the sandbar. The ratio of the transport gradients is even more relevant than sediment transport ratio, because the gradient determines coastal change. Figure 4.8 shows the sediment transport mechanisms over the three measured locations. The gradients can be distinguished in two types: the overall gradient over the bar ($\Delta S_{13}/\Delta x_{13}$, Table 4.2) and the gradients offshore and onshore of the bar crest ($\Delta S_{12}/\Delta x_{12}$ & $\Delta S_{23}/\Delta x_{23}$, Table 4.2). The down-ward overall gradient enlarges the bar and an upward overall gradient makes the bar smaller. The gradients around the bar crest relocate the crest of the bar onshore or offshore.

For both gradient types, the *time-averaged short wave related transport* has the largest gradients and is thus *the dominant mechanism* in onshore sandbar migration. The short wave related transport decreases towards the shore with the steepest gradient onshore of the bar. Hence short wave related transport enlarges the sandbar, because the sediment transport decreases towards the shore, and moves the bar in onshore direction, because the bar grows fastest on the onshore side. The current related transport and long wave related transport both move the bar onshore. The current related transport with a maximum in onshore transport and the long wave related transport with a minimum in offshore transport. Table 4.2 shows an overview of the gradient ratios. The short wave related transport is fully responsible for enlarging the sandbar with a downward overall gradient. The gradients that cause erosion at the offshore side of the sandbar and accretion at the onshore side of the sandbar are both caused for 50 % by the short wave related transport, for

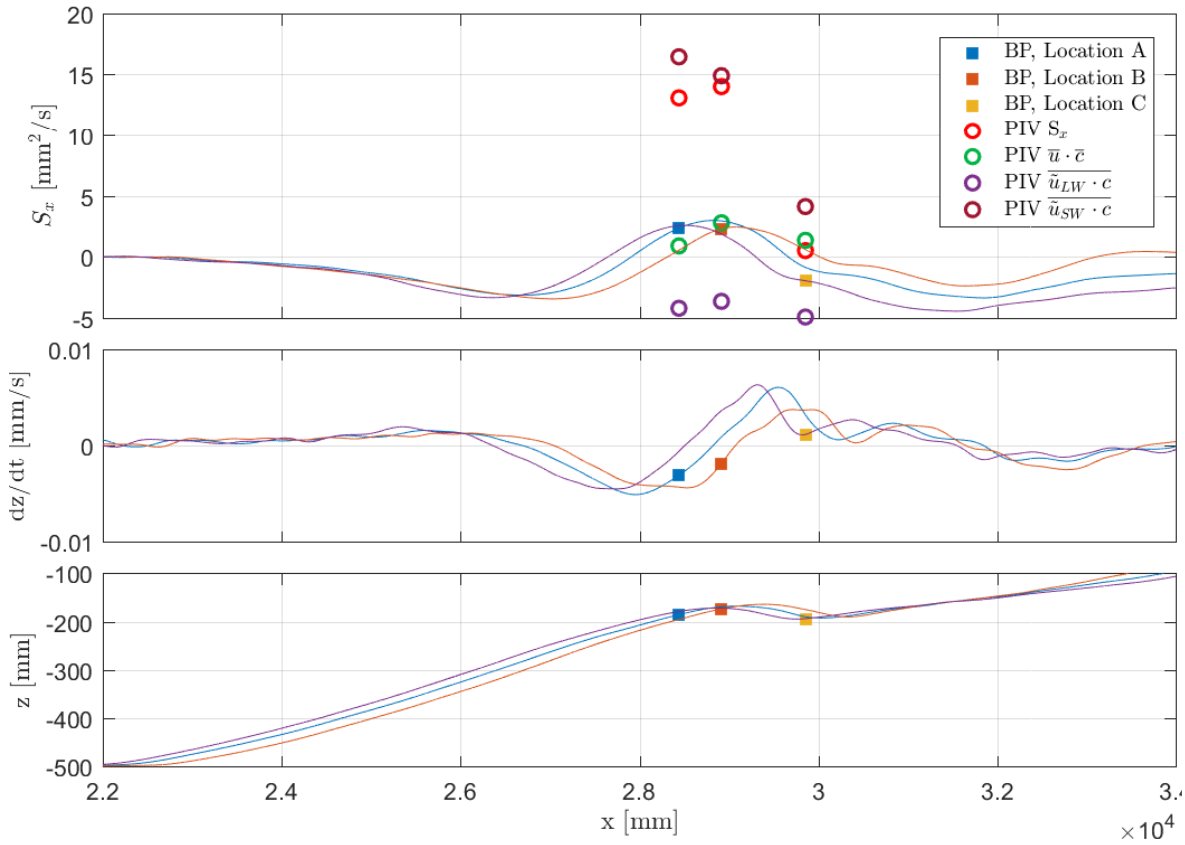


Figure 4.8: Mechanisms of sediment transport per location. The total transport (red) has a maximum on top of the bar and a strong decrease on the onshore side. The short wave related transport (dark red) decreases over the bar with a strong decrease on the onshore side. The long wave related transport (purple) has a minimum in offshore transport at the bar crest and the current related transport (green) a maximum in onshore transport at the bar crest.

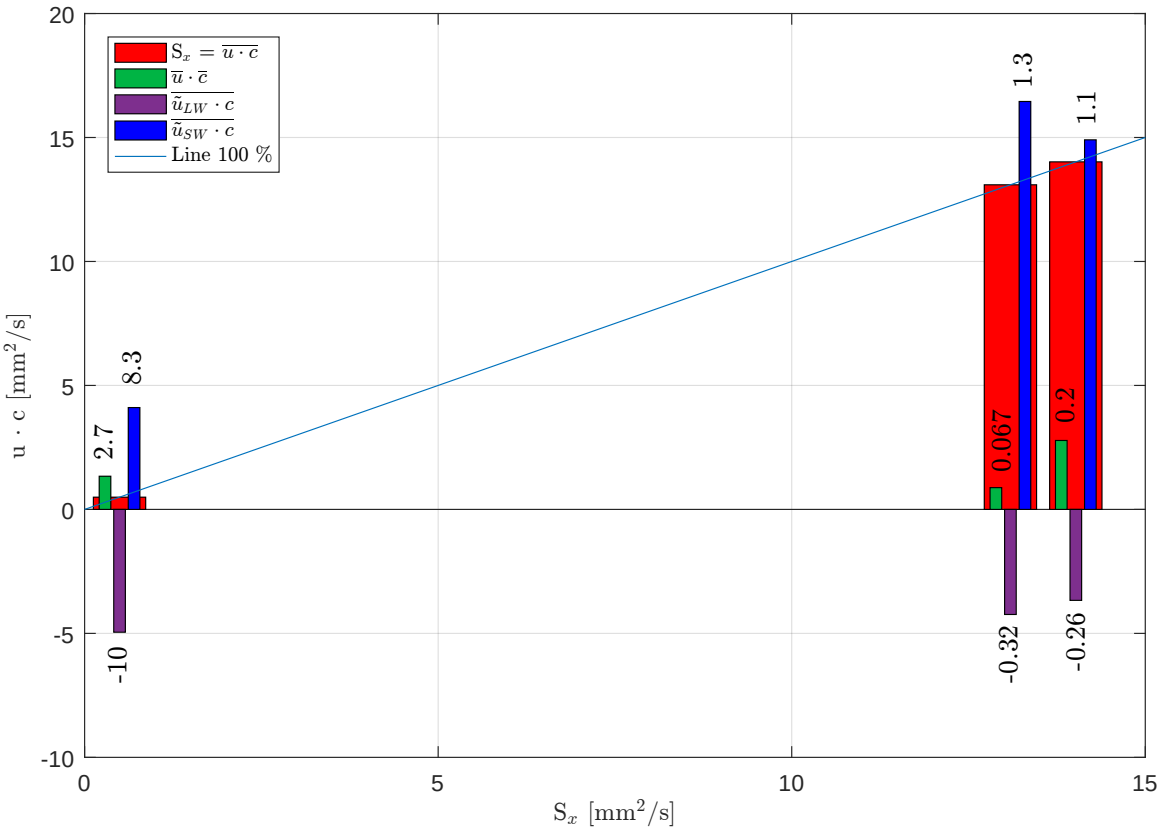


Figure 4.9: Mean ratio of sediment mechanisms. The red bars are the total sediment transport. The green bars are the current related transport, the purple bars the net long wave related transport and the blue bars the net short wave related transport. The number at each bar indicates the ratio between the bar and the total sediment transport at that location.

Table 4.2: Comparison of sediment gradients at different measurement locations between the different sediment transport mechanisms. Figure 3.8 shows the location of the calculated gradients.

| **Property** | $\overline{S_x}$ [mm/s] | *Ratio* $\overline{S_x}/\overline{S_x}$ | *Ratio* $\overline{u}\cdot\overline{c}/\overline{S_x}$ | *Ratio* $\overline{\tilde{u}_{LW}\cdot\tilde{c}}/\overline{S_x}$ | *Ratio* $\overline{\tilde{u}_{SW}\cdot\tilde{c}}/\overline{S_x}$ |
|---|---|---|---|---|---|
| $\Delta S_{13}/\Delta x_{13}$ | -9.8 $\cdot 10^{-3}$ | 1 | -0.04 | 0.04 | 1 |
| $\Delta S_{12}/\Delta x_{12} - \Delta S_{13}/\Delta x_{13}$ | 12.1 $\cdot 10^{-3}$ | 1 | 0.3 | 0.2 | 0.5 |
| $\Delta S_{23}/\Delta x_{23} - \Delta S_{13}/\Delta x_{13}$ | -6.1 $\cdot 10^{-3}$ | 1 | 0.3 | 0.2 | 0.5 |

30 % by the current related transport and for 20 % by the long wave related transport.

The *vertical distribution* of the sediment transport mechanisms shows the elevation of transport per mechanism (Figure 4.12). The maximum sediment transport of the short wave related transport occurs at the highest elevation above the bed and the maximum transport of the current related transport at the lowest elevation above the bed. The height of the maximum sediment transport is related to the wave phase with maximum sediment transport, because the still bed elevation and suspension height vary during the wave phases. In other words, the high elevation of maximum transport shows a large correlation between sediment suspension and horizontal velocities. Hence the first conclusion from this observation is that the current related transport occurs more equally over time, while the short wave related transport occurs at the moment of high suspension. The second conclusion is that for short wave related transport skewness is relatively more important than asymmetry, because the short wave related transport is caused at moment of high suspension and thus during maximum orbital velocity. However it difficult to fully understand the mechanisms based on a mean analysis, because the wave related sediment mechanisms strongly depend on timing. For future research it is recommend to create a phase-averaged wave to study the timing of suspension.

Lastly, it is interesting to observe that the offshore directed total transport above the wbbl (Figure 4.12c, measured onshore of the sandbar) is mainly due to long waves. But the other two mechanisms also slightly contribute to this.

It is important to note that vertical distribution is established by first taking the mean per test of fifteen minutes and second averaging nine test after calibrating the still bed level of each test to the same position. Hence between tests the still bed elevation is calibrated, but within a test the still bed variation is not taken into account. The bed level variation in the fifteen minutes will spread the vertical distribution over height. If the still bed level would be calibrated at shorter time intervals, for example every minute, the distribution in Figure 4.12 would show a thinner sheet flow layer with larger sediment transport.

The ratios in Figure 4.9 become 1 % lower or higher between the different calibration methods (linear, quadratic and exponential). So, this ratio is not very sensitive to the calibration method. This can indicate that the ratio gives a realistic results despite the mismatch in sediment transport between the PIV measurements and the bottom measurements.

### 4.2.1. Preliminary conclusion

Time-averaged short wave related transport is the dominant cause of onshore bar migration. The short wave related transport enlarges the bar and moves the bar onshore. Current related transport and time-averaged long wave related transport both move the bar towards the shore, but with a small contribution. Because the largest part is due to short wave related transport, the wave related sediment transport is analysed in section 4.3.

## 4.3. Time-averaged short wave related transport analysis

This analysis of the short wave related transport studies the importance of two intra-wave processes, namely skewness and asymmetry, on the short wave related sediment transport. These intra-wave processes are explained in the literature study (section 2.4). This analysis combines two ways to study these wave properties: the mean values per location (Figures 4.13 to 4.17) and the values per individual wave (Figures 4.23 to 4.22). This section is structured along three results of the short wave analysis. First, the main result of this analysis is that skewness increases and asymmetry decreases towards the bottom and both properties have a maximum on the bar crest (section 4.3.1). Next, the results indicate that sediment transport depends mainly on the near-bed skewness (section 4.3.1). Lastly, the possibility to calculate the near-bed skewness based on the phase lead is studied as suggested by Henderson et al. [2004] and Berni et al. [2013] (section 4.3.2). With the

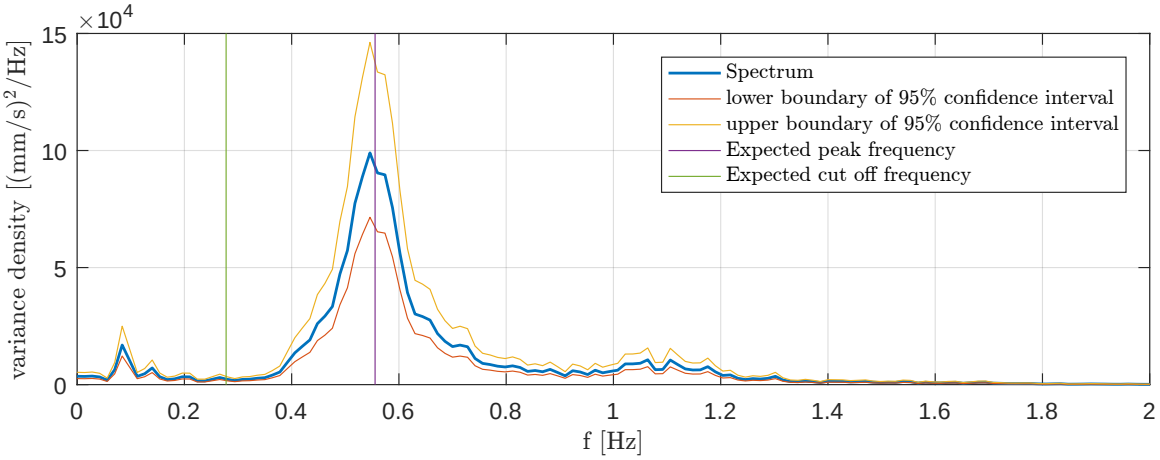


(a) Measured velocity spectrum offshore of the sandbar (location A) during test 1.1.1.

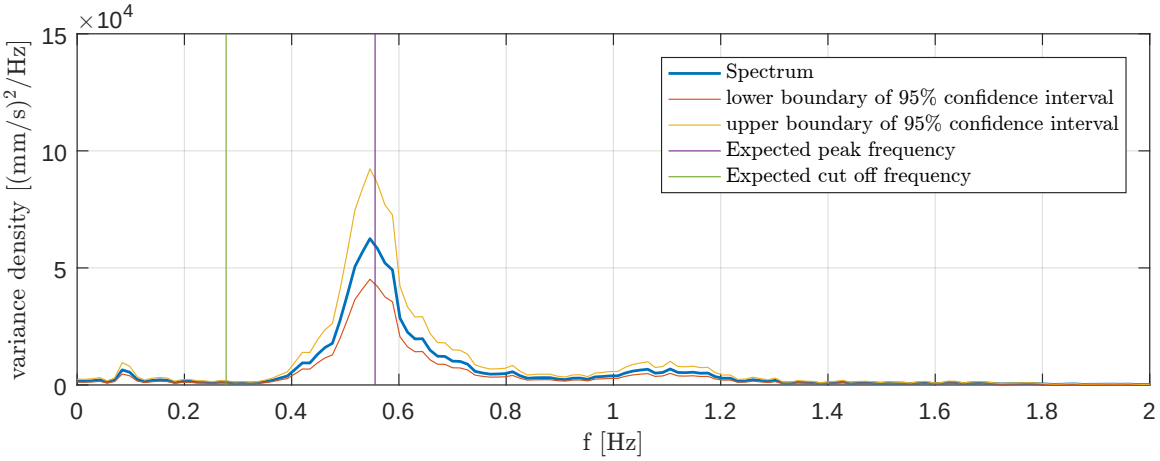


(b) Measured velocity spectrum on top of the sandbar (location B) during test 2.1.1.

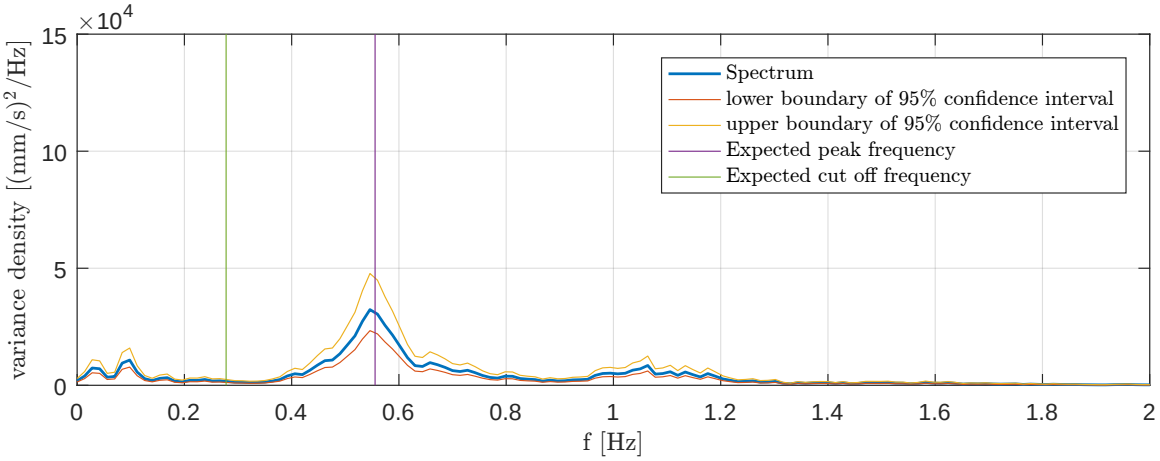


(c) Measured velocity spectrum onshore of the sandbar (location C) during test 3.1.1.

Figure 4.10: The measured velocity spectra at the locations A, B and C. The purple line shows the peak frequency based on the peak period of 1.8 seconds. The cut off frequency (green line) is chosen at half the peak frequency to filter the long waves from the frequency spectrum. The peak variance of the spectrum decreases over the bar. This is due to wave breaking on the bar. The largest waves of the irregular field break on the bar. Because the wave field is used in all tests, the velocity spectra represent all tests of that specific measurement location.

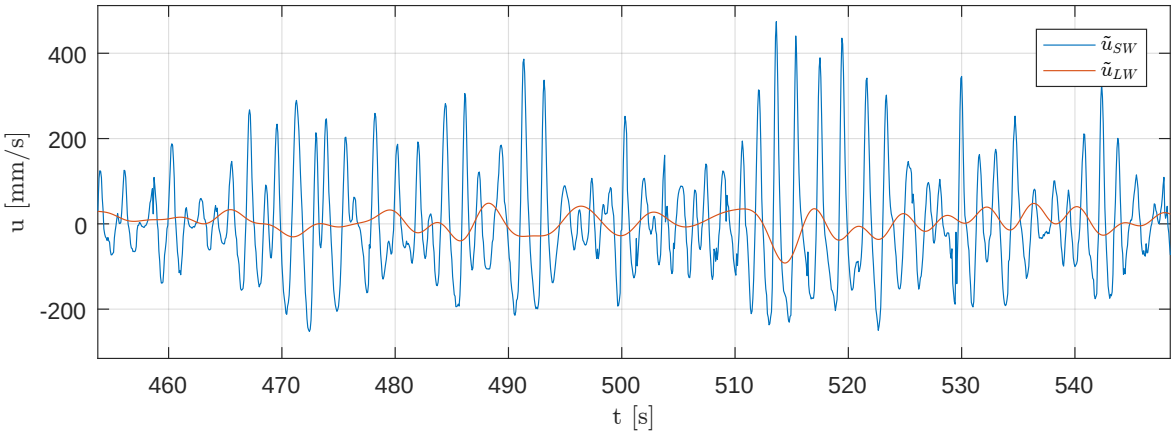


Figure 4.11: An impression of the time-series of short and long waves. The long wave vary at the scale of the variation in short wave groups. This figure shows an example of test 1.1.1.

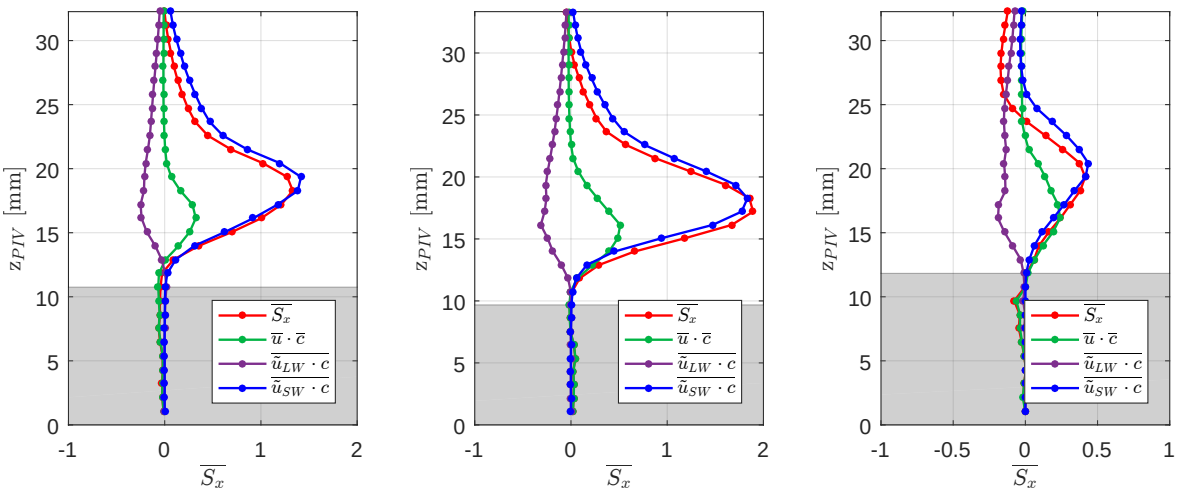


(a) Offshore of the sandbar (Location A, Testseries 1)

(b) On top of the sandbar (Location B, Testseries 2)

(c) Onshore of the sandbar (Location C, Testseries 3)

Figure 4.12: Vertical distribution of the different sediment transport mechanisms. Displayed are the total sediment transport ($\overline{S}$, red), the current related sediment transport ($\overline{u} \cdot \overline{c}$, green), the time-averaged long wave related transport ($\overline{\tilde{u}_{LW} \cdot c}$, purple) and the time-averaged short wave related transport ($\overline{\tilde{u}_{SW} \cdot c}$, blue). The still bed is displayed in grey.

dependence of short wave related sediment transport depends on near-bed skewness, a relation to predict near-bed skewness can improve sediment transport calculations.

### 4.3.1. Relation between wave shape and sediment transport

The main result of the short wave analysis is that *skewness increases* towards the bottom and *asymmetry decreases* towards the bottom and even becomes positive. Positive asymmetry indicated pitched backwards wave. This is phenomenon that what is further not observed in nature. Figure 4.13 shows the vertical development of the skewness and asymmetry in the wave bottom boundary layer. The three characteristic heights are marked in the figure: free-stream, maximum sediment transport and close to the bottom. Figure 4.15 shows the development of the properties at the characteristic height over the sandbar. The increase of skewness and decrease of asymmetry is also in this Figure clearly visible. A physical explanation of this process is given by Nielsen [1992] for shear stress. With asymmetric free-stream velocities, the wave bottom boundary layer has less time to develop during the steep front of the wave than during the gentle back of the wave. A thinner wbbl results in higher velocity gradients and thus larger shear stress. The same explanation holds for the orbital velocities close to the bottom. Figure 4.14 shows the near-bed velocity gradients for the onshore and offshore velocities. The velocity gradient is stronger for the onshore velocities. This confirms the explanation of Nielsen [1992].

Figure 4.15 shows that both skewness and asymmetry have a maximum (or minimum) on the bar crest. This confirms the theoretical expectation, because both processes are depended on depth. If the short wave related transport would purely rely on these two properties, the transport would need to have a maximum on the bar crest. Since there is no maximum in short wave transport observed on the bar crest (Figure 4.15), there will be other short wave processes that play a role in onshore bar migration.

Note in Figure 4.13 that the skewness and asymmetry in the still bed is not zero. This effect is due to rhythmic sinusoidal high frequency noise signal in the measurement. This noise is observed in all measurements and is probably due to vibrations in the wave-flume or camera. In Figure 4.23a the noise becomes visible close to the bed (third plot) and in the bed (lowest plot), because the orbital velocities are very small. The high frequency noise is also visible in the variance density spectrum in the bed (Figure 4.23b) with a peak frequency of 1.4 Hz and the first higher harmonics at 2.8 Hz. Because the resulting mean skewness and asymmetry are small (Figure 4.13) and constant over height, this high frequency noise is neglected.

Both *near-bed skewness* and *an asymmetric pressure gradient* due to near-bed asymmetry can cause sediment transport. Near-bed skewness and an asymmetric pressure gradient both cause a skewed sediment transport (Figure 4.16). Therefore the skewness of the sediment transport is larger than the skewness of the velocities (Figure 4.17). Near-bed skewness by suspending sediment during high orbital velocities and the asymmetric pressure gradient by affecting grains that are already in suspension or grains in the top layers of the bed. Hence the sediment transport at every elevation relates to the near-bed skewness, while the sediment transport at every elevation relates to the asymmetric pressure gradient at that specific elevation. However, because asymmetry both affects the near-bed skewness and the asymmetry pressure gradient, these processes are difficult to separate. The next paragraph and Figure 4.18 explain these processes in more detail.

Free-stream skewness and asymmetry transform towards the bed into near-bed skewness and asymmetry (step (1) in Figure 4.18). The near-bed skewness suspends sediment (step (2) in Figure 4.18). Because the near-bed skewness will cause skewed concentrations and sediment transport is the result of velocity times concentration, the sediment transport has a larger skewness than the sediment velocity (step (3) in Figure 4.18, Figure 4.16a). Next to that, the asymmetry can cause sediment transport through an asymmetric pressure gradient. Pressure gradient refers to the gradient in cross-shore direction of the horizontal pressure. Due to the pressure gradient the sediment can start to move as a block, called pug flow (section 2.4). Hence the asymmetric pressure gradient acts on the sediment grains at the elevation at which sediment transport occurs, so mainly at the elevation of maximum sediment transport (step (4) in Figure 4.18). Asymmetric waves have skewed accelerations. Because the sediment transport due to a pressure gradient depends on the accelerations, the pressure gradient of asymmetric waves will also cause a skewed sediment transport (Figure 4.16b). Negative asymmetry, referring to forward pitched waves, causes onshore transport and positive asymmetry offshore sediment transport.

When looking at Figure 4.13 the velocity asymmetry is around two-third of the free-stream asymmetry or close to zero at the location of maximum sediment transport. Below the elevation of maximum sediment transport the asymmetry becomes positive, which would cause offshore sediment transport. However, at only onshore sediment transport is observed near the bed. These results indicate that *asymmetric pressure gradient* has none or small influence on the sediment transport compared to the *near-bed skewness*.

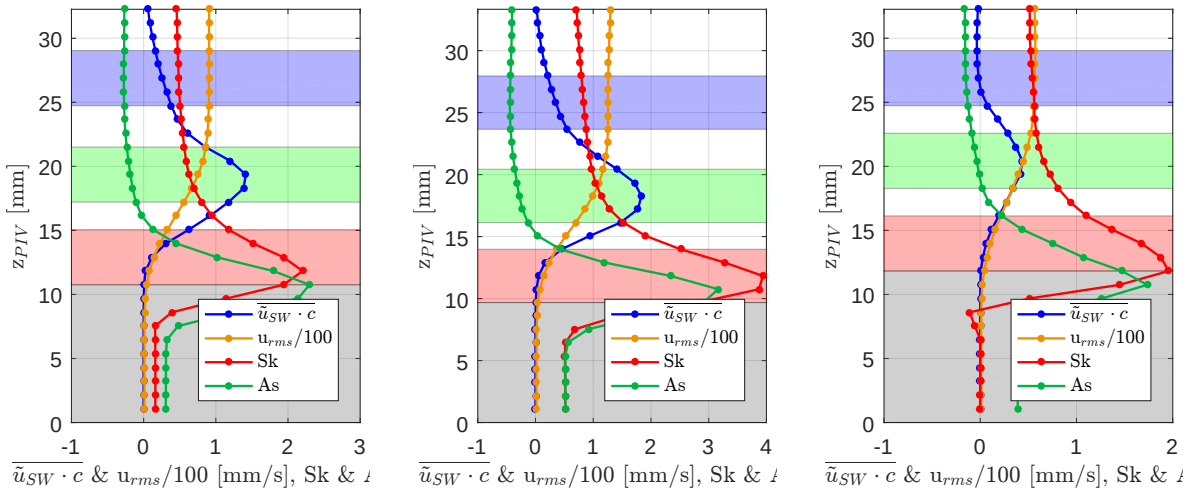


(a) Offshore of the sandbar (Location A, Testseries 1)

(b) On top of the sandbar (Location B, Testseries 2)

(c) Onshore of the sandbar (Location C, Testseries 3)

Figure 4.13: Vertical distribution of the sediment transport, horizontal velocity and the wave properties skewness and asymmetry. The coloured areas indicate the characteristics elevations: free-stream (blue), maximum sediment transport (green) and close to the bottom (red). The non-moving bottom is displayed in grey.

These findings can be studied further by analysing the data per wave. The results of the analysis per wave (Appendix K) have low correlations to draw strong conclusions. However the main trend shows that relation between short wave sediment transport and skewness increases towards the bottom. The relation between asymmetry and sediment transport is the strongest at elevation of maximum sediment transport. That this relation both includes the effect of the pressure gradient and the effect that asymmetry increases near-bed skewness and with that causes sediment transport, makes interpretation difficult.

Note for the analysis per wave that the characteristic elevations remain fixed per test. Hence due to the fixed characteristic elevations per test, the parameters not only depend on the specific wave but also on the current bottom height. This will widen the scatter, but this will not influence the mean trend.

### 4.3.2. Relation between phase lead and the wave shape in the wbbl

Because sediment transport depends on the near-bed skewness instead of free-stream skewness, methods have been developed to determine the near-bed skewness based on the free-stream skewness, free-stream asymmetry and the near-bed phase lead. Therefore this section studies the relation between *phase lead* and wave shape development in the wbbl. Berni et al. [2013] gives two equations to describe the wave shape development in the wbbl (section 2.4). Equations 4.1 and 4.2 recap these equation of Berni et al. [2013]. Equation 4.1 describes the wave shape change for laminar flow and Equation 4.2 for turbulent flow. The phase lead, $\phi$, for laminar flow is $45^o$.

Figure 4.19 shows the resulting skewness of the laminar solution. It is notable that the laminar skewness is equal to the observed skewness at the elevation of maximum sediment transport. If other research confirms this observation, the laminar solution would be an easy an accurate way to determine skewness at the elevation of maximum sediment transport.

Figure 4.20 shows the resulting phase lead of the turbulent equation. Equation 4.2 is used to determine the phase lead. This results in phase leads of $30.3^o$, $29.2^o$, $14.1^o$, offshore at the bar, on the bar crest and onshore of the sandbar. However equation 4.2 can not be resolved below the elevation of maximum sediment transport. Below this elevation the error increases (Figure 4.20, Equation 4.3). The error, $error\ \phi_b$, in Equation 4.3 is the dimensionless error. Equation 4.2 assumes a constant phase lead of all harmonic frequencies. The assumption that all harmonics have the same phase lead limits the amount of skewness increase towards the bottom. Hence for very large observed skewness increase, this assumption does not hold. So, Equation 4.2 cannot predict the observed near-bed skewness in this study.

Figure 4.21 shows the relation between the bottom skewness parameter and the free-stream skewness and asymmetry parameters. In the analysis per wave, the skewness parameter, $R_u$, and the asymmetry parameter,

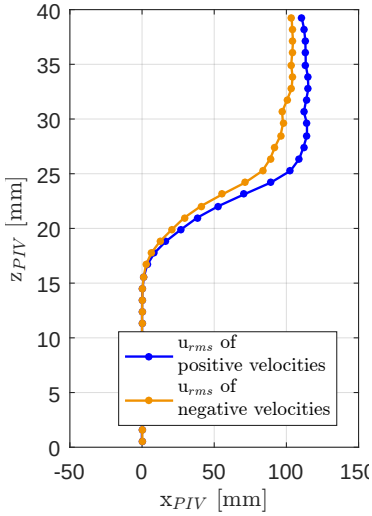


Figure 4.14: The vertical distribution of the root-mean-square value of all onshore (positive) horizontal velocities and of all offshore (negative) horizontal velocities. The velocity gradient in the sheet flow layer is stronger for the onshore velocities. This confirms the explanation of Nielsen [1992].

$R_a$, are used to describe wave shape (Equation 2.7 and 2.8). The skewness and asymmetry will always be positive: values larger than 0.5 indicate positive skewness or negative asymmetry and values smaller than 0.5 mean negative skewness or positive asymmetry. This way the resultscan be compared to the findings of Berni et al. [2013] and Henriquez [2016] (Figure 2.17, section 2.4). However the resulting phase leads do not match, as in the study of Berni et al. [2013]. Where Berni found phase leads of $44^o$ and $42^o$, this study gives the contradictory results of 10 $^o$ versus 32 at the elevation of maximum sediment transport and of 35 $^o$ versus 61 $^o$ at the near-bed elevation. This confirms above conclusion the assumption of constant phase lead does not hold.

$$\frac{Sk_b}{Sk_\infty} = 1 - \frac{As_\infty}{Sk_\infty} \tag{4.1}$$

$$\frac{Sk_b}{Sk_\infty} = \cos\phi_b - \sin\phi_b \frac{As_\infty}{Sk_\infty} \tag{4.2}$$

$$\frac{Sk_b}{Sk_\infty} = \cos\phi_b - \sin\phi_b \frac{As_\infty}{Sk_\infty} + error\ \phi_b \tag{4.3}$$

Lastly, it is found that the sediment transport per wave is related to the third order of the free-stream orbital amplitude (Figure 4.22). Hence larger waves cause more sediment transport. This confirms the theoretical assumption that sediment transport is related to the third power of the velocity. The relation decreases towards the bottom. It is possible that the high frequency noise signal in the bottom causes this decrease in relation towards the bottom.

### 4.3.3. Preliminary conclusion

The results show that wave skewness increases towards the bottom and wave asymmetry decreases and even becomes positive (backward tilted waves). The observed skewness in sediment transport is larger than the skewness in the sediment velocities. Both near-bed skewness and an asymmetry pressure gradient due to near-bed skewness can cause sediment transport and both mechanisms will cause a skewed sediment transport. The results do not show evidence to firmly conclude or skewness or asymmetry is more important. However there is no effect of the pressure gradient observed. Between the bed and the elevation of maximum sediment transport, the asymmetry is small or even positive. Positive asymmetry would cause offshore near-bed sediment transport, while no offshore sediment transport is observed. Therefore the results indicate that sediment transport mainly depends on near-bed skewness and that the asymmetric pressure gradient has a small or no effect.

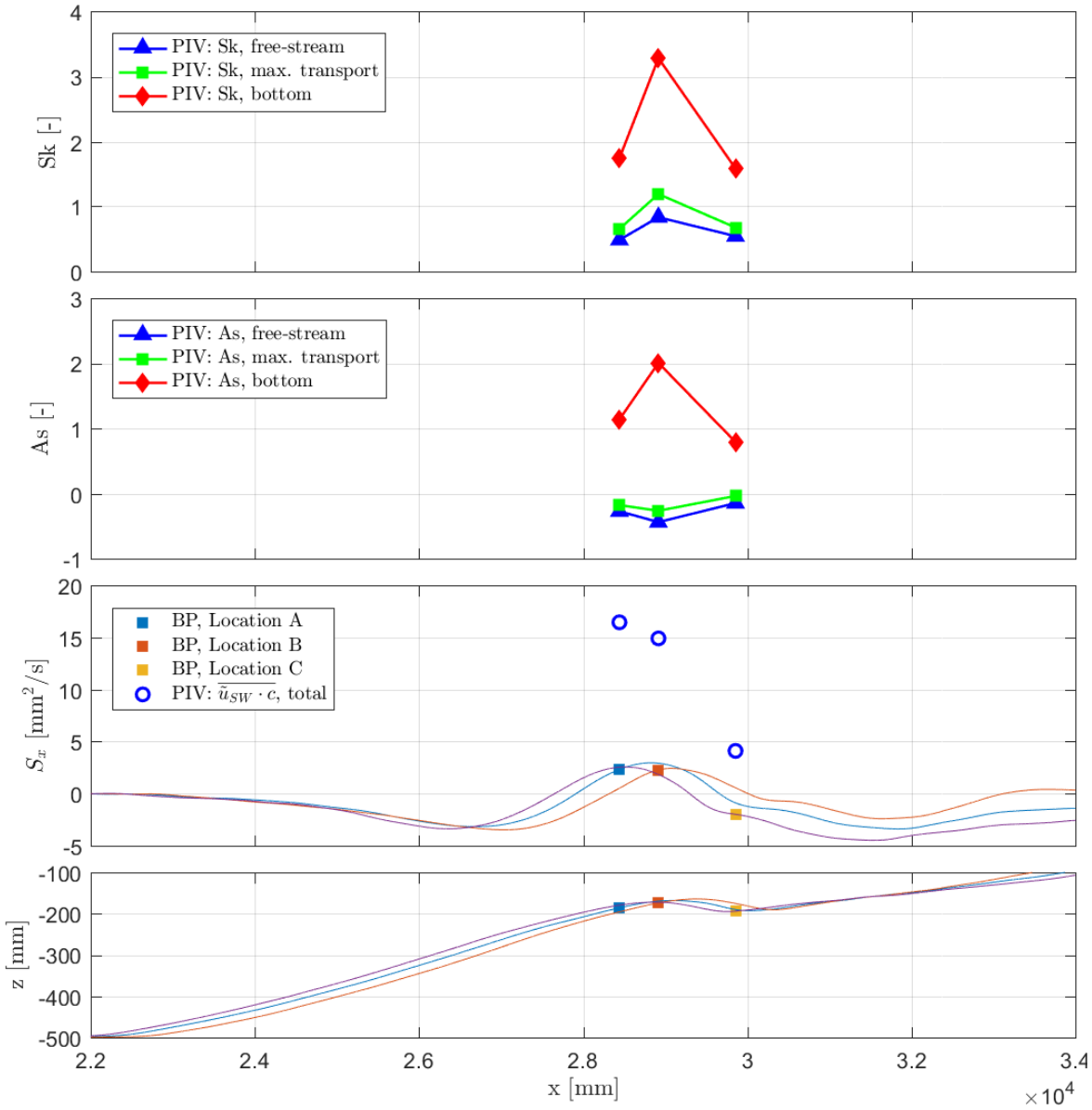


Figure 4.15: Skewness and asymmetry per location in the cross-shore at the three characteristic elevations above the bed. For both wave properties the gradient over the sandbar increases towards the bottom and asymmetry becomes positive close to the bottom.

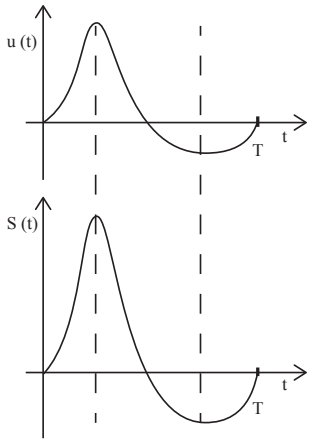


(a) Sediment transport due near-bed skewness

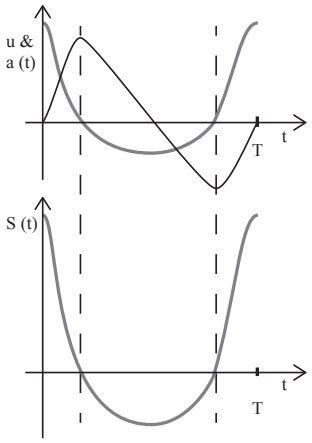


(b) Sediment transport due to an asymmetric pressure gradient

Figure 4.16: Visual explanation of the sediment transport wave shape

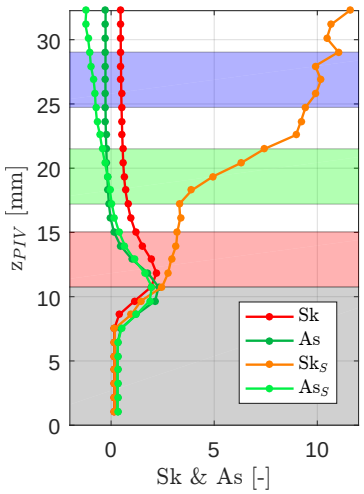


(a) Offshore of the sandbar (Location A, Testseries 1)

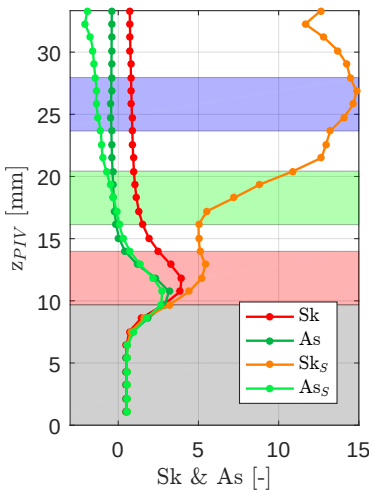


(b) On top of the sandbar (Location B, Testseries 2)

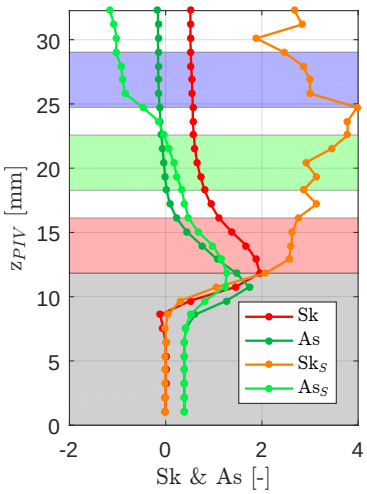


(c) Onshore of the sandbar (Location C, Testseries 3)

Figure 4.17: Vertical distribution of skewness and asymmetry based on the sediment velocities and the sediment transport.

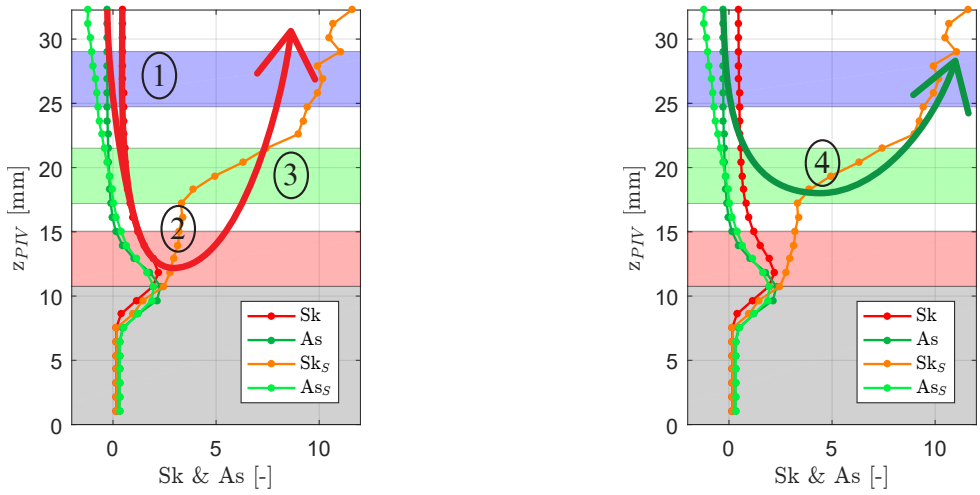


(a) Sediment transport due near-bed skewness

(b) Sediment transport due to asymmetric pressure gradient

Figure 4.18: Schematic visualisation of different steps in the short wave related sediment transport mechanisms: (1) free-stream skewness and asymmetry transform to near-bed skewness, (2) near-bed skewness causes sediment suspension, (3) the orbital velocities transport the suspended sediment and (4) the near-bed asymmetry causes sediment transport due to the asymmetric pressure gradient.

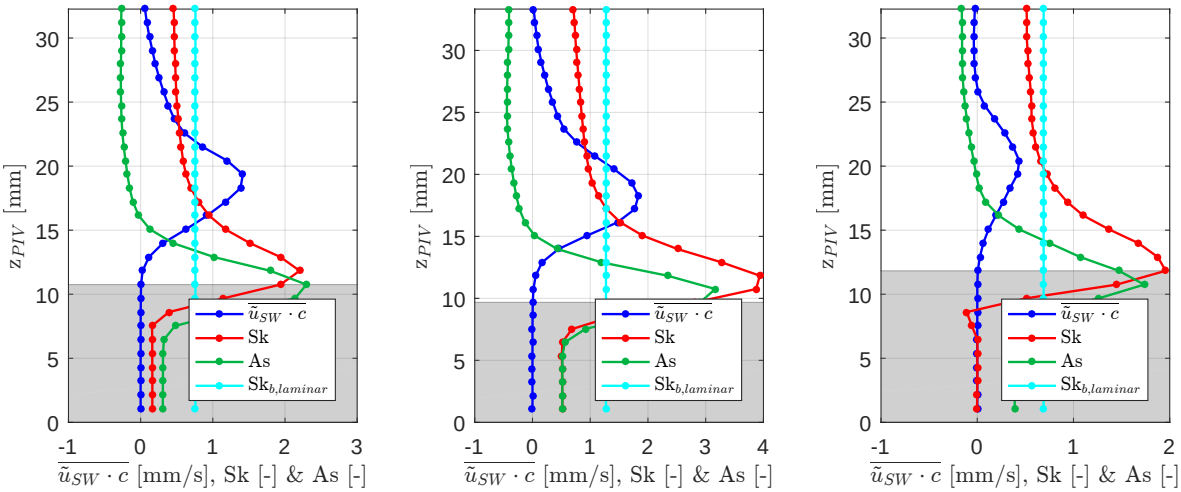


(a) Offshore of the sandbar (Location A, Testseries 1)

(b) On top of the sandbar (Location B, Testseries 2)

(c) Onshore of the sandbar (Location C, Testseries 3)

Figure 4.19: Vertical distribution of the skewness, asymmetry and bottom skewness predicted based on laminar flow. The cyan line shows the bottom skewness predicted with laminar flow, Sk$_{b,laminar}$.

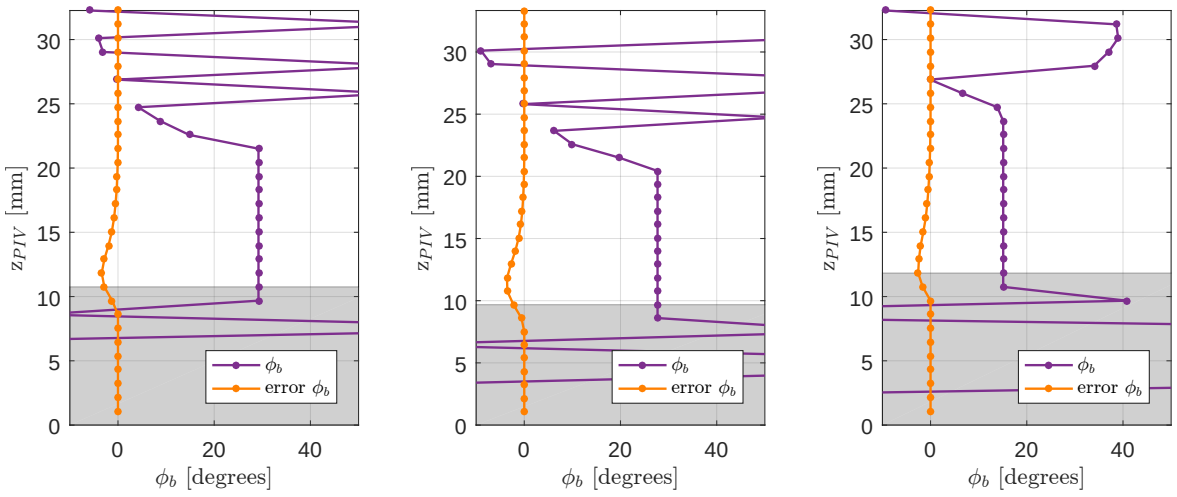


(a) Offshore of the sandbar (Location A, Testseries 1)

(b) On top of the sandbar (Location B, Testseries 2)

(c) Onshore of the sandbar (Location C, Testseries 3)

Figure 4.20: Vertical distribution of the phase lead, $\phi_b$, based on the equation of Berni (Equation 4.2). The orange line shows the elevations at which the equation of Berni et al. [2013] could not be resolved.

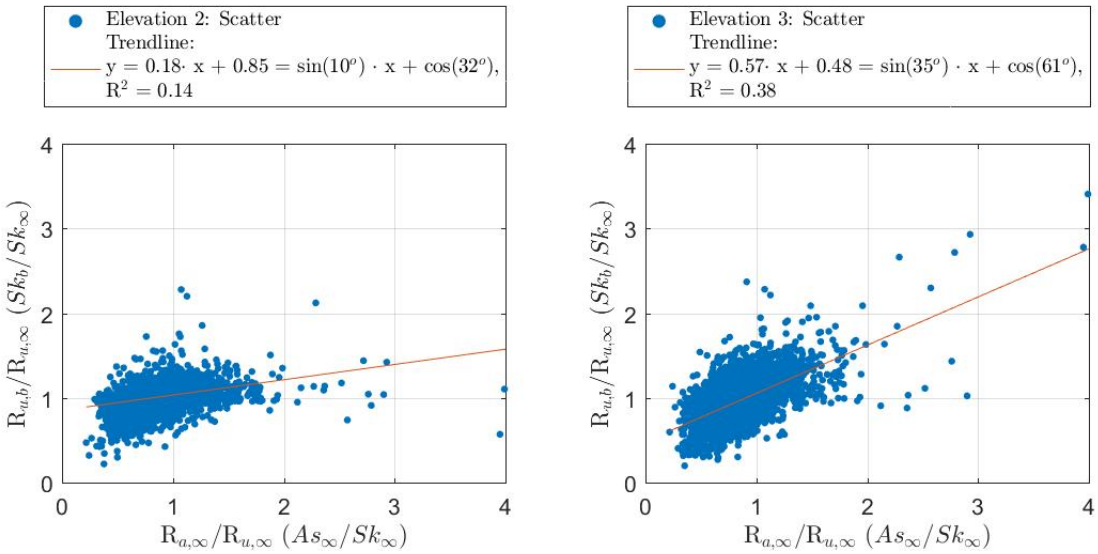


Figure 4.21: Scatter of all waves: The relation between near-bed skewness and free-stream skewness and asymmetry. The left figure shows the relation with the skewness at elevation of maximum short wave related sediment transport and the right figure shows the relation with the near-bed skewness.

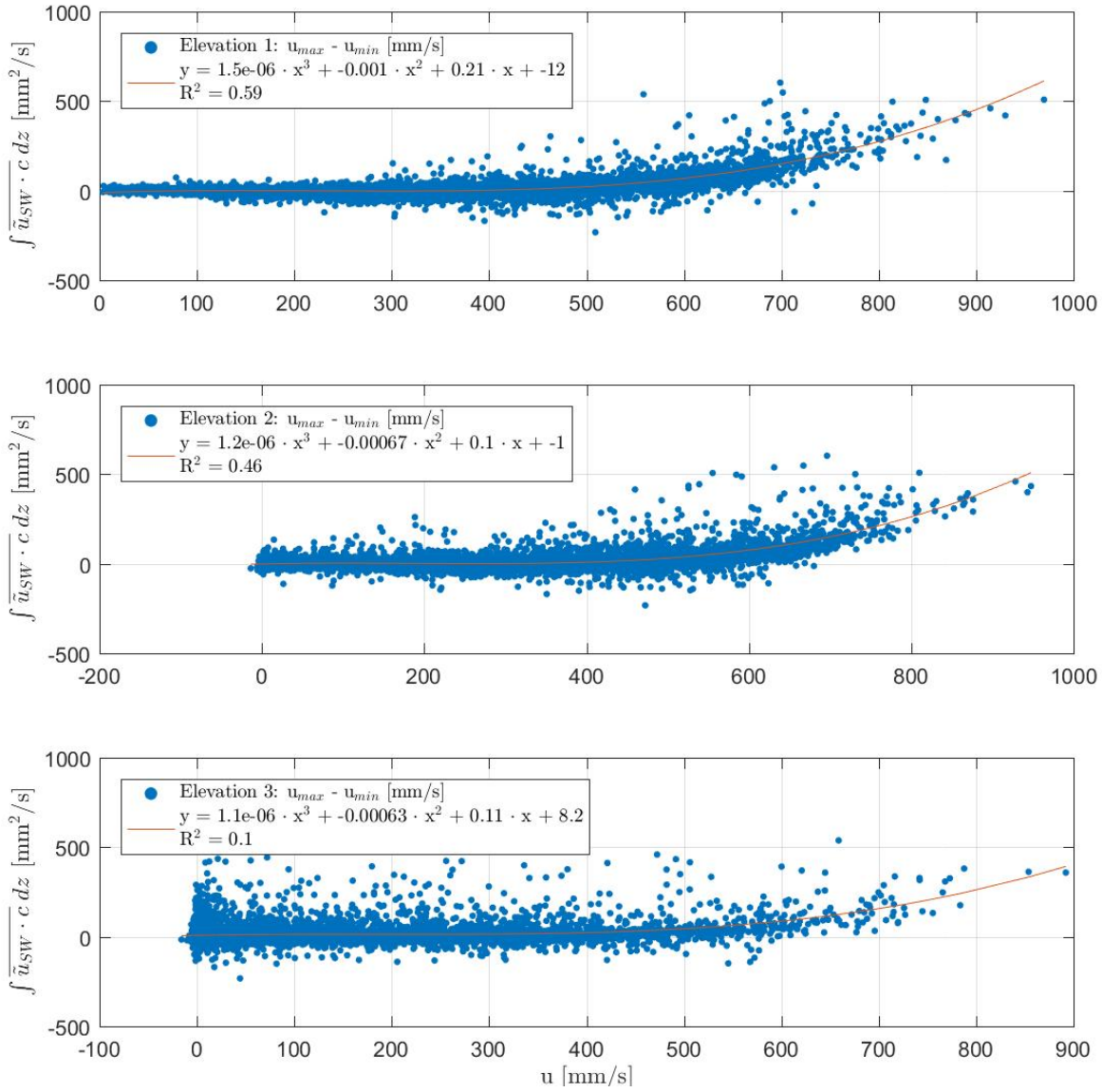


Figure 4.22: Scatter of all waves: Orbital amplitude.

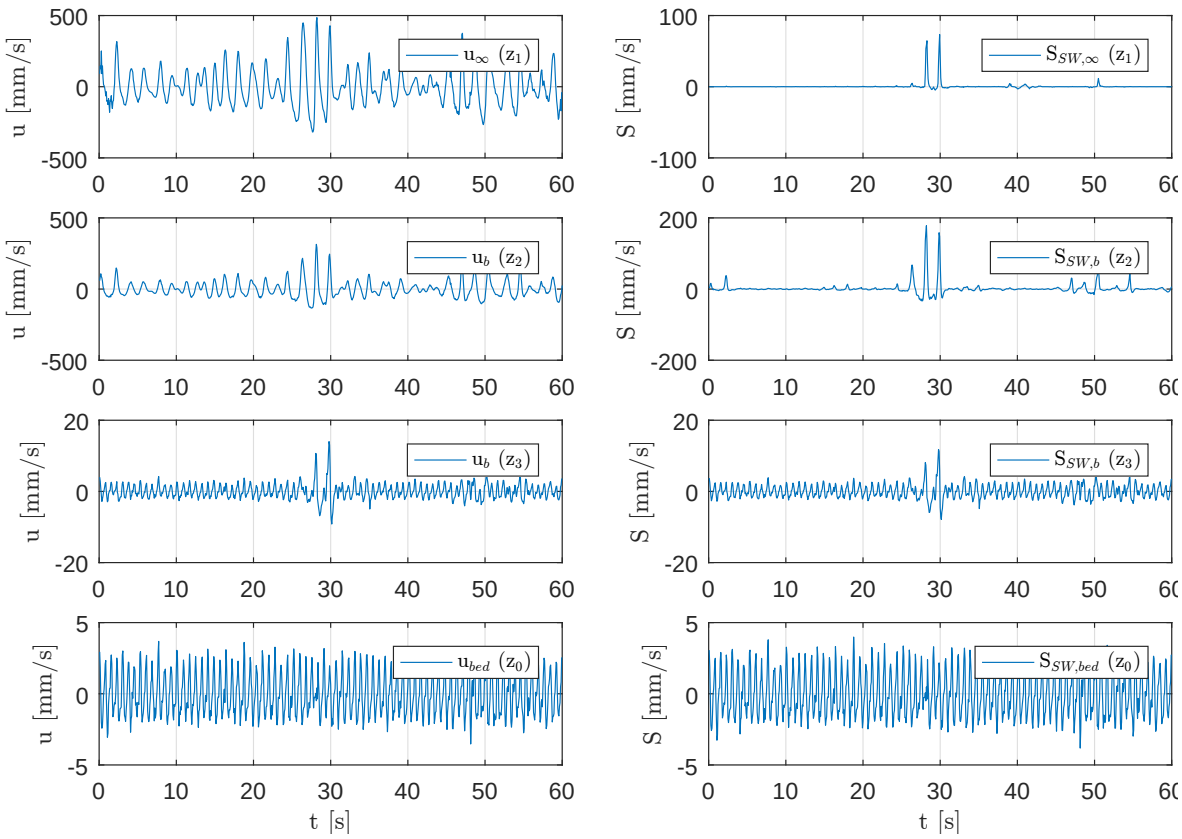


(a) Velocity signal in the first minute

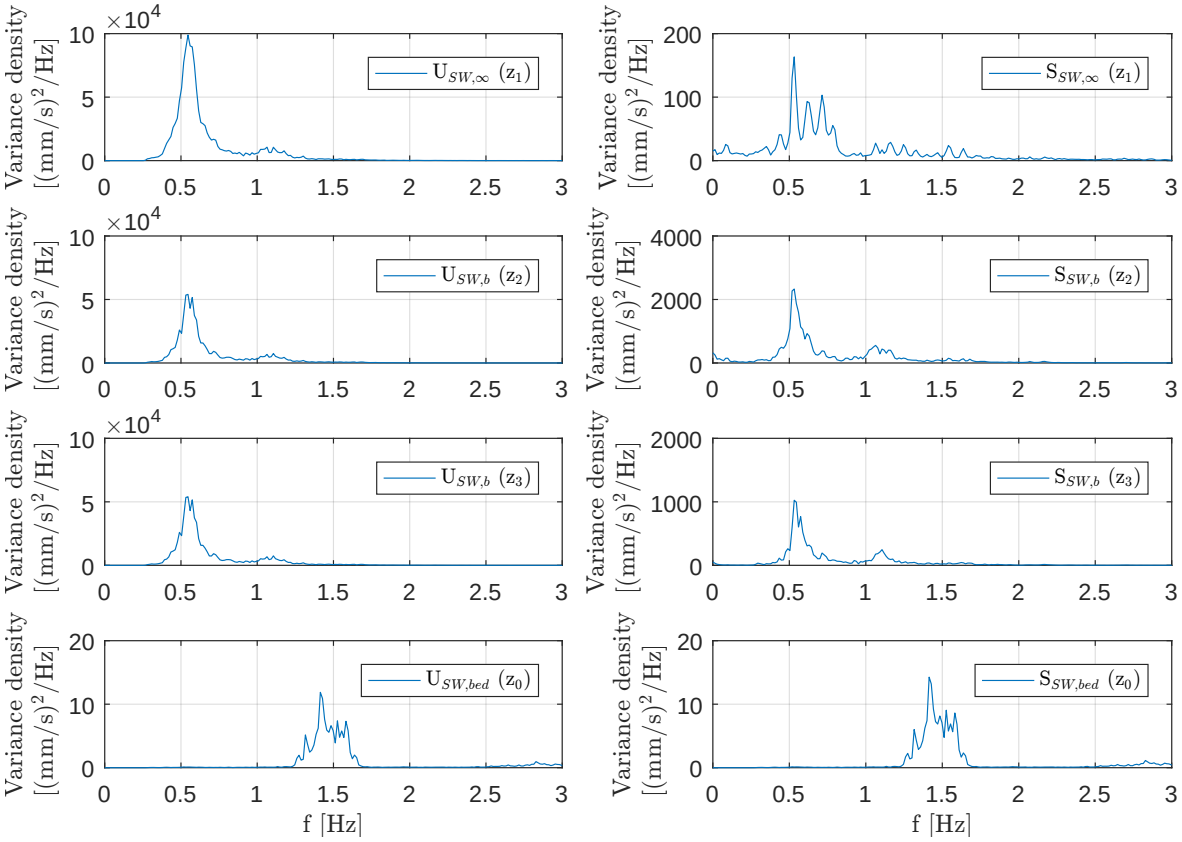


(b) Spectrum

Figure 4.23: Example of velocity and sediment transport of the first minute of test 1.1.1 together with the spectrum of test 1.1.1. The top plots shows the free-stream velocity and transport, the middle plots show the velocity and transport at the elevation of maximum mean transport and the lowest plots shows the velocities and transport just above the bottom.

# 5

# Discussion

*This chapter relates the results of this study to the literature (section 5.1). How can the results be interpreted and related to the state of the art research about wave driven sediment transport in the nearshore? Next to that, the methodological relevance of the present study is to enable calculating sediment transport based on PIV measurements. The methodological relevance will be discussed in section 5.2. Finally, the practical relevance (section 5.3) and the limitations of the study (section 5.4) are discussed.*

## 5.1. Contribution to the literature

The goal of this research is to determine the dominant mechanism in wave driven onshore sandbar migration and thereby to improve the understanding of wave driven onshore sediment transport. In the two dimensional experiment, the sediment transport is studied in the cross-shore direction. This section discusses the contribution to the literature for the following topics: (1) the dominant sediment mechanism in onshore sandbar migration, (2) understanding wave related sediment transport, (3) the effect of the constantly varying bed level and (4) the effect of scaling on the interpretation of the results.

### 5.1.1. Dominant sediment mechanism in onshore sandbar migration

The time-averaged short wave related transport is found to cause the largest net sediment transport and sediment gradient. The short wave related sediment transport enlarges the sandbar and moves the bar onshore. Both other mechanisms, long wave related transport and current related transport, contribute to the onshore movement of the bar. The enlargement of the sandbar is fully caused by short wave related sediment transport and the onshore movement of the sandbar is caused for around 50 % by short wave related sediment transport, for 30 % by current related sediment transport and for 20 % by long wave related sediment transport. These percentages are based on the sediment gradients over the bar, because the sediment gradients cause morphological change.

In the literature the dominant sediment mechanisms have been studied abundantly. Ruessink et al. [1999] compares the influence of sediment mechanisms in field observations with velocity and concentration measurements close to the bottom. Ruessink et al. [1999] finds a ratio in sediment transport of around 40-50 % high frequency, 20 % low frequency and 30-40 % current related transport for non-breaking waves close to the shore during low-energetic conditions. In addition, Ruessink et al. [1999] finds that the influence of non-breaking high-frequency waves increases towards the shore. This ratio is strikingly similar to the ratio in sediment gradient over the bar in this study.

With numerical simulations Ruessink et al. [2007] finds that onshore bar migration is caused by near-bed skewness with negligible effects of streaming and long waves. Hence in this study the short wave dominance is even more pronounced.

Yu et al. [2010] found that skewness was the dominant cause of onshore sediment transport and streaming contributed for 36 %, when comparing skewness and streaming in a two-phased model. These findings are in line with my results, because the short wave-related transport (i.a. skewness) is more important than current related transport (mainly streaming). When only taking the onshore movement due to short wave and current related transport into account, the ratio of my findings would become around 70 % to 30 %. This is close to the established ratio of Yu et al. [2010].

Kranenburg [2013] finds that onshore streaming, as part of the current related sediment transport, largely contributes to largely to wave driven onshore sediment transport in wave flume measurements compared to tunnels. In wave tunnels no LH-streaming occurs due to the absence of vertical velocities. In addition, Kranenburg et al. [2013] found 40 % contribution of streaming in a numerical model study when comparing the effect of streaming and skewness. When neglecting long waves and the enlargement of the bar again, the influence of streaming found by Kranenburg et al. [2013] is slightly larger than the 30 % of current related transport of this study.

The conclusion is that the findings of Yu et al. [2010] and Kranenburg et al. [2013] are in line with the results of this study if we neglect the effects of long waves and the enlargement of the bar. This suggests that streaming and skewness are the dominant intra-wave processes in current related transport and short wave related transport. That Longuet-Higgins and skewness streaming seem to be the important intra-wave processes can also be seen in the results by looking at the sediment transport elevation above the bed as will be described in the next paragraphs.

First, the *current related transport* indeed shows that almost all current related transport is located at the elevation of onshore velocities close to the bottom. These onshore velocities close to the bottom are the result of Longuet-Higgins streaming. The relatively low elevation of sediment transport due to Longuet-Higgins streaming indicates that this intra-wave process is relatively constant over time compared to short wave transport. In other words, the transport occurs both at moments of high suspension and at moments of low suspension.

Second, the maximum sediment transport of *short wave related transport* is located at a high elevation above the still bed compared to the other sediment mechanisms. This shows that the horizontal velocities and concentration have a relative strong correlation and are in phase. In other words, the sediment transport occurs at moments of high suspension. Skewness causes sediment transport in phase with the velocities, because skewness causes sediment suspension and simultaneously transports this suspended sediment. The asymmetric horizontal pressure gradient affects the sediment grains, but does not suspend them. Because the pressure gradient is out of phase with the velocities, the horizontal pressure gradient causes sediment transport out of phase with the velocities. Therefore sediment transport caused by skewness occurs higher above the bed than sediment transport due to an asymmetric pressure gradient. So, the relatively high sediment transport of short waves indicates the importance of skewness. Next to that, the relatively strong correlation between concentration suspension and orbital velocities indicates that the short waves are the main cause of sediment suspension. This confirms the theory that short waves stir up the sediment due to the high orbital velocities close to the bed [Bosboom and Stive, 2015].

When interpreting the results it has to be kept in mind that the intensity variation due to reflection of laser light can influence sediment transport. The intensity variation will only influence the sediment transport if the variation in mean bed intensity is correlated with the horizontal orbital velocities by having a similar frequency. If the two fluctuations are correlated and (almost) in phase this effect increases the time-averaged short wave related transport and if the fluctuations are correlated and (almost/close to) out of phase the short wave transport decreases. Hence the variation in mean bed intensity can possibly have an effect on the mean total sediment transport and the relative importance of the short wave related transport.

### 5.1.2. Understanding short wave related sediment transport

The main result of the short wave related sediment transport analysis is that skewness increases towards the bottom and asymmetry decreases and even becomes positive. Next to that, the results seem to show that short wave related sediment transport is caused by the near-bed skewness and not by an asymmetry in pressure gradient. Hence short wave related sediment transport is due to the orbital velocities. Because large orbital velocities stir up more sediment, near-bed skewness causes a net transport. The effect of the asymmetric pressure gradient underneath asymmetric waves seems small, because the asymmetry is negative and small or even positive between the bed and the elevation of maximum sediment transport. The positive near-bed asymmetry, indicating backward tilted waves, would cause an offshore transport, which is not observed. However asymmetry is importance for sediment transport because free-stream asymmetry enlarges the near-bed skewness. Based on these results numerical models should be able to accurately predict wave driven onshore sediment transport purely based on velocities if the change in skewness and asymmetry towards the bottom is taken into account.

Hence based on these results, the conclusion seems to be that onshore wave driven sediment transport can be accurately predicted based on the near-bed skewness without taking the asymmetric pressure gradient into account. So, free-stream asymmetry causes onshore sediment transport by increasing the near-bed

skewness, but probably not or only slightly with the asymmetric pressure gradient. Because the wave driven calculations should be based on the near-bed skewness, the calculations should take both free-stream skewness and asymmetry into account.

Nielsen [1992] explains the how free-stream asymmetry increases the skewness of the bottom shear stress. This same explanation holds for velocities. Under the steep wave front the wbbl has no time to grow. In the thin wbbl the velocity gradient is steep and high velocities can occur close to the bottom. These high velocities cause sediment suspension and the still bed lowers. So, the still bed level and top of wbbl are constantly changing over height, while the measurement study the velocity or sediment signal at a fixed point. When looking at a fixed point this result in strongly skewed velocities close to the bottom. Figure 5.1 shows this intra-wave variation in bed level and wbbl layer thickness for a single wave. Figure 5.1 also displays the suspension height due to the near-bed skewness.

These findings confirm Henderson et al. [2004], who did find that the sediment transport is related to the near-bed velocities and not to the free-stream velocities, and Berni et al. [2013] and Henriquez [2016], who describe the change from free-stream asymmetry to near-bed skewness. This also confirms the findings of Horikawa et al. [1982], who found that the concentration is almost in phase with the velocity in vicinity of the bed indicating the importance of skewness. The result argues against Gallagher et al. [1998] and Hoefel [2003], who find that acceleration-based transport is important to predict sediment transport. Ribberink and Al-Salem [1995] found that asymmetric waves give onshore sediment transport in the sheet flow layer and a small offshore transport in the suspension layer. The onshore transport is probably due to skewness. The offshore transport in the suspension layer is in this study only observed onshore of the sandbar and is mainly due to long waves. However short waves also slightly contribute to this offshore transport in the suspension layer, which could be due to vortex tubes. This is an interesting process to study in future research.

However Ruessink et al. [2007] neglects in simulations the free-stream asymmetry and the conversion to near-bed skewness and result in a realistic onshore bar migration. This indicates that the effect of asymmetry is not important.

The skewness increase from free-stream towards the bottom is quite a bit larger than the observed skewness in the studies of Henriquez [2016] and Berni et al. [2013], where the bottom skewness reaches a maximum of 1.5. In this study the maximum bottom skewness is 4. Besides that, in both the studies of Henriquez [2016] (fixed bed) and Berni et al. [2013] (mobile bed) the wave bottom boundary layer is thinner, namely 6-8 and 3 millimeters. For a fixed bed it is understandable that the wbbl is thinner. The mobile-bed experiment of Berni et al. [2013] should give comparable results. If in this study the still bed level would be calibrated at smaller time intervals (currently 15 minutes), the height of the wave bottom boundary layer and sheet flow layer would decrease (section 5.1.3). However this does not explain the high bottom skewness in this study. More regular bed level calibrations would decrease the height, due to smaller spread over height the maximum skewness, asymmetry and sediment transport values would increase.

In these results the bottom skewness cannot be calculated based on a constant phase lead for every harmonic as proposed by Henderson et al. [2004] and Berni et al. [2013] (Equation 2.31). The assumption that the phase shift is constant for all harmonic frequencies does hold for the large near-bed skewness increase that is found in this study. Next to that, it is surprising that the bottom skewness based on the laminar relation (Equation 2.32, [Berni et al., 2013]) predicts the observed skewness at the elevation of maximum sediment transport quite accurately. If this is confirmed in future research, it could be an easy method to determine bottom skewness.

Note that the skewness and asymmetry are based on the sediment velocities, which differs from literature. In literature the skewness and asymmetry are based on the flow velocities. However in this study the sediment velocities are assumed equal to the orbital velocities.

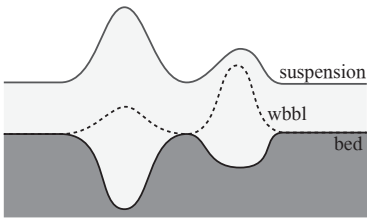


Figure 5.1: The bed level and suspension height variation underneath skewed waves together with the wave bottom boundary layer thickness variation due to wave asymmetry. This tickness variation of the wbbl enlarges the near-bed skewness.

### 5.1.3. Effect of the constantly varying bed level on the results

During the measurements the bed level varies continuously. At long time scales the bed level varies due to the sandbar migration: the bed on average eroding or accreting. At short time scales there is intra-wave bed level variation. During each wave there are moments of sediment suspension and sediment settling. The bed level, top of the wave bottom boundary layer and suspension height all vary continuously during every wave (Figure 5.1). Currently the mean results are obtained by first time-averaging per test (15 minutes), second calibrating the bed level of all tests at the same measurement location and then averaging all tests at this location. Hence the bed level variation within each test influences the mean results. This effect has to be kept in mind when interpreting the vertical distribution of sediment transport and wave properties and when interpreting the analysis per wave.

The *vertical distribution* shows the mean bed level and mean elevation of maximum sediment transport. Because the bed level varies continuously during each test, all wave properties disperse in vertical direction. The distribution widens and the maximum value of the wave properties decreases. For future research, it is advisable to first calculate the time-average over a shorter time period (ea. 1 or 2 minutes), second calibrate the mean bed level and then averaging again. This will decrease the dispersion and thus will result in a thinner wave bottom boundary layer.

In the *analysis per wave* the properties are studied at constant characteristic elevations. The characteristic elevations are based on the mean vertical distribution per test. Because these characteristic elevations vary actually with every wave, the constant characteristic elevations will widen the scatter of the analysis per wave and thus decrease the r-square value of the correlations. However, because the analysis is based on the mean characteristic elevation of all these waves, the obtained trend line will not be influenced by the widening scatter. Thus, it is possible to determine the characteristic elevations per wave. Because the properties per wave are more capricious, this calculation has to be done very carefully and checked thoroughly.

### 5.1.4. Effect of scaling on interpretation

Since the experiment is done with light-weight sediment, the sediment density (1200 $kg/m^3$) is close to the water density ($\pm$ 1000 $kg/m^3$). In this study the flow velocities is assumed equal to the sediment velocities. However on natural beaches the relative sediment density is larger and the grain size is relatively smaller than in the experiment. Do the results of the experiment, e.g. the sediment mechanism ratio and vertical distribution of the sediment transport, apply to natural beaches?

When designing the experiment, the scaling effects are considered carefully [Henriquez et al., 2009] (Appendix F). The wave conditions and coastal profile of the experiment matches observations on a natural beach during the Duck94 experiment in North Carolina [Gallagher et al., 1998]. The experiment is scaled based on the Reynolds number, Shields number and relative settling velocity. Only the Sleath parameter cannot be taken into account in this scaling relation. Due to incorrect scaling of the Sleath parameter, the mobility of the sediment can be larger than predicted and thus the influence of the pressure gradient can be larger in the experiment than in the field [Henriquez et al., 2009]. However, the results of this study don't show an important role of the pressure gradient. So apparently, this effect is negligible.

The observed transport regimes in the experiment meet the theoretical expectations and the morphological evolution is similar to nature. This is a solid basis to assume that the mobile-bed experiment correctly represents the sediment mechanism ratio on natural beaches. Dubarbier et al. [2013a] compared full scale wave flume observations [Dubarbier et al., 2013b, Matias et al., 2013] and observations on natural beaches (Duck and Egmond) to scaled laboratory experiments with the coarse lightweight sediment strategy [Grasso et al., 2009]. They concluded that small-scale experiments with coarse and lightweight sediment can be used to study the contribution of different sediment transport mechanisms, ea. wave non-linearities and undertow, and the overall beach profile evolution.

However, the vertical distribution of the velocities and transport close to the bottom can be slightly different for coarse lightweight sediment experiments. Do skewness and asymmetry develop in a similar way towards the bottom for light scale sediment? Based on the scaling relations, this development should be equal. However due to the relatively large sediment diameters the sheet flow layer and wave bottom boundary layer can be slightly thicker in the wave-flume experiment. This effect is assumed negligible.

## 5.2. Methodological relevance

PIV measurements contain exceptionally detailed information over space and time. Hence the possibility to determine sediment transport from PIV measurements enables very detailed sediment transport analyses.

With all intra-wave processes occurring simultaneously, this level of detail is highly helpful in the search for the dominant wave mechanisms.

This research contributes to the development of a method to determine sediment transport based on PIV measurements without additional concentration measurements. Determining sediment transport from PIV measurements without additional concentration measurements is uncommon in the literature (section 2.5). The present study shows that PIV measurements have potential to determine sediment transport. However determining sediment transport from PIV data also has its drawbacks. Therefore the important steps and difficulties in the method will be discussed in the following sections. Overall, the most complex and sensitive part of the calculation is using intensity as measure of concentration.

*First*, when carrying out the *mobile-bed experiment*, it is essential to place the laser in front of the wave flume to illuminate the sheet flow and bed equally. Commonly the laser is placed on top of the experiment to create a laser sheet in the middle of the flume. With a placement on top, the light reflects on top of the sediment particles and does not penetrate into the sheet flow and bed. With a placement in front, the image brightness correlates to concentration, because sediment reflects more light than water.

Because the reflected light is used as measurement of concentration, it is important to avoid all other possible influences on the image brightness. Hence the experiment has to be covered to avoid light from entering the experiment. Even though the experiment was covered, the mean image intensity of the still bed varies over time due to light reflection of the laser on the bed and water surface (section 4.1). In future research this effect can be reduced by placing a cover between the laser and the flume with only a rectangular gap at the PIV window. The variation in mean bed intensity due to reflection can influence the results, when it is correlated with the horizontal orbital velocities. If there is a correlation between the mean bed intensity variation and the orbital velocities, the reflection will affect the short wave related transport and thus the ratio between the sediment mechanisms.

*Second*, the *velocity* is determined from the measurements with a PIV analysis. In the measurement and calculation of the velocities there are two main points two discuss: (1) measurement of the orbital velocities based on dust and sediment grains and (2) the assumption that the orbital flow velocities and sediment velocities are equal.

The velocities are calculated based on the correlation between two images in a PIV analysis. In the experiment no tracers are added, because the sediment and accompanying dust supply enough particles to find a correlation. Because the sediment grains are larger than dust, the correlation will be based mainly on the grains if the interrogation window contains sediment grains. Higher in the water column without present grains, the correlations is based on dust. This study assumes that the flow and sediment velocities are equal, so with this assumption the dust and grain velocities would be equal. However, if this assumption is not entirely valid, the dust velocities will be higher than the grain velocities. This means that the velocities higher in the water column are measured as being relatively larger than the velocities close to the bed. This effect results in an offshore sediment transport and thus decreases the total sediment transport. Because the total PIV sediment transport is a lot larger than the sediment transport based bottom profile change, this effect is assumed to be negligible.

Because the sediment velocities are measured, the assumption that the orbital flow velocities and sediment velocities are equal does not influence the sediment transport. However, when comparing velocity characteristics to the literature, this assumption should be kept in mind. In the literature velocity characteristics are always (to the author's knowledge) based on orbital flow velocities. Hence if this assumption is not entirely true, the sediment velocity characteristics cannot be compared one-to-one with the flow velocity characteristics in the literature. However the use of light-weight sediment in the experiment is a strong support of the assumption.

*Third*, the *concentration* is estimated from image intensity through a calibration relationship. This research gives a method to create this calibration relationship without additional concentration measurements by basing the calibration between the intensity and concentration on the mean bed intensity and mean water intensity. The intensity might vary over space and time (unsteady and non-uniform), but it is certain that the mean bed intensity has to be equal to a concentration including pores of 1 $m^3/m^3$, and that the mean water intensity has to be equal to a concentration of 0 $m^3/m^3$. The reason is that the bed and the water concentration are the definition of the maximum and minimum packing of sediment. Because the intensity varies with every experiment, it is important that the calibration relationship is based on the specific data. It is not possible to re-use calibration relations of other experiments as is sometimes found in literature.

The relation between intensity and concentration is the most complex part of the calculation, because image intensity depends on more factors than concentration. The factors that cause a variation of intensity

with constant concentration should be taken into account. The most important factors are discussed here: (1) the non-linear relation between intensity and concentration, (2) the effect of the assumption that the concentration increases linear in the sheet flow layer, (3) the intensity variation over time and (4) uneven photo-exposure (intensity variation over space).

Concentration relates *non-linearly* to intensity, because a lower concentration reveals sediment grains deeper in the flow. These distant sediment grains reflect more light than water and thus increase the image brightness of the PIV photo. This effect causes a non-linear relation between intensity and concentration. Horikawa et al. [1982] compared image brightness to additional concentration measurements based on the electrical resistance of the water/sand mixture and found an exponential relation. In the present study, a linear concentration profile is assumed to avoid additional concentration measurements (section 2.4.4) [Al-Salem, 1993, O'Donoghue and Wright, 2004c]. Based on this assumption a quadratic relation is established between intensity and concentration, because the quadratic relation results in the best fit and best sediment transport results. Hence the resulting quadratic calibration relation in this study is different from the exponential calibration relation found in literature.

What is the effect on the results if the concentration in the sheet flow layer cannot be *assumed linear*? If the concentration profile does not increase linear in the sheet flow layer, the profile can be either convex or concave. That the quadratic trend line gives the best fit and the best sediment transport results shows that the concentration profile will be either linear or convex. If the concentration profile has a convex curve instead of a linear increase, the calibration between intensity and concentration would become more non-linear. This would mean that the total sediment transport based on the current method would be an overestimation, especially in the upper part of the sheet flow layer. Since the total sediment transport is too large, this can be the case. As recommendation to future research, the base of this assumption can be improved with a very extensive review of concentration measurements in literature and additional concentration measures besides the PIV measurement.

Even though the experiment was covered, the mean bed intensity varies *over time* due to laser reflection. This effect influences the decision on the size of the calibration data set. Where a large data set increases the reliability of the calibration, a small data set increases the accuracy of the calibration by eliminating the intensity variation over time. In this study it was decided to base the calibration on all tests with comparable light exposure. It would be interesting to study the influence of a smaller data set per calibration. With a large calibration data set and the standard deviation around this calibration relation, some intensities will result in negative concentrations. Since negative concentration cannot occur physically, the requirement is set that all concentration has to be positive. All negative values are replaced by zero. This requirement increases the sediment transport up to 10 %. A smaller data set per calibration would decrease this effect.

An *uneven photo-exposure* causes a gradient in the bed intensity in cross-shore direction. When determining the sediment gradient, this error has to be taken into account. In the present study the sediment gradient due to uneven exposure is an order larger than the sediment gradient based on bottom change. With an error as large as this and an unknown effect of an intensity correction on the concentration in the sheet flow layer, an accurate correction is very difficult. If you want to be able to determine the sediment gradient based on PIV measurement the set-up has to be checked for an exposure gradient before executing the experiment.

*Fourth*, the velocity and concentration are multiplied at every data point to obtain the *sediment transport*. However, the sediment transport based on the PIV measurements is found to be larger than the sediment transport based on the bottom profile measurements. What could cause this overestimation of sediment transport in the PIV calculation besides the calibration between intensity and concentration? A possible cause could be the alignment of the velocities and concentration. Since the velocity is calculated in Davis and the intensity in Matlab, the alignment of the properties has to be done very carefully. If the concentration is determined slightly lower, the concentration would be slightly too high at every grid point. Besides that, the velocity in the bottom is not exactly zero. This can cause around 1 % of sediment transport.

Another solution is *particle tracking*. With particle tracking individual particles are automatically detected and traced until exiting the image. Combining the particle displacement and particle diameter or surface, the sediment transport can be calculated. Using particle tracking is a more time consuming and complicated calculation than using intensity as a measure for concentration. Therefore it will very practical to develop an accurate calibration method between intensity and concentration.

## 5.3. Practical relevance

To accurately predict future morphological development, both coastal erosion and recovery have to be included in coastal prediction models. Current coastal prediction models accurately simulate erosion in cross-shore direction, but lack in predicting cross-shore wave driven recovery. An improved understanding of wave driven onshore sediment transport in the nearshore, with as clear example onshore sandbar migration, will contribute to improving these prediction models. With improved prediction models nourishments and other coastal protection measures can be designed more efficiently and effectively.

## 5.4. Limitations

This study has some limitations regarding the use of PIV measurements to determine sediment transport. First, the PIV photos have to be taken at the side of the flume and thus wall effects cannot be avoided. According to Dohmen-Janssen [1999] the side-wall effects on the velocities are negligible but the sediment transport can be decreased with 20 % by the side-wall. In the present study the bottom measurements are done in the middle of the wave flume, for future studies it is advised to measure the bottom closer to the wall where the PIV camera is located.

Next, the PIV frame is only 4 centimetres high. It is assumed that all sediment transport takes place within the PIV frame, but it is possible that the sediment transport calculated from the PIV data is slightly less than the sediment transport from the bottom measurements, thus leading to discrepancies between both calculations.

# 6

# Conclusion & Recommendations

*In this chapter I will present the main findings concerning the three main research questions (section 6.1) and give recommendations for future research (section 6.2). A more extensive interpretation of the results is given in the discussion (Chapter 5).*

## 6.1. Conclusion

I *Can the bottom profile development be predicted from the results of the PIV analysis?*

A PIV data analysis has the potential to determine sediment transport without additional concentration measurements. This study developed a method to determine sediment transport from PIV data without additional concentration measurements. There are three essential steps to enable transport calculation. (1) Place the laser in front of the wave flume during the PIV measurements instead of the common placement on top of the wave flume to illuminate the both the flow and the bed. (2) Determine a calibration relationship between the intensity and concentration based on the mean bed intensity, the mean water intensity and the mean intensity at every elevation of the sheet flow layer. This way the resulting calibration relation is specifically valid for the used data set, because image intensity varies with every experiment (unsteady and non-uniform). (3) Multiply at each data point the sediment velocities from the PIV calculation with the concentration to obtain sediment transport.

With a maximum in onshore sediment transport on top of the bar, the PIV sediment transport is in line with theory and the sediment transport based on the bottom profile development. This qualitative comparison indicates the validity of the proposed method. However qualitatively the net volume flux of the sand transport is not validated with the change in bottom profile. The PIV measurements result in a larger transport than the bottom profile measurements. Deviations are due to complexities in the relation between image intensity and concentration. First, sediment grains deeper into the flow become visible with a decreasing concentration. This effect is eliminated with a non-linear calibration between intensity and concentration. Next, the image brightness of the PIV measurements varies over space and time, while the mean bed concentration remains constant. In future research this problem can be solved with a calibration per PIV image or by using particle tracking.

Because the upcoming analysis will study the relative importance of different sediment mechanism and the PIV results are valid in a qualitative manner, it is assumed that the results are valid for further analysis. However the uncertainty of the sediment transport has to be kept in mind when interpreting the conclusions.

II *What contributes most to the time-averaged sediment transport: the current related, the time-averaged long wave related or the time-averaged short wave related sediment transport?*

Based on the data, the largest part of the sediment transport and sediment gradient is caused by time-averaged short wave related sediment transport. Hence most of the sediment transport is due to the timing of concentration suspension. The short wave related transport enlarges and moves the bar onshore due to a steepening decrease of onshore sediment transport. Also the current related transport and

long wave related transport move the bar onshore, but both slowly. The current related transport causes the onshore movement with a maximum in onshore transport and the long wave related transport with a minimum in offshore transport.

III *When comparing skewness and asymmetry, which periodic short wave mechanism is the dominant cause of onshore bar migration?*

The main result of the short wave related sediment transport analysis is that skewness increases towards the bed and asymmetry decreases towards the bed. Asymmetry even becomes positive near the bed, referring to backward tilted waves. The results seem to indicate that sediment transport mainly depends on near-bed skewness and not or slightly on the asymmetric pressure gradient, because the asymmetry at the elevations of sediment transport is small of positive. A small or positive near-bed asymmetry would cause a small onshore transport or a offshore transport, while only near-bed onshore transport is observed. Hence, free-stream asymmetry causes onshore sediment transport by increasing the near-bed skewness, but probably not or only slightly with the asymmetric pressure gradient. Based on these results numerical models should be able to accurately predict wave driven onshore sediment transport purely based on the near-bed skewed orbital velocities.

Consequently, the wave shape development in the wave bottom boundary layer needs to be calculated in order to predict sediment transport. In the results of this study, the observed skewness increase towards the bed in the wave bottom boundary layer is too large to be predicted with the theory of Berni et al. [2013] and Henderson et al. [2004]. For future studies it is advised to investigate alternative methods to determine the near-bed skewness.

## 6.2. Recommendation

Based on this project some recommendations can be made to improve future research. The most important and easy to implement recommendation is to perform particle tracking.

### 6.2.1. Particle tracking

Instead of using image intensity as measure of concentration, the individual sediment particles can be tracked digitally with image recognition. The displacement of the particle combined with the particle size will give the sediment transport.

Using particle tracking to calculate the sediment transport will solve the problems with intensity. Since the PIV data in this research are more detailed (more zoomed in) than in the studies of Horikawa et al. [1982] and Ahmed and Sato [2001], and the current image processing techniques are more advanced, particle tracking seems possible for the data in this research.

### 6.2.2. Additional wave related transport analyses

Carrying out the phase-averaged analysis, the instantaneous wave analysis and the cross-spectral analysis (section 3.3.2) can give more elaborate information and new insights about the wave driven sediment transport in the wave bottom boundary layer. A phase-averaged analysis can give more clarity about the importance of near-bed skewness versus the asymmetric pressure gradient for short wave related sediment transport.

In a phase-averaged analysis the average wave is constructed through phase averaging. This visually shows the velocity, concentration and sediment transport over the wave phases. The moment of occurrence of the maximum sediment transport can be related to a wave mechanism.

In an instantaneous analysis the values at each time step and each location (ea. $u(x_1, z_1, t_1)$) are compared to the sediment transport at the same time step and location ($S(x_1, z_1, t_1)$). The instantaneous analysis gives insight in the relation between velocity, acceleration, sheet flow height and sediment transport.

A cross-spectral analysis shows the coherence between frequencies of velocities and sediment transport. This gives insight in the differences in wave shape and phase lag between the velocities and the sediment transport.

### 6.2.3. Experiment

In future PIV experiments some improvements can be made:

#### 6.2.3.1 Concentration measurement

Measuring the concentration in sheet flow to calibrate the PIV data will improve the accuracy of the results. With additional concentration data the PIV calculation can be validated and improved. The concentration can be measured with for example a backscatter point sensors (ASTM) or an acoustic backscatter profiler (ABS).

#### 6.2.3.2 Light during experiment

Avoid the influence of light during the experiment. Cover the whole experiment can be covered with black sheets. Also place a sheet between the laser and the wave flume with only a rectangular gap around the PIV window. This avoids that more laser light than necessary enters the experiment and reflects on the bottom and water surface.

#### 6.2.3.3 Sand colour

The sediment grains had different colours (white, grey, black in the photo) and thus give a different intensity. It is assumed that this intensity difference averages over time. Future research can improve the accuracy of the intensity-concentration relation by using sediment in one colour.

#### 6.2.3.4 Multiple PIV camaras

Place multiple PIV camaras. With mutliple PIV camaras a 2D measurement can be done. With a 2D measurement the concentration can be based on the front particles. Hence a two dimensional sheet is used for the calculation and the concentration can be calculated more accurately.

#### 6.2.3.5 PIV location

All PIV measurement locations are close to the bar top, which results in small differences in sediment transport. For following research it could be nice to measure the PIV at characteristic points in the sediment transport curve (Figure 6.1). To determine these points, the first test can be done with only bottom measurements to calculate the sediment transport curve.

### 6.2.4. Filter noise

In the bottom velocities a high frequency noise is found. It is advisable to filter this noise to avoid influence on sediment transport, skewness or asymmetry.

### 6.2.5. Sheet flow layer development

Since PIV shows the velocities in the sheet flow layer over time, it is interesting to compare the development of the sheet flow layer due to waves and the development of the sheet flow layer due to a current. This can give a more fundamental understanding of 'waves stir up the sediment and currents transport it'.

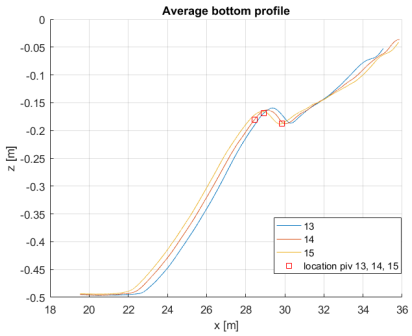


(a) PIV location in bottom profile

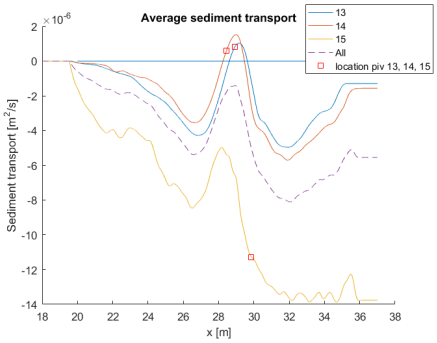


(b) PIV location in sediment transport

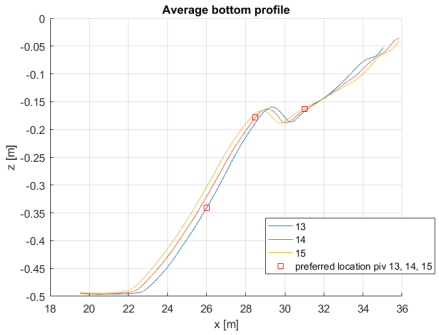


(c) Preferred piv location in bottom profile

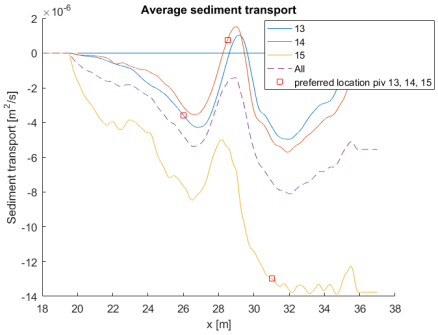


(d) Preferred piv location in sediment transport

Figure 6.1: Location PIV

# Bibliography


Abreu, T., Silva, P. A., Sancho, F., and Temperville, A. (2010). Analytical approximate wave form for asymmetric waves. *Coastal Engineering*, 57(7):656–667.

Ahmed, A. S. M. and Sato, S. (2001). Investigation of bottom boundary layer dynamics of a movable bed by using enhanced PIV technique. *Coastal Engineering Journal*, 43(04):239–258.

Al-Salem, A. (1993). *Sediment transport in oscillatory boundary layers under sheet-flow conditions*. PhD thesis, Delft University of Technology.

Aubrey (1979). Seasonal patterns of onshore/offshore sediment movement. *Journal of Geophysical Research*, 84(C10):6347–6354.

Bagnold, R. A. (1966). *An Approach to the Sediment Transport Problem from General Physics*. Washington.

Bailard, J. a. (1981). An energetics total load sediment transport model for a plane sloping beach. *Journal of Geophysical Research*, 86(C11):10938.

Battjes, J. (1986). *Korte golven*. TU Delft, Section Hydraulic Engineering.

Battjes, J. A. (1974). Computation of set-up, longshore currents, run-up and overtopping due to wind-generated waves.

Beji, S. and Battjes, J. A. (1993). Experimental investigation of wave propagation over a bar. *Coastal Engineering*, 19(1-2):151–162.

Berni, C., Barthélemy, E., and Michallet, H. (2013). Surf zone cross-shore boundary layer velocity asymmetry and skewness: An experimental study on a mobile bed. *Journal of Geophysical Research: Oceans*, 118(4):2188–2200.

Bosboom, J. and Klopman, G. (2001). Intra-Wave Sediment Transport Modelling. In *Coastal Engineering 2000*, pages 2453–2466. American Society of Civil Engineers.

Bosboom, J. and Stive, M. J. F. (2015). *Coastal Dynamics I*. VSSD, Delft.

Carstensen, S., Sumer, B. M., and Fredsøe, J. (2010a). Coherent structures in wave boundary layers. Part 1. Oscillatory motion. *Journal of Fluid Mechanics*, 646:169.

Carstensen, S., Sumer, B. M., Jensen, P. M., Sørensen, L., Fredsøe, J., and Liu, P. (2010b). Coherent structures in wave boundary layers. Part 1. Oscillatory motion. *Journal of Fluid Mechanics*, 646:207–231.

Carter, R. W. G. and Balsillie, J. H. (1983). A note on the amount of wave energy transmitted over nearshore sand bars. *Earth Surface Processes and Landforms*, 8(3):213–222.

Deigaard, R., Jakobsen, J. B., and Fredsoe, J. (1999). Net sediment transport under wave groups and bound long waves. *Journal Of Geophysical Research-Oceans*, 104(C6):13559–13575.

Dibajnia, M. and Watanabe, A. (1998). Transport rate under irregular sheet flow conditions. *Coastal Engineering*, 35:167–183.

Doering, J. C. and Bowen, A. J. (1995). Parametrization of orbital velocity asymmetries of shoaling and breaking waves using bispectral analysis. *Coastal Engineering*, 26(1):15–33.

Dohmen-Janssen, C. M. and Hanes, D. M. (2005). Sheet flow and suspended sediment due to wave groups in a large wave flume. *Continental Shelf Research*, 25(3):333–347.

Dohmen-Janssen, M. (1999). *Grain size influence on sediment transport in oscillatory sheet flow*. PhD thesis, Delft University of Technology.

Drake, T. G. and Calantoni, J. (2001). Discrete particle model for sheet flow sediment transport in the nearshore. *Journal of Geophysical Research*, 106(C9):19859–19868.

Dubarbier, B., Castelle, B., Marieu, V., Michallet, H., Grasso, F., and Ruessink, G. (2013a). Numerical modelling of equilibrium and evolving lightweight sediment laboratory beach profiles. In *Coastal Dynamics 2103-7th International Conference on Coastal Dynamics*, pages 521–530, Arcachon, France.

Dubarbier, B., Castelle, B., Marieu, V., and Ruessink, G. (2013b). Numerical modelling of pronounced sloping beach profile evolution: comparison with the large-scale BARDEX II experiment. *Journal of Coastal Research*, 65(sp2):1762–1767.

Dudley, R. D. (2007). *A Boroscopic Quantitative Imaging Technique for Sheet Flow Measurements*. Master thesis, Cornell University.

Einstein, H. A. (1950). *The bed-load function for sediment transportation in open channel flows*. Number 1026. US Department of Agriculture.

Elgar, S., Gallagher, E., and Guza, R. (2001). Nearshore sandbar migration. *Journal of Geophysical Research*, 106(C6):11623.

Elgar, S. and Guza, R. T. (1985). Observations of bispectra of shoaling surface gravity waves. *Journal of Fluid Mechanics*, 161:425–448.

Flores, N. Z. and Sleath, J. F. A. (1998). Mobile layer in oscillatory sheet flow. *Journal of Geophysical Research: Oceans*, 103(C6):12783–12793.

Foster, D. L., Bowen, A. J., Holman, R. A., and Natoo, P. (2006). Field evidence of pressure gradient induced incipient motion. *J. Geophys. Res. C Oceans*, 111.

Foster, D. L., Guenther, R. A., and Holman, R. A. (1999). An analytic solution to the wave bottom boundary layer governing equation under arbitrary wave forcing. *Ocean Engineering*, 26:595–623.

Gallagher, E. L., Elgar, S., and Guza, R. T. (1998). Observations of sand bar evolution on a natural beach. *Journal of Geophysical Research*, 103(C2):3203–3215.

Graaff, van de, J. (2009). *Coastal Morphology and Coastal Protection*. Delft.

Grasso, F., Michallet, H., Barthélemy, E., and Certain, R. (2009). Physical modeling of intermediate cross-shore beach morphology: Transients and equilibrium states. *Journal of Geophysical Research: Oceans*, 114(C9).

Hallermeier, R. J. (1981). Terminal settling velocity of commonly occurring sand grains. *Sedimentology*, 28(6):859–865.

Heijboer, D. (1988). *Zandconcentratie- en stroomsnelheids-verdelingen onder golven en stroom*. PhD thesis, TU Delft.

Henderson, S. M., Allen, J. S., and Newberger, P. A. (2004). Nearshore sandbar migration predicted by an eddy-diffusive boundary layer model. *Journal of Geophysical Research*, 109(C06024).

Henriquez, M. (2016). Onshore sandbar migration in the nearshore (working paper).

Henriquez, M., Reniers, A., and Ruessink, B. G. (2009). On the scaling of sediment transport in the nearshore. *Second International Conference on the Application of Physical Modelling to Port and Coastal Protection*, (January 2009).

Hoefel, F. (2003). Wave-Induced Sediment Transport and Sandbar Migration. *Science*, 299:1885–1887.

Holthuijsen, L. (2007). *Waves in Oceanic and Coastal Waters*. Cambridge University Press.

Horikawa, K., Watanabe, A., and Katori, S. (1982). Sediment transport under sheet flow conditions. pages 1335–1352.

Hsu, T., Elgar, S., and Guza, R. (2006). Wave-induced sediment transport and onshore sandbar migration. *Coastal Engineering*, 53(10):817–824.

Hughes, S. A. (1993). *Physical models and laboratory techniques in coastal engineering*, volume 7. World Scientific.

Inman, D., Jenkins, S., and Hicks, D. (1985). Oscillatory Bursting. *EOS, transactions, American Geophysical Union*, 65(45):995.

Jonsson, I. (1966). Wave boundary layers and friction factors. In *Coastal Engineering Proceedings*, chapter Chapter 10, pages 127–148. Copenhagen.

Kajiura, K. A. (1968). A Model of the Bottom Boundary Layer in Water Waves. *Bulletin Earthquake Research Institute*, 46:75–123.

Kamphuis, J. W. (1973). Short wave models with fixed bed boundary layer. *Journal of the Waterways, Harbors and Coastal Engineering Division*, 99(4):471–483.

Kamphuis, J. W. (1985). On understanding scale effect in coastal mobile bed models. *Physical Modelling in Coastal Engineering*, pages 141–162.

Kamphuis, J. W. (1991). Alongshore sediment transport rate. *Journal of Waterway, Port, Coastal, and Ocean Engineering*, 117(6):624–640.

King, D. (1991). *Studies in oscillatory flow bedload sediment transport*. Phd, University of California.

Kranenburg, W. (2013). *Modeling sheet-flow sand transport under progressive surface waves*.

Kranenburg, W. M., Ribberink, J. S., Schretlen, J. J. L. M., and Uittenbogaard, R. E. (2013). Sand transport beneath waves: The role of progressive wave streaming and other free surface effects. *Journal of Geophysical Research: Earth Surface*, 118(1):122–139.

Liu, H. and Sato, S. (2005). Laboratory Study on Sheetflow Sediment Movement in the Oscillatory Turbulent Boundary Layer Based on Image Analysis. *Coastal Engineering Journal*, 47(01):21–40.

Longuet-Higgins (1953). Mass Transport in Water Waves. *Philosophical Transactions of the Royal Society of London. Series A, Mathematical and Physical Sciences*, 245(903):535–581.

Madsen, O. and Grant, W. (1976). *Sediment transport in the coastal environment*. PhD thesis, Massachusetts Inst. of Tech.

Madsen, O. S. (1974). Stability of a sand bed under breaking waves. *Coastal engineering proceedings*, 1(14).

Madsen, O. S., Mathisen, P. P., and Rosengaus, M. M. (1990). Movable bed friction factors for spectral waves, paper presented at the 22nd International Conference on Coastal Engineering. In *Am Soc. Civ. Eng*, Delft.

Matias, A., Masselink, G., Kroon, A., Blenkinsopp, C. E., and Turner, I. L. (2013). Overwash experiment on a sandy barrier. *Journal of Coastal Research*, 65(sp1):778–783.

Mogridge, G., Modridge, G., and Kamphuis, J. (1972). Experiments on bed form generation by wave action. In *Coastal Engineering Proceedings*, page 13.

Naqshban, Ribberink, Kranenburg, and Schretlen (2009). *Wave Boundary Layer Streaming*. PhD thesis, University of Twente.

Nielsen, P. (1992). *Coastal bottom boundary layers and sediment transport*. World Scientific, Singapore.

Nielsen, P. and Callaghan, D. P. (2003). Shear stress and sediment transport calculations for sheet flow under waves. *Coastal Engineering*, 47(3):347–354.

Nieuwstadt, F. T. M. (1992). *Turbulentie : inleiding in de theorie en toepassingen van turbulente stromingen*. Epsilon,, Utrecht :.

O'Donoghue, T. and Wright, S. (2004a). Concentrations in oscillatory sheet flow for well sorted and graded sands. *Coastal Engineering*, 50(3):117–138.

O'Donoghue, T. and Wright, S. (2004b). Flow tunnel measurements of velocities and sand flux in oscillatory sheet flow for well-sorted and graded sands. *Coastal Engineering*, 51:1163–1184.

O'Donoghue, T. and Wright, S. (2004c). Flow tunnel measurements of velocities and sand flux in oscillatory sheet flow for well-sorted and graded sands. *Coastal Engineering*, 51(11-12):1163–1184.

Pape, L., Plant, N. G., and Ruessink, B. G. (2010). On cross-shore migration and equilibrium states of nearshore sandbars. *Journal of Geophysical Research: Earth Surface*, 115(3):1–16.

Peskin, C. S. (2010). Wave momentum. pages 1–26.

Pietrzak, J. (2015). *Class Notes for CIE5302: An Introduction to Stratified Flows for Civil and Offshore Engineerings*. TU Delft, Delft.

Plant, N. (1998). The role of morphologic feedback in surf zone sand bar response. Technical report, Oregon State University, Oregon.

Ribberink, J. and Al-Salem, A. (1995). Sheet flow and suspension of sand in oscillatory boundary layers. *Coastal Engineering*, 25(3-4):205–225.

Ribberink, J. S. (1998). Bed-load transport for steady flows and unsteady oscillatory flows. *Coastal Engineering*, 34:59–82.

Ribberink, J. S. and Al-Salem, A. a. (1994). Sediment transport in oscillatory boundary layers in cases of rippled beds and sheet flow. *Journal of Geophysical Research*, 99(C6):12707–12727.

Roelvink, D. and Reniers, A. (2011). *A guide to modeling coastal morphology*. Advances in coastal and ocean engineering ; vol. 12; Advances in coastal and ocean engineering ; vol. 12. World Scientific,.

Roelvink, J. and Stive, M. (1989). Bar-Generating Cross-Shore Flow Mechanisms on a Beach. *Journal of Geophysical Research*, 94(C4):4785–4800.

Ruessink, B. G., Houwman, K. T., and Hoekstra, P. (1999). Medium-term frequency distributions of cross-shore suspended sediment transport rates in water depth of 3 to 9 m. *Coastal Eng.*, 38:25–46.

Ruessink, B. G., Kuriyama, Y., Reniers, A. J. H. M., Roelvink, J. A., and Walstra, D. J. R. (2007). Modeling cross-shore sandbar behavior on the timescale of weeks. *Journal of Geophysical Research: Earth Surface*, 112(3):1–15.

Ruessink, B. G., Miles, J. R., Feddersen, F., Guza, R. T., and Elgar, S. (2001). Modeling the alongshore current on barred beaches. *Journal of Geophysical Research*, 106(C10):22451.

Ruessink, B. G., Ramaekers, G., and Van Rijn, L. C. (2012). On the parameterization of the free-stream non-linear wave orbital motion in nearshore morphodynamic models. *Coastal Engineering*, 65:56–63.

Schipper, M. (2015). Slides Coastal Dynamics II.

Shields, a. (1936). Application of Similarity Principles and Turbulence Research to Bed-Load Movement. *Mitt. Preuss. Versuchsanst. Wasserbau Schiffbau*, 26(5-24):47.

Sleath, J. F. A. (1999). Conditions for plug formation in oscillatory flow. *Continental Shelf Research*, 19(13):1643–1664.

Smyth, C. and Hay, A. E. (2002). Wave Friction Factors in Nearshore Sands. *Journal of Physical Oceanography*, 32(12):3490–3498.

Stokes, G. (1847). On the theory of oscillatory waves. *Trans. Cambridge Phil. Soc*, 8:441–455.

Swart, D. H. (1974). *Offshore sediment transport and equilibrium beach profiles*. PhD thesis, TU Deft.

Tapia, H. S. (2006). spherical Particles .

Terrile, E., Reniers, A. J. H. M., and Stive, M. J. F. (2009). Acceleration and Skewness Effects on the Instantaneous Bed-Shear Stresses in Shoaling Waves. *Journal of Waterway, Port, Coastal and Ocean Engineering*, 135(5):228–234.

Thornton, E. B. and Humiston, R. T. (1996). Bar / trough generation on a natural beach. *Journal of Geophysical Research*, 101(96):12097–12110.

Thorpe, S. A. (1971). Experiments on the instability of stratified shear flows: miscible fluids. *Journal of Fluid Mechanics*, 46(2):299–319.

Trowbridge, J. and Madsen, O. (1984). Turbulent wave boundary layers, 2. Second order theory and mass transport. *Journal of Geophysical Research*, 89:7999–8007.

Trowbridge, J. and Young, D. (1989). Sand transport by unbroken water-waves under sheet flow conditions. *J. Geophys. Res.*, 97:10971–10991.

van Rijn, L. C. (1990). *Principles of fluid flow and surface waves in rivers, estuaries, seas, and oceans*. Aqua Publications, Amsterdam.

Van Rijn, L. C. (1993). *Principles of sediment transport in rivers, estuaries and coastal seas*, volume 1006. Aqua publications Amsterdam.

Van Rijn, L. C., Tonnon, P. K., Sánchez-Arcilla, A., Cáceres, I., and Grüne, J. (2011). Scaling laws for beach and dune erosion processes. *Coastal Engineering*, 58(7):623–636.

Wallet, A. and Ruellan, F. (1950). Trajectories of particles within a partial clapotis. *La Houille Blance*, 5:483–489.

Watanabe, A. and Sato, S. (2004). A sheet-flow transport rate formula for asymmetric, forward-leaning waves and currents. In *COASTAL ENGINEERING CONFERENCE*, volume 29, page 1703. World Scientific.

Wilson, K. C. (1987). Analysis of bed-load motion at high shear stress. *Journal of Hydraulic Engineering*, 113(1):97–103.

Wright, L. D. and Short, a. D. (1984). Morphodynamic variability of surf zones and beaches: A synthesis. *Marine Geology*, 56(1–4):93–118.

Yu, X., Hsu, T. J., and Hanes, D. M. (2010). Sediment transport under wave groups: Relative importance between nonlinear waveshape and nonlinear boundary layer streaming. *Journal of Geophysical Research: Oceans*, 115(2):1–18.

# Appendices

# A

# Waves: Mass, momentum and energy transport

## A.1. Introduction

A wave is a pressure disturbance traveling through a medium, for example air or water. Waves can transport mass, momentum and energy. Well known waves are sound waves (Figure 2.3a) or surface gravity waves (Figure A.1b). Due to the scale difference between these wave types, a different mechanism is dominant: compression versus gravity. *Sound waves* are longitudinal compression waves with a high frequency. In a longitudinal wave the particles move in direction of wave propagation. The individual particles move back and forward as the wave (a region of high pressure) moves through (Figure A.1a). The wave speed depends on the compressibility of the medium; a lower compressibility ('stiffer') gives a higher speed. With this the waves are non-dispersive, all wave lengths have the same speed.

*Surface gravity waves* occur at lower frequencies and larger scales. Due to bottom friction and the free surface the wave becomes asymmetrical over the vertical, hence the motion becomes two dimensional. The free surface allows the particles to move perpendicular to the wave. This creates a circular motion of the individual particles, named the orbital motion (Figure 2.3b).

Three conservative properties: mass, momentum and energy form the basis of fluid mechanics. This appendix will explain the mass, momentum and energy transport in deep water waves.

## A.2. Mass transport

Sinusoidal deep water waves have a small wave driven mean current [Battjes, 1986] which can influence the sediment transport. It is surprising that an oscillatory motion has an average mass transport, since the expectation would be one step forth, same step back. There are two theories to calculate the time averaged flow for sinusoidal waves:

1. Stokes drift — Mass transport due to the non-linear orbital motion of free stream.
2. Longuet-Higgins streaming — Mass transport due to the downward transport of momentum [Longuet-Higgins, 1953].

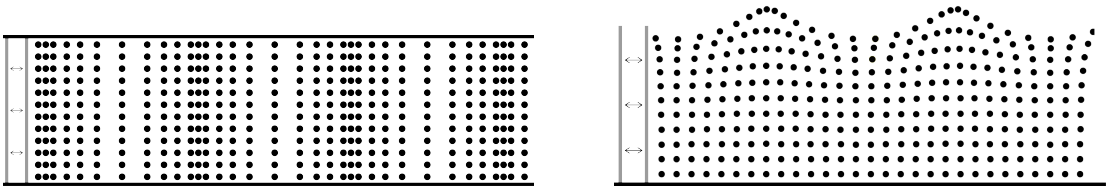

(a) Sound wave

(b) Surface wave

Figure A.1: Waves

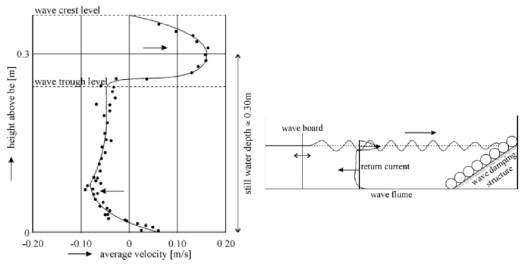


(a) Longuet-Higgins vertical velocity profile with a smooth bottom [Heijboer, 1988] p.14

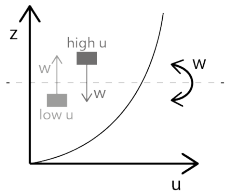


(b) Downward momentum transfer

Figure A.2: Longuet-Higgins streaming

In coastal waters the wave driven mass flow can cause large currents that strongly influence the sediment transport, like for example undertow (section 2.1.1).

### A.2.1. Stokes drift

For irrational flow (ideal fluid, non-viscous flow) Stokes [1847] pointed out that the particles have a mean velocity in the direction of wave propagation. Since the horizontal orbital velocity increases with the height above the bed (Figure **??**), the fluid particle experiences a different forward and backward velocity during a orbit. The resulting forward movement is called Stokes drift [van Rijn, 1990, p.244] (Figure 2.13).

Including the first non-linear term in the integration of the orbital velocity over time gives the resulting mass flow (Equation A.1 & A.2). This non-linear term of the orbital velocity describes the height variation of the particle during an orbit. In other words, the average transport is caused by the correlation between water level and horizontal velocity: the water moves forward at the moment of high water level. Analogous, the mean transport of sound waves is caused by the correlation between density and velocity: the air moves forward at a region of high density [Peskin, 2010].

$$\bar{u}_{st} = \frac{1}{8}\omega k H^2 \frac{\cosh(2k(z-z_b))}{\sinh^2(-z_b \cdot k)} \tag{A.1}$$

$$M = \int_{z_b}^{0} \rho \cdot \bar{u}_{st}(z)\ dz = \frac{E}{c} = \frac{1}{8}\frac{\rho g H^2}{c} \tag{A.2}$$

### A.2.2. Longuet-Higgins streaming

Longuet-Higgins considers rotational flow (real fluid) and includes viscosity in the equations [Longuet-Higgins, 1953]. Viscosity incites a downward transfer of momentum into the boundary layer [van Rijn, 1990, p.247]. Bottom friction now affects the whole flow. This results in a strong forward current near the bottom, called streaming (Figure A.2a). Since viscosity is important in the wbbl, this wbbl streaming is a realistic prediction. With most sediment concentrated near the bottom, streaming can have an important effect on the sediment transport.

The downward transfer of horizontal momentum is described by the term $\partial\overline{\tilde{u}\tilde{w}}/\partial z$ (Appendix B.2). The vertical orbital velocities mix horizontal velocities (Figure A.2b). This is only possible if $\tilde{u}$ and $\tilde{w}$ occur at the same time, not 90 degrees out of phase as in the free-stream. Hence streaming only occurs if there is a phase shift between the horizontal and vertical velocities in the wbbl [Kranenburg et al., 2013, Longuet-Higgins, 1953].

Equation A.3 describes the mass-transport velocity just outside the boundary layer for smooth oscillatory flow [Longuet-Higgins, 1953]. The theory also gives fairy good predictions for shallow water in the range of approximately $1/10 < h/L < 1/4$ [van Rijn, 1990, p.248].

$$\overline{u}_{\infty} = \frac{3}{4}\frac{\hat{u}_{\infty}^2}{c} \tag{A.3}$$

## A.3. Momentum transport

Momentum is mass times velocity. Therefore momentum density ($\rho u_x$) equals mass transport and wave momentum equals the wave driven current (Equation A.4). Momentum can be transported in the direction

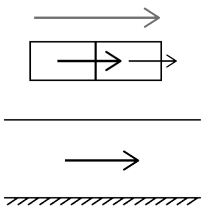

(a) Momentum transport in direction of mass transport through normal stress

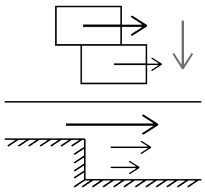

(b) Momentum transport perpendicular to mass transport through shear stress or mixing

Figure A.3: Direction of momentum transport

of mass transport through normal stresses or mixing (Figure A.3a) or perpendicular to the mass transport through shear stress or mixing (Figure A.3b). Mixing can be caused by turbulence, quantified in Reynolds stresses, or by orbital motion, quantified in radiation stresses. Hence the radiation stresses in the momentum equation describe the influence of waves on the flow (Appendix B.3). Radiation stress is not a physical stress, but does affects the flow comparable to a stress.

$$M_x = \overline{\int_{z_b}^{\eta} \rho u_x dz} \tag{A.4}$$

$$u = \overline{u} + \tilde{u} + u' \tag{A.5}$$

Radiation stresses and Reynold stresses result from decomposing the velocity in the momentum equation in a constant velocity and a fluctuating velocity (Equation A.5 & Appendix B.3). Horizontal variation in radiation stress acts as a force on the water, see section 2.2.1.

## A.4. Energy transport

A wave is a balance between potential and kinetic energy, potential energy changes to kinetic energy and through inertia back to potential energy. At the crest and through the potential energy has its extreme values and at the inflection point between the crest and through the vertical kinetic energy has its extreme value. Averaged over the wave period the potential and kinetic energy are equal and together they form the total time-averaged wave-induced energy density (Equation A.6) [Holthuijsen, 2007, p.132]. This wave energy is proportional to the square of the wave height and thus a second-order wave property.

$$E = \frac{1}{8}\rho g H^2 \tag{A.6}$$

The wave energy is transported with the group velocity (Equation A.7) [Holthuijsen, 2007, p.136]. Without an additional current, the wave energy transport is in the direction of wave propagation.

$$P_{energy} = E \cdot c_g = E \cdot n \cdot c \qquad \text{with} \qquad n = \frac{1}{2}\left(1 + \frac{2kd}{sinh(2kd)}\right) \tag{A.7}$$

# B

# Wave equations

## B.1. Mass and momentum balance

In fluid mechanics there are three conservative properties: energy, mass and momentum. For all conservative properties the basic equations can be derived from the elementary cube (Figure B.1). For a random property with density $\mu$ adding the inflow and outflow of the cube in all three directions results in equation B.2.

$$Storage = Import - Export + Source \tag{B.1}$$

$$\frac{\partial \mu}{\partial t} = -\frac{\partial \mu u}{\partial x} - \frac{\partial \mu v}{\partial y} - \frac{\partial \mu w}{\partial z} + S \tag{B.2}$$

When replacing $\mu$ by the densities of the conservative properties mass and momentum, it results in the continuity equation and momentum equations. This is shown in Table B.1. The equations in Table B.1 are structured the following: storage + advection = source/sink.

| | density | assumption | equation | | | | | | | | | |
|---|---|---|---|---|---|---|---|---|---|---|---|---|
| *Compressible fluid* | | | | | | | | | | | | |
| **mass** | $\rho$ | | $\frac{\partial \rho}{\partial t}$ | + | $\frac{\partial \rho u}{\partial x}$ | + | $\frac{\partial \rho v}{\partial y}$ | + | $\frac{\partial \rho w}{\partial z}$ | = | 0 | |
| **momentum** | $\rho\vec{u}$ | | $\frac{\partial \rho u}{\partial t}$ | + | $\frac{\partial \rho u^2}{\partial x}$ | + | $\frac{\partial \rho uv}{\partial y}$ | + | $\frac{\partial \rho uw}{\partial z}$ | = | $-\frac{\partial p}{\partial x}$ | |
| | | | $\frac{\partial \rho v}{\partial t}$ | + | $\frac{\partial \rho uv}{\partial x}$ | + | $\frac{\partial \rho v^2}{\partial y}$ | + | $\frac{\partial \rho vw}{\partial z}$ | = | $-\frac{\partial p}{\partial y}$ | |
| | | | $\frac{\partial \rho w}{\partial t}$ | + | $\frac{\partial \rho uw}{\partial x}$ | + | $\frac{\partial \rho vw}{\partial y}$ | + | $\frac{\partial \rho w^2}{\partial z}$ | = | $-\frac{\partial p}{\partial z} - \rho g$ | |
| *Incompressible fluid* | | | | | | | | | | | | |
| **mass** | $\rho$ | $\partial\rho = 0$ | | | $\frac{\partial u}{\partial x}$ | + | $\frac{\partial v}{\partial y}$ | + | $\frac{\partial w}{\partial z}$ | = | 0 | |
| **momentum** | $\rho\vec{u}$ | $\partial\rho = 0$ | $\frac{\partial u}{\partial t}$ | + | $\frac{\partial u^2}{\partial x}$ | + | $\frac{\partial uv}{\partial y}$ | + | $\frac{\partial uw}{\partial z}$ | = | $-\frac{1}{\rho}\frac{\partial p}{\partial x}$ | |
| | | | $\frac{\partial v}{\partial t}$ | + | $\frac{\partial uv}{\partial x}$ | + | $\frac{\partial v^2}{\partial y}$ | + | $\frac{\partial vw}{\partial z}$ | = | $-\frac{1}{\rho}\frac{\partial p}{\partial y}$ | |
| | | | $\frac{\partial w}{\partial t}$ | + | $\frac{\partial uw}{\partial x}$ | + | $\frac{\partial vw}{\partial y}$ | + | $\frac{\partial w^2}{\partial z}$ | = | $-\frac{1}{\rho}\frac{\partial p}{\partial z} - g$ | |

Table B.1: Mass and momentum balance

When including turbulence, the momentum equation results in the Navier Stokes equations (Table B.2).

## B.2. Linear wave theory

Linear wave theory assumes that the quadratic velocity terms that describe advection are negligible, since for small wave heights these velocities are small. The square of small velocities is even smaller and therefore it

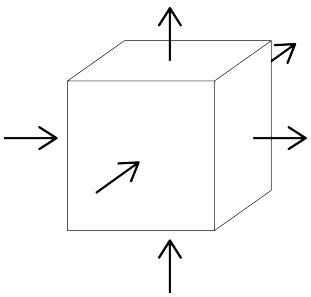

Figure B.1: Elementary cube to calculate mass and momentum balance

$$\begin{array}{lcll} \frac{Du}{Dt} & = & -\frac{1}{\rho}\frac{\partial p}{\partial x} & + \quad \nu\left[\frac{\partial^2 u}{\partial x^2}+\frac{\partial^2 u}{\partial x^2}+\frac{\partial^2 u}{\partial x^2}\right] \\ \frac{Dv}{Dt} & = & -\frac{1}{\rho}\frac{\partial p}{\partial y} & + \quad \nu\left[\frac{\partial^2 v}{\partial x^2}+\frac{\partial^2 v}{\partial x^2}+\frac{\partial^2 v}{\partial x^2}\right] \\ \frac{Dw}{Dt} & = & -\frac{1}{\rho}\frac{\partial p}{\partial z}-g & + \quad \nu\left[\frac{\partial^2 w}{\partial x^2}+\frac{\partial^2 w}{\partial x^2}+\frac{\partial^2 w}{\partial x^2}\right] \end{array}$$

Table B.2: Navier Stokes equations

is assumed that the gradient over space of the quadratic velocities is also small. This results in equations B.3, B.4 and B.5.

$$\frac{du}{dt} = -\frac{1}{\rho}\frac{\partial p}{\partial x} \tag{B.3}$$

$$\frac{dv}{dt} = -\frac{1}{\rho}\frac{\partial p}{\partial y} \tag{B.4}$$

$$\frac{dw}{dt} = -\frac{1}{\rho}\frac{\partial p}{\partial z} - g \tag{B.5}$$

Secondly the flow is assumed rotation free, which is valid in the free stream motion. Now the continuity and momentum equation can be expressed in the velocity potential as given in Equation B.6. Doing this makes the flow per definition rotation free, because all rotation terms equal zero (Equation B.7).

$$\Delta\phi = \vec{u}; \qquad u = \frac{\partial\phi}{\partial x}, v = \frac{\partial\phi}{\partial y}, w = \frac{\partial\phi}{\partial z} \tag{B.6}$$

$$\Omega_y = \frac{\partial w}{\partial x} - \frac{\partial u}{\partial z} = \frac{\partial}{\partial x}\frac{\partial\phi}{\partial z} - \frac{\partial}{\partial z}\frac{\partial\phi}{\partial x} = 0 \tag{B.7}$$

With the velocity potential, the continuity equation can be rewritten to the Laplace equation (Equation B.8) and the momentum equation can together be rewritten to the Bernoulli equation (Equation B.9) [Holthuijsen, 2007, p.115].

$$\frac{\partial^2\phi}{\partial x^2} + \frac{\partial^2\phi}{\partial y^2} + \frac{\partial^2\phi}{\partial z^2} = 0 \tag{B.8}$$

$$\frac{\partial\phi}{\partial t} + \frac{p}{\rho} + gz = 0 \tag{B.9}$$

Together with the boundary conditions at the bottom and water surface these equations result in the kinematic solution and the dynamic solution. The kinematic solution describes the orbital velocities (Equation B.10, B.11 and Figure B.2). Equation 2.6 specifically describes the orbital velocities at the transition between free-stream motion and wbbl [van Rijn, 1990, p.260]. The dynamic solution gives the wave celerity and is called the dispersion relation (Equation B.13). For shallow water the wave celerity approaches $c = \sqrt{g \cdot |z_b|}$.

$$u = \hat{u} \cdot cos(\omega t - kx), \qquad \hat{u} = \frac{\omega a \cdot \cosh(k(z - z_b))}{\sinh(-z_b \cdot k)} \tag{B.10}$$

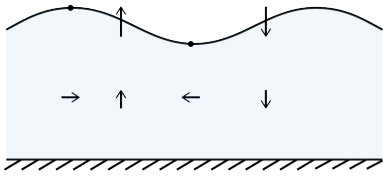

(a) Momentary orbital velocities

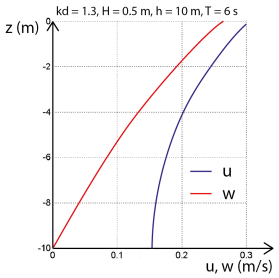


(b) Orbital velocities by linear wave theory [Schipper, 2015]

Figure B.2: Orbital velocities by linear wave theory

$$w = \hat{w} \cdot \sinh(\omega t - kx), \qquad \hat{w} = \frac{-\omega a \cdot \sinh(k(z - z_b))}{\sinh(-z_b \cdot k)} \tag{B.11}$$

$$\hat{u}_\infty = \frac{\omega a}{\sinh(-z_b \cdot k)} \tag{B.12}$$

$$c = \frac{\omega}{k}, \qquad \omega^2 = gk \tanh(-z_b \cdot k) \tag{B.13}$$

$$L = \frac{gT^2}{2\pi} \tanh\left(\frac{2\pi \cdot -z_b}{L}\right) \tag{B.14}$$

The velocities decrease with increasing depth ($\hat{u}$ and $\hat{w}$), because the hydrostatic pressure increases. For deep water the velocities become zero above the bottom. For shallow water the orbital velocities are not yet zero at the bottom and bottom friction decelerates the velocities to zero. The area with bottom influence in shallow water is called the wave bottom boundary layer (wbbl).

With the linear wave theory it is possible to have horizontal orbital velocities at the bottom, since there is no viscosity. In practise this is not the case. Therefore it is assumed that equation B.12 describes the velocity at the top of the wbbl layer. To compare the theoretical velocity to measurements, the velocities at the top of the wbbl (Appendix C.4.3) have to be used.

### B.2.1. Linearised equations in the wbbl

In the wbbl, the forcing term is the free-stream orbital motion, $u_\infty$. Equation B.15 is the linear momentum equation in wbbl [Foster et al., 1999, p.597], in which $\hat{u}$ is maximum cross-shore orbital velocity and z is positive upwards from the bed. Rewriting equation B.15 gives equation B.16. All homogeneous terms stand on the left side and the forcing term on the right side. The homogeneous and the forcing part can be solved separately. The total solution is Equation B.17 [Foster et al., 1999, eq. 28], of which $\Phi$ is defined as expression B.18.

$$\frac{\partial \hat{u}}{\partial t} - \frac{\partial u_\infty}{\partial t} = \frac{1}{\rho} \frac{\partial \tau_{zx}}{\partial z} \tag{B.15}$$

$$\frac{\partial u}{\partial t} - g \frac{dp}{dz} \frac{\partial u}{\partial z} - pg \frac{\partial^2 u}{\partial z^2} = \frac{z - z_b}{z_0 - z_b} \frac{\partial u_\infty}{\partial t} + g \frac{dp}{dz} \frac{u_\infty}{-z_b - z_0} \tag{B.16}$$

$$\hat{u}(z,t) \sum_{n=1} \infty a_n(t) \Phi_n(z) + \frac{z - z_0}{-z_b - z_0} u_\infty \tag{B.17}$$

$$\Phi = Y_0(2\lambda_n z_0^{1/2}) J_0(2\lambda_n z^{1/2}) - J_0(2\lambda_n z^{1/2}) Y_0(2\lambda_n z_0^{1/2}) \tag{B.18}$$

## B.3. Radiation stress

In the nearshore, wave momentum causes a set-down and set-up. In the wave momentum equation this effect can be found in the the non-linear advection terms. Therefore the non-linear terms can not be neglected. To simplify the non-linear terms, the terms are described as a stress: radiation stress. Radiation stress is the depth-integrated, wave-averaged momentum flux due to waves.

To rewrite the non-linear terms to a stress, velocity decomposition and time-averaging are applied. This approach is the same as Reynolds decomposition of turbulent velocities. Therefore first Reynolds averaging is explained (section B.3.1), after which the same decomposition is done for the wave velocities (section B.3.2). The last section (section B.3.3) describes the effect of radiation stress on set-down and set-up in the nearshore.

### B.3.1. Reynolds decomposition and stress

To split the main flow from turbulence the velocity is decomposed in a mean velocity and a fluctuating velocity. This is called Reynolds decomposition (Equation B.19, B.20). [Nieuwstadt, 1992] For a two dimensional flow, this decomposition is substituted in the 2D momentum equations. When averaging, all terms with a single fluctuating velocity are zero (Figure B.3).

$$u = \overline{u} + u' \tag{B.19}$$

$$w = \overline{w} + w' \tag{B.20}$$

The momentum equation in x for a two dimensional flow:

$$\frac{\partial u}{\partial t} + \frac{\partial u^2}{\partial x} + \frac{\partial uw}{\partial z} = -\frac{1}{\rho}\frac{\partial p}{\partial x} \tag{B.21}$$

After substitution and averaging:

$$\frac{\partial \overline{u}}{\partial t} + \frac{\partial \overline{u}^2}{\partial x} + \frac{\partial \overline{uw}}{\partial z} + \frac{\partial \overline{u'u'}}{\partial x} + \frac{\partial \overline{u'w'}}{\partial z} = -\frac{1}{\rho}\frac{\partial p}{\partial x} \tag{B.22}$$

The remaining fluctuating terms describe the effect of turbulence on the main flow. These terms can be written as stresses (Equation B.23). Turbulence relocates momentum and is in that way comparable to shear stress. The Reynolds stresses are unknown and therefore every numerical model using these equations needs an additional turbulence equation, the turbulence closure.

$$\frac{\partial \overline{u}}{\partial t} + \frac{\partial \overline{u}^2}{\partial x} + \frac{\partial \overline{uw}}{\partial z} + \frac{1}{\rho}\frac{\partial p}{\partial x} + \frac{1}{\rho}\left[\frac{\partial \tau_{xx}}{\partial x} + \frac{\partial \tau_{xy}}{\partial z}\right] = 0 \tag{B.23}$$

The same can be done for the momentum equation in z.

### B.3.2. Radiation stress

The same decomposition can be done for the effects of waves. The velocities are now decomposed in a mean velocity and the fluctuating wave velocity ($\overline{\tilde{u}} = 0$):

$$u = \overline{u} + \tilde{u} \tag{B.24}$$

$$w = \overline{w} + \tilde{w} \tag{B.25}$$

The momentum equation in x for a two dimensional flow:

$$\frac{\partial u}{\partial t} + \frac{\partial u^2}{\partial x} + \frac{\partial uw}{\partial z} = -\frac{1}{\rho}\frac{\partial p}{\partial x} \tag{B.26}$$

Substitute the decomposition in the x-momentum equation:

$$\frac{\partial(\overline{u}+\tilde{u})}{\partial t} + \frac{\partial(\overline{u}+\tilde{u})^2}{\partial x} + \frac{\partial(\overline{u}+\tilde{u})(\overline{w}+\tilde{w})}{\partial z} = -\frac{1}{\rho}\frac{\partial(p+p_{wave})}{\partial x} \tag{B.27}$$

$$\frac{\partial \overline{u}}{\partial t} + \frac{\partial \tilde{u}}{\partial t} + \frac{\partial \overline{u}^2}{\partial x} + \frac{\partial \overline{u}\tilde{u}}{\partial x} + \frac{\partial \tilde{u}^2}{\partial x} + \frac{\partial \overline{uw}}{\partial z} + \frac{\partial \overline{u}\tilde{w}}{\partial z} + \frac{\partial \tilde{u}\overline{w}}{\partial z} + \frac{\partial \tilde{u}\tilde{w}}{\partial z} = -\frac{1}{\rho}\frac{\partial p + p_{wave}}{\partial x} \tag{B.28}$$

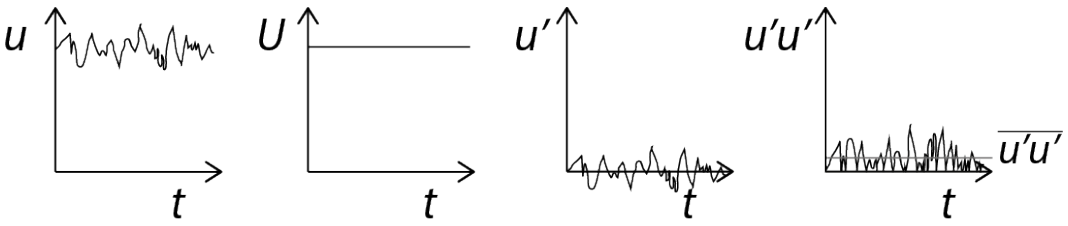


Figure B.3: The concept of Reynolds averaging [Pietrzak, 2015] (Figure 5.2, p.43)

When averaging over the wave period, all terms with a single oscillating velocity drop out:

$$\frac{\partial \overline{u}}{\partial t} + \frac{\partial \overline{u}^2}{\partial x} + \frac{\partial \overline{uw}}{\partial z} + \frac{\partial \overline{\tilde{u}^2}}{\partial x} + \frac{\partial \overline{\tilde{u}\tilde{w}}}{\partial z} = -\frac{1}{\rho}\frac{\partial p}{\partial x} - \frac{1}{\rho}\frac{\partial \overline{p_{wave}}}{\partial x} \tag{B.29}$$

For the free-stream, where $\tilde{u}$ and $\tilde{w}$ are 90 degrees out of phase, the second radiation stress averaged over the wave period ( $\overline{\tilde{u}\tilde{w}}$ ) is zero as well. In the wbbl, this term ($\overline{\tilde{u}\tilde{w}}$) causes Longuet-Higgins streaming.

To now solve the radiation stress, the equation will be further simplified. First the time averaged velocities are neglected, because these velocities are small for small amplitude waves:

$$\frac{\partial}{\partial x}[\rho\overline{\tilde{u}^2} + \overline{p_{wave}}] + \frac{\partial}{\partial z}[\rho\overline{\tilde{u}\tilde{w}}] = -\frac{\partial p}{\partial x} \tag{B.30}$$

Second the vertical velocities can be neglected for shallow water:

$$\frac{\partial}{\partial x}[\rho\overline{\tilde{u}^2} + \overline{p_{wave}}] = -\frac{\partial p}{\partial x} \tag{B.31}$$

To write the equation in terms of radiation stress both sides are now integrated over z:

$$\frac{\partial}{\partial x}[\overline{\int_{z_b}^{\eta} \rho\tilde{u}^2 \, dz} + \overline{\int_{z_b}^{\eta} p_{wave} \, dz}] = -\frac{\partial \int p dz}{\partial x} \tag{B.32}$$

$$\frac{\partial}{\partial x}[S_{xx}] = -\frac{\partial \eta}{\partial x} \tag{B.33}$$

$S_{xx}$ is the radiation stress in cross-shore direction (Equation B.34) [Bosboom and Stive, 2015]. The radiation stress consists of two parts: a horizontal velocity and a pressure part, the latter related to the horizontal particle acceleration. Since pressure works in all directions, there is also a radiation stress in alongshore direction (Equation B.35). And since linear wave theory assumes non-viscous flows, there is no perpendicular momentum transport (Equation B.36). Integrated to the $2^{nd}$ order and wave-averaged, the radiation stresses can be written in terms of wave energy. Note that momentum and energy progress with the group velocity, but the relationship between the two is the phase velocity.

$$S_{xx} = \overline{\int_{z_b}^{\eta} (\rho u_x \cdot u_x + p_{wave}) dz} = nE + (n - \frac{1}{2})E \tag{B.34}$$

$$S_{yy} = \overline{\int_{z_b}^{\eta} p_{wave} dz} = 0 + (n - \frac{1}{2})E \tag{B.35}$$

$$S_{xy} = S_{yx} = 0 \tag{B.36}$$

### B.3.3. Radiation stress in the nearshore

In the nearshore influence shoaling and wave breaking the radiation stress (Equation B.29). Since radiation stress is related to wave height, shoaling increases radiation stress and breaking decreases radiation stress. Radiation stress is related to wave height through orbital velocity ($\overline{\tilde{u}^2}$ in Equation B.29).

Assuming conservation of momentum and including the fact that there is no mass exchange at the shoreline (bounded situation), the change in radiation stress is balanced by a water level gradient (Equation B.37). The increase of radiation stress due to shoaling causes a set-down. The decrease of radiation stress in the

surf-zone causes a set-up (Figure B.4) [Bosboom and Stive, 2015]. The change in radiation stress is called the wave force.

$$\frac{dQ_x}{dt} = -\frac{\partial S_{xx}}{\partial x} - \rho g(\eta - z_b)\frac{\partial \overline{\eta}}{\partial x} = 0 \tag{B.37}$$

In other words: wave skewness causes onshore acceleration of the water particles, because the maximum onshore orbital velocity increases. Due to the quadratic relation between the wave momentum and velocity, the wave-averaged momentum increases while wave-averaged velocity is still (around) zero. Therefore this acceleration needs 'a push'. This push is given by the pressure force of the set-down. For the set-up this happens in the opposite direction.

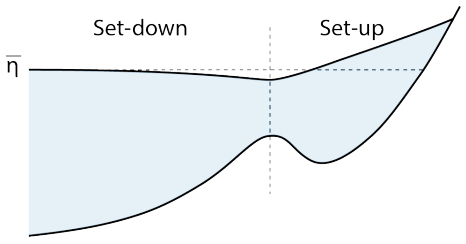


Figure B.4: Set-down and set-up

# C

# Sediment transport

## C.1. Advection-diffusion equation

The concentration profile is described with the advection-diffusion equation. A possible solution for the concentration profile is the Rouse profile. The terms in the 2D-advection-diffusion equation (Equation C.1) [Henderson et al., 2004, p.5] are organised as: storage + advection = diffusion (sink).

$$\frac{\partial c}{\partial t} + u\frac{\partial c}{\partial x} + (w - w_s)\frac{\partial c}{\partial z} = \frac{\partial}{\partial z}\left(\nu\frac{\partial c}{\partial z}\right) \tag{C.1}$$

## C.2. Sediment grain forces

Formulas per grain for spherical grains [Graaff, 2009, p.57]:

Gravity force (Figure C.1c)

$$F_G = (\rho_s - \rho) \cdot g \cdot \frac{\pi}{6} D^3 \tag{C.2}$$

Drag force (Figure C.1d)

$$F_D \approx c_D \cdot \frac{1}{2}\rho u^2 \cdot \frac{\pi}{4} D^2 \tag{C.3}$$

Lift force (Figure C.1c)

$$F_L \approx c_L \cdot \frac{1}{2}\rho u^2 \cdot \frac{\pi}{4} D^2 \tag{C.4}$$

Friction with other grains (Figure C.1d)

$$F_F = \mu * F_N \tag{C.5}$$

The drag force is caused by friction of the horizontal flow on the grains (skin friction and sub pressure behind the grain). The contraction of the fluid lines around the grain gives the lift force. In these formulas $c_D$ and $c_L$ are the drag and lift coefficients. Initiation of motion starts when the moment around the highest downstream contact point becomes positive and the grain starts to roll. The Shields parameter is the drag force over the gravity force.

These equations describe the forces due to a flow velocity. Orbital or turbulent velocities give similar equations, which lead to wave driven sediment transport.

## C.3. Shields and Sleath parameter

The initiation of motion can be calculated with the Shields parameter or a combination of the Shields and Sleath parameter. Figure C.2 shows the wave velocity, acceleration and combinations of these to investigate the pattern of the Shields parameter, Sleath parameter or a combination in waves.

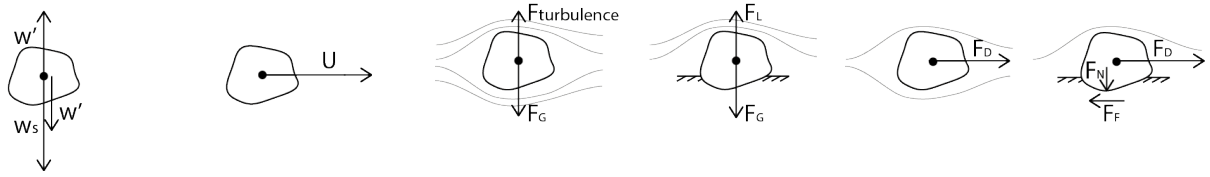


(a) Vertical velocities (b) Transporting velocities (c) Vertical forces (d) Horizontal forces

Figure C.1: Velocities and forces on sand particles in the flow or on the bottom. For waves the orbital velocities can be added.

### C.3.1. Shields (velocity)

Incipient motion is traditionally parametrized with the Shield parameter (Equation C.6) [Shields, 1936]. This ratio of shear stress (mobilizing force) over gravity (stabilizing force) represents the vertical shear stress gradient over a single grain thickness. The layer starts to move when a critical limit is exceeded. This limit is given in the Shields curve.

$$\theta(t) = \frac{\tau_b(t)}{(\rho_s - \rho)gD_{50}} = \frac{\rho u_*^2}{(\rho_s - \rho)gD_{50}} \sim \frac{u^2}{(\rho_s - \rho)gD_{50}} \tag{C.6}$$

For waves the grain roughness Shields parameter can be calculated (Equation C.7) [Nielsen, 1992].

$$\theta = \frac{1/2 f_{2.5}(A\omega)^2}{(\rho_s/\rho - 1)gd}, \qquad f_{2.5} = \exp\left\{[5.213\left(\frac{2.5d_{50}}{A}\right)^{0.194} - 5.977]\right\} \tag{C.7}$$

At higher shear stresses, the thickness of the sheet flow layer (around 0.01 meter [Henriquez, 2016]) seems to linear increase with the Shield parameter [Dohmen-Janssen and Hanes, 2005].

### C.3.2. Sleath (pressure gradient)

The non-dimensional parameter for the horizontal pressure gradient is the Sleath parameter in equation C.8 [Sleath, 1999]. The Sleath parameter is the ratio of inertial forces to gravitational forces. According to linear wave theory the non linear part of the pressure gradient can be neglected (Equation C.8).

$$S(t) \equiv \frac{p_x(t)}{(\rho_s - \rho)g} = \frac{\rho\left(\frac{\partial u_\infty}{\partial t} + u_\infty \frac{\partial u_\infty}{\partial t}\right)}{(\rho_s - \rho)g} \sim \frac{\rho \frac{\partial u_\infty}{\partial t}}{(\rho_s - \rho)g} \tag{C.8}$$

## C.4. Empirical sediment transport

### C.4.1. Empirical sediment transport formulas

There are many emperical formulas that describe the wave-driven sediment transport. Most well known formulas are quasi-steady or semi-unsteady. Quasi-steady formulas give the dimensionless transport as function of the Shield parameter (ea. Bagnold [1966], Bailard [1981], Ribberink [1998]).

For bed load transport often an instantaneous response is assumed, which is valid for coarse sediment that stays close to the bed (section 2.4.6.6). When assuming an instantaneous response, in all sediment formulas the sediment transport relates to a power of the velocity (Equation C.9), in which $m$ = 1.5-2 and $n$ = 3-4. For sinusoidal waves the wave-averaged transport is zero, but for skewed waves it is positive (see section 2.4.6.1). Due to this higher order, a small mean current can have important on skewness induced sediment transport. $\overline{\tilde{u}^3}$ can differ significantly from $\overline{(\overline{u} + \tilde{u})^3}$. Often, waves stir up the sediment and additional currents transport it. Also net wave currents, like streaming, can therefore have an important influence on wave-induced sediment transport.

$$\overline{S} \sim \overline{\tau_{c,w}|\tau_{c,w}|^{m-1}} \sim \overline{u|u|^{n-1}} \tag{C.9}$$

A quasi-steady approach is the energetics approach Bagnold [1966], Bailard [1981]. The energetics approach is based on the assumption that the fluid has to deliver work to keep the sediment in motion.

Semi-unsteady formulas include a phase-lag parameter, which is the ratio of sediment settling time and wave period [Dibajnia and Watanabe, 1998, Dohmen-Janssen, 1999].

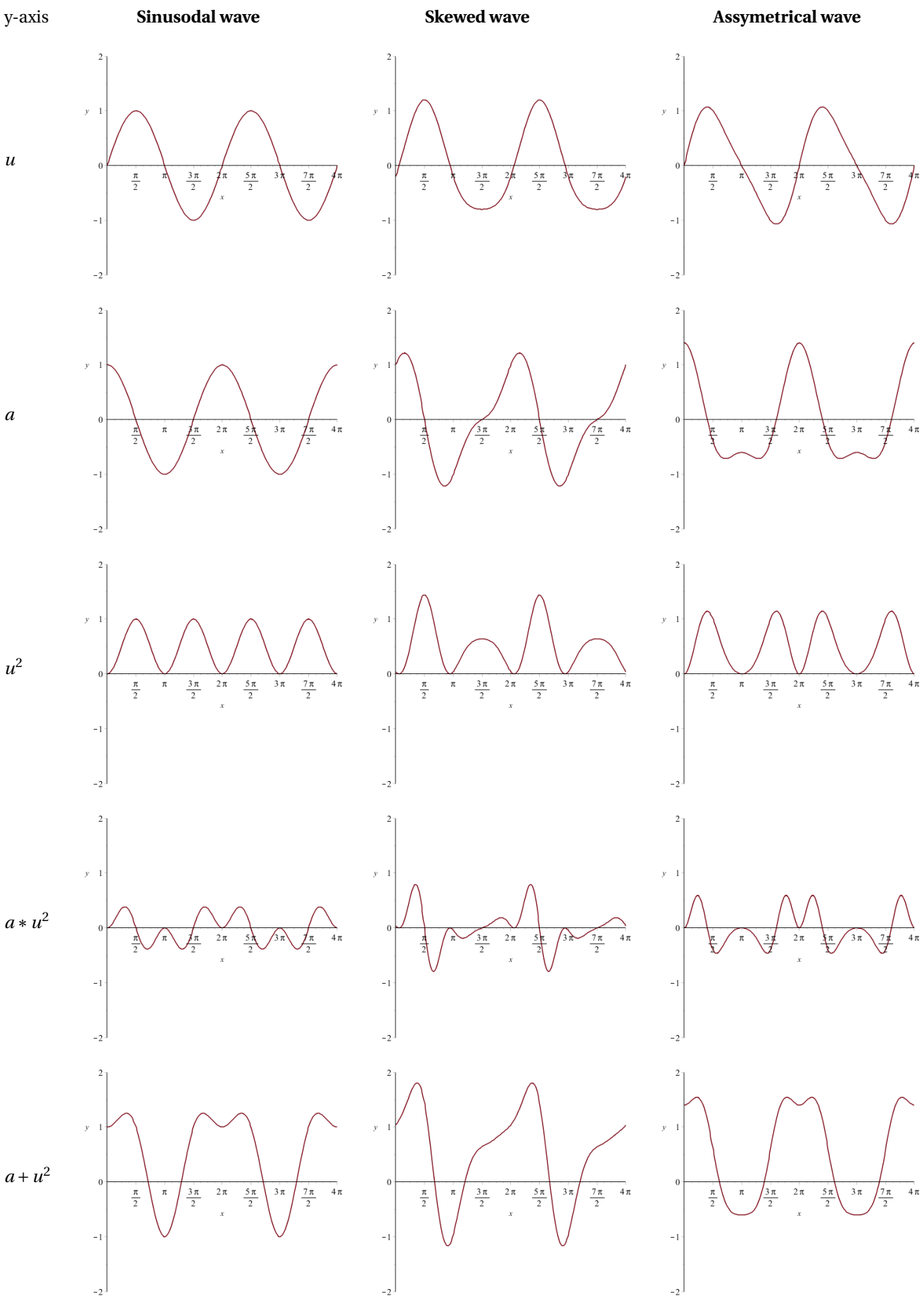


Figure C.2: Wave velocity, acceleration and combinations

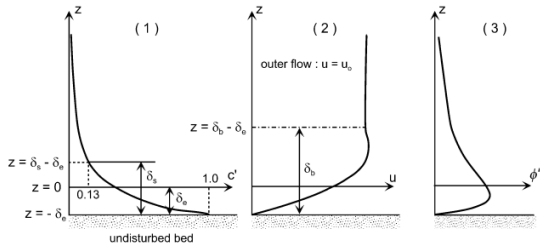


Figure C.3: Definition sketch sheet flow [O'Donoghue and Wright, 2004b, fig.1]

Unsteady models (ea. Ribberink and Al-Salem,1995) model the time-dependent flow velocity and sediment concentration with the momentum equation and advection-diffusion equation [Dohmen-Janssen, 1999].

## C.4.2. Bottom shear stress

The main cause of sediment suspension is the bottom shear stress. Shear stress acts between the sediment particles and the orbital velocities (Equation C.11). The shear stress depends bed roughness and the amount of turbulence in the flow (Reynolds number and $\epsilon$), because turbulence influences the velocity gradient close to the bottom (Figure C.4b). Equation C.10 describes the shear stress in case of a current [Heijboer, 1988, p.11]. For waves the wave friction factor, $f_w$, is defined to relate the shear stress to the orbital velocity (Equation C.11) [Dohmen-Janssen, 1999, p.10]. This friction factor depends on the orbital velocity.

Empirical formulas use bottom shear stress as measure of sediment suspension and describe a quadratic relation between bottom shear stress and the horizontal velocities. This quadratic relation between concentration can be explained with classical mechanics. From classical mechanics we know that shear stress depends on the normal force ($F_f = \mu F_N$). The normal force between sand particles and the bed is determined by the lift forces that result from horizontal velocities ($u$) next to the amount of turbulence ($w'$) and the fall velocity ($w_s$) (Appendix C.2). Hence, the higher the orbital velocities, the higher the lift force and the less shear stress is required to move the grains. Therefore shear stress is non-linearly related to orbital velocities. Because sediment transport is concentration times velocity, the sediment transport relates to the third order velocities.

Sheet flow influences the bed roughness [Dohmen-Janssen, 1999]. The roughness height is in the order of the sheet flow thickness. A thicker sheet flow increases flow resistance through inter-granular shear stress, the inertia of the grains and damping of the turbulence above the sheet flow layer [Dohmen-Janssen, 1999, p.204]. Therefore shear stress could be divided in a fluid and an inter-granular component [Bagnold, 1966].

$$\tau(z) = \rho \nu_f \frac{du}{dz} \tag{C.10}$$

$$\tau_{b,max} = \frac{1}{2} \rho f_w \hat{u} |\hat{u}| \tag{C.11}$$

A friction factor, $f$, usually expresses the connection between the velocities and the bottom shear stress.Bed roughness and the amount of turbulence cause this connection between the near-bed orbital velocities and the bottom shear stress [Dohmen-Janssen, 1999, p.11].

Assuming a logarithmic velocity profile, the current shear stress can be calculated with:

$$\tau_b = \frac{1}{2} \rho f_c \hat{u}_b^2 \tag{C.12}$$

With the current friction factor:

$$f_c = 2\kappa^2 \left[ \ln\left( \frac{z_b}{z_0} \right) \right]^{-2} \tag{C.13}$$

Calculation of the maximum shear stress during a wave cycle [Jonsson, 1966].

$$\hat{\tau}_b = \frac{1}{2} \rho f_w \hat{u}^2 \tag{C.14}$$

With wave friction factor [Swart, 1974]:

$$f_w = \exp\left\{\left(-5.997 + 5.213\left(\frac{k_s}{a}\right)^{0.194}\right)\right\} \tag{C.15}$$

Measurements with mobile bed and irregular waves result in equation C.16 [Madsen et al., 1990, Smyth and Hay, 2002], in which $\theta_d$ is the grain roughness Shields parameter and $\theta_c$ the critical shear stress (of initiation of grain motion).

$$f_w = 0.29\left(\frac{\theta_d}{\theta_c}\right)^{-1.5}, \qquad 1.2 < \frac{\theta_d}{\theta_c} < 3 \tag{C.16}$$

The upper limit of $f_w$ is 0.3 [Jonsson, 1966]. For a fully developed rough turbulent regime, wave friction factor is based on the relative roughness height $k_s/a$ [Dohmen-Janssen, 1999, p.11].

The current and wave friction factor can be combined by [Madsen and Grant, 1976]:

$$f_{cw} = \alpha \cdot f_c + (1-\alpha)\cdot f_w, \qquad \text{with} \qquad \alpha = \frac{\hat{u}_b}{\hat{u}+\hat{u}_b} \tag{C.17}$$

### C.4.3. Boundary layer thickness

There are different definitions of the wave bottom boundary layer thickness, here some examples will be given (ea. Jonsson 1966, Kajiura 1968, Sleath 1987). All equations are for smooth laminar flow [Nielsen, 1992, p.29].

In general terms:

$$\delta \propto \sqrt{\nu_t T} \tag{C.18}$$

**Stokes**

Stokes length is used as laminar length scale: [Nielsen, 1992]

$$\delta_s = \sqrt{\frac{2\nu}{\omega}} \tag{C.19}$$

**Sleath**

Sleath [1999] defines the top of the wbbl as the level were the velocity defect equals 5 % fo the free-stream velocity. The thickness becomes [Dohmen-Janssen, 1999]:

$$\delta_{0.05} = 0.26 \cdot k_s \left(\frac{a}{k_s}\right)^{0.70} \approx 3\sqrt{\frac{2\nu}{\omega}} \tag{C.20}$$

**Kajiura**

Kajiura [1968] also has a quite thin layer:

$$\delta_d = \frac{1}{A\omega} Max\left\{\int_0^\infty (u_\infty - u)dz\right\} \approx \sqrt{\frac{\nu}{\omega}} \tag{C.21}$$

**Jonsson**

Jonsson [1966] defined the top of the boundary layer as the minimum elevation where $u$ is $u_\infty$ (Figure C.4a), giving a quite thin boundary layer [Nielsen, 1992, p.29]. For smooth laminar flow the equation becomes:

$$\delta_j = \frac{1}{2}\pi\sqrt{\frac{2\nu}{\omega}} \tag{C.22}$$

**Practical limit of wbbl**

A practical limit of the wbbl is the level where the velocity defect is 1% of the free-stream velocity.

$$\delta_{0.01} \approx 4.5\sqrt{\frac{2\nu}{\omega}} \tag{C.23}$$

As shown in Figure C.4a, the relation between the different levels is [Nielsen, 1992, p.30]:

$$\delta_{0.01} \approx 1.5\delta_{0.05} \approx 3\delta_j \approx 4.5\delta_s \approx 6.4\delta_d \tag{C.24}$$

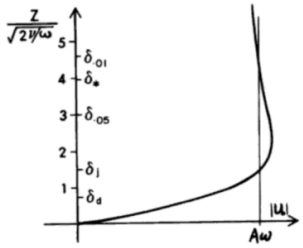


(a) Different thicknesses of the wbbl [Nielsen, 1992] (p.30)

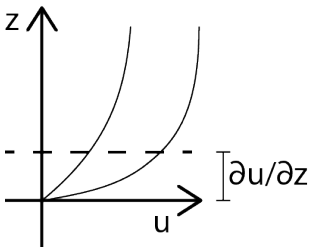


(b) Velocity gradient close to the bottom

Figure C.4: Sediment transport processes

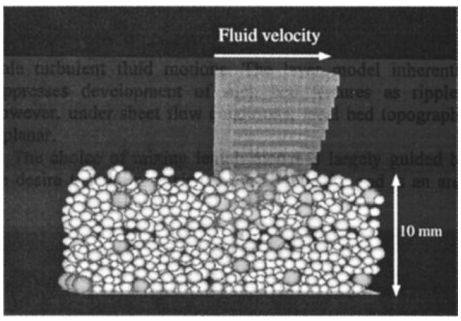


Figure C.5: Schematic picture of discrete particle simulation [Drake and Calantoni, 2001, p.19861]

### C.4.4. Sediment modelling

Modelling intra-wave sediment transport is very time consuming. To practically model sediment transport, the effect of waves should be taken into account without modelling intra-wave transport. Therefore sediment transport formulas, bed load and/or suspended load, can be added to a numerical wave model to calculate the wave driven transport. To study sediment transport it is interesting to actually model the sand particles. Discrete particle computation (Figure C.5) is therefore useful for research.

The acceleration-based transport (pressure force) is included in the energetics model by including an empirical acceleration term with equation C.25 [Hoefel, 2003].

$$Q_{acc}(x) = \begin{cases} K_a(a_{spike} - sgn[a_{spike}] * a_{crit}) & \text{for } |a_{spike}| \geq a_{crit} \\ 0 & \text{for } |a_{spike}| < a_{crit} \end{cases} \tag{C.25}$$

# D

# Wave driven sediment transport: equations

## D.1. Overview equations

Momentum equation in x-direction:

$$\frac{\partial \overline{u}}{\partial t}+\frac{\partial \overline{u}^2}{\partial x}+\frac{\partial \overline{uw}}{\partial z}+\frac{\partial \overline{\tilde{u}^2}}{\partial x}+\frac{\partial \overline{\tilde{u}\tilde{w}}}{\partial z}+\frac{\partial \overline{u'^2}}{\partial x}+\frac{\partial \overline{u'w'}}{\partial z}=-\frac{1}{\rho}\frac{\partial p}{\partial x}-\frac{1}{\rho}\frac{\partial \overline{p_{wave}}}{\partial x} \tag{D.1}$$

Momentum equation in z-direction:

$$\frac{\partial \overline{w}}{\partial t}+\frac{\partial \overline{uw}}{\partial x}+\frac{\partial \overline{w}^2}{\partial z}+\frac{\partial \overline{\tilde{u}\tilde{w}}}{\partial x}+\frac{\partial \overline{\tilde{w}^2}}{\partial z}+\frac{\partial \overline{u'w'}}{\partial x}+\frac{\partial \overline{w'^2}}{\partial z}=-\frac{1}{\rho}\frac{\partial p}{\partial z}-\frac{1}{\rho}\frac{\partial \overline{p_{wave}}}{\partial z} \tag{D.2}$$

Advection-diffusion equation:

$$\frac{\partial c}{\partial t}+\overline{u}\frac{\partial c}{\partial x}+\overline{\tilde{u}\frac{\partial c}{\partial x}}+(\overline{w}-w_s)\frac{\partial c}{\partial z}+\overline{(\tilde{w}-w_s)\frac{\partial c}{\partial z}}=\frac{\partial}{\partial z}\left(\nu\frac{\partial c}{\partial z}\right) \tag{D.3}$$

## D.2. Sediment transport: current related and wave related part

To calculate the mean sediment transport (Equation D.4) the velocity and concentration can be decomposed in mean and oscillating components (Equation D.5). The time-average of the oscillatory component is per definition zero (Equation D.6). When multiplying (Equation D.7) and time-averaging (Equation D.8), all terms with one oscillating term are zero. With this two sediment transport components remain: the current related sediment transport ($\overline{u}\cdot\overline{c}$) and the time-averaged wave related sediment transport ($\overline{\tilde{u}\cdot\tilde{c}}$) (Equation D.9).

$$S=c\cdot u \tag{D.4}$$

$$\begin{aligned} u&=\overline{u}+\tilde{u}\\ c&=\overline{c}+\tilde{c}\end{aligned} \tag{D.5}$$

$$\begin{aligned} \overline{\tilde{u}}&=0\\ \overline{\tilde{c}}&=0\end{aligned} \tag{D.6}$$

$$S=uc=\overline{u}\cdot\overline{c}++\overline{u}\cdot\tilde{c}+\tilde{u}\cdot\overline{c}+\tilde{u}\cdot\tilde{c} \tag{D.7}$$

$$\overline{S}=\overline{uc}=\overline{\overline{u}\cdot\overline{c}++\overline{u}\cdot\tilde{c}+\tilde{u}\cdot\overline{c}+\tilde{u}\cdot\tilde{c}} \tag{D.8}$$

$$\overline{uc}=\overline{u}\cdot\overline{c}+\overline{\tilde{u}\cdot\tilde{c}} \tag{D.9}$$

It is also possible to only decompose the velocity (Equation D.10):

$$\overline{S}=\overline{\overline{u}\cdot c}+\overline{\tilde{u}\cdot c} \tag{D.10}$$

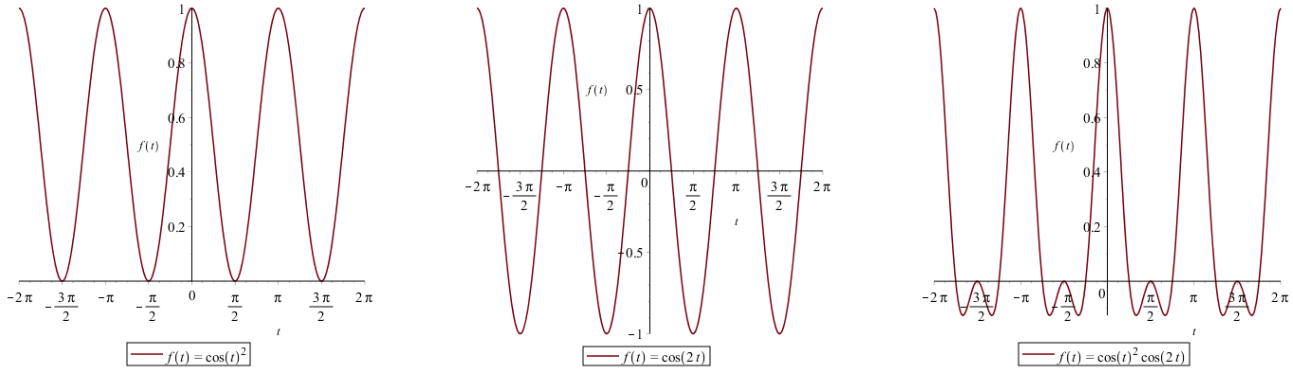


(a) $\cos^2(t)$ (b) $\cos(2t)$ (c) $\cos^2(t)+\cos(2t)$

Figure D.1: Trigonometry: the same frequency of $\cos^2(t)$ and $\cos(2t)$ aligns the positive peak with 1 and the negative peak with 0

## D.3. Skewness

This section explains the analytical solution for sediment transport due to skewness. Equation D.11 describes the skewed velocity signal and Equation D.12 the calculation of sediment transport. The higher order component in the velocity causes a time-averaged sediment transport, because $\cos^2(t)$ has the same frequency as $\cos(2t)$ (Equation D.13, Figure D.1). With a constant concentration skewness does not give sediment transport (section D.3.1). If it is assumed that with skewness the concentration stays sinusoidal, this results in a small sediment transport (section D.3.2). However it is more probable that skewness does affect the concentration and that increases the time-averaged sediment transport (section D.3.3). Hence the more aligned the peak of the concentration is with the peak of the velocity, the more sediment transport occurs.

$$\tilde{u} = \cos(t) + \cos(2t) \tag{D.11}$$

$$\tilde{S} = \tilde{u} \cdot \tilde{c} \tag{D.12}$$

$$\cos^2(t) = \frac{1}{2}\cos(2t) + \frac{1}{2} \tag{D.13}$$

### D.3.1. Step 1: skewed velocity with constant concentration

$$\tilde{c} \propto 1 \tag{D.14}$$

$$\overline{\tilde{S}} = \overline{(\cos(t) + \cos(2t)) \cdot 1} = 0 \tag{D.15}$$

### D.3.2. Step 2: skewed velocity with sinusoidal concentration

Concentration without influence of skewness:

$$\tilde{c} \propto u^2_{sinusoidal} = \cos^2(t) - \frac{\pi}{2} \tag{D.16}$$

Sediment transport ( Figure D.2c ):

$$\tilde{S} \propto (\cos(t) + \cos(2t)) \cdot [\cos^2(t) - \frac{\pi}{2}] \tag{D.17}$$

When averaging over time all sinusoidal terms to an uneven power are zero:

$$\overline{\tilde{S}} = \overline{cos^3(t) + \cos^2(t)\cos(2t)\frac{\pi}{2}(\cos(t) + \cos(2t))} = \overline{\cos^2(t)\cos(2t)} \tag{D.18}$$

Substituting Equation D.13:

$$\overline{\tilde{S}} = \overline{\left[\frac{1}{2}\cos(2t) + \frac{1}{2}\right]\cos(2t)} = \overline{\left[\frac{1}{2}\cos^2(2t) + \frac{1}{2}\cos(2t)\right]} = \left[\frac{1}{4}\pi + 0\right] = \frac{1}{4}\pi \tag{D.19}$$

Hence skewness results in a small time-averaged sediment transport of $\pi/4$.

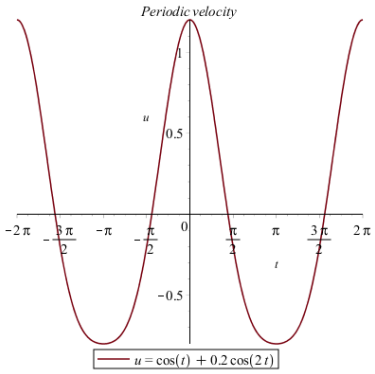


(a) Horizontal velocity, $\tilde{u}$

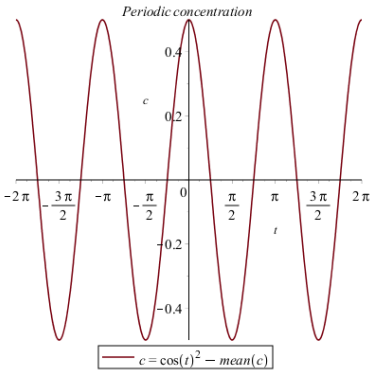


(b) Option 1: concentration, $\tilde{c}$

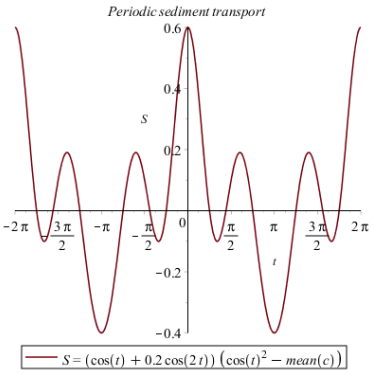


(c) Option 1: Sediment transport, $\tilde{S}$

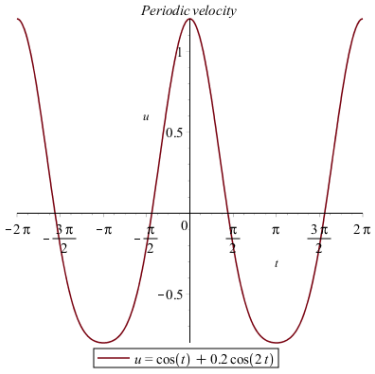


(d) Horizontal velocity, $\tilde{u}$

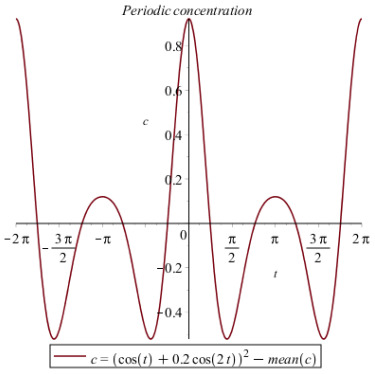


(e) Option 2: concentration, $\tilde{c}$

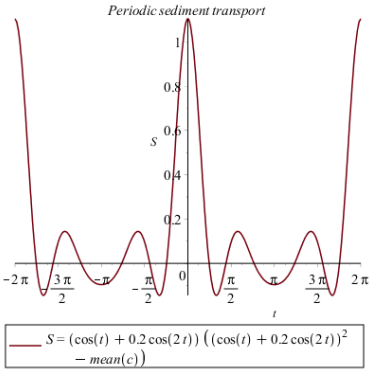


(f) Option 2: Sediment transport, $\tilde{S}$

Figure D.2: Graphically calculating sediment transport

### D.3.3. Step 3: skewed velocity with skewed concentration

Concentration based on skewed velocity:

$$c \propto u_{skewed}^2 = (\cos(t) + \cos(2t))^2 - 1 \tag{D.20}$$

Sediment transport ( Figure D.2f ):

$$\tilde{S} \propto (\cos(t) + \cos(2t)) \cdot [(\cos(t) + \cos(2t))^2 - 1] \tag{D.21}$$

When averaging over time all sinusoidal terms to an uneven power are zero:

$$\overline{\tilde{S}} = \overline{(\cos(t) + \cos(2t)) \cdot [(\cos(t) + \cos(2t))^2 - 1]} = \overline{3\cos^2(t)\cos(2t)} \tag{D.22}$$

$$\overline{\tilde{S}} = \overline{3\left[\frac{1}{2}\cos(2t) + \frac{1}{2}\right]\cos(2t)} = \overline{3\left[\frac{1}{2}\cos^2(2t) + \frac{1}{2}\cos(2t)\right]} = 3\left[\frac{1}{4}\pi + 0\right] = \frac{3}{4}\pi \tag{D.23}$$

If the concentration depends on the skewed velocity, the higher harmonic term is included in the third power. With this the time-averaged sediment transport becomes three times larger than the time-averaged sediment transport with independent concentration.

# E

# Mobile bed experiment

*This appendix is written by Martijn Henriquez:*

Two tests were conducted in a medium-sized wave flume using synthetic sediment. The first part of a test consisted of an erosive wave condition where a single bar profile developed. This was followed with an accretive wave condition. After generating the accretive wave condition the bar disappeared rapidly in the first test and during the second test the bar migrated onshore.

The test were compared to prototype cases conducted in the Großer Wellenkanal (GWK) in Hannover and during the Duck94 field experiment. Morphological evolution that was dominantly forced by intra-wave transport was similar in prototype and model. The scale relation for net bedload by waves predicts the correct order of magnitude. However, the physical model experienced lower net onshore sediment transports. Including velocity skewness in conventional bedload formula estimated the net bedload within a factor of 10.

## E.1. DUT wave flume experiments

### E.1.1. Facility

The experiments took place in September 2008 and April-May 2010, in a wave flume of the hydraulic laboratory of the Faculty of Civil Engineering and Geosciences at the Delft University of Technology (DUT) in the Netherlands. The flume had a length of 40 m, a width of 0.8 m and a height of 1.0 m. The piston-type wave maker was equipped with second-order steering and active reflection compensation. At the back of the flume a concrete slope was present with a single bar profile of approximately 1:20 that would be fully covered by the sediment.

### E.1.2. Sediment

The sediment for the experiment was blast media from Maxi-Blast Inc and the type was: Enduro Grade 4. The material was a thermoset polyester polymer and the shape was granular. The specific density $\rho_s$ was $1200\,\mathrm{kg\,m^{-3}}$. The median diameter $d_{50}$ was 524 µm, the $d_{10}$ was 439 µm and the $d_{90}$ was 598 µm.

### E.1.3. Wave conditions

Four wave conditions were used for the experiment that can be divided in erosive- and accretive conditions. The waves were generated using a standard JONSWAP spectrum. Second-order steering and active reflection compensation were switched on. The initial bottom profile, incident wave height, wave period and sub-test duration for the different sub-tests are presented in Table E.1.

The starting profile for test 1 was a plane slope of 1:15 and the mean water depth was 0.42 m. First, the erosive wave condition was generated for 30.6 h. Hereafter, the accretive wave condition was generated for 15.3 h. The starting profile test 2 was also a plane slope of 1:15 except the mean water depth was 0.50 m. First, the erosive wave condition was run for 42 h to create a stable profile. Hereafter, the accretive- and erosive wave conditions were alternated resulting in 9 accretive sub-tests.

The time series of a wave file had a length of 12.6 min, 16.5 min, 15 min and 15 min for sub-test 1a, 1b, 2a and 2b, respectively. At the end of the time series, the wave maker automatically repeated the series. Wave

| Test code | Initial profile | $H_{m0}$ [m] | $T_p$ [s] | $h$ [m] | Duration [h] |
|---|---|---|---|---|---|
| 1a | plane slope 1:15 | 0.100 | 1.80 | 0.42 | 30.6 |
| 1b | result of 1a | 0.060 | 2.37 | 0.42 | 15.3 |
| 2a | plane slope 1:15 | 0.145 | 1.80 | 0.50 | 42 |
| 2b | result of 2a | 0.085 | 1.80 | 0.50 | 1.05 |
| 2c | result of 2b | 0.145 | 1.80 | 0.50 | 2.14 |
| 2d | result of 2c | 0.085 | 1.80 | 0.50 | 1.27 |
| 2e | result of 2d | 0.145 | 1.80 | 0.50 | 3.11 |
| 2f | result of 2e | 0.085 | 1.80 | 0.50 | 1.01 |
| 2g | result of 2f | 0.145 | 1.80 | 0.50 | 3.01 |
| 2h | result of 2g | 0.085 | 1.80 | 0.50 | 1.01 |
| 2i | result of 2h | 0.145 | 1.80 | 0.50 | 2.99 |
| 2j | result of 2i | 0.085 | 1.80 | 0.50 | 0.76 |
| 2k | result of 2j | 0.145 | 1.80 | 0.50 | 2.00 |
| 2l | result of 2k | 0.085 | 1.80 | 0.50 | 0.76 |
| 2m | result of 2l | 0.145 | 1.80 | 0.50 | 2.10 |
| 2n | result of 2m | 0.085 | 1.80 | 0.50 | 0.77 |
| 2o | result of 2n | 0.145 | 1.80 | 0.50 | 1.26 |
| 2p | result of 2o | 0.085 | 1.80 | 0.50 | 0.76 |
| 2q | result of 2p | 0.145 | 1.80 | 0.50 | 2.01 |
| 2r | result of 2q | 0.085 | 1.80 | 0.50 | 0.75 |

Table E.1: Test conditions of the DUT experiments.

generation was paused to measure bottom profiles and/or start a new recording of the surface elevation. A complete overview of the experimental program can be found in the Appendix.

## E.1.4. Instrumentation

Surface elevations were measured using 4 resistance type wave gauges with a sampling rate of 200 Hz. Three wave gauges were permanently positioned in the horizontal approach of the flume at a distance of 15.581 m, 15.877 m and 16.277 m from the wave board. The fourth wave gauge was positioned over the barred profile at a distance 28.916 m, 28.441 m and 29.855 m for sub-test 2b-2f, 2g-2l and 2m-2r, respectively.

The bottom profiles of test 1 were measured with a profile follower (PROVO) that has an accuracy of 0.1 mm). The shaft of the PROVO does not touch the bed and actually feels the bottom due to distortion of the electric field by the bed. The PROVO was mounted on a carriage that drove on tracks along the flume. The carriage drove with a speed of 10 cm s$^{-1}$. The starting location of the carriage was determined by an electronic switch that was activated when the carriage passes. Time, the vertical position and switch signal were recorded with a sampling rate of 500 Hz.

The bottom profiles of test 2 were measured with an echo sounder from General Acoustics, UltraLab UWS; maximum accuracy: 1 mm. The echo sounder had a maximum sampling rate of 10 hertz, however, the output was analog. The carriage drove with a speed of 2 cm s$^{-1}$. In effect, this results in a bed level update every 2 mm. Electronic spools on one of the carriage wheels generated electronic pulses to derive distance traveled. The output of the echo sounder and electronic spools were sampled with 500 Hz. The starting location of the carriage was determined by measuring the distance between carriage and wave board using a laser distance meter, the Leica Disto D3 with a maximum accuracy of 1 mm.

Erroneous points were detected and removed during post processing. Hereafter, bottom profiles were interpolated on the horizontal axis with a resolution of 1 mm.

## E.1.5. Bed level profiles

### E.1.5.1 Sub-test 1a

Figure E.1 shows the measured bottom profiles where the development of a plane slope to a single bar profile can be seen. After 30.73 h the water depth at the bar crest was 12 cm and the toe migrated 2 m offshore. Ripples were presents where the water depth was larger than 0.2 m. Ripple lengths were around 7 cm and ripple amplitudes were around 2 cm.

### E.1.5.2 Sub-test 1b

Figure E.1 shows the measured bottom profiles where the existing bar disappeared rapidly and later on large-scale bed undulations formed further inshore at $x = 31.5$ m. Ripples were presents over most of the profile. Ripple lengths were around 7 cm and ripple amplitudes were around 4 cm.

### E.1.5.3 Sub-test 2a

Figure E.2 shows the measured bottom profiles of sub-test 2a where the development of a plane slope to a single bar profile can be seen. After 36.84 h the water depth at the bar crest was 16 cm and the toe migrated 3 m offshore. Ripples appeared and disappeared over the bar depending on the local wave height. Unfortunately, the echo sounder did not capture the small-scale features as the PROVO did. The cross-sectional area of the transducer beam was probably larger than the effective area of the PROVO shaft. In addition, the sampling rate of the PROVO was an order larger.

### E.1.5.4 Sub-test 2b-2r

During test 2 the erosive- and accretive wave condition was alternated from sub-test to sub-test. This lead to subtle on- and offshore bar migration from one sub-test to the other while the overall profile was fairly stable. Figure E.3 shows the measured bottom profiles of sub-test 2b to 2f. The other sub-tests, 2g to 2r had similar results. On average, the accretive tests were run for approximately 1 h and the erosive tests for 2.5 h.

On the offshore side of the bar at $x = 26$ m the depth decreased over time. This trend was similar during both wave conditions. The long-term erosion rate of the slope at $x = 26$ m was of order $10^{-3}$ m h$^{-1}$ while the maximum erosion and accretion rate during onshore bar migration was of order $10^{-2}$ m h$^{-1}$. Thus, an order-of-magnitude difference. Also part of the long-term trend was the offshore migration of the average bar crest position.

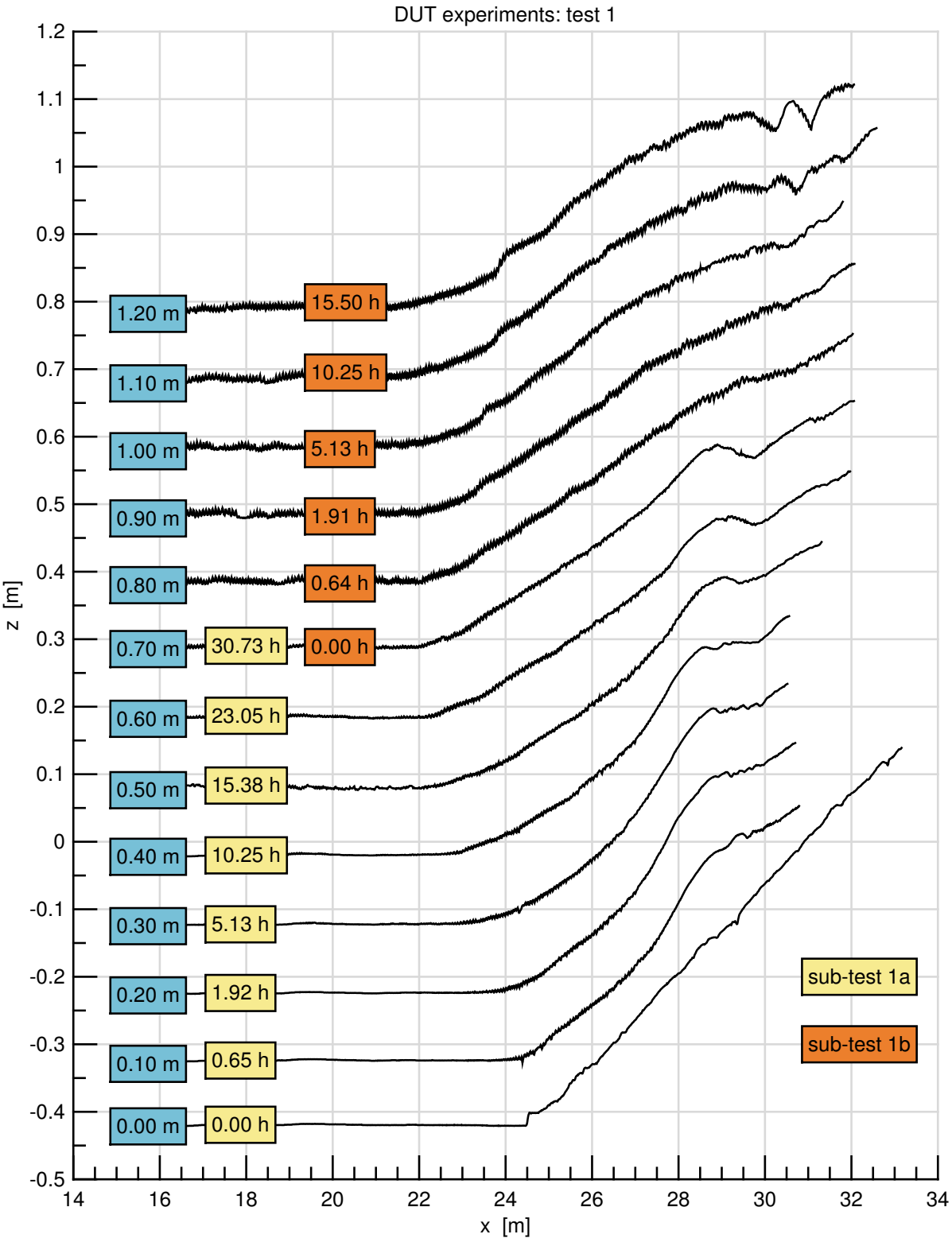


Figure E.1: Bottom profiles of test 1 of the DUT experiments. First text box from the left indicates the vertical offset and second text box the number of wave hours.

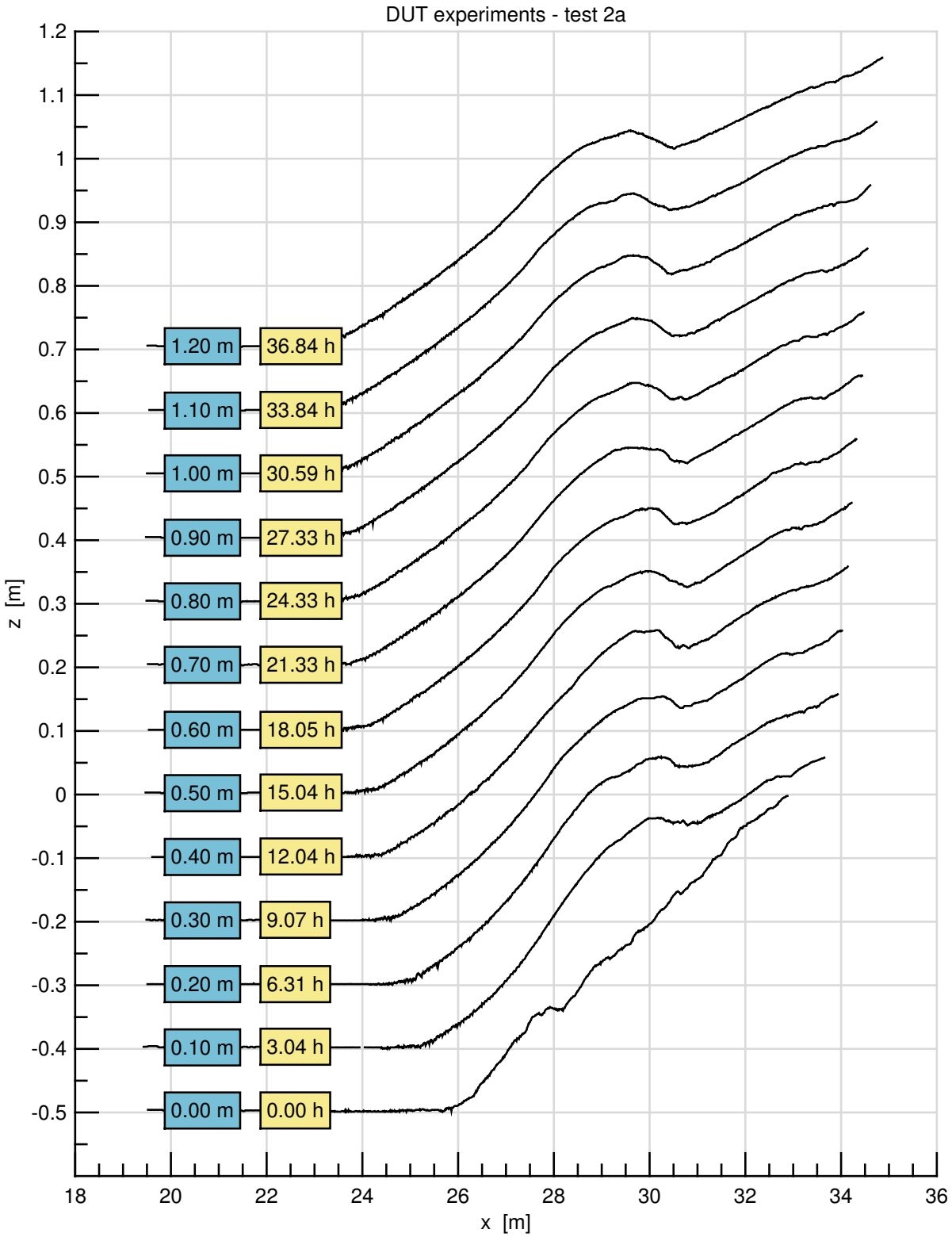


Figure E.2: Bottom profiles of test 2a of the DUT experiments. First text box from the left indicates the vertical offset and second text box the number of wave hours.

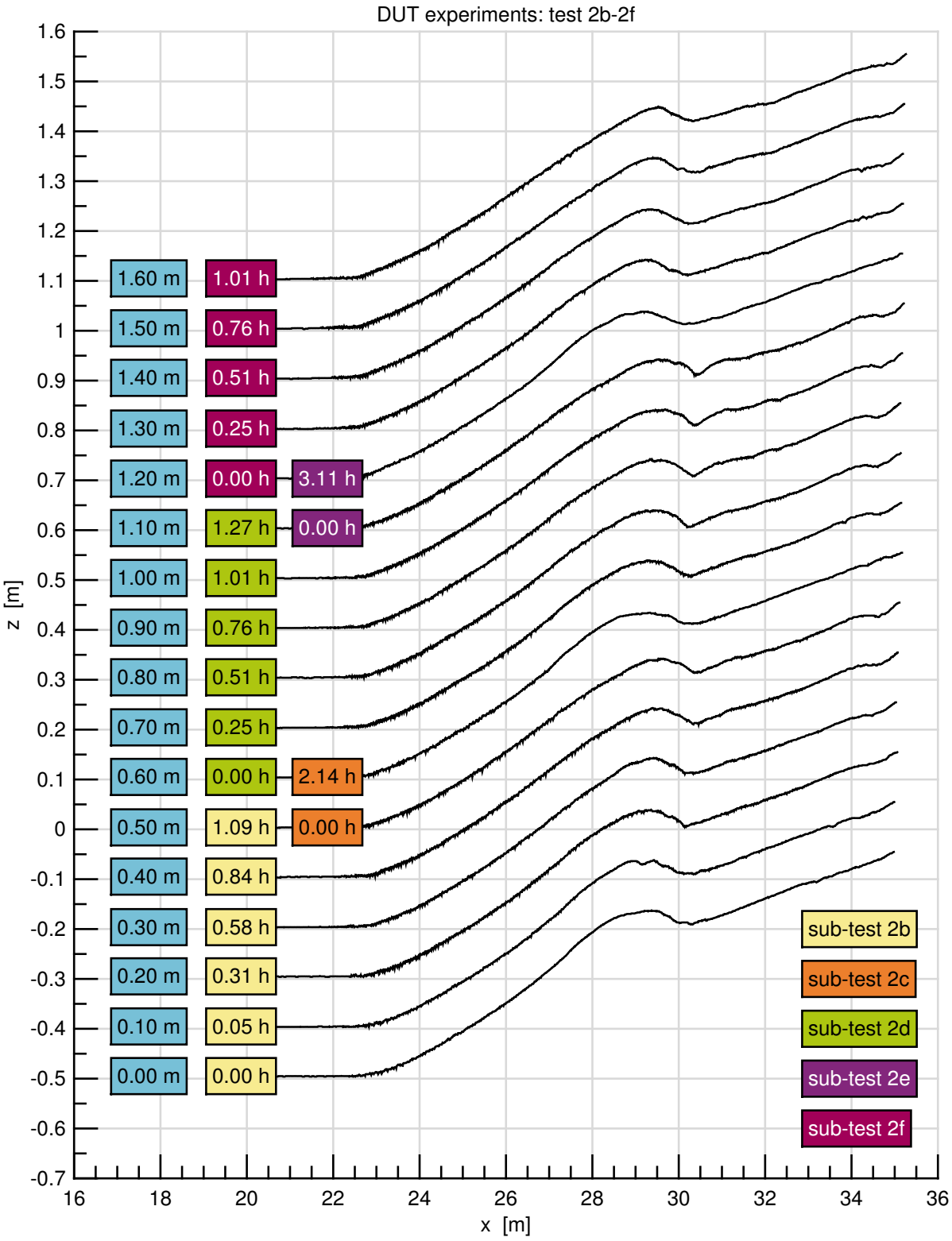


Figure E.3: Bottom profiles of test 2b-f of the DUT experiments. First text box from the left indicates the vertical offset and second or third text box the number of wave hours.

## E.2. SANDS-GWK wave flume experiments

In 2007-2008 the SANDS experiments were carried out in 3 different wave flumes: the Großer Wellenkanal (GWK) in Hannover, the Canal d'Investigació i Experimentació Marítima (CIEM) in Barcelona and the Scheldt flume of Deltares in Delft. The experiments were designed to investigate scale relations and included a mobile bed and accretive- and erosive hydrodynamic conditions. For this study we only use the results from Hannover.

The GWK has a length of 307 m, a width of 5 m and a depth of 7 m. Waves were generated by a piston-type wave maker. Bed profiles were measured with a wheel that followed the bottom (accuracy: 10 mm).

The wave condition for the erosive experiment was a JONSWAP spectrum with a peak period of 5.7 s, a significant wave height of 1.0 m and consisted of 500 waves. The wave condition for the accretive experiment was a JONSWAP spectrum with a peak period of 7.5 s, a significant wave height of 0.6 m and consisted of 500 waves.

The starting profile was a plane slope of 1:15. The erosive wave condition was run for 32.8 h. Hereafter, the accretive wave condition was run for 31.75 h.

## E.3. Duck94 field experiment

In 1994 the Duck94 field experiment was carried out at the Field Research Facility (FRF) near Duck, North Carolina, US. During the experiment an onshore bar migration occurred over the course of a few days at the end of September, see e.g. Gallagher et al. [1998], Henderson et al. [2004], Hsu et al. [2006], Ruessink et al. [2007], while the bathymetry was relatively long-shore uniform [Ruessink et al., 2001].

The bottom topography was regularly measured with the Coastal Research Amphibious Buggy (CRAB) that drove cross-shore transects. Survey lines of September 24 (08:00 EST) and 26 (12:00 EST) were interpolated on the cross-shore transect with the FRF longshore coordinate 925 m that coincided with the Elgar & Guza cross-shore array [Gallagher et al., 1998] (see Figure E.7). The survey was referenced to the National Geodetic Vertical Datum (NGVD29), which lies about 0.25 m below the mean water level at the FRF site [Plant, 1998].

The wave height and period were measured with a Waverider buoy. Over the course of the two days there was first, 40 h of bimodal sea with peak periods alternating between 7 and 10 s with an average wave height of $H_{m0} = 0.7$ m followed by 12 h of swell sea with a dropping peak period from 16 to 13 s with an average wave height of $H_{m0} = 1$ m (see Figure E.5).

From the two profiles, the bed-level change in time was derived. Using Eq. E.1 and integrating over space gives the sediment transport. Integration was done from 4 m below mean sea level. The maximum erosion rate on the bar front was $4.5 \times 10^{-7}$ m s$^{-1}$. The maximum deposition rate at the bar back was $9.5 \times 10^{-7}$ m s$^{-1}$. The maximum transport was $1.5 \times 10^{-5}$ m$^3$ m$^{-1}$ s$^{-1}$ and was 4 m before the bar crest. See Figure E.7.

## E.4. Scale effects

### E.4.1. Methodology

The scale ratio of a model represents the proportional ratio of a model feature to the same feature of the prototype (Appendix F). When comparing spatial features it is essential to have a reference point, for example, the shoreline. In this study the horizontal reference point is the bar crest position at 0 h. The vertical reference point is the still water level.

Some bottom profiles were deformed around the bar crest by the impact of large waves at the end of wave generation. The turbulence generated by a single breaking wave could temporarily cause a dent in the bar that is smoothed out after the passing of a few non-breaking waves. See for example the profile of sub-test 2b 0.05 h in Figure E.3. The bar crest position was determined by finding the maximum bottom elevation between the toe and bar trough. It must be noted that the bar crest position was sensitive to relatively small irregularities of the bed. Therefore, bottom profiles that include such a dent were not included in the analysis. Furthermore, bottom profiles were smoothed by applying a moving average over space with weights based on a hamming window with a span of 0.5 m for DUT profiles and 5 m for GWK and Duck94 profiles.

The bed level changes of a sub-test were determined by subtracting the first and last profile of a sub-test. Bed level changes of the accretive DUT tests were averaged over the nine sub-tests to give one representative bed-level change profile for test 2.

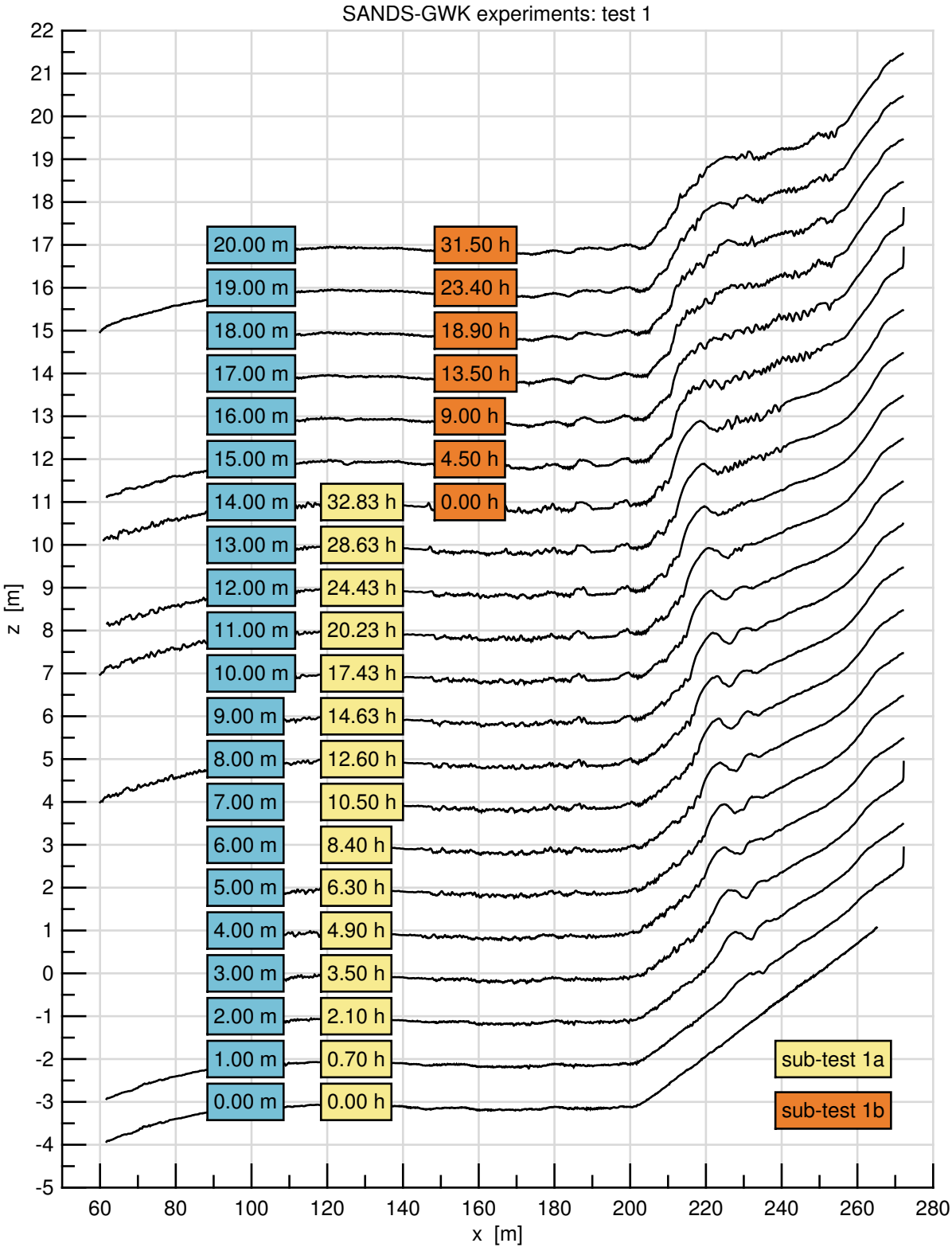


Figure E.4: Tests at GWK.

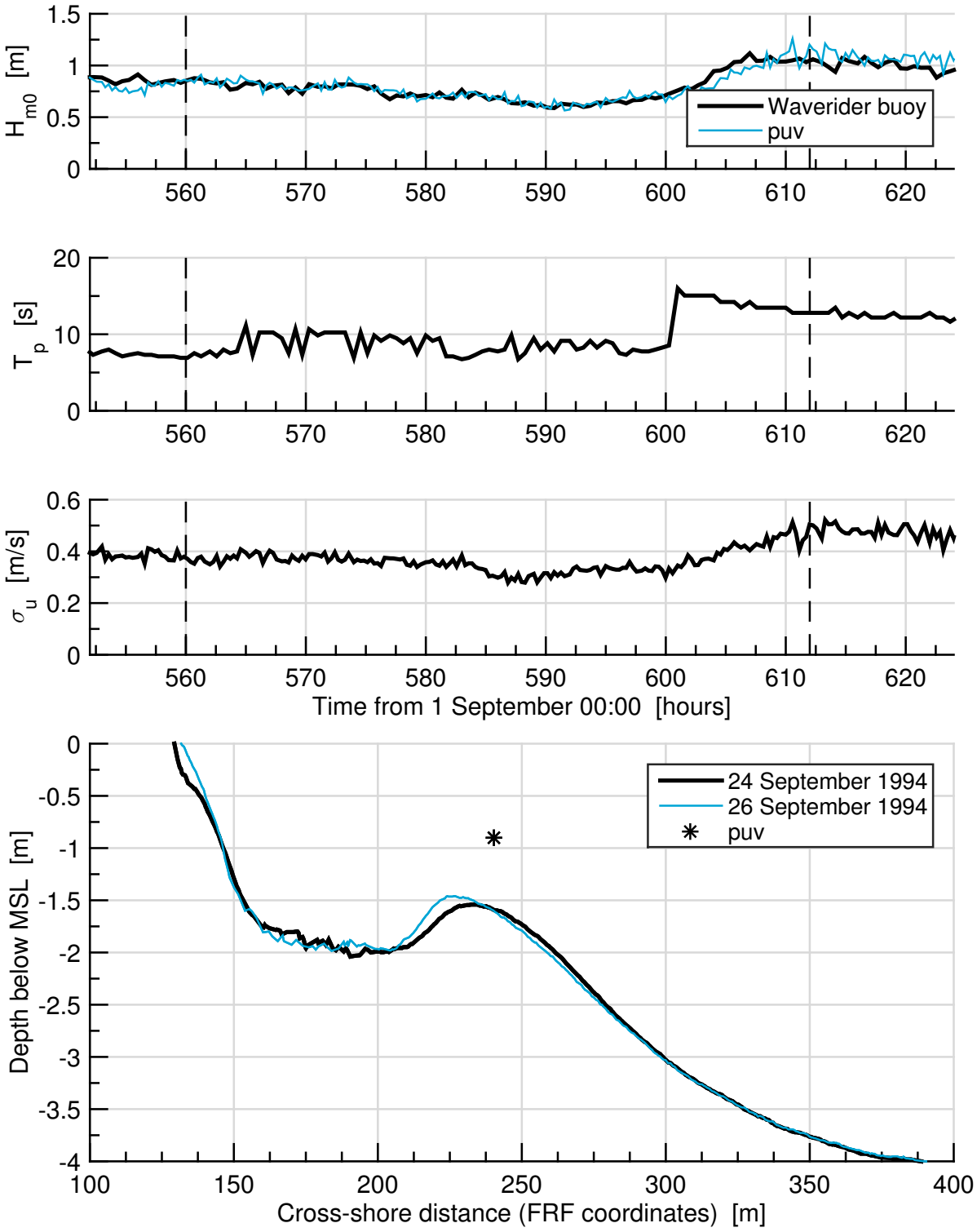


Figure E.5: Conditions during Duck94 experiment. First plot, significant wave height. Second plot, peak wave period. Third plot, standard deviation of cross-shore velocity. Fourth plot, the bottom elevation. Vertical dashed lines correspond with the times of the survey of September 24 (08:00 EST) and 26 (12:00 EST).

| Description | GWK | DUT | scale $n$ |
|---|---|---|---|
| Bottom elevation $z$ at bar crest [m] | 1.2 | 0.12 | 10 |
| Wave height $H_{m0}$ [m] | 0.6 | 0.06 | 10 |
| Peak wave period $T_p$ [s] | 7.7 | 2.37 | 3.25 |
| Grain size $d_{50}$ [µm] | 270 | 524 | 0.52 |
| Specific density $\rho_s$ [km] | 2650 | 1200 | 2.21 |
| Orbital velocity $u_{b,\infty}$ [m s$^{-1}$] | 0.79 | 0.25 | 3.16 |
| Shields number $\theta$ | 0.68 | 0.70 | 0.97 |
| Reynolds number $Re$ | 14.7 | 14.1 | 1.04 |
| Relative settling velocity $V$ | 0.64 | 0.62 | 1.04 |
| Dean number $D$ | 2.29 | 1.53 | 1.50 |
| Sleath number $S$ | 0.04 | 0.34 | 0.12 |
| Ursell number $Ur$ | 2.12 | 2.12 | 1.00 |
| Velocity Skewness at bottom $Sk_u$ | 0.73 | 0.73 | 1.00 |
| Sediment transport Eq. F.42 [m$^3$ m$^{-1}$ s$^{-1}$] | $3.0 \times 10^{-5}$ | $3.0 \times 10^{-5}$ | 1.01 |
| Erosion rate $dz/dt$ [m s$^{-1}$] | $1.0 \times 10^{-5}$ | $1.0 \times 10^{-5}$ | 1 |
| Deposition rate $dz/dt$ [m s$^{-1}$] | $0.4 \times 10^{-5}$ | $0.6 \times 10^{-5}$ | 0.67 |
| Sediment transport $S$ [m$^3$ m$^{-1}$ s$^{-1}$] | $7.6 \times 10^{-5}$ | $1.2 \times 10^{-5}$ | 6.3 |

Table E.2: GWK - DUT comparison.

Transport gradients were derived from the bed level changes using the sediment balance:

$$\frac{\partial z_b}{\partial t} + \frac{\partial S}{\partial x} = 0 \tag{E.1}$$

where $S$ is the sediment transport. Integration of the transport gradients over $x$ gives sediment transport. The sediment transport was assumed to be zero at the toe of the profile.

Furthermore, predictions of net bedload on the bar crest were made with Eq. F.42 using the root-mean-square wave height, linear wave theory, included wave shoaling and assumed no wave breaking.

### E.4.2. SANDS-GWK and DUT

In this section the GWK sub-test 1b (prototype) are compared to the DUT sub-test 1b (model). Table E.2 lists the scale of dimensional numbers and parameters that were predicted based on the deep water wave height, wave period, water depth at bar crest, grain diameter and density. The vertical scale was $n_h = n_H = 10$. Wave period scale followed regular Froude scaling and was $n_T = 5.6$. The sediment of the model was about twice as large and light as in GWK. The velocity scale $n_{u_b}$ at the bar crest was 3.16. The scales of the Shields number, Reynolds number, relative settling velocity, Ursell number were close to unity except for the Dean- and Sleath number scales. The Sleath number was one order larger in the model.

Figure E.6 shows the first and second bottom profiles of the accretive sub-tests. Furthermore, the erosion- and deposition rate and sediment transport are shown. See also Table E.2 for the maximum erosion- and deposition rates and transports. In both, the prototype and model, the bar shrunk rapidly. Maximum erosion rates were $1.0 \times 10^{-5}$ m s$^{-1}$ and $1.0 \times 10^{-5}$ m s$^{-1}$ for GWK and DUT, respectively. Maxiumum deposition rates were $0.4 \times 10^{-5}$ m s$^{-1}$ and $0.6 \times 10^{-5}$ m s$^{-1}$ for GWK and DUT, respectively. Maximum transports over the bar were $7.6 \times 10^{-5}$ m s$^{-1}$ and $1.2 \times 10^{-5}$ m s$^{-1}$ for GWK and DUT, respectively. The location of maximum transport was about 2 m inshore of the bar crest at GWK and 40 cm at DUT. The maximum measured transport was 2 times larger than the predicted transport at GWK.

The maximum transport was 6 times larger at GWK than at DUT. From visual observation during the DUT sub-test 1b it was evident that the bar shrunk within minutes, well before the measurement of the first bottom profile at 38 min. The transport that corresponds with the actual bar evolution can therefore not be resolved. However, after the bar evolution no significant profile changes occurred and it can be concluded that the maximum transport over the bar must have been 5 to 10 times larger.

### E.4.3. Duck94 and DUT

In this section the onshore bar migration during the Duck94 field experiment (prototype) is compared to the accretive DUT sub-tests (model). Table E.3 lists the scale of dimensional numbers and parameters that were

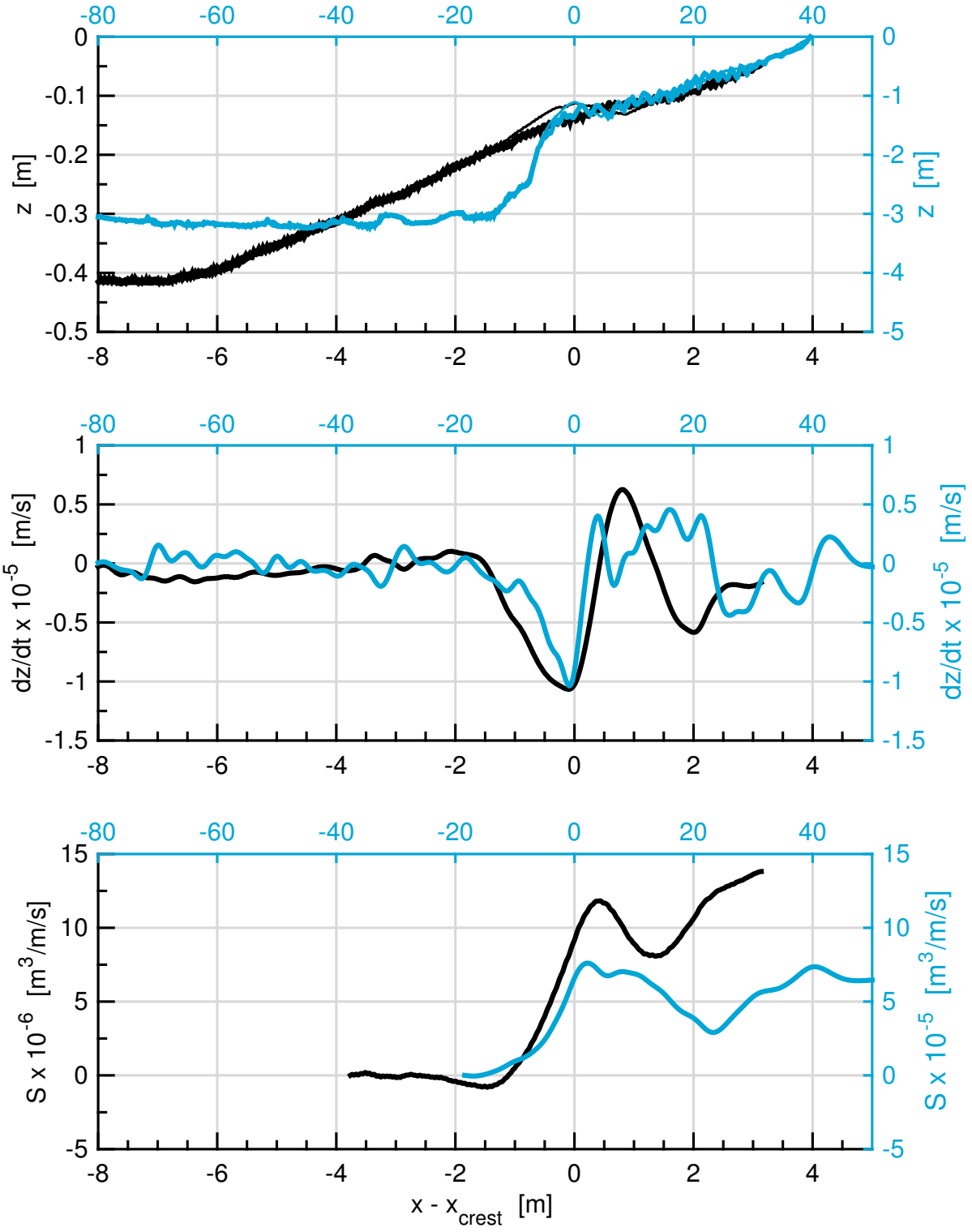


Figure E.6: Comparison of the test 1b at GWK and test 1b at DUT. Black lines represent DUT and cyan lines GWK. Top panel shows the bottom profile of DUT1b at 0 h (thin line), DUT1b at 0.64 h (thick line), GWK1b at 0 h (thick line) and GWK1b at 4.5 h (thick line). Middle panel shows the corresponding erosion- and deposition rate. Lower panel shows the corresponding net sediment transport.

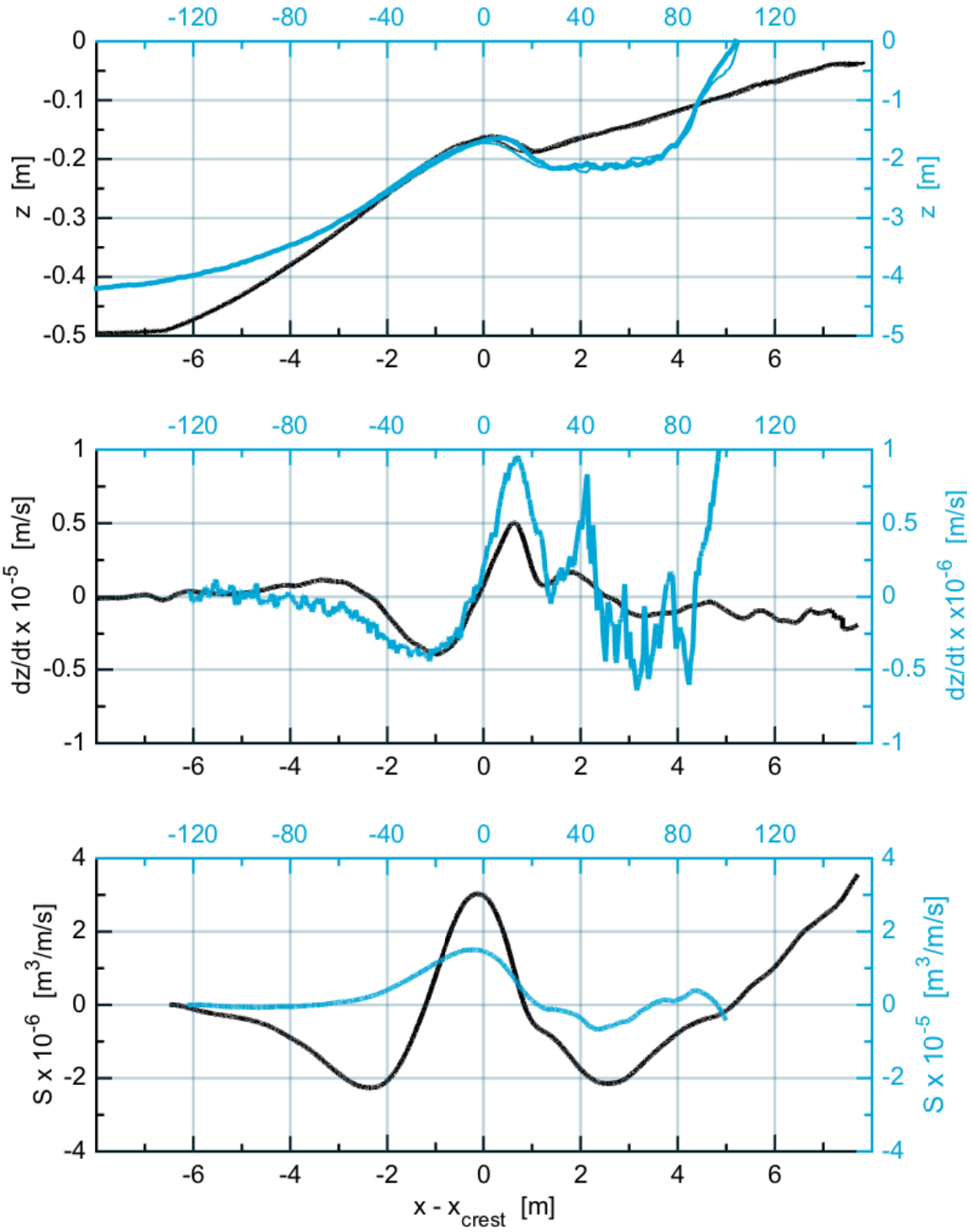


Figure E.7: Comparison of the onshore bar migration at Duck94 with the accretive tests of DUT2. Black lines represent DUT and cyan lines Duck94. Top panel shows the average bottom profiles of DUT2b-r 0h (thin line), the average bottom profile DUT2b-r 0.86h (thick line), bottom profile at Duck94 24-Sept-1994 08:00 (thin line) and Duck94 26-Sept-1994 12:00 (thick line). Middle panel shows the corresponding erosion- and deposition rate. Lower panel shows the corresponding net sediment transport.

| Description | Duck94 | DUT | scale $n$ |
|---|---|---|---|
| Bottom elevation $z$ at bar crest [m] | 1.6 | 0.16 | 10 |
| Wave height $H_{m0}$ [m] | 0.8 | 0.08 | 10 |
| Peak wave period $T_p$ [s] | 10 | 1.8 | 5.56 |
| Grain size $d_{50}$ [µm] | 250 | 524 | 0.48 |
| Specific density $\rho_s$ [km] | 2650 | 1200 | 2.21 |
| Orbital velocity $u_{b,\infty}$ [$m\,s^{-1}$] | 0.99 | 0.23 | 4.25 |
| Shields number $\theta$ | 1.0 | 0.7 | 1.4 |
| Reynolds number $Re$ | 15 | 14 | 1.1 |
| Relative settling velocity $V$ | 0.5 | 0.6 | 0.8 |
| Dean number $D$ | 2.5 | 2.7 | 0.9 |
| Sleath number $S$ | 0.04 | 0.40 | 0.09 |
| Ursell number $Ur$ | 2.8 | 0.9 | 3.2 |
| Velocity Skewness at bottom $Sk_u$ | 0.7 | 0.7 | 1.00 |
| Sediment transport Eq. F.42 [$m^3\,m^{-1}\,s^{-1}$] | $4.3\times10^{-5}$ | $2.6\times10^{-5}$ | 1.6 |
| Erosion rate $dz/dt$ [$m\,s^{-1}$] | $4.3\times10^{-7}$ | $3.5\times10^{-6}$ | 0.12 |
| Deposition rate $dz/dt$ [$m\,s^{-1}$] | $9.5\times10^{-7}$ | $5.6\times10^{-6}$ | 0.17 |
| Sediment transport $S$ [$m^3\,m^{-1}\,s^{-1}$] | $1.5\times10^{-5}$ | $0.3\times10^{-5}$ | 5 |

Table E.3: Duck94 - DUT comparison.

predicted based on the deep water wave height, wave period, water depth at bar crest, grain diameter and density. The depth scale was $n_h = n_H = 10$. Wave period scale did not follow regular Froude scaling and was $n_T = 5.6$. The sediment of the model was about twice as large and light as in Duck94. The velocity scale $n_{u_b}$ at the bar crest was 3.16. The scales of the Shields number, Reynolds number, relative settling velocity, and Ursell number were close to unity except for the Dean- and Sleath number scales. The Sleath number was one order larger in the model.

Figure E.7 shows the first and second bottom profiles of the accretive sub-tests. Furthermore, the erosion- and deposition rate and sediment transport are shown. See also Table E.3 for the maximum erosion- and deposition rates and transports. In both, the prototype and model, Duck94 and DUT, an onshore bar migration occurred. At Duck94 the bar seemed to grow in amplitude while at DUT stayed constant. Maximum erosion rates were $4.3\times10^{-7}\,m\,s^{-1}$ and $3.5\times10^{-6}\,m\,s^{-1}$ for Duck94 and DUT, respectively. Maxiumum deposition rates were $9.5\times10^{-7}\,m\,s^{-1}$ and $5.6\times10^{-6}\,m\,s^{-1}$ for Duck94 and DUT, respectively. Maximum net transports over the bar were $1.5\times10^{-5}\,m\,s^{-1}$ and $0.5\times10^{-6}\,m\,s^{-1}$ for Duck94 and DUT, respectively. The location of maximum net transport was about 8 m offshore of the bar crest at Duck94 and 0 cm at DUT.

The maximum net sediment transport $S$ at the bar crest during the accretive DUT test was $3\times10^{-6}\,m^3\,m^{-1}\,s^{-1}$ and was at the bar crest. The net sediment transport before and after the crest were $2\times10^{-6}\,m^3\,m^{-1}\,s^{-1}$ in the offshore direction. This transport may be explained by the suspended transport carried by the undertow. Therefore, the actual bedload by waves would then be $5\times10^{-6}\,m^3\,m^{-1}\,s^{-1}$.

The erosion- and deposition rates differed by one order. The maximum net transport was 3 times larger at Duck94 than at DUT. The maximum measured net transport at the bar crest was 3 and 5 times smaller than predicted at Duck94 and DUT, respectively.

The horizontal length scale is necessary to estimate the morphological time scale. From Figure E.7 its apparent that the horizontal length scale is $n_l \approx 20$ when the curves of the erosion- and sedimentation rates are compared. The morphological time scale of the actual tests was $n_{TM} = n_l n_h n_S^{-1} = 20\times10/5 = 40$. The predicted value using the net transports predicted by Eq. F.42, see values in Table E.3, lead to a morphological time scale of $n_{TM} = 20\times10/1.6 = 125$.

The net transport in the model is smaller than predicted and can be considered a significant scale effect. The enhanced offshore directed suspended sediment transport in the model explains only part of the scale effect.

## E.5. Conclusions

Experiments have been conducted in a medium sized wave flume to investigate the scale effects of the lightweight model for bedload by waves. The experiments involved erosive wave conditions followed by accretive wave condition. The sediment was synthetic with a specific density of $1200\,kg\,m^{-3}$ and a grain diameter of $d_{50}$ =

524µm. The Shields number, Reynolds number and relative settling velocity were approximately similar to prototype values. The experiments were compared to a large wave flume test at Hanover and the Duck94 field experiment. The most significant results from the study are summarized below.

1. Scaling according to the lightweight model reproduced morphological bar behavior associated with intra-wave sediment transport.

2. The scale effect by non-similarity of transport by horizontal pressure gradients, captured by the Sleath number, was not apparent during the bar evolution and the maximum net transports over the bar.

3. Scale effects in the model reduced the predicted maximum net transport. Part of the scale effect can be explained by the enhanced suspended sediment transport in the model.

4. Including velocity skewness effects in the Meyer-Peter and Muller type transport formula predicted the maximum net sediment transport within a factor of 10.

# F

# Scaling laws for bed-load by waves (Mobile bed experiment)

*This appendix is written by Martijn Henriquez:*

This chapter describes the onshore sandbar migration measurements in a wave flume with a mobile bed. The chapter investigates the scaling of sediment transport by waves in the nearshore. Scale relations are necessary to choose proper sediment for physical models. The use of lightweight synthetic sediment makes it possible to preserve the Reynolds number, Shields number and relative settling velocity altogether. These parameters are essential for the correct reproduction of intra wave sediment transport and hence the net transport by waves in the nearshore.

Two tests were conducted in a medium-sized wave flume using synthetic sediment. The first part of a test consisted of an erosive wave condition where a single bar profile developed. Hereafter, accretive wave condition were generated. After generating the accretive wave condition the bar disappeared rapidly in the first test and during the second test the bar migrated onshore.

The test were compared to prototype cases conducted in the Großer Wellenkanal (GWK) in Hannover and during the Duck94 field experiment. Morphological evolution that was dominantly forced by intra-wave transport was similar in prototype and model. The scale relation for net bedload by waves predicts the correct order of magnitude. However, the physical model experienced lower net onshore sediment transports. Including velocity skewness in conventional bedload formula estimated the net bedload within a factor of 10.

## F.1. Introduction

Scaling of sediment is often needed in laboratory wave flumes where spatial dimensions are about a factor 10 smaller, see for example Hughes 1993 for an elaborate literature review. Generally, for the physical model, regular sand is chosen with a relatively small diameter. Scaling relations are consulted to translate the spatial dimension and sediment flux to prototype values. Often, the correct scaling of processes are ignored such as the transport modes 'bedload' and 'suspended load', and turbulence regimes, 'laminar', 'smooth turbulent' and 'rough turbulent'. However, when the objective is to study intra-wave sediment transport it is essential to ensure that the laboratory model has the same flow and transport regimes as in the prototype. For example, ripples may cause phase lags between sediment concentration and flow velocity and consequently generate a net sediment transport in the direction opposite to the wave propagation.

The cycle of sediment transport within a wave cycle, where sediment is mobilized and comes to rest, determines the amount of net sediment transport. Mobilization of sediment is largely caused by fluid shear stresses and can be predicted with the Shields number. Once sediment is moving it can be transported as bedload where grains make regular contact with the bed, or as suspended load where grains are entrained in the water column. This action is governed by the amount of turbulence at the bed and the settling velocity of the grains. Turbulence is closely related to the Reynolds number and the settling velocity depends heavily on grain diameter and weight. Thus, the interrelation between flow properties flow and sediment properties represented by, among others, the Shields- and Reynolds number determine the similitude of net transport by waves.

The objective was to perform a physical model test where the bed-load by waves is correctly reproduced. First, a scale model was derived. Second, physical model tests were conducted. Finally, the physical model tests were compared to prototype tests to quantify the scale effects of the scale model.

Existing scale- relations and models are summarized and extended in Section F.2. Physical model tests are described in Section E.1 and scale effects are assessed in Section E.4.

# F.2. Scale relations

## F.2.1. Froude number

The water motion in short waves is mainly determined by gravitational and inertial forces. In prototype and model the gravitational force is the same. Therefore, the inertial forces should also be the same in prototype and model. This leads to the following scale relation for short waves (known as the Froude scale):

$$n_H = n_L = n_T^2 = n_t^2 = n_u^2 = n_h \tag{F.1}$$

where
$n$ is the ratio between the prototype value and the model value of the index parameter
$H$ is wave height
$L$ is wave length
$T$ is wave period
$t$ is time
$u$ is orbital flow velocity
$h$ is water depth.
Scaling according to the Froude scale leads to the correct reproduction of wave steepness, shoaling, refraction and diffraction.

The spatial dimensions of the wave flume (e.g. water depth) and the specifications of the wave maker (e.g. wave height) lead to a general spatial scale. Short wave properties (e.g. wave period) are further obtained by using the general spatial scale in combination with the Froude scale. For practical purposes the wave flume is usually filled with natural water which leads to

$$n_\rho = n_\nu = 1 \tag{F.2}$$

where
$\rho$ is water density
$\nu$ is kinematic viscosity.
This leaves only two other scalable variables: the sediment diameter and density.

At present there are various papers and reference books that deal with scaling sediment. Usually, they describe a set of dimensionless numbers and parameters representing processes and magnitudes. Having the same values for the numbers in prototype and model promotes similitude and reduces scale effects. In the following, the dimensionless numbers and parameters are summarized, elaborated on, and rewritten as scale relations.

## F.2.2. Iribarren number

The shape of a breaking wave can be categorized in four types, spilling, plunging, collapsing or surging. Breaker types can be predicted with the Iribarren number defined as [Battjes, 1974]:

$$\xi = \frac{\tan\beta}{\sqrt{H/L}} \tag{F.3}$$

where $\beta$ is the local bottom slope ($dh/dl$). The physical interpretation of the parameter can be seen as the ratio between the slope steepness and the wave steepness. A Iribarren number smaller than 0.4 corresponds with spilling, from 0.4 to 2.3 with plunging and larger than 2.3 with surging. Rewriting the Iribarren number in a scale relation and substituting the Froude scale relations $n_H = n_h$ and $n_L = n_T^2$ yields

$$n_\xi = n_h n_l^{-1} n_H^{-0.5} n_L^{0.5} \tag{F.4}$$

$$= n_l^{-1} n_h^{0.5} n_T \tag{F.5}$$

where $n_l$ is the horizontal length scale. When $n_l$ is not equal to the vertical length scale $n_h$, the model is considered distorted. To retain breaker shape, the Iribarren number should be unity $n_\xi = 1$. Consequently the wave period scale becomes:

$$n_T = n_l n_h^{-0.5} \tag{F.6}$$

Eq. F.6 is referred to as the distorted Froude scaling [Van Rijn et al., 2011]. In a distorted model where the slope is steeper, $n_l/n_h > 1$, the wave length has to be shorter to obtain similar breaker shapes [Van Rijn et al., 2011].

### F.2.3. Ursell number

The Ursell number indicates the degree of wave nonlinearity and can be used to estimate wave asymmetry and skewness [Ruessink et al., 2012]. The Ursell number is calculated following [Doering and Bowen, 1995],

$$Ur = \frac{3}{32\pi^2}\frac{HL^2}{h^3} \tag{F.7}$$

and can be written as a scale relation

$$n_{Ur} = n_H n_L^2 n_h^{-3} \tag{F.8}$$

### F.2.4. Reynolds number

The flow conditions near the bed can be divided in laminar, smooth turbulent and rough turbulent. These regimes can be predicted with the grain size Reynolds number

$$Re = \frac{u_* \, d}{\nu} \tag{F.9}$$

which can be expressed in the scale relation

$$n_{Re} = n_{u_*} n_d n_\nu^{-1} \tag{F.10}$$

where
$u_*$ is shear velocity
$d$ is grain diameter.

### F.2.5. Shields number

The densimetric Froude number (named Shields number from hereon)

$$\theta = \frac{\rho u_*^2}{\gamma d} \tag{F.11}$$

is important for mobile beds and leads to the scale relation

$$n_\theta = n_\rho n_{u_*}^2 n_\gamma^{-1} n_d^{-1} \tag{F.12}$$

where
$\gamma$ is submerged unit weight of sediment defined as $\left(\rho_s - \rho\right) g$
$g$ is the gravitational acceleration
$\rho_s$ is sediment density.

If the Shields number is not preserved it is be possible that there is no movement of sediment at all. The Shields number is also a good indicator for the different transport regimes which are divided in saltating motion, rippled bed and sheet flow. During half a wave cycle sediment is picked up, brought in suspension and settles again.

### F.2.6. Relative settling velocity

The suspended sediment distribution over the water depth is strongly related to the relative settling velocity [Van Rijn, 1993]

$$V = \frac{w_s}{u_*} \tag{F.13}$$

which Kamphuis [1991] introduced as a scale relation

$$n_V = n_{w_s} n_{u_*}^{-1} \tag{F.14}$$

where $w_s$ is settling velocity of sediment. A physical interpretation of the parameter is the ratio of the settling velocity to turbulence generated by bed friction (expressed with the friction velocity). The settling velocity can be approximated using the relationship Hallermeier [1981]

$$w_s = \frac{\gamma^{0.7} d^{1.1}}{6\rho^{0.7}\nu^{0.4}} \tag{F.15}$$

which is convenient to rewrite as a scale relation. The scale relation for the relative settling velocity becomes

$$n_V = n_\gamma^{0.7} n_d^{1.1} n_\rho^{-0.7} n_\nu^{-0.4} n_{u_*}^{-1}. \tag{F.16}$$

### F.2.7. Dean number

The Dean number

$$D = \frac{H/T}{w_s} \tag{F.17}$$

is another popular scale relation

$$n_D = n_H n_T^{-1} n_{w_s}^{-1}. \tag{F.18}$$

The parameter is thought of as the ratio of settling time to the wave period.

### F.2.8. Sleath number

The relative density of sediment is important when considering particle accelerations. Horizontal pressure gradients and inertia forces can have a significant impact on the total force balance of a sediment particle. This impact can be expressed with the parameter S (named Sleath number from hereon)

$$S = \frac{\rho u}{(\rho_s - \rho) g} \frac{2\pi}{T} \tag{F.19}$$

which is the ratio of inertial forces to gravitational forces acting on individual grains of sediment [Flores and Sleath, 1998]. High Sleath numbers ($S > 0.2$) suggests that sediment will start to move earlier than predicted by the Shields curve. In addition, the mode of transport can become different and sediment will start to move as a block, also known as plug flow [Foster et al., 2006, Madsen, 1974]. Rewriting the Sleath number in a scale relation and substituting the Froude scale relation $n_u = n_T$ yields

$$\begin{aligned} n_S &= n_\rho n_u n_\gamma^{-1} n_T^{-1} && \text{(F.20)} \\ &= n_\rho n_T n_\gamma^{-1} n_T^{-1} && \text{(F.21)} \\ &= n_\rho n_\gamma^{-1} && \text{(F.22)} \end{aligned}$$

suggesting that the scale relation only depends on sediment density.

### F.2.9. Relative length parameter

Another similarity parameter is the relative length parameter which is the ratio of a typical length (e.g. wave amplitude) to the sediment diameter

$$\frac{\lambda}{d}. \tag{F.23}$$

Scale effects from dissimilarity of the relative length parameter are unclear. Mogridge et al. [1972] conducted experiments with various sediment densities and indicated that bedform patterns depend on the relative length parameter. On the other hand, Nielsen [1992] showed that ripple steepness is predominantly related to the Shields number but this does not account for the ripple height. The bed porosity depends on the sediment grain diameter is therefore directly related to the relative length parameter. Dissimilarity of the ratio between the pore space and the wave orbital motion will result in dissimilarity of the wave energy absorption by porosity effects [Kamphuis, 1991] Due to the nontransparent relation between scale effects and the relative length scale, it will only be used qualitatively. The scale relation would be

$$n_{\lambda/d} = n_\lambda n_d^{-1}. \tag{F.24}$$

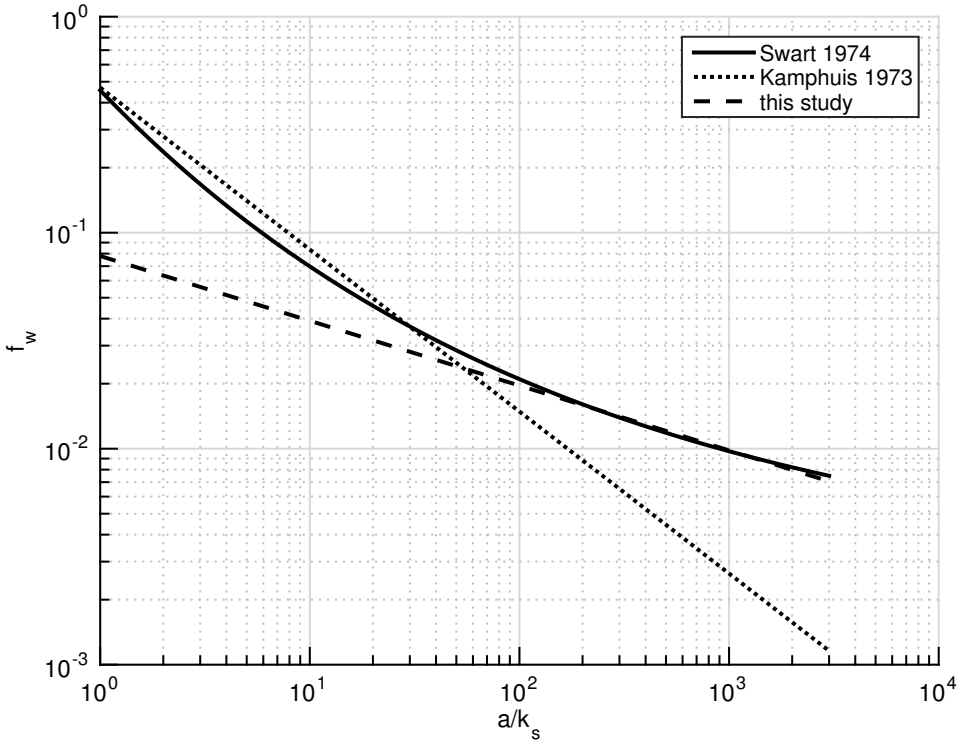


Figure F.1: Comparison of friction factor formulations.

## F.2.10. Friction factor

To complement the set of scale relations, the relation between flow velocity and friction velocity is defined according to Jonsson [1966]

$$u_*^2 = 0.5 f_w u^2 \tag{F.25}$$

where $f_w$ is the friction factor. This gives the scale relation

$$n_{u_*} = n_{f_w}^{0.5} n_u. \tag{F.26}$$

Now the only variable that still needs to be expressed in short wave and sediment properties is the friction factor. This expression depends on the flow regime which is assumed rough turbulent in both prototype and model. This assumption should be checked with the use off e.g. diagrams by Jonsson [1966]. The most well-known relation for the friction factor in the rough turbulent regime is given by Swart [1974]:

$$f_w = \exp\left[-5.997 + 5.213\left(\frac{a}{k_s}\right)^{-0.194}\right] \tag{F.27}$$

where
$a$ is the horizontal excursion of the orbital motion at the bottom
$k_s$ is the effective bed roughness height (e.g. $k_s = 3d$ ).
The form of this expression is not convenient to rewrite as a scale relation. Therefore, the formula is approximated with

$$f_w = 0.078\left(\frac{a}{k_s}\right)^{-0.3} \tag{F.28}$$

which has a correlation of 0.98 with Swart [1974] relation for the range $100 \leq a/k_s \leq 3000$ . Rewriting the relation in a scale relation and substituting the Froude scale relation $n_a = n_h$ yields

$$n_{f_w} = n_h^{-0.3} n_d^{0.3}. \tag{F.29}$$

Therefore, the relation between friction velocity and flow velocity can be written as

$$n_{u_*}^2 = n_h^{-0.3} n_d^{0.3} n_u^2 \tag{F.30}$$

and in combination with the Froude scale relation $n_u^2 = n_h$ leads to

$$n_{u_*}^2 = n_h^{0.7} n_d^{0.3}. \tag{F.31}$$

Kamphuis [1973] proposed a the friction factor relation

$$f_w = 0.47 \left( \frac{k_s}{a} \right)^{0.75} \tag{F.32}$$

that is different from Eq. F.28. With the friction factor relation by Kamphuis [1973] the scale relation for the friction would become

$$n_{u_*}^2 = n_h^{0.25} n_d^{0.75} \tag{F.33}$$

where a significant difference in the power of $n_h$ can be seen. Figure F.1 illustrates the difference between the formulations.

## F.2.11. Bedload

Bedload is the transport of saltating grains that are in regular contact with the bottom. Wilson [1987] derived a bedload formula at high shear stress

$$q = 11.8 \frac{\rho}{(\rho_s - \rho) g} \left( \frac{\tau}{\rho} \right)^{1.5} \tag{F.34}$$

Einstein [1950] introduced the non-dimensional transport $\Phi$ where the transport is divided by $\sqrt{\frac{(\rho_s - \rho) g}{\rho} d_{50}^3}$ which transforms Eq. F.34 in the simple and better known expression of

$$\Phi = 11.8\, \theta^{1.5} \tag{F.35}$$

Eq. F.34 can be expressed in terms of the free-stream velocity by substituting the bottom stress relation $\tau = 0.5 \rho f_w u^2$ in Eq. F.34 giving

$$\begin{aligned} q &= 11.8 \frac{\rho}{(\rho_s - \rho) g} \left( 0.5 f_w u^2 \right)^{1.5} && \text{(F.36)} \\ &= 4.17 \frac{\rho}{(\rho_s - \rho) g} f_w^{1.5} u^3 && \text{(F.37)} \end{aligned}$$

Net bed-load transport by waves is determined by time averaging over the wave period or between two up- or down-crossings of a time series. Time-averaging is denoted by an over-line. The net bed-load is given as

$$\overline{q} = 4.17 \frac{\rho}{(\rho_s - \rho) g} f_w^{1.5} \overline{u^3} \quad . \tag{F.38}$$

The velocity $u$ can be decomposed in a time-averaged component $\overline{u}$ and periodic component $\widetilde{u}$. The mean cube velocity $\overline{u^3}$ can than be expressed in the following terms

$$\begin{aligned} \overline{u^3} &= \overline{\left( \overline{u} + \widetilde{u} \right)^3} && \text{(F.39)} \\ &= \overline{u}^3 + 3 \overline{u} \overline{\widetilde{u}^2} + \overline{\widetilde{u}^3} && \text{(F.40)} \\ &= \mu_u^3 + 3 \mu_u \sigma_u^2 + Sk_u \sigma_u^3 && \text{(F.41)} \end{aligned}$$

where
$\mu_u$ is the time average of velocity $u$,
$\sigma_u$ is the standard deviation of velocity $u$,
$Sk_u$ is the skewness of $u$ defined by $Sk_u = \overline{\left( u - \mu_u \right)^3} / \sigma_u^3$. In the *absence of a mean current* $\overline{u}$, the net transport can be written as

$$\overline{q} = 4.17 \frac{\rho}{(\rho_s - \rho) g} f_w^{1.5} Sk_u \sigma_u^3 \quad . \tag{F.42}$$

Writing Eq.F.42 as scale relation gives

$$n_{\overline{q}} = n_\rho n_\gamma^{-1} n_{f_w}^{1.5} n_{Sk_u} n_{\sigma_u}^3 \quad . \tag{F.43}$$

Free-stream velocity skewness and asymmetry can be predicted using the Ursell number [Doering and Bowen, 1995]. The last parameterization was done by Ruessink et al. [2012]

$$B = \frac{0.857}{1+\exp\frac{-0.471-\log Ur}{0.297}} \quad , \tag{F.44}$$

$$\phi = -90+90\tanh\frac{0.815}{Ur^{0.672}} \quad , \tag{F.45}$$

$$Sk_u = B\cos\phi \quad , \tag{F.46}$$

$$As_u = B\sin\phi \quad . \tag{F.47}$$

Under asymmetric waves the skewness further increases in the wbbl. Based on the work of Elgar and Guza [1985] and Henderson et al. [2004], Berni et al. [2013] formulated the relation,

$$\frac{Sk_b}{Sk_\infty} = \cos\left(\phi_b\right) - \sin\left(\phi_b\right)\frac{As_\infty}{Sk_\infty} \quad . \tag{F.48}$$

### F.2.12. Morphological time scale

The morphological time scale $n_{TM}$ is the ratio of the prototype response time to the model response time. The morphological time scale can be derived from the sediment balance

$$\frac{\partial z_b}{\partial t} + \frac{\partial S}{\partial x} = 0 \tag{F.49}$$

where $S$ is the sediment transport and when rewritten as scale relation becomes

$$n_{TM} = n_h n_l n_S^{-1} \quad . \tag{F.50}$$

From this equation it becomes apparent what the consequence is when the model is distorted ($n_h \neq n_l$). Often steeper slopes are used in models and consequently decreasing the response time of the model. When the net bedload scale relation (Eq. F.43) is substituted in Eq. F.50 the morphological time scale law is defined as

$$n_{TM} = n_\rho^{-1} n_\gamma (n_l/n_h) n_h^{0.95} n_{Sk}^{-1} n_d^{-0.45} \quad . \tag{F.51}$$

## F.3. Lightweight scale model

Kamphuis [1985] introduced the lightweight model for bed-load using lightweight synthetic sediment (see also Hughes [1993] for an extensive description). The goal of the lightweight model is to maintain similarity of the Reynolds- and Shields number ($n_{Re} = n_\theta = 1$). Furthermore, we assume the usage of water $n_\rho = n_\nu = 1$ and scale according to the Froude number ($n_H = n_L = n_T^2 = n_t^2 = n_u^2 = n_h$). Similarity of the Reynolds number scale relates the friction velocity to the grain diameter

$$n_{u_*} = n_d^{-1} \quad . \tag{F.52}$$

Substituting Eq. F.52 into $n_\theta = 1$ relates the the submerged specific weight to the grain diameter

$$n_\gamma = n_d^{-3} \quad . \tag{F.53}$$

It is surprising that when the settling velocity formulation of Hallermeier [1981] (Eq. F.15) is used and similarity of the Reynolds- and Shields number ($n_{Re} = n_\theta = 1$) are maintained, similarity of the relative settling velocity is always attained ($n_V = 1$).

The depth scale $n_h$ comes into play through the friction velocity scale relation $n_{u_*}$ (Eq. F.30). The friction velocity depends on the friction factor and flow velocity. The formulation of the friction factor significantly impacts the exponent of the friction velocity scale relation. Using the friction factor by Kamphuis [1973] leads to

$$n_d = n_h^{-0.09} \quad , \tag{F.54}$$

and using the friction factor formulation of Eq. F.28 leads to

$$n_d = n_h^{-0.3} \quad . \tag{F.55}$$

In this study we try to follow the widely-used friction factor relation by Swart (1974). Considering prototype coasts with grain diameters of $d_{50} = 250\,\mu\text{m}$ and moderate wave heights $H_s = 1\,\text{m}$ leads to $a/k_s$ values of the order 1000. For the model, a vertical scale of $n_h = 10$ leads to $a/k_s$ values of the order 10. From Figure F.1 it can be seen that Eq. F.28 is a closer approximation of the relation by Swart [1974] for this range of $a/k_s$ values.

Scale effects may occur by not maintaining the Sleath number and relative length parameter. Scaling according to the bedload model described above, will result in a mismatch of the Sleath number equal to $n_S = n_h^{-0.9}$. It is challenging to asses the corresponding scale effect since the number is only partially validated. Nonetheless, it is fair to conclude that the mobility of sediment can be larger than predicted due incorrect scaling of the relative density. The mismatch of the relative length $n_{\lambda/d} = n_h^{1.3}$ suggests that ripple geometry will not be scaled correctly and the model bed porosity will be relatively larger.

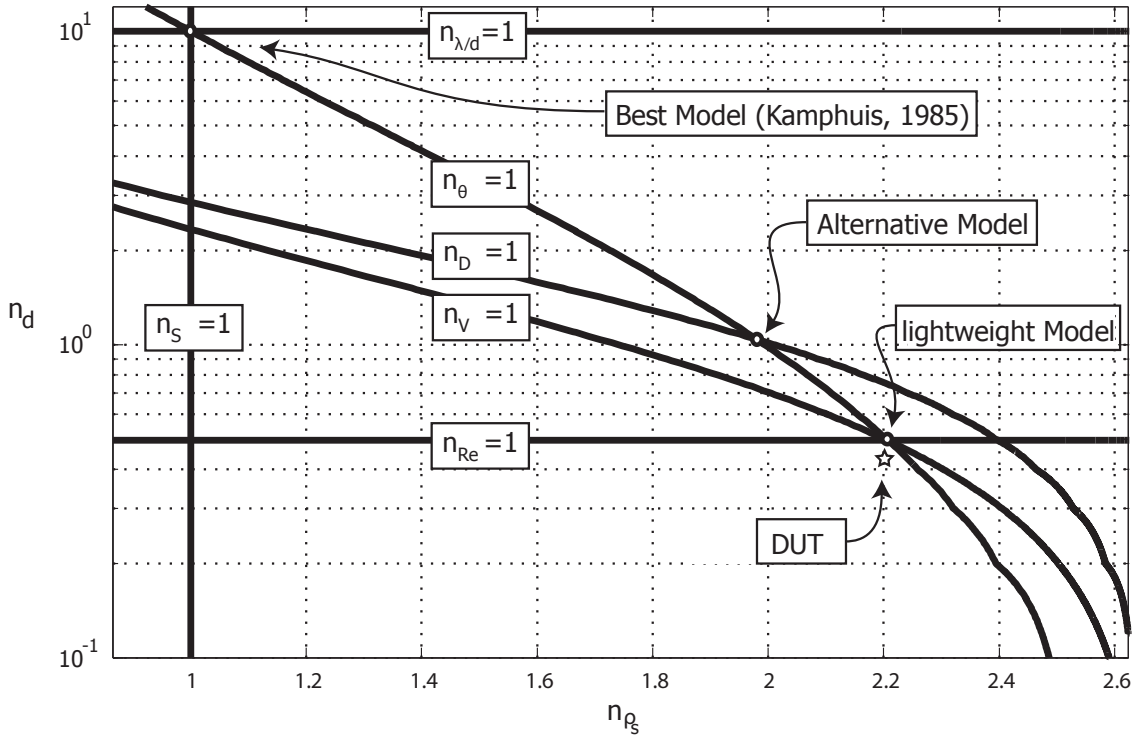


Figure F.2: Similarity parameters equal to 1 as a function of relative sediment density and relative grain diameter. The depth scale is set equal to 10. The star indicates sediment properties of the DUT tests.

For a given depth scale $n_h$, the scale relations can be plotted as a function of relative density and relative grain diameter. The lines in Figure F.2 indicate where the scale relation is equal to 1 (corresponding to preserving the scale number or parameter). It can be seen that at some point the lines cross and some scale relations are simultaneously equal to 1. Besides the lightweight model we can identify the 'Best Model' by Kamphuis [1985] with similarity of the Shields number, relative sediment density $\rho_s/\rho$ and relative length parameter $\lambda/d$. Note that when the best model is used with a prototype grain diameter of 250 µm and the depth scale $n_h = 10$, the grain diameter would be 25 µm. Thus, sand becomes silt in the model and cohesive properties may play a role. In addition, the relative settling velocity is poorly scaled $n_V = n_h^{0.5}$ (not considering turbulence by wave breaking). Figure F.2 illustrates another model with similarity of the Dean- and Shields number. Such a scale model may be useful to scale suspended transport in the surfzone.

### F.3.1. Discussion

For the bedload model the friction factor is important. In the description above the flow regime is assumed rough turbulent for prototype and model. Similar results are obtained if the flow regime is assumed laminar or smooth turbulent. Using the expression for the friction factor that corresponds with these regimes also results in a bedload model where the Reynolds number, Shields number and the relative settling velocity are preserved. The scaling rules will slightly change.

In a geometrically undistorted model the vertical length and horizontal length of the bottom topography scale with the same factor. Present literature suggests that preserving the Dean number results in geometrically undistorted models (Hughes, 1993; Vellinga, 1986). To the authors' knowledge, this has only been confirmed for models with natural sand and does not necessarily apply for lightweight sediment. Hughes (1993) mentioned that different model laws which incorporate distortion converge when models are geometrically undistorted and use natural sand. In other words, all these model laws have the same expression as the Dean number if the model is to be geometrically undistorted and uses natural sand. Strangely, when the density of sediment is included in the model law of Vellinga (1986) there is no convergence with the Dean number for a geometrically undistorted model with lightweight sediment. This also applies for the model law of Wang, et al. (1990).

Bedforms are often related to the Shields parameter (Nielsen, 1992; Van Rijn, 1993). These relations are often derived from experiments with natural sand and do not necessarily apply for lightweight sediment. Nonetheless, preserving the Shields number suggests preserving the ripple steepness. But the relations of lightweight sediment to ripple height and ripple length remain unclear to the authors.

### F.3.2. Conclusions

Lightweight sediment gives the opportunity to preserve several similarity parameters. This is valid for the combination of the Reynolds number, Shields number and relative settling velocity (referred to as bedload model). Also the combination of the Dean number with the Shields number is possible (referred to as suspended model). As a consequence, the sediment grain diameter is larger and the sediment density is smaller in the physical model compared to the prototype.

A wave flume experiment was conducted using the bedload model. Transport regimes observed for the bedload model agreed well with the expectations based on the Shields number and relative settling velocity. The morphological evolution of the coastal profile in the wave flume was similar to that observed in nature.

Both models will have similar scale effects since their mismatch in the Sleath number and relative length parameter is about the same. There is a large chance that liquefaction of the bed occurs under energetic monochromatic waves. This has not been evident for irregular waves.

# G

# Overview measurements

The data set of this research contains 48 tests, of which 27 tests are processed and analysed. The data set is structured in three test series, with each three onshore sandbar migrations, with each three tests of 15 minutes. Table G.1 gives an overview of all processed data. The columns in Table G.1 are:

| | | |
|---|---|---|
| 1 | Test series | All measurements with the same PIV location. |
| 2 | Bar migration | All measurements between two storm wave climates. |
| 3 | Test | Measurement of 15 minutes. |
| 4 | PIV location | Offshore, on top of and onshore of the bar. |
| 5 | Bottom calibration | The mean total sediment transport per location is based on all tests, but in the mean vertical distribution not all tests are taken into account. To be able to study the vertical distribution after averaging tests, the bottom height of each test has to be set at the same height. Tests with a very high or low bottom are not used in the averaging, because those tests constrain the remaining area. The tests that are not used in the average vertical distribution per location are listed in this column. |
| 6 | File name | Used in Matlab. |
| 7 | Comment | Comments about the data. |

| Test series | Bar migration | Test | PIV location | Use after bed level calibration | *File name* | Comment |
|---|---|---|---|---|---|---|
| 1 | 1.1 | 1.1.1 | A | | *1110* | |
| | | 1.1.2 | A | | *1120* | |
| | | 1.1.3 | A | Not used | *1130* | |
| | 1.2 | 1.2.1 | A | | *1210* | |
| | | 1.2.2 | A | | *1220* | |
| | | 1.2.3 | A | Not used | *1230* | |
| | 1.3 | 1.3.1 | A | Not used | *1310* | |
| | | 1.3.2 | A | | *1320* | |
| | | 1.3.3 | A | | *1330* | |
| 2 | 2.1 | 2.1.1 | B | | *2120* | Error during PIV measurement 2110. |
| | | 2.1.2 | B | | *2140* | Error during PIV measurement 2130. |
| | | 2.1.3 | B | | *2150* | |
| | 2.2 | 2.2.1 | B | | *2210* | |
| | | 2.2.2 | B | | *2220* | |
| | | 2.2.3 | B | | *2230* | |
| | 2.3 | 2.3.1 | B | | *2310* | |
| | | 2.3.2 | B | | *2320* | |
| | | 2.3.3 | B | | *2330* | |
| 3 | 3.1 | 3.1.1 | C | | *3110* | |
| | | 3.1.2 | C | | *3130* | Error during PIV measurement 3120. |
| | | 3.1.3 | C | Not used | *3140* | |
| | 3.2 | 3.2.1 | C | Not used | *3210* | |
| | | 3.2.2 | C | | *3220* | |
| | | 3.2.3 | C | | *3230* | |
| | 3.3 | 3.3.1 | C | Not used | *3310* | Not used at all, because bottom partly out of image. |
| | | 3.3.2 | C | Not used | *3320* | |
| | | 3.3.3 | C | | *3330* | |

Table G.1: Overview of all measurements with corresponding PIV location

# H

# Data analysis: process and settings

*This appendix describes the data processing in Matlab and Davis. The model in Matlab is built entirely for this study, while DaVis is an existing software programm to perform PIV analyses. First the data processing in Matlab is described (section H.1) with additional information about the version management (section H.1.1) and data storage (section H.1.2). Next the calculation in DaVis is explained (section H.2). Lastly, the executed test cases are described (section H.3).*

## H.1. Matlab

In this study, data from different measurement techniques are processed and compared. Figure H.1b gives an visual overview of the validation strategy. During the calculation the general calculation process approach is followed: load, select, reshape, calculate, plot (Figure H.1b). The processing of both the PIV data and bottom profile data follows this structure (Figure H.2).

Figure H.2c shows the calculation during the data process and Figure H.4 shows a complete overview of all calculation steps and matrix sizes in the Matlab analysis. The data is saved in three data sets: L0, L1 and L2. L0 contains the raw data as measured. L1 is a selection of the useful data and the data is reshaped to practical matrix dimensions. Because the PIV measurement starts before the waves pass (Figure **??**), the first part of the measurement is cut off between L0 and L1. L2 are the results of the calculation. The calculations are tested by using a few simple test cases as input and comparing the results with the analytical solution (Section H.3). It is especially important to test the calculation between L1 and L2 with a test case.

### H.1.1. Version management

Version management enables comparison and reproduction of intermediate results of the calculation. With version management every calculation has a unique version number. In this research the versions are man-

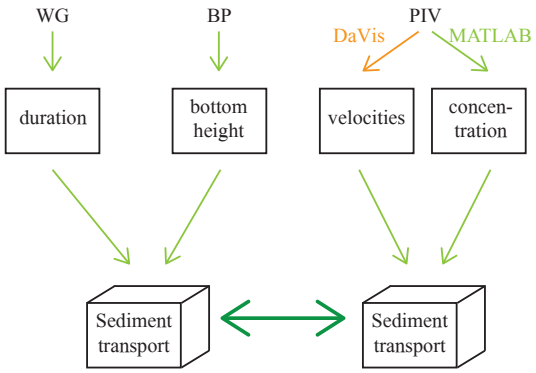


(a) Validation strategy: comparison between the PIV data and bottom data.

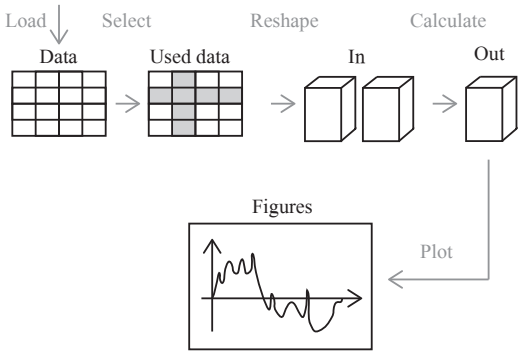


(b) Process approach

Figure H.1: Data analysis overview

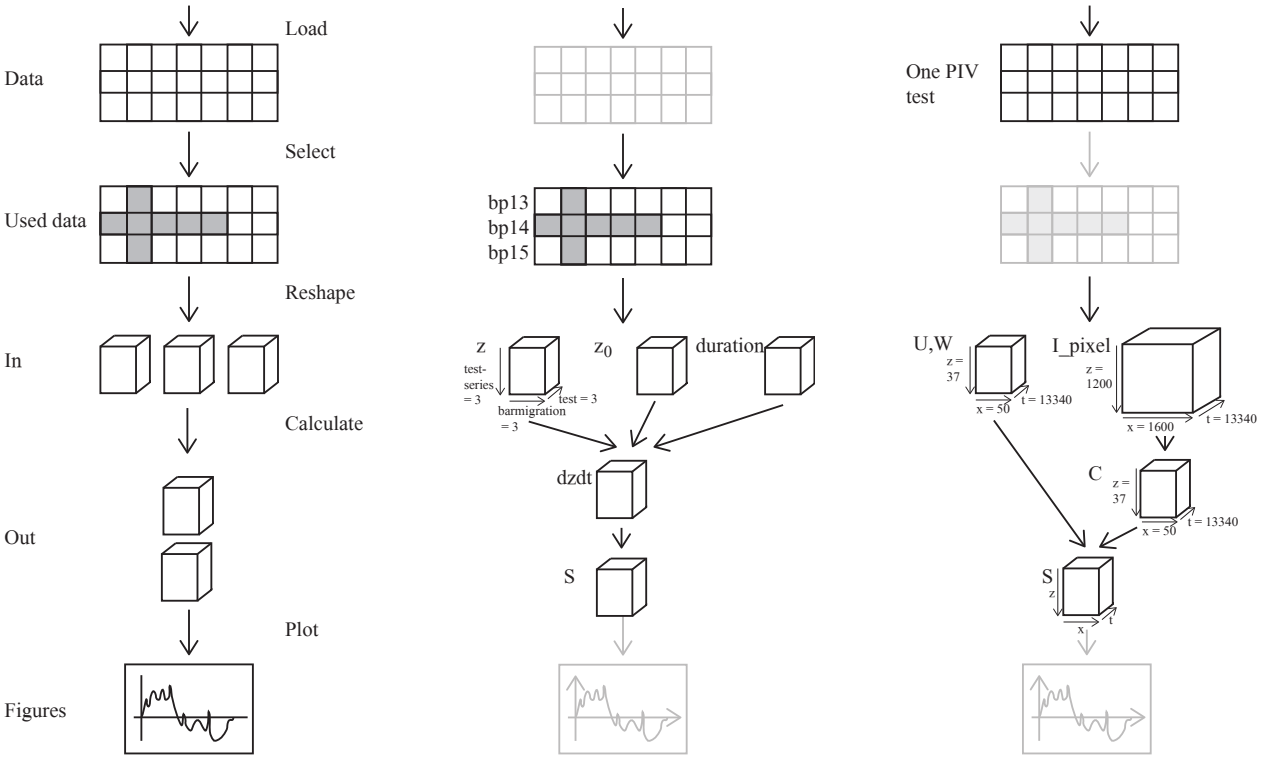


(a) General (b) Bottom data (c) PIV data

Figure H.2: Process approach of the Matlab analysis.

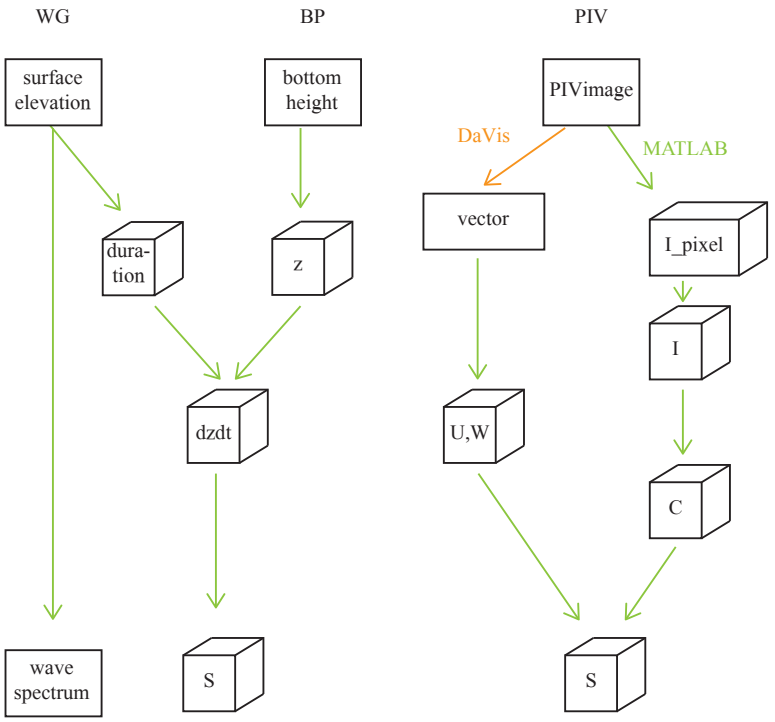


Figure H.3: All variables in the data process.

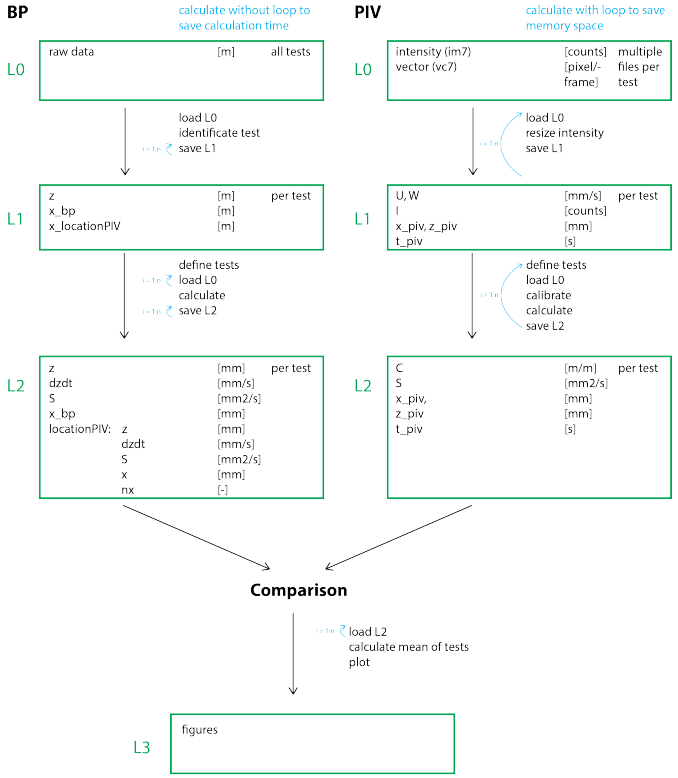


(a) Data content and calculation steps

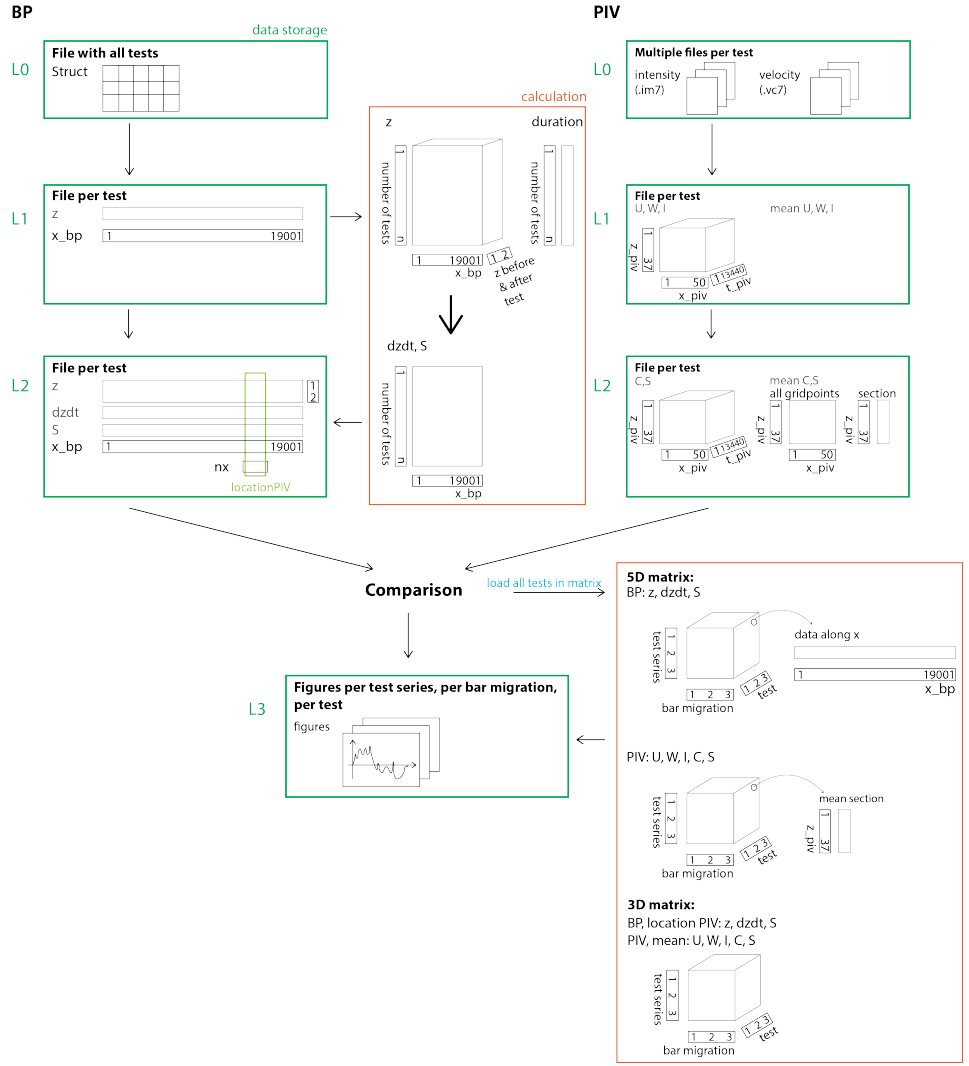


(b) Matrix size

Figure H.4: Overview of all calculation steps and matrices in the calculation.

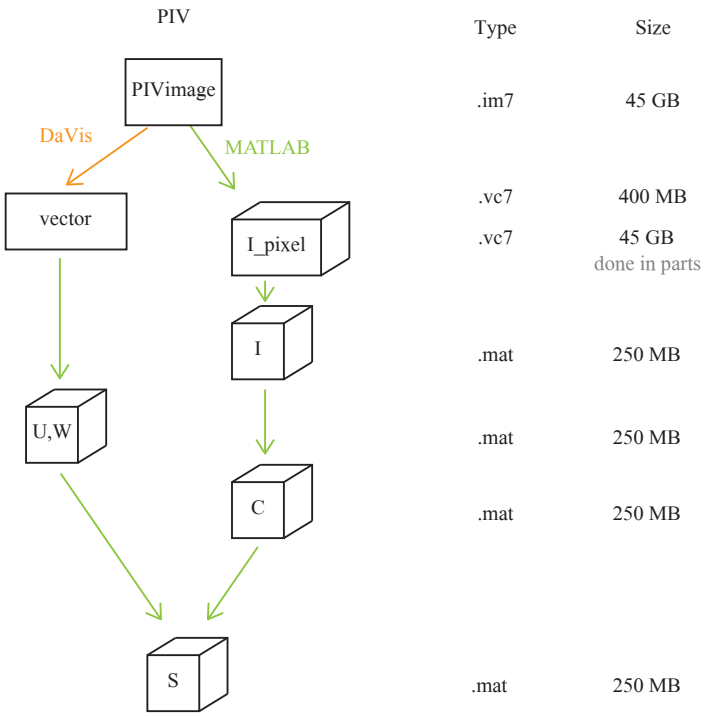


Figure H.5: Steps in data analysis and data storage size. The largest matrix is the intensity at origin size. For one test this matrix needs around 45 GB storage space. Therefore this part of the calculation is done in parts.

aged with a database combined with Github.

### H.1.2. Storage

Due to all the images the PIV data is very large. During the data processing the file type and size of the PIV data changes (Figure H.5). Since the data is very large, it should not be stored efficiently.

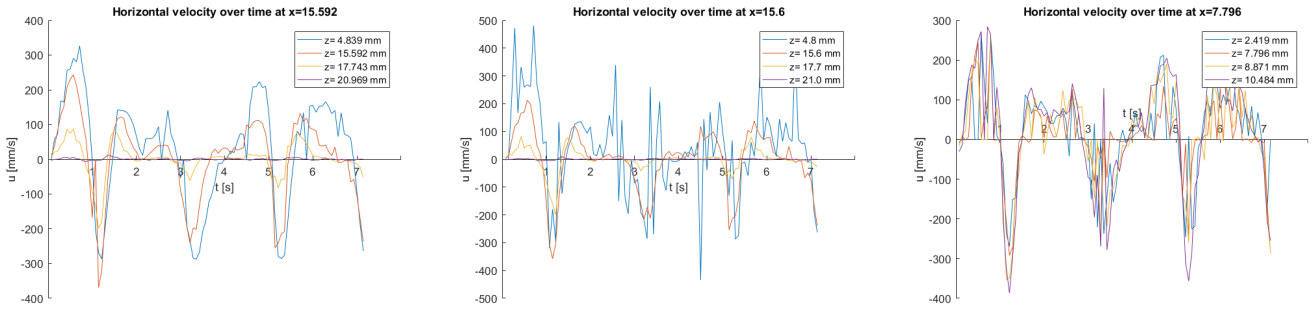


(a) Multipass 64x64 PIV (b) Singlepass 64x64 PIV (c) Multipass 32x32 PIV

Figure H.6: Results for 7 seconds at location x=0.008 to compare different PIV settings (same part of the data)

## H.2. Davis

The first step of the PIV analysis will be done in the Lavision software "Davis 7.2". Davis calculates the velocity vectors by analysing the correlation between images. To create a reproducible calculation, the settings are listed in the following sections.

### H.2.1. Grid size

Before running the PIV analysis in DaVis the grid size is determined. For the minimum grid size it is important that particles don't move out of the grid within the time period (CFL-condition). According to the DaVis manual the grid size should be larger than 4 times this condition (equation H.1).

To reach a maximum accuracy, the grid size should be as small as possible. Table H.1 gives the possible grid sizes that fit in the image size. Since $\Delta x$ is between 64 and 128 pixels, the multi-pass option in DaVis will be used with a grid of 128 pixels in the first cycle and 64 pixels in the second cycle. Figure H.6 proves that smaller grid sizes give a noisy result.

$$\Delta x > 4 \cdot u_{max} \cdot \Delta t, \qquad \Delta x > 4 \cdot \frac{0.3 m/s}{500 Hz} = 4 \cdot 0.8 mm = 3.2 mm \tag{H.1}$$

| | | |
|---|---|---|
| 16 x 16 pixels | = | 0.54 x 0.54 mm |
| 32 x 32 pixels | = | 1.08 x 1.08 mm |
| 64 x 64 pixels | = | 2.15 x 2.15 mm |
| 128 x 128 pixels | = | 4.30 x 4.30 mm |

Table H.1: Possible grid sizes

### H.2.2. Settings

Table H.2 gives the settings of the PIV analysis in DaVis. Multipass correlation is used. After the first past it is necessary to do post-processing. Therefore the vector field is smoothed after the first pass with a peak ratio and median filter. The peak ratio is the ratio between the highest and the second highest peak (Equation H.2 in which $min$ is the lowest correlation in the specific grid box). The median filter compares a vector with the average of the surrounding vectors and removes vectors that differ more than 2 times the root-mean-square of the neighbours and replaces it with the average of the neighbours (Figure H.7).

To calculate the correlation the standard correlation function is used (FFT, no zero-padding, equation H.3) and not the normalized function (FFT, zero-padding, equation H.4). The standard correlation method is 5 times faster than the normalized method. The normalized method especially performs better with varying background intensity, which is not the case in my data.

$$Q = \frac{Peak1 - min}{Peak2 - min} > 1 \tag{H.2}$$

| **Options** | **Done** | **Notes** |
|---|---|---|
| Cross-correlation | | Double frame, double exposure |
| Calibration in DaVis | Not used | |
| Error level | Low | |
| Image preprocessing | Not used | |
| Mask | Not used | |
| Pixel mask | Used | First pass = 0.3, Second pass =0.6<br>(amount of valid pixels necessary to calculate vector) |
| Correlation | Multipass | Multipass decreasing size:<br>First pass: 128x128, Overlap 50 %, Gaussian weighting<br>Second pass: 64x64, Overlap 50 %, no weighting function |
| Correlation function | Standard | |
| Multi-pass post-processing | Used | Post-processing after first pass:<br>Peak ratio Q < 1.1<br>Median filter: strongly remove & iteratively replace<br>for differences larger than 2 r.m.s. of average<br>Smoothing: 1x Smooth 3x3 |

Table H.2: Davis settings

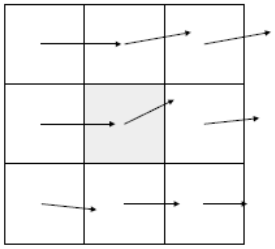

Figure H.7: The local median filter

$$C(dx,dy) = \sum_{x=0,y=0}^{x<n,y<n} I_1(x,y)I_2(x+dx,y+dy), -\frac{n}{2} < dx,dy < \frac{n}{2} \tag{H.3}$$

$$C(dx,dy) = \frac{\sum_{x=0,y=0}^{x<n,y<n}(I_1(x,y) - I_{1avg}(x,y))(I_2(x+dx,y+dy) - I_{2avg}(x+dx,y+dy))}{RMS(I_1(x,y) - I_{1avg}(x,y))RMS(I_2(x+dx,y+dy) - I_{2avg}(x+dx,y+dy))} \tag{H.4}$$

## H.3. Test cases

Test cases are performed to proof the validity of the data model. This section describes those test cases.

### H.3.1. DaVis: PIV velocities

To test DaVis the PIV analysis is done for synthetic data. The synthetic data are two photos with equally spread dots that relocate with one pixel (Figure H.8). Hence the calculated velocity should be 1 pixel/frame and constant over the PIV frame. The output of this test case was correct.

### H.3.2. Matlab

#### H.3.2.1 Test 1: PIV sediment transport

In this test the sediment transport caused by a constant velocity is tested. A synthetic velocity field, intensity and calibration are generated as input (Figure H.9a). The results are shown in Figure H.10. The velocity, concentration and sediment transport show the correct values. All transport is indeed current related and the sediment gradient is zero. Concluding: the script is correct for this test case.

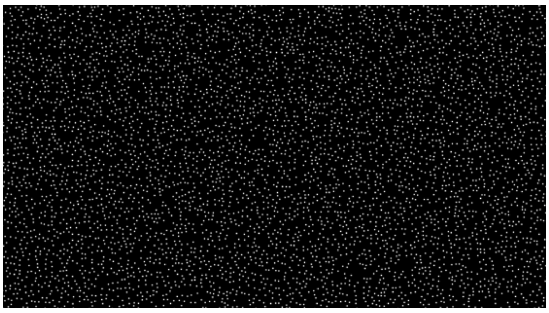

(a) Input 1

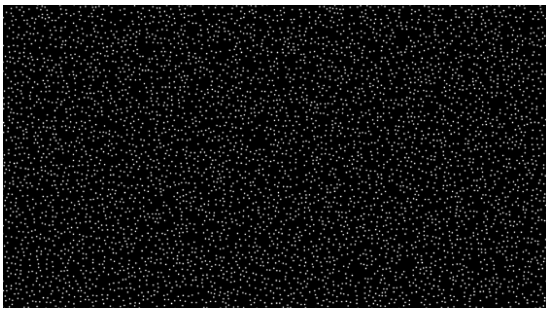

(b) Input 2

Figure H.8: input of Test Case 0

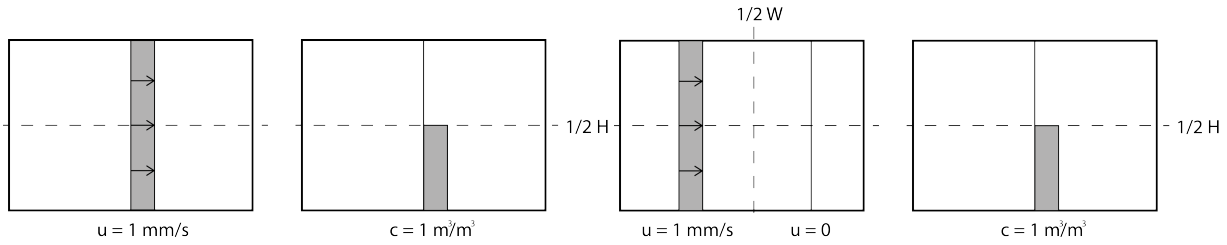


(a) Test case 1: PIV




(b) Test case 2: PIV

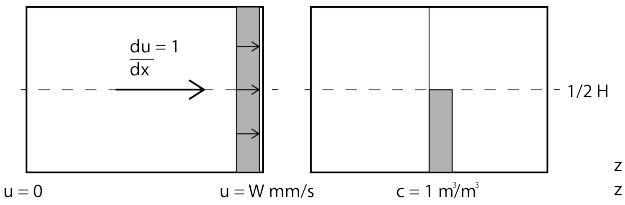


(c) Test case 3: PIV

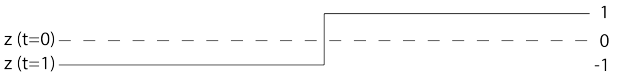


(d) Test case 4: BP

Figure H.9: Input of test cases

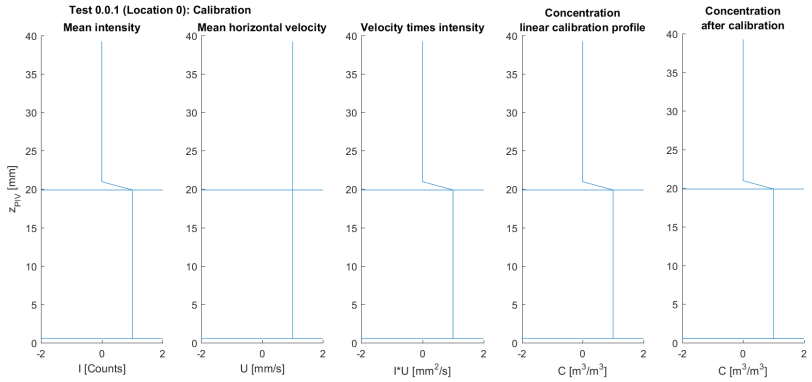


(a) Calibration

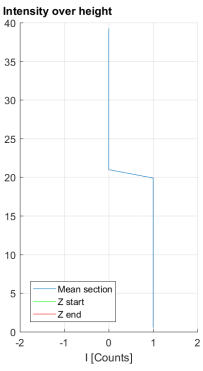


(b) Intensity

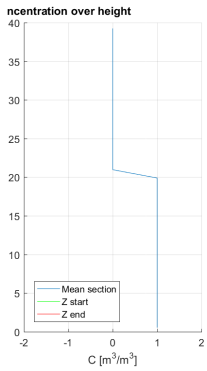


(c) Concentration

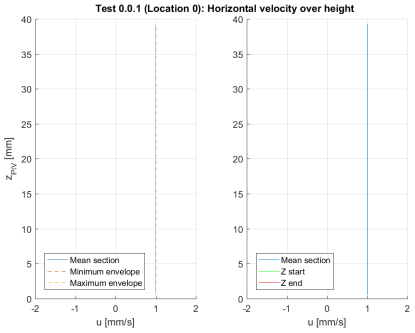


(d) Velocity

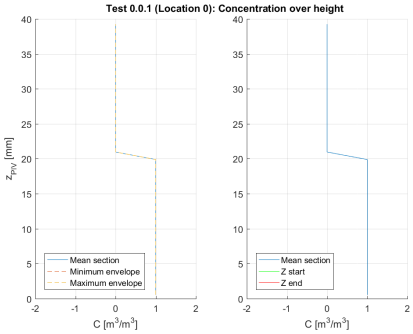


(e) Concentration

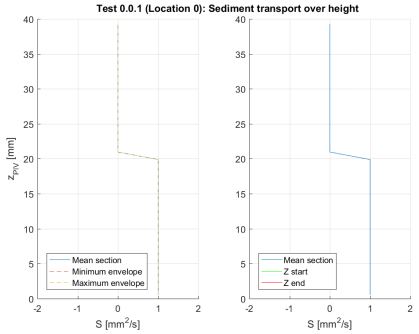


(f) Sediment transport

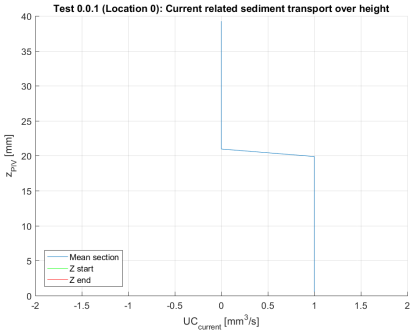


(g) Current related sediment transport

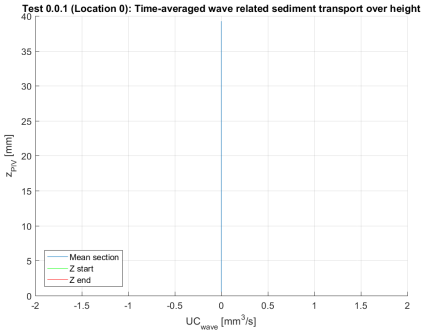


(h) Mean wave related sediment transport

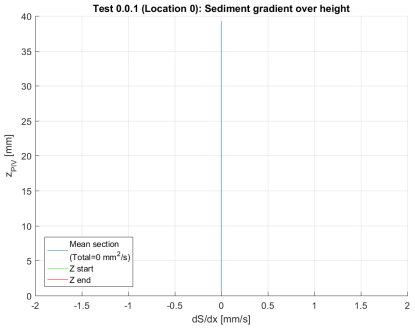


(i) Sediment gradient

Figure H.10: Results of Test Case 1

#### H.3.2.2 Test 2: PIV sediment gradient

In this test the sediment transport caused by a velocity gradient over x is tested. The horizontal velocity is divided in two boxes: the left half of the picture has a velocity of 1 mm/s and the right half has no velocity. This causes a mean velocity of 0.5 mm/s. A synthetic velocity field, intensity and calibration are generated as input (Figure H.9b). The results are shown in Figure H.11. The velocity, concentration and sediment transport show the correct values. Also the sediment gradient is correct (Equation H.5). Concluding: the script is correct for this test case.

$$\frac{dS}{dx} = \frac{S_2 - S_1}{\frac{1}{2} \cdot \Delta x} = \frac{0-1}{\frac{1}{2} \cdot 54mm} = -0.04mm/s \tag{H.5}$$

#### H.3.2.3 Test 3: PIV sediment gradient

In this test the sediment transport caused by a velocity gradient over x is tested. The velocity gradient is set on 1 mm/s/mm (Figure H.9c). This causes a minimum velocity of 0 mm/s and a maximum velocity of 54 mm/s. Hence the mean velocity is 27 mm/s and the sediment gradient is 1 mm/s.

The results are shown in Figure H.12. The velocity, concentration and sediment transport show the correct values. The sediment gradient is 0.98 mm/s. This shows that the approximation error is quite high (Equation H.6). Disregarding the accuracy, the calculation method of dS/dx is correct.

$$\eta_S = \frac{|1 - 0.98|}{1} = 0.02 = 2\% \tag{H.6}$$

### H.3.3. Test 4: BP sediment transport and gradient

To test the calculation of the bottom measurements a synthetic bottom height is created (Figure H.9d). The duration ($D$) is 10 seconds. Figure H.13 shows the results of the calculation. The results are the same as the analytic solution (Equation H.7, H.8), so the calculation is assumed valid.

$$\frac{dS}{dx} = -\frac{dz}{dt} = -\frac{z_1 - z_2}{D} \tag{H.7}$$

$$S_{max} = \frac{1}{2} L \cdot \overline{\frac{dS}{dx}} = \frac{1}{2} \cdot (37000 - 18000)mm \cdot 0.1mm/s = 950mm^2/s \tag{H.8}$$

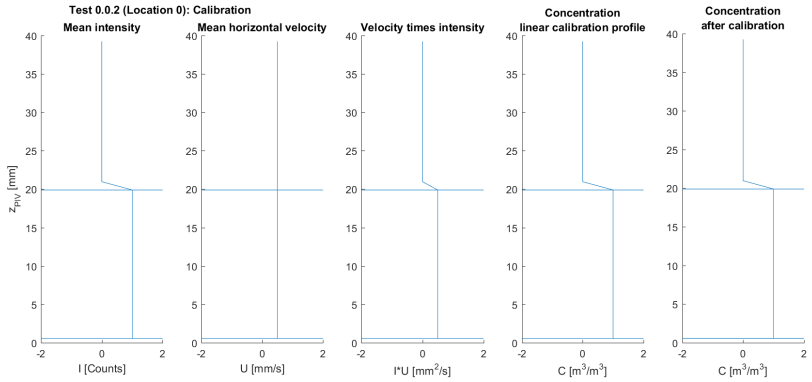


(a) Calibration

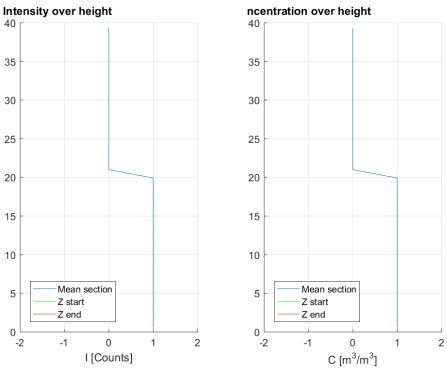


(b) Intensity (c) Concentration

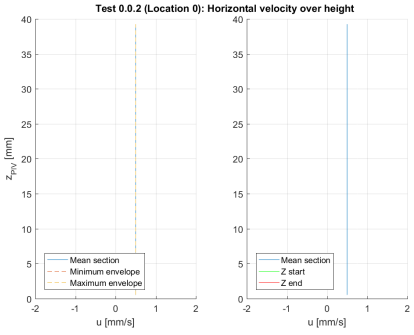


(d) Velocity

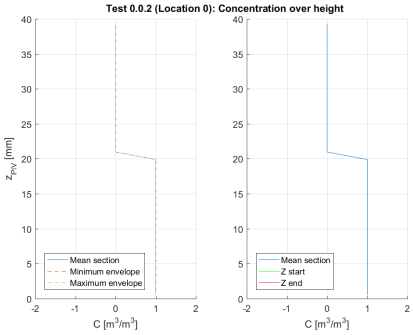


(e) Concentration

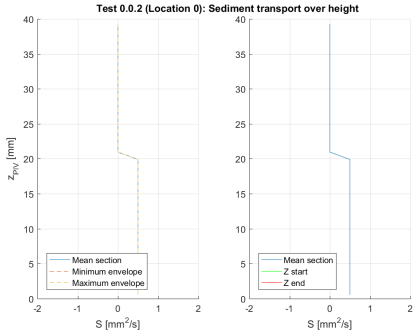


(f) Sediment transport

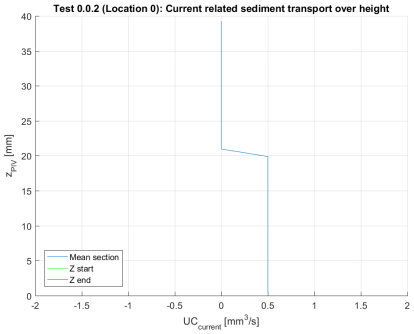


(g) Current related sediment transport

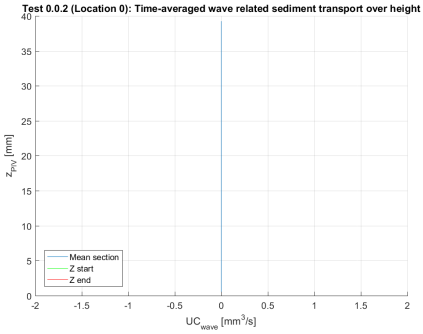


(h) Mean wave related sediment transport

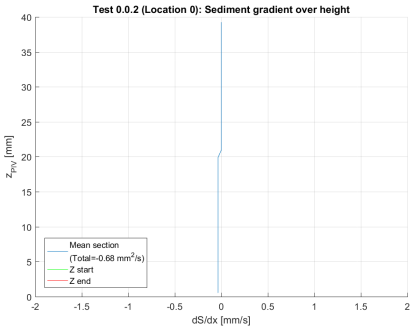


(i) Sediment gradient

Figure H.11: Results of Test Case 2

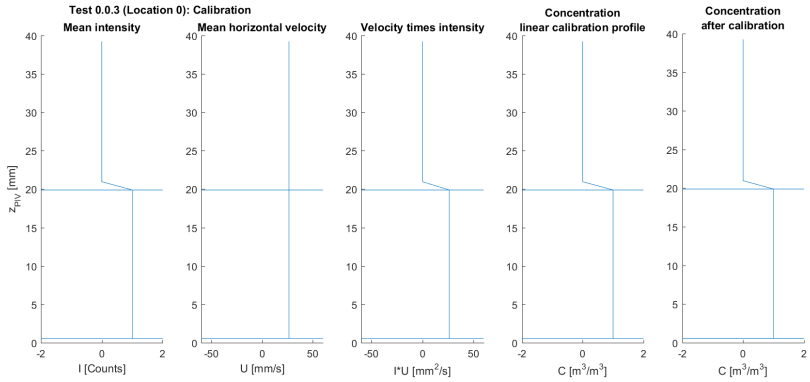


(a) Calibration

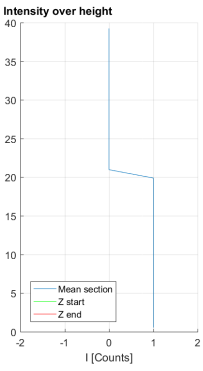


(b) Intensity

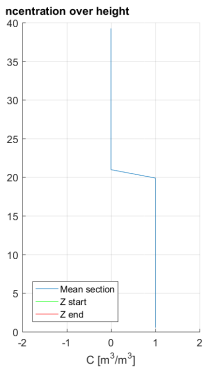


(c) Concentration

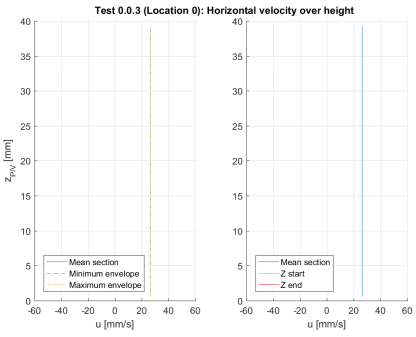


(d) Velocity

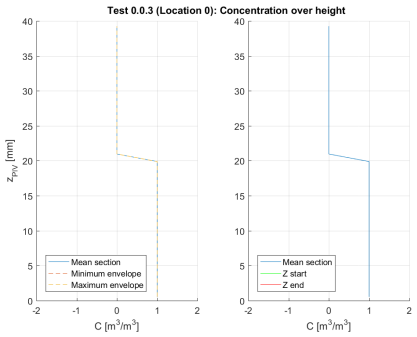


(e) Concentration

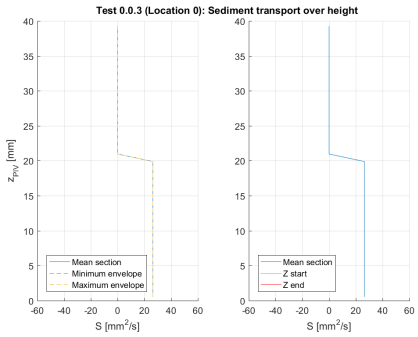


(f) Sediment transport

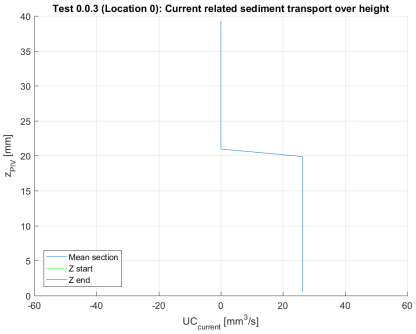


(g) Current related sediment transport

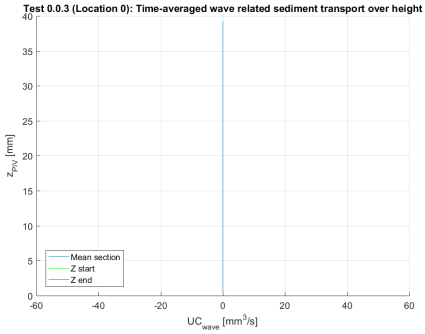


(h) Mean wave related sediment transport

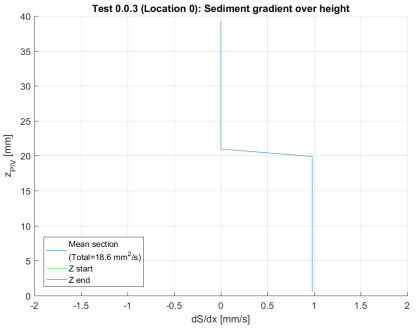


(i) Sediment gradient

Figure H.12: Results of Test Case 3

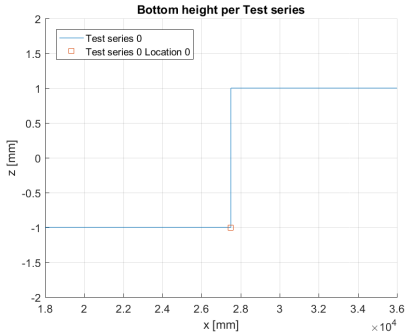


(a) Bottom height

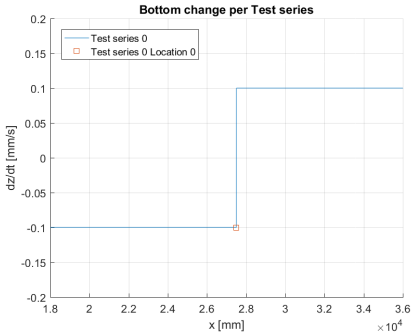


(b) Bottom change

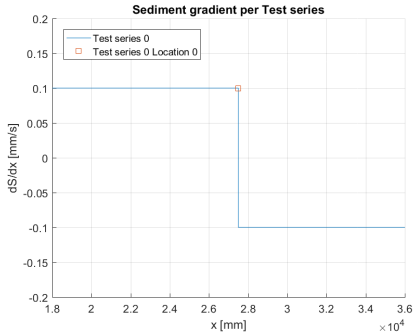


(c) Sediment gradient

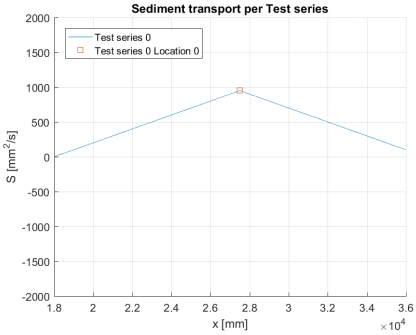


(d) Sediment transport

Figure H.13: Results of Test Case 4

# Calibration

A calibration relation has is established between intensity and concentration. With this calibration relationship the concentration can be calculated. Three methods are applied to determine the best calibration fit: linear, quadratic and an exponential trend line.

There are two main parts of the calibration process: (1) the mean bed and water intensity and (2) the sheet flow layer. First the mean bed and water intensity have to be equal to the mean bed and water concentration (1 $m^3/m^3$ and 0 $m^3/m^3$). This gives two fixed points through which every calibration trend line has to go. Hence the linear trend line is determined based on these two fixed point. Second the intensities in the sheet flow layer are compared to a linear concentration profile. The data points in the sheet flow layer determine the curve of the non-linear calibration methods.

But how to create a non-linear curve that is fixed in two points and adjusts shape to the other points? Figures I.1 and I.2 show the steps for the quadratic calibration and Figure I.3 and I.4 for the exponential calibration. All figures show the example of the first calibration set. The same method can be applied to the other calibration sets.

The *quadratic* calibration starts with the linear trend line (Figure I.1a). First a vertical translation is applied by distracting the linear trend line (Equation I.1, Figure I.1b). In Equation I.1, $a_L$ and $b_L$ are the coefficients of the linear trend line. This translation is to locate the fixed points at the horizontal axis. Second a horizontal translation is applied to locate the fixed point symmetrically around the vertical axis (Equation I.2, Figure I.1c). Hence the quadratic relation will go through zero in these fixed points. In Equation I.2, $x_1$ and $x_2$ are the x-values of the fixed points. Because the data set is now symmetrical around the vertical axis (Figure I.1c), the square of the data will locate both fixed points at exactly the same position. Hence there is only one resulting fixed point (Figure I.2a). Now the quadratic relation can be determined with a linear fit through the single fixed point and with a slope dependent on the data in the sheet flow layer. Figure I.2a shows this linear fit.

Now the linear fit on a quadratic axis with translated data has to be rewritten to the quadratic fit on normal axis and without translated data. The linear fit on a quadratic axis gives Equation I.3. In this equations the translated properties can be substituted. This results in Equations I.4 and I.5. Rewriting this to the standard notation of a quadratic fit (Equation I.6), results in Equation I.7. The result can also be written in terms of intensity and concentration (Equation I.8). Figure I.2b shows the final result.

$$y^* = y - y_0, \qquad y_0 = a_L \cdot x + b_L \tag{I.1}$$

$$x^* = x - x_0, \qquad x_0 = \frac{x_2 - x_1}{2} \tag{I.2}$$

$$y^* = a_{Q,L} \cdot x^{*2} + b_{Q,L} \tag{I.3}$$

$$y - y_0 = a_{Q,L} \cdot (x - x_0)^2 + b_{Q,L} \tag{I.4}$$

$$y - (a_L \cdot x + b_L) = a_{Q,L} \cdot (x - (\frac{x_2 - x_1}{2}))^2 + b_{Q,L} \tag{I.5}$$

$$y = a_Q \cdot x^2 + b_Q \cdot x + c_Q \tag{I.6}$$

$$y = a_{Q,L} \cdot x^2 + \left[ -a_{Q,L} \cdot 2 \cdot \left( \frac{x_2 - x_1}{2} \right) + a_L \right] \cdot x + \left[ a_{Q,L} \cdot \left( \frac{x_2 - x_1}{2} \right)^2 + b_{Q,L} + b_L \right] \tag{I.7}$$

$$C = a_{Q,L} \cdot I^2 + \left[ -a_{Q,L} \cdot \left( I_{bed,mean} - I_{water,mean} \right) + a_L \right] \cdot I + \left[ a_{Q,L} \cdot \left( \frac{I_{bed,mean} - I_{water,mean}}{2} \right)^2 + b_{Q,L} + b_L \right] \tag{I.8}$$

The *exponential calibration* starts with plotting the vertical axis at logarithmic scale (Figure I.3a). However because $log(0)$ results in infinity, a vertical translation is applied. To locate the fixed point of the mean water intensity at the horizontal axis, a $y_0$ of 1 is added to all y-values (Equation I.9, Figure I.3b). Next a horizontal translation is applied to locate fixed point of the mean water intensity in the origin (Equation I.10, Figure I.3c). Now the linear fit can be done resulting in Equation I.11 (Figure I.4a). Substituting the translations in Equation I.11 results in Equation I.12. When plotted at normal axis this results in the exponential curve (Figure I.4b). Equation I.11 can be rewritten to the common form of an exponential equation (Equation I.14). This results in Equation I.14.

$$y^* = y - y_0, \qquad y_0 = -1 \tag{I.9}$$

$$x^* = x - x_0, \qquad x_0 = x_1 \tag{I.10}$$

$$log(y^*) = a_{Q,L} \cdot x^* \tag{I.11}$$

$$log(y - y_0) = a_{Q,L} \cdot (x - x_0) \tag{I.12}$$

$$y = a_E \cdot e^{b_E \cdot x} + c_E \tag{I.13}$$

$$y = e^{-a_E \cdot x_0} \cdot e^{a_E \cdot x} + y_0 \tag{I.14}$$

Figure I.5 shows the resulting trend lines of all three calibration methods. The distributions in the top and bottom plot show the spread of water and bed intensities. The mean values of this spreads are the fixed points in the calibration. Figure I.5 shows the results of the first calibration set. The final results of each calibration set are shown in Chapter 4, section 4.1.

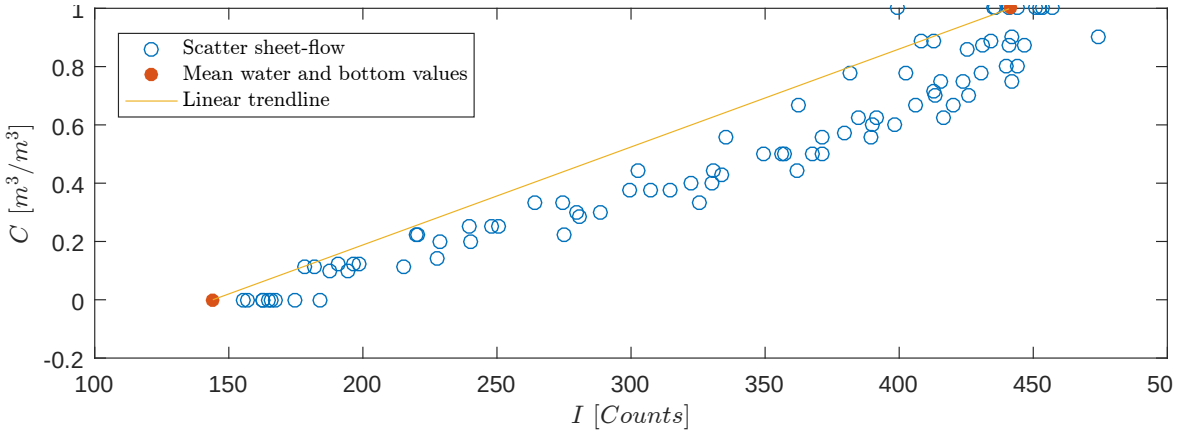


(a) Step 1: Linear calibration.

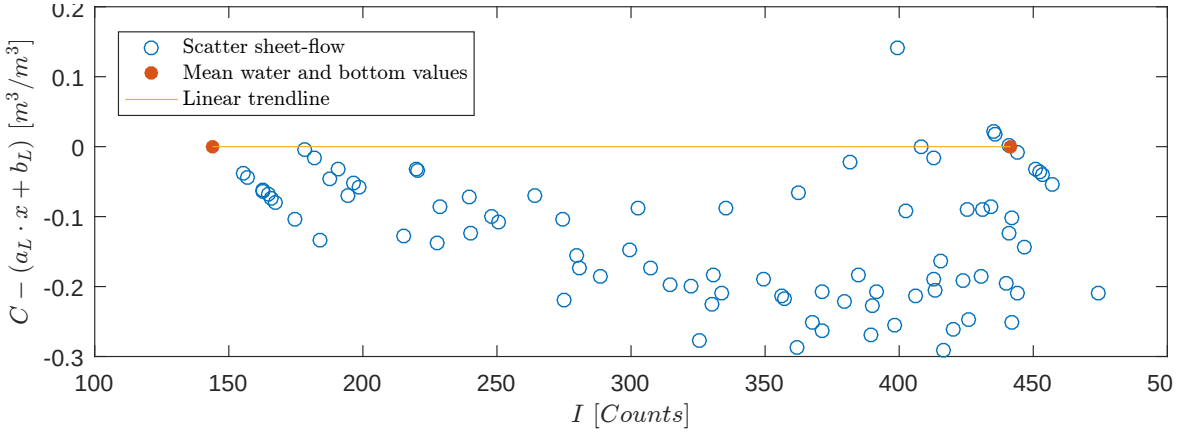


(b) Step 2: Vertical translation. Substract the linear calibration relation from the y-values.

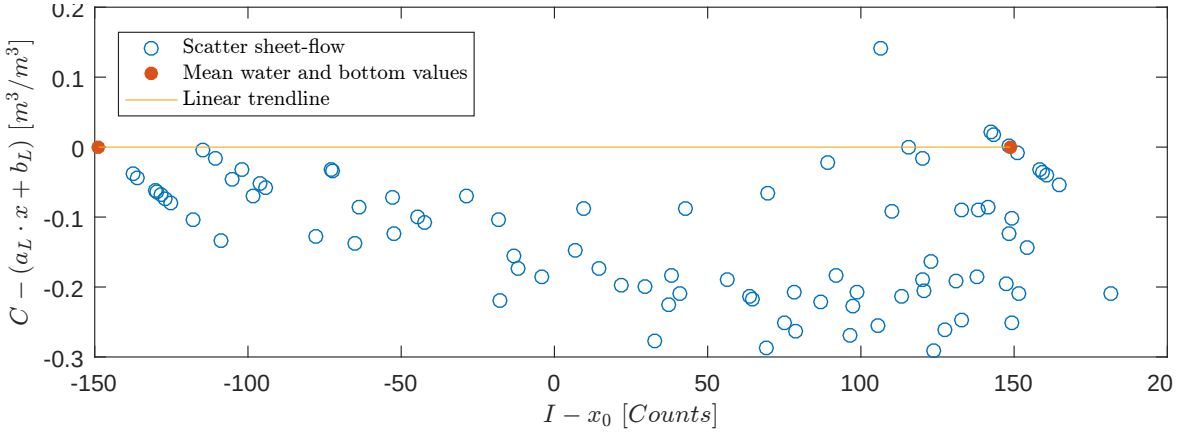


(c) Step 3: Horizontal translation. Subtract the mean x-value of the two fixed points to relocate around the origin.

Figure I.1: Quadratic calibration, part 1.

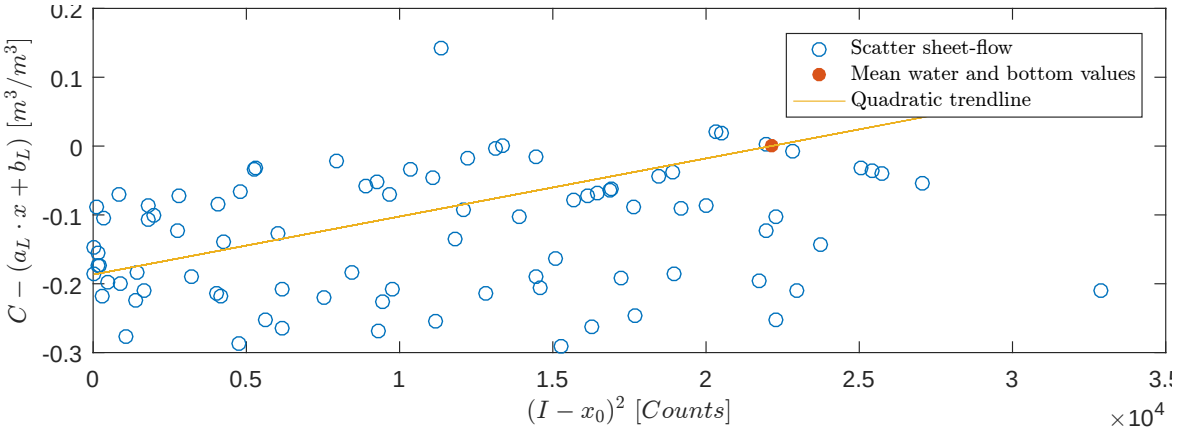


(a) Step 4: linear fit on quadratic horizontal axis. By taking the square of all x-values, all data becomes positive and both fixed points are located at exactly the same position. In this data set a linear fit can be applied to find the quadratic trend line.

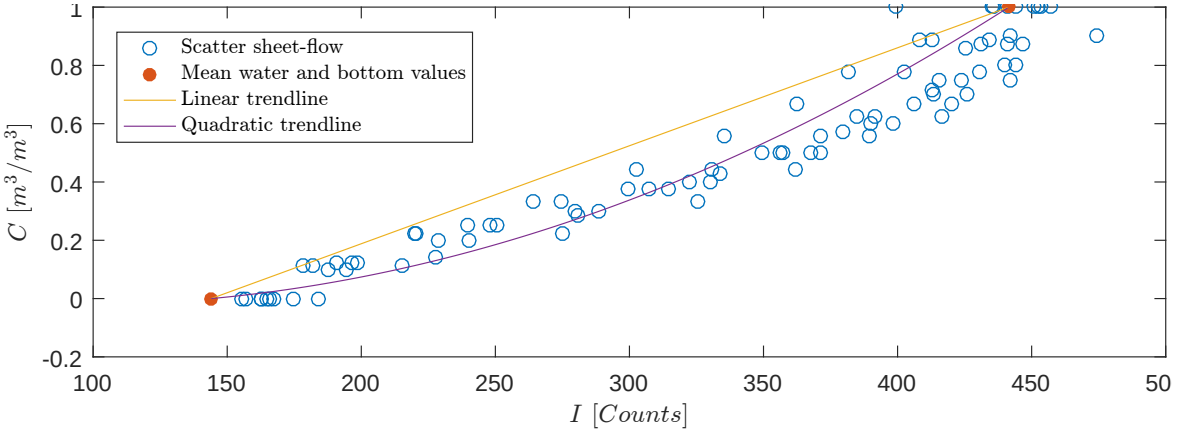


(b) Step 5: Result of the quadratic fit.

Figure I.2: Quadratic calibration, part 2.

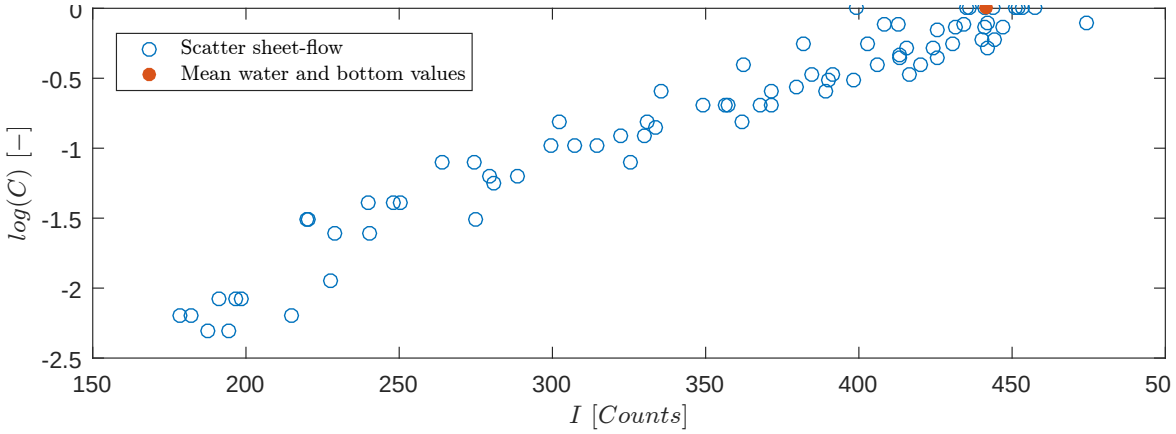


(a) Step 1: Plot the vertical axis on logarithmic scale.

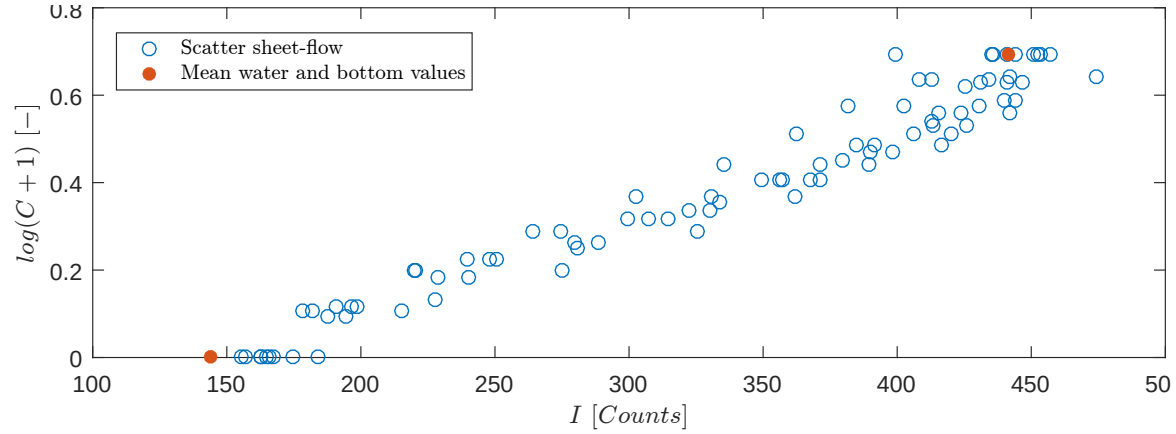


(b) Step 2: Vertical translation. Add 1 to all y values.

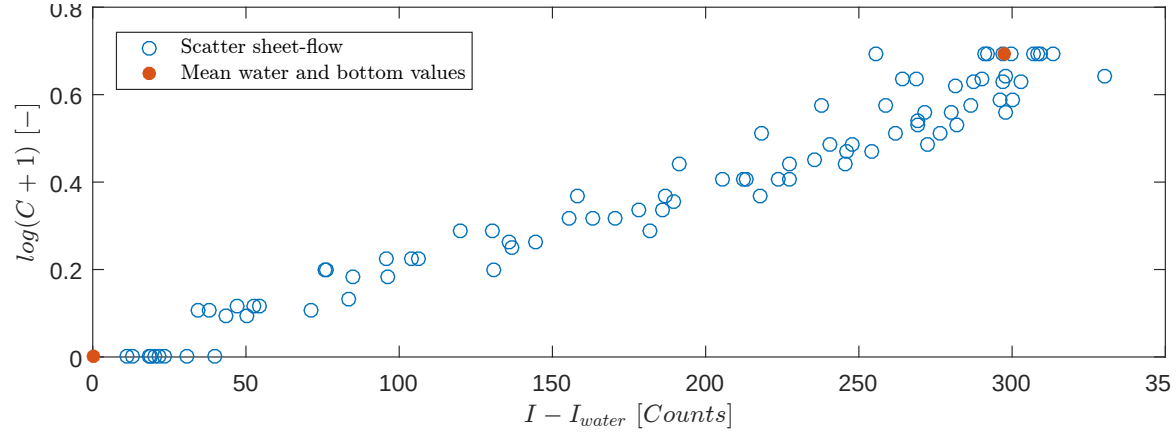


(c) Step 3: Horizontal translation. $I_{water,mean}$ is subtracted from the intensities.

Figure I.3: Exponential calibration, part 1.

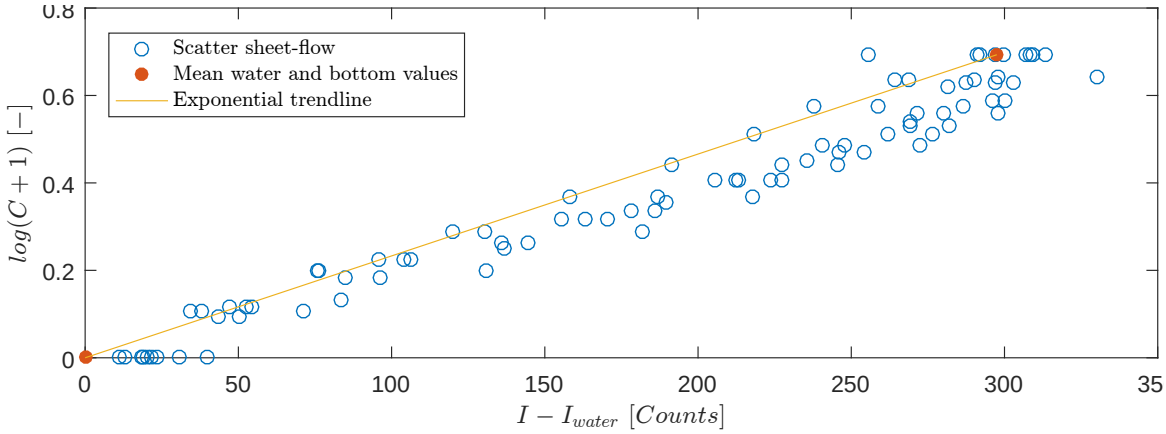


(a) Step 4: Exponential fit

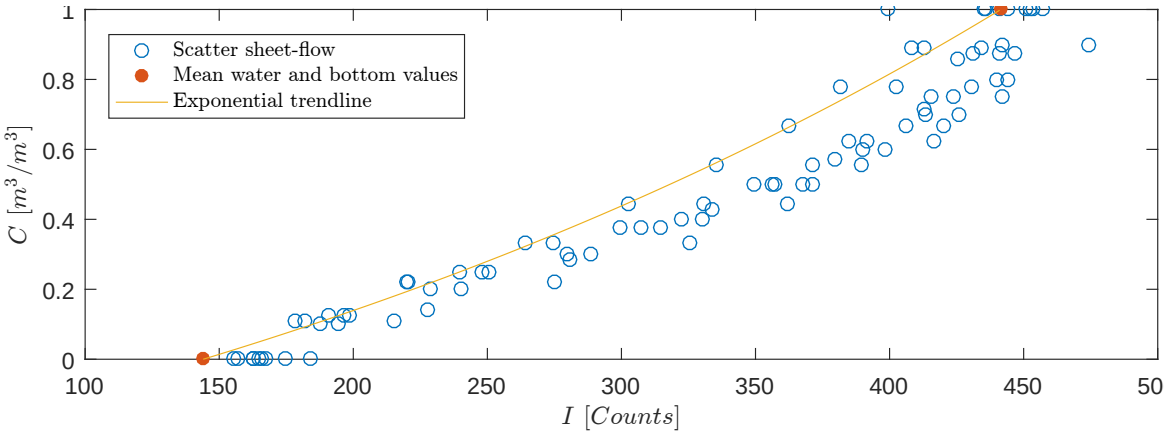


(b) Step 5: Plot on normal scale

Figure I.4: Exponential calibration, part 2.

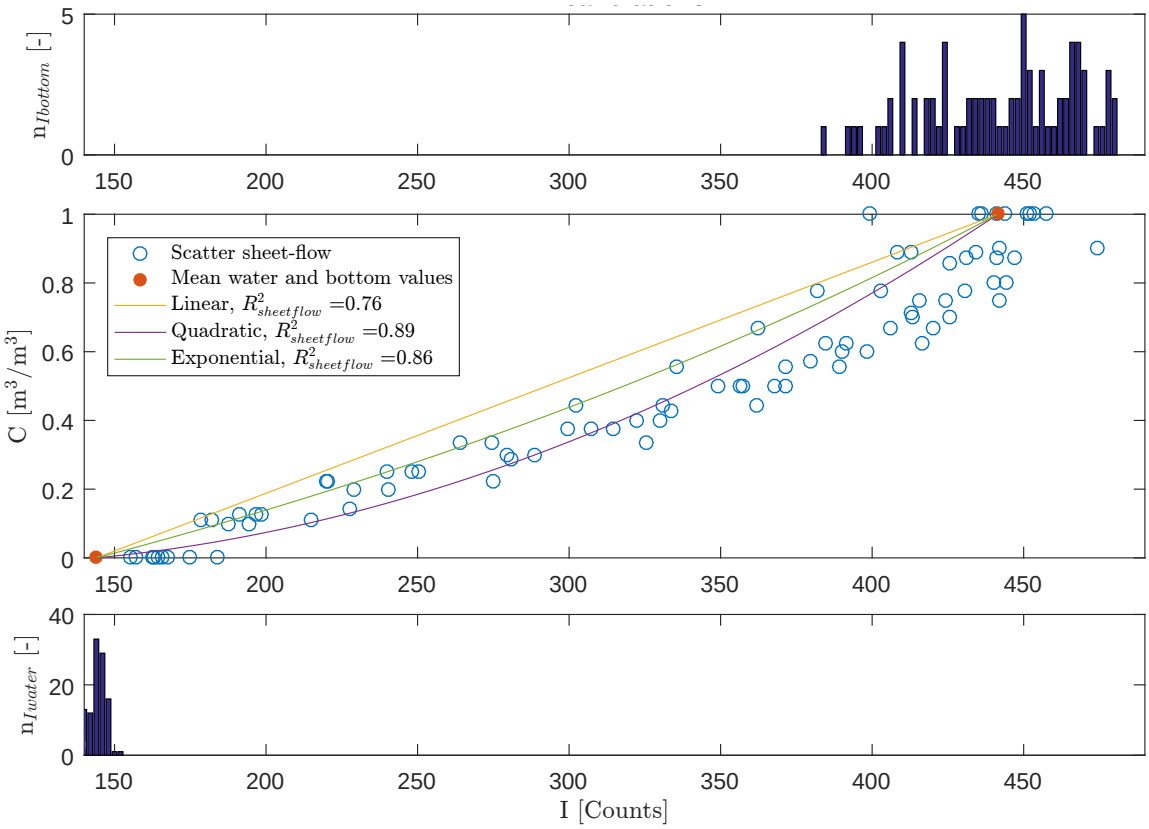


Figure I.5: Final result of all calibration methods. The middle plot shows the data set and the trend lines. The top an bottom plot show the spread in bed and water intensities. This plot is the example of calibration set 1 (Offshore of the sandbar, test series 1).

# J

# Overview of the figures of all tests

## J.1. Bottom profile measurements

### J.1.1. Figures per test

Figure J.1, J.2 and J.3 show the results of the bottom profile measurements per test. The sediment transport per test is often tilted: the sediment at the end of the flume is not zero. The tilt is due to the summation of all errors in cross-shore direction. This influences the result at the PIV locations. When averaging multiple tests, this random tilt strongly decreases. Therefore only the mean value per location (per test series, average of 9 tests) is used.

### J.1.2. Figure per test series

Figure J.6.

## J.2. PIV measurements

### J.2.1. Figures per test

The results per test are displayed in Figures J.7, J.8, J.9, J.10, J.11, J.12 and J.13. The results are time-averaged over the test duration. Because the PIV measurement starts before the waves pass (Figure **??**), the first part of the measurement is cut off.

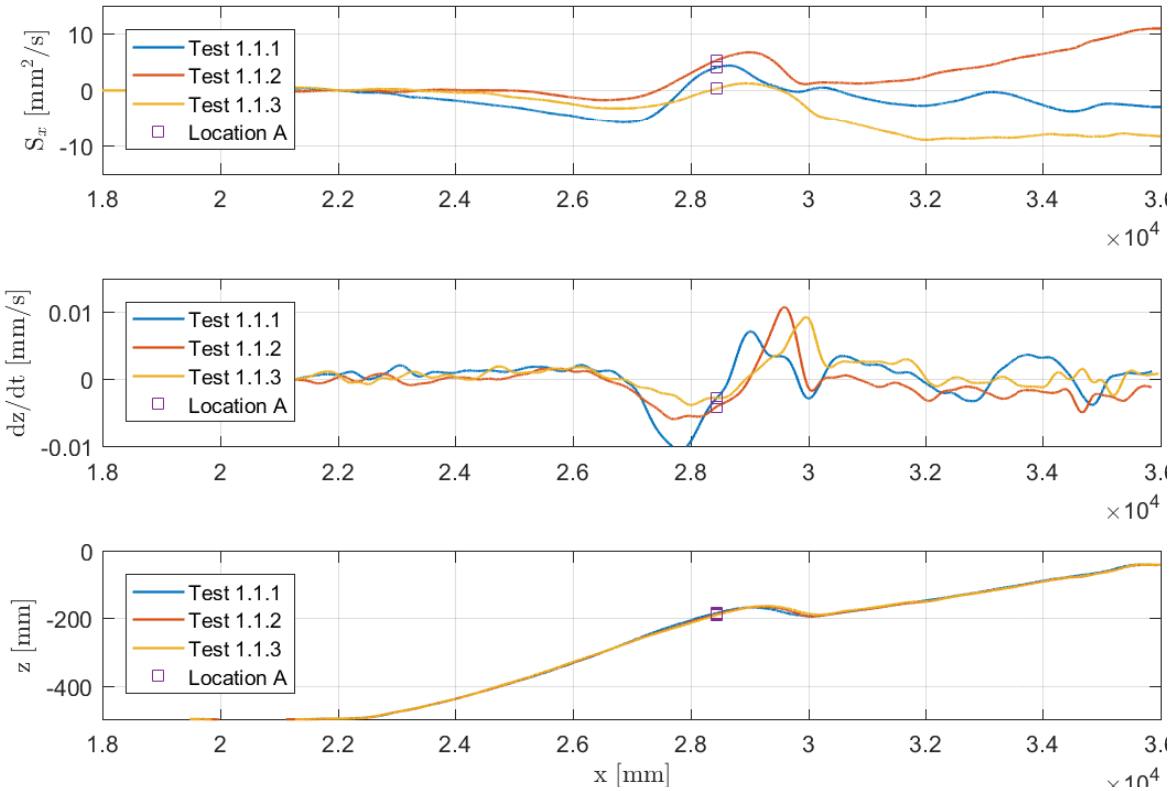


(a) Test series 1 migration 1

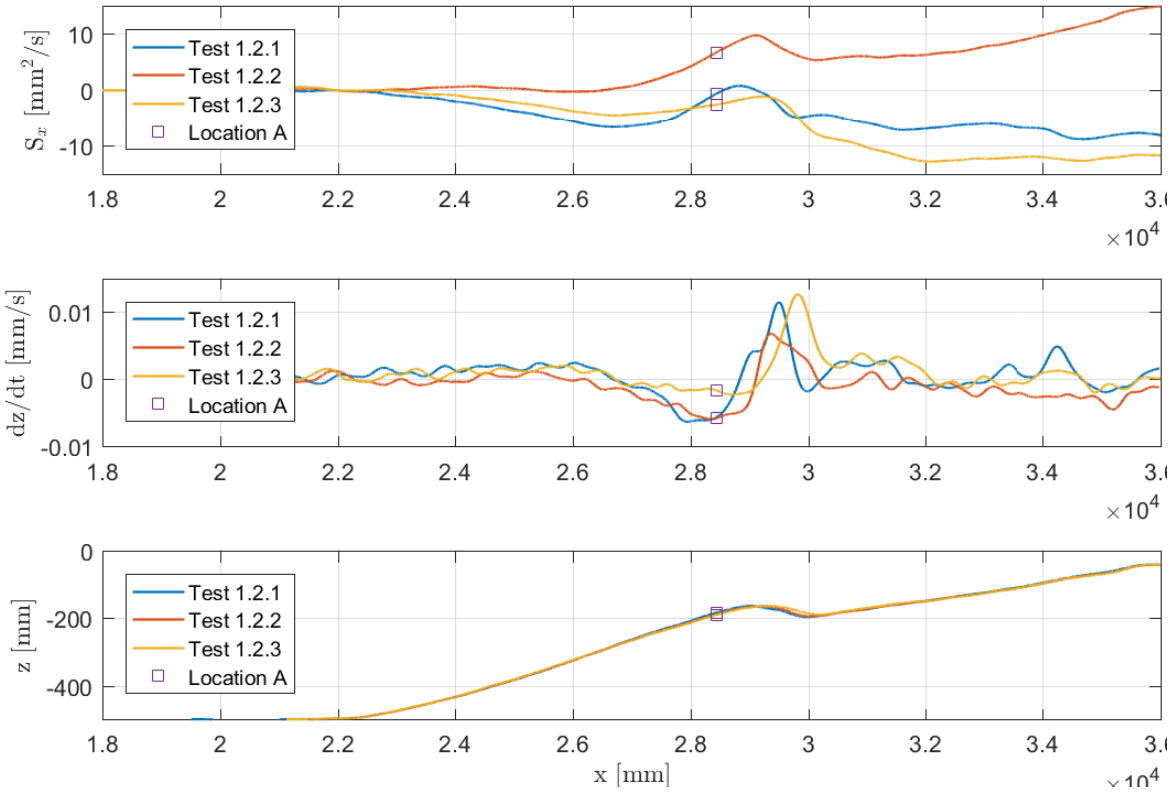


(b) Test series 1 migration 2

Figure J.1: Results of bottom measurement per test

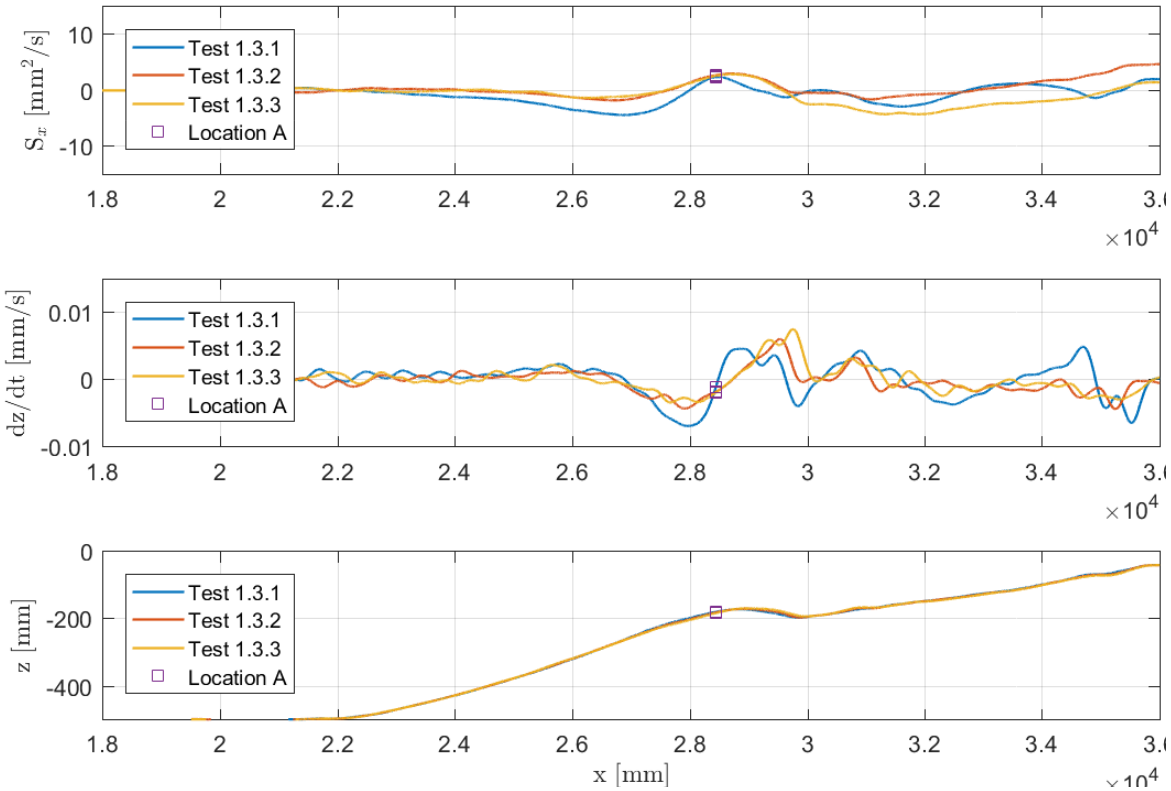


(a) Test series 1 migration 3

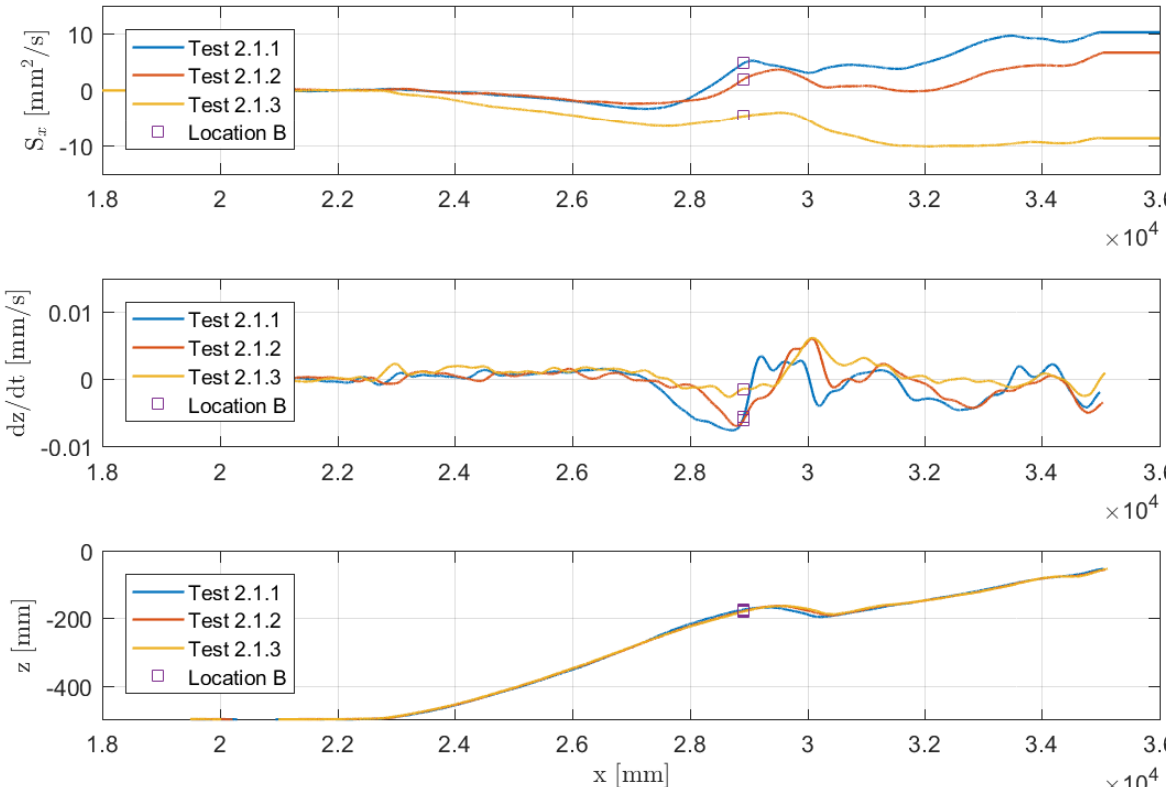


(b) Test series 2 migration 1

Figure J.2: Results of bottom measurement per test

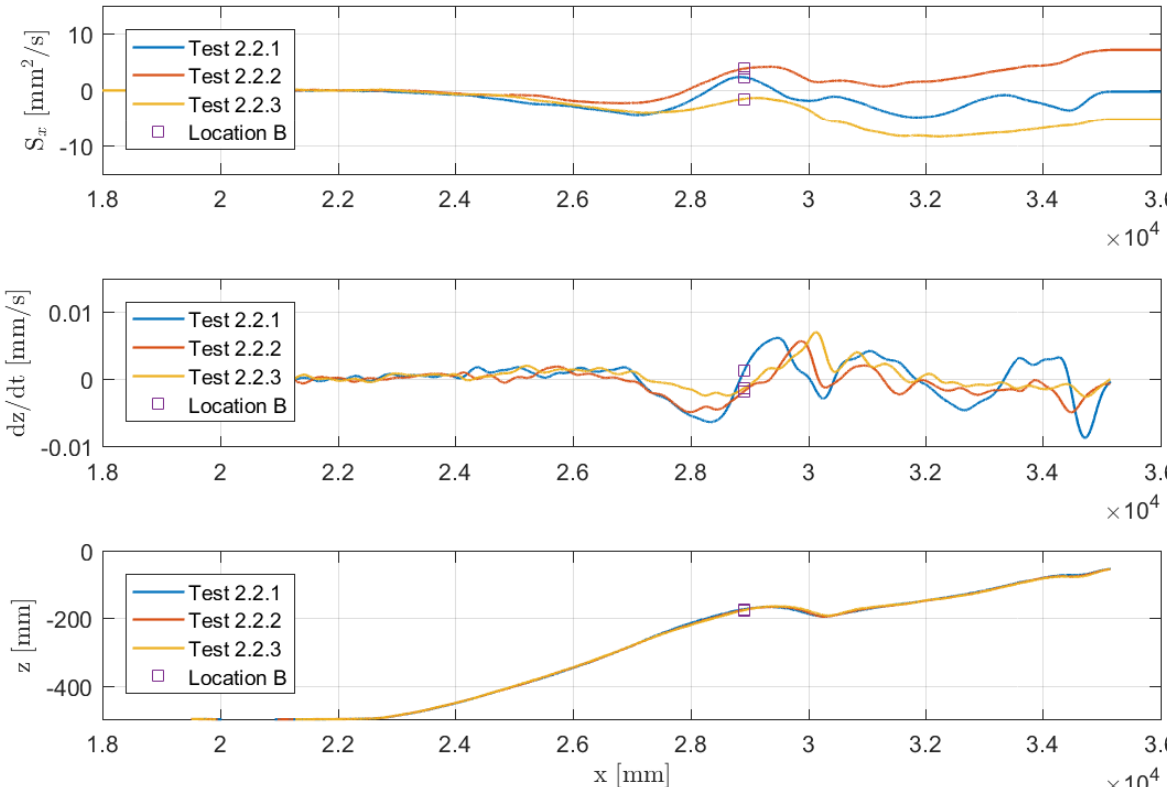


(a) Test series 2 migration 2

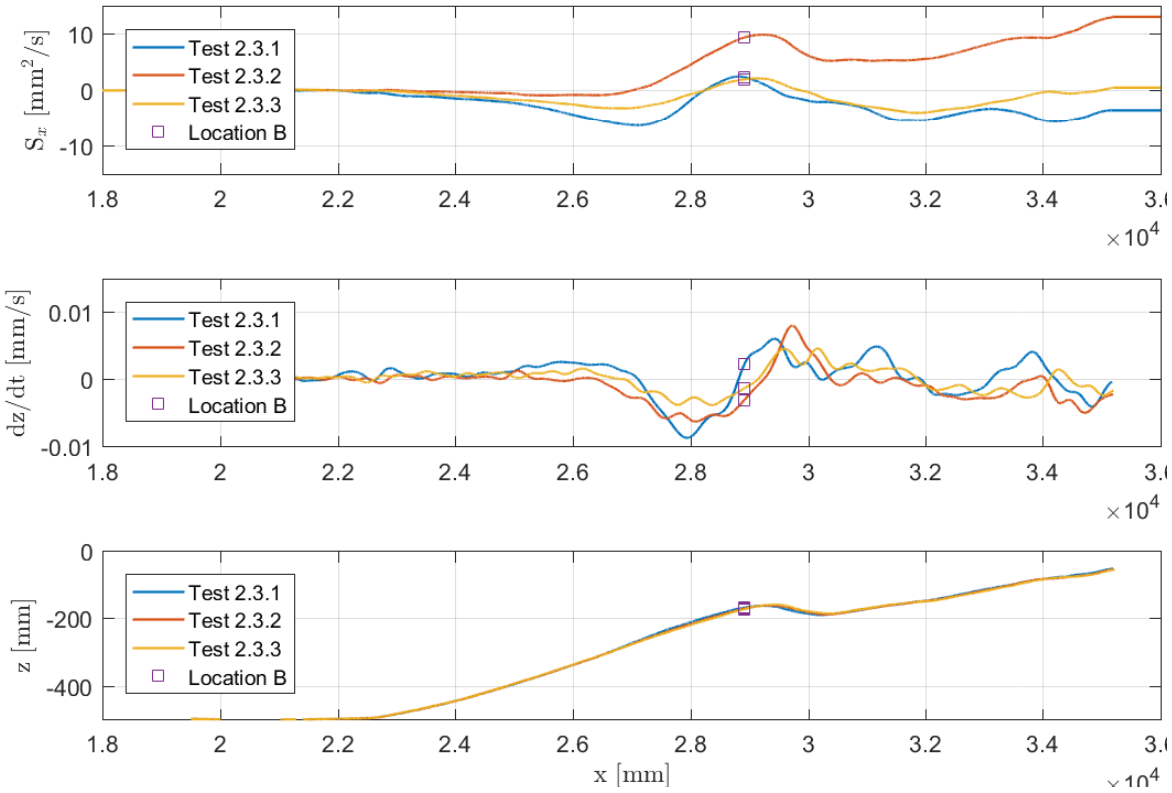


(b) Test series 2 migration 3

Figure J.3: Results of bottom measurement per test

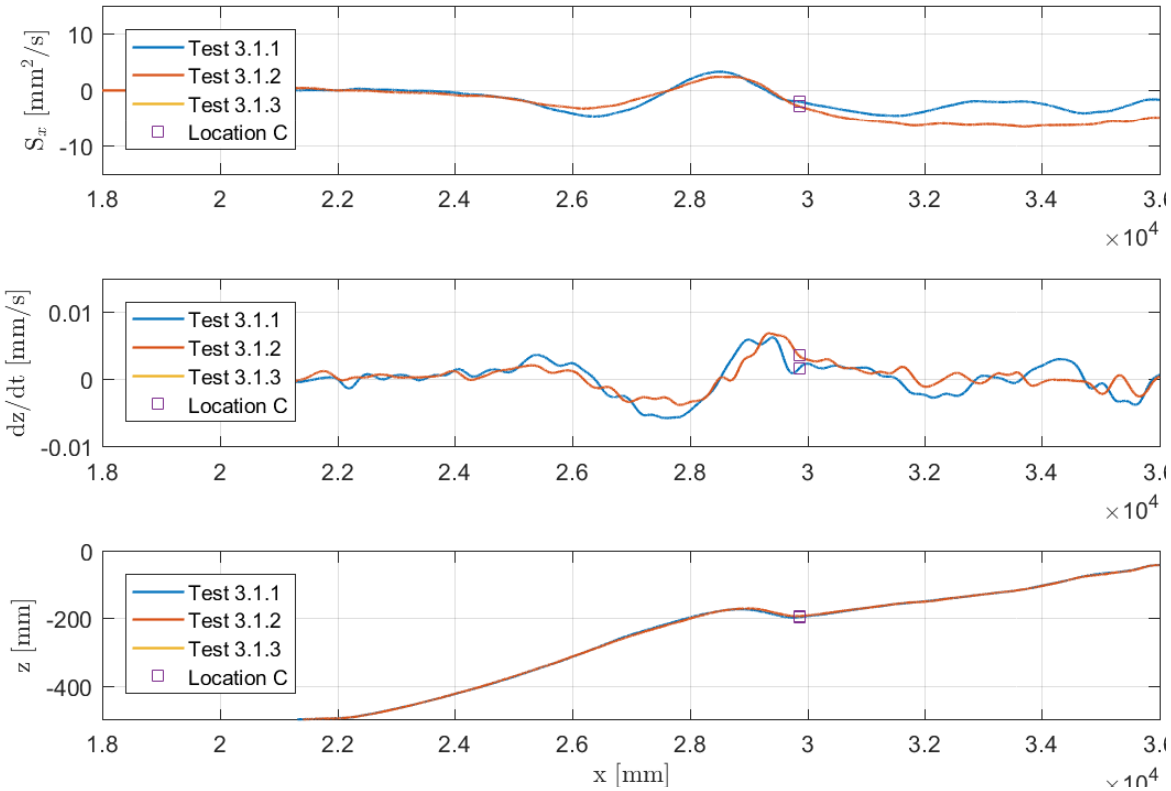


(a) Test series 3 migration 1

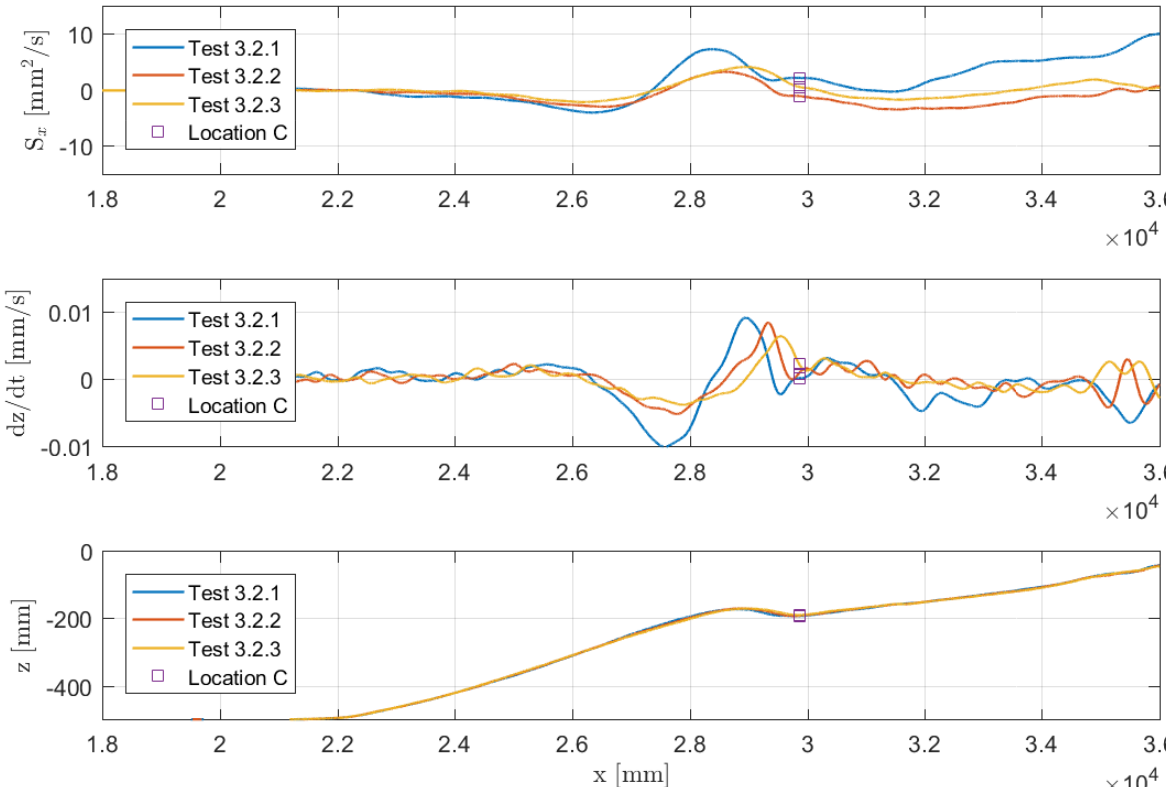


(b) Test series 3 migration 2

Figure J.4: Results of bottom measurement per test

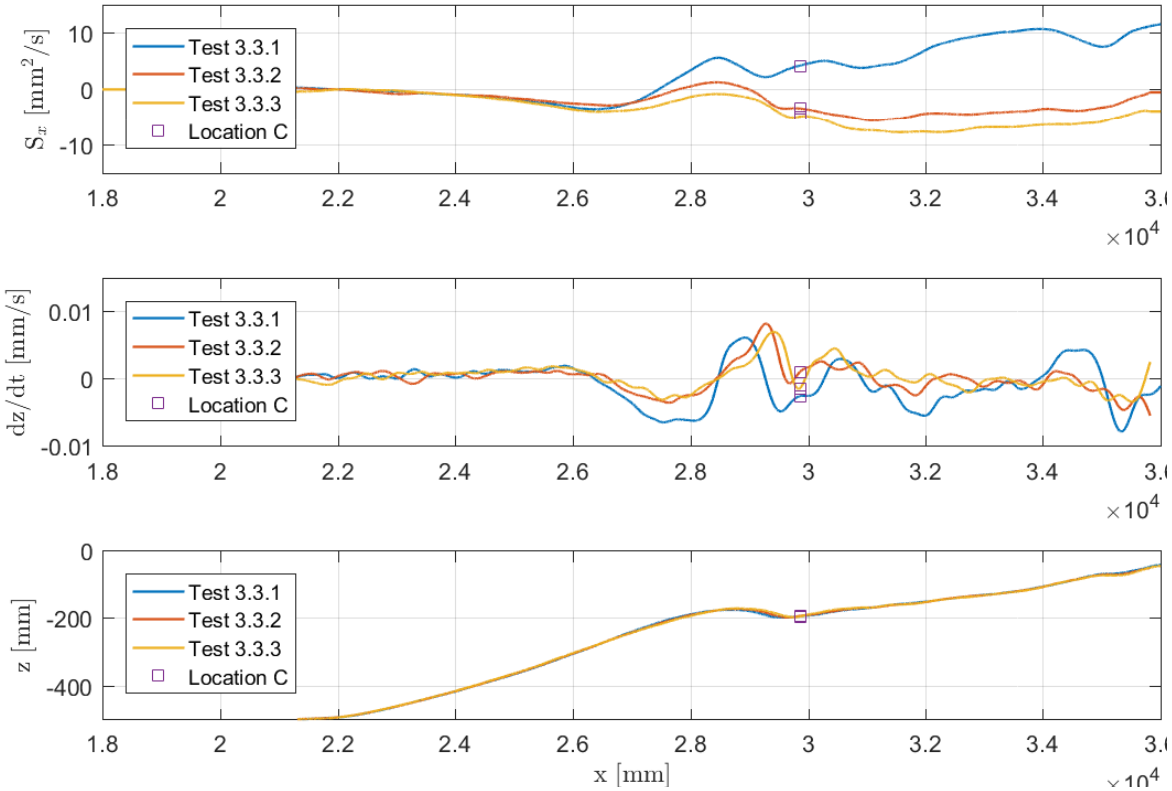


(a) Test series 3 migration 3

Figure J.5: Results of bottom measurement per test

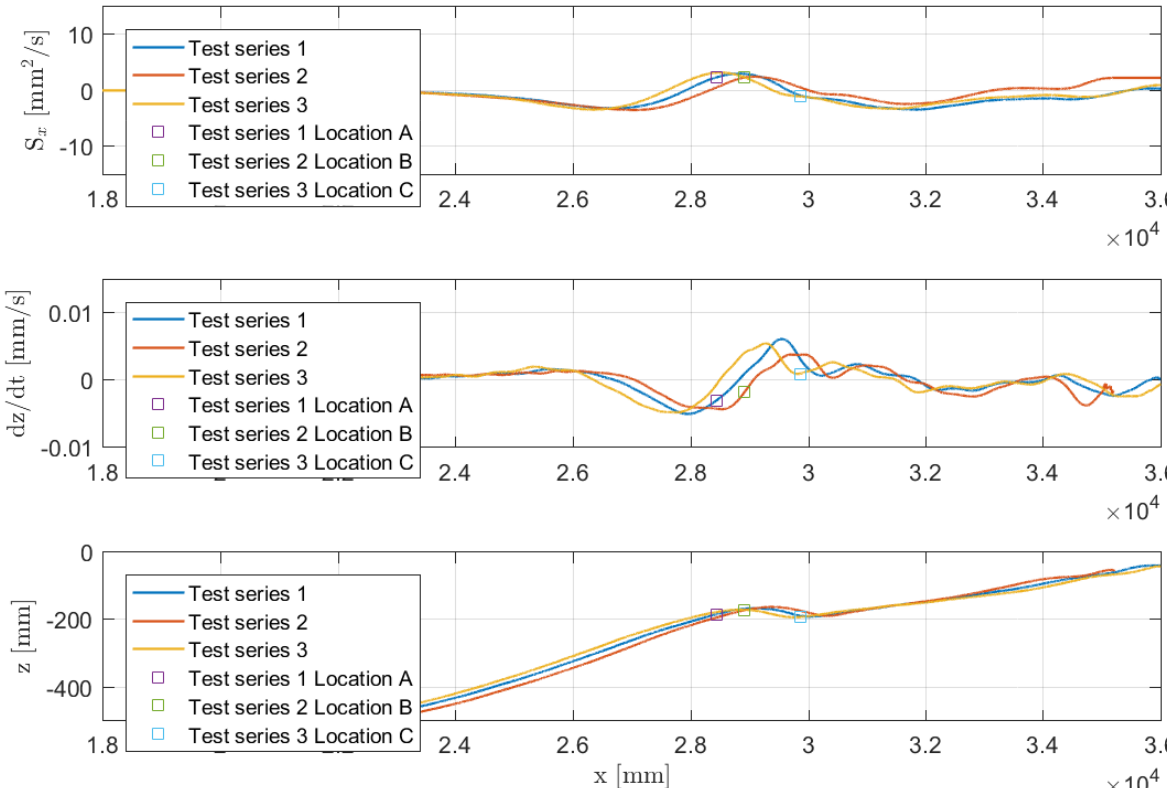


(a) Test series 3 migration 3

Figure J.6: Results of bottom measurement per test series.

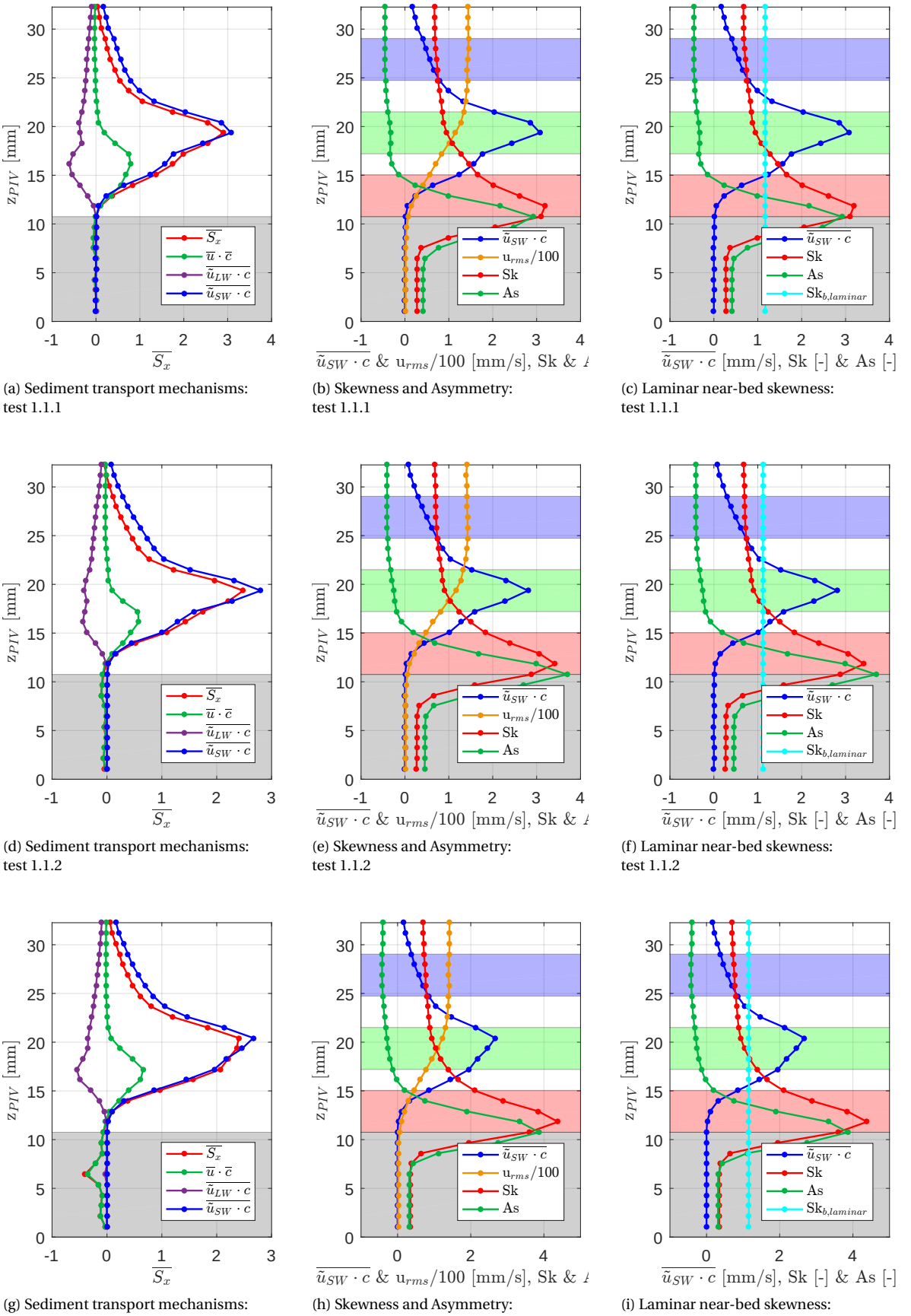


(a) Sediment transport mechanisms: test 1.1.1

(b) Skewness and Asymmetry: test 1.1.1

(c) Laminar near-bed skewness: test 1.1.1

(d) Sediment transport mechanisms: test 1.1.2

(e) Skewness and Asymmetry: test 1.1.2

(f) Laminar near-bed skewness: test 1.1.2

(g) Sediment transport mechanisms: test 1.2.1

(h) Skewness and Asymmetry: test 1.2.1

(i) Laminar near-bed skewness: test 1.2.1

Figure J.7: Vertical distribution of the different sediment transport mechanisms and wave properties per test. The still bed is displayed in grey. The coloured areas indicate the characteristics elevations: free-stream (blue), maximum sediment transport (green) and close to the bottom (red). Only the tests used to calculate the mean vertical distribution over height are displayed (Appendix G).

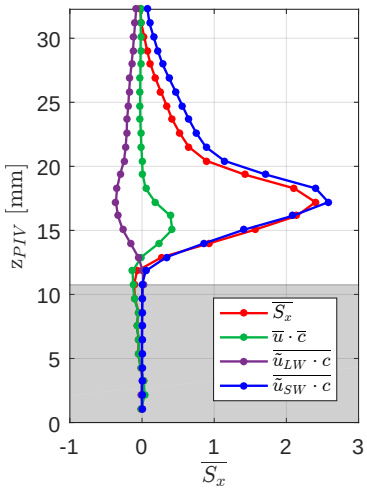


(a) Sediment transport mechanisms: test 1.2.2

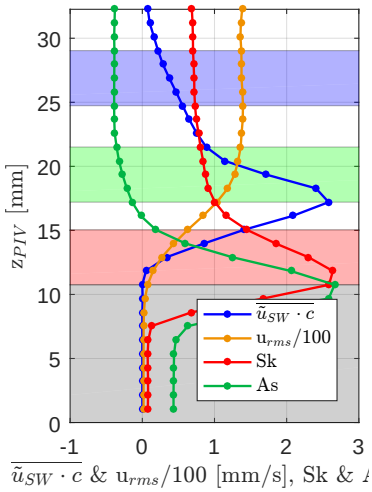


(b) Skewness and Asymmetry: test 1.2.2

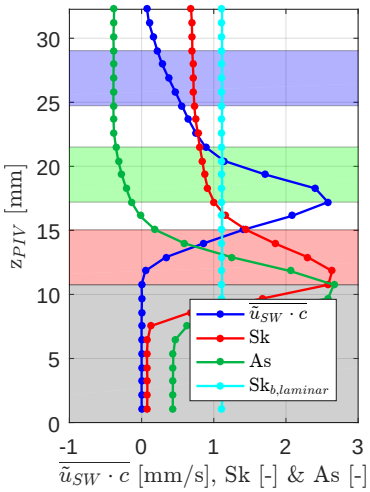


(c) Laminar near-bed skewness: test 1.2.2

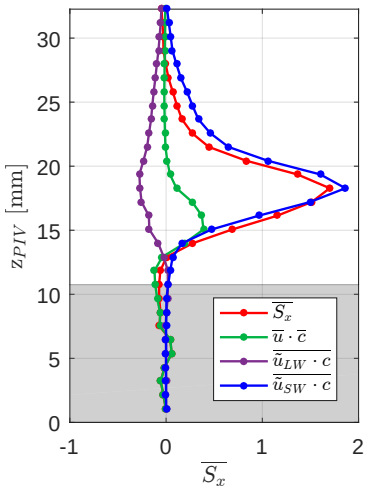


(d) Sediment transport mechanisms: test 1.3.2

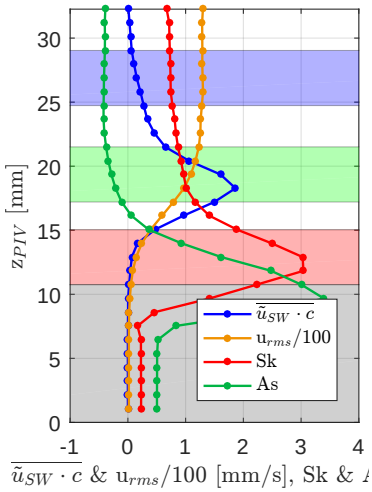


(e) Skewness and Asymmetry: test 1.3.2

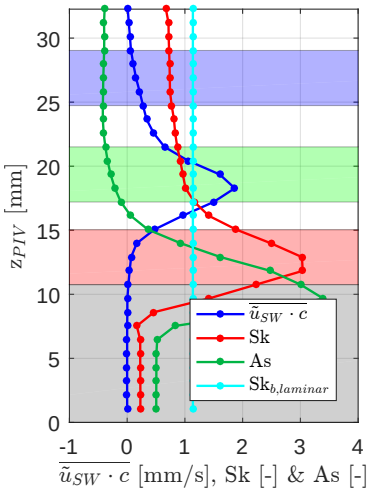


(f) Laminar near-bed skewness: test 1.3.2

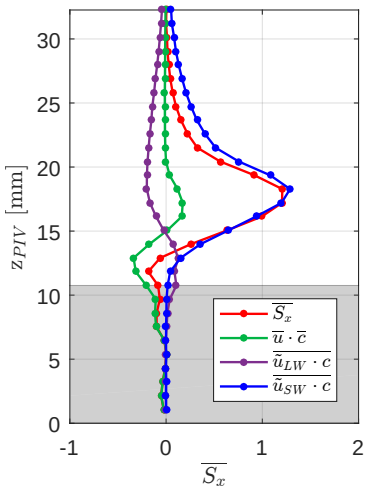


(g) Sediment transport mechanisms: test 1.3.3

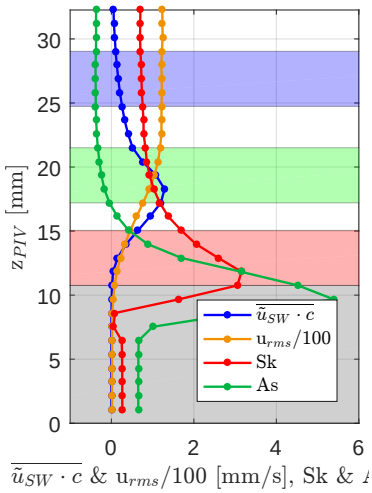


(h) Skewness and Asymmetry: test 1.3.3

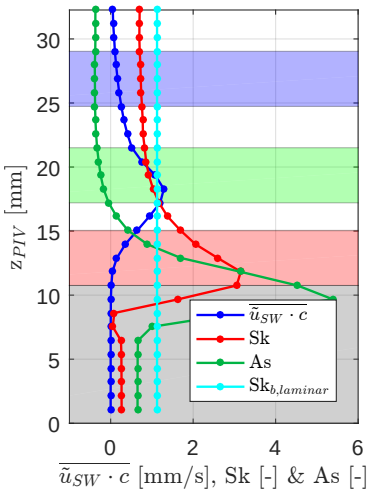


(i) Laminar near-bed skewness: test 1.3.3

Figure J.8: Vertical distribution of the different sediment transport mechanisms and wave properties per test. The still bed is displayed in grey. The coloured areas indicate the characteristics elevations: free-stream (blue), maximum sediment transport (green) and close to the bottom (red). Only the tests used to calculate the mean vertical distribution over height are displayed (Appendix G).

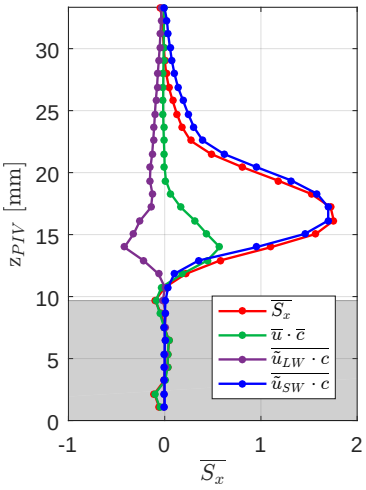


(a) Sediment transport mechanisms: test 2.1.1

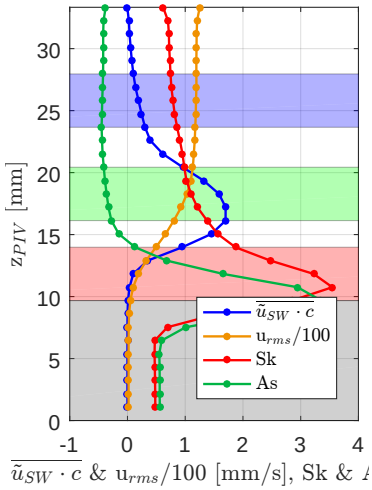


(b) Skewness and Asymmetry: test 2.1.1

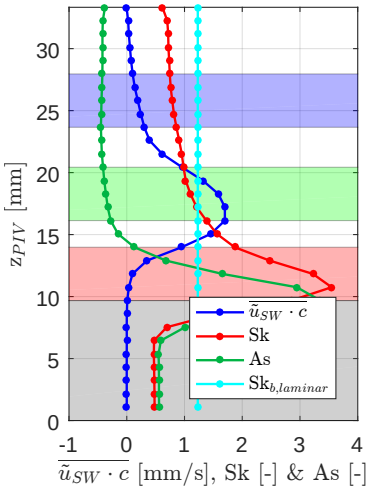


(c) Laminar near-bed skewness: test 2.1.1

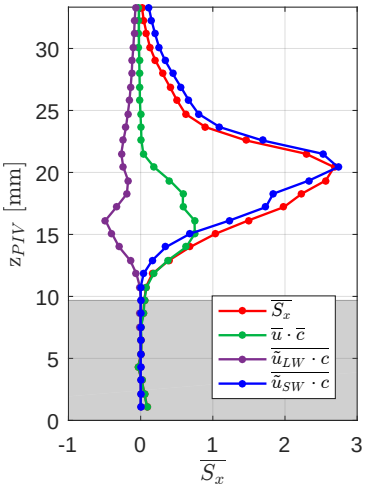


(d) Sediment transport mechanisms: test 2.1.2

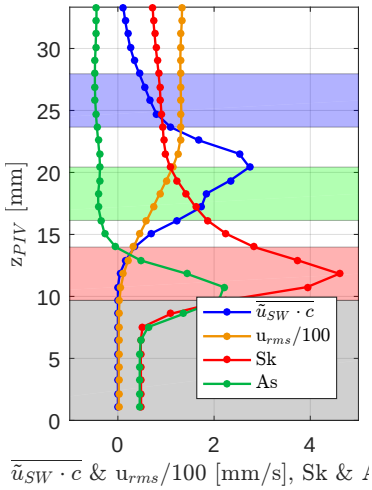


(e) Skewness and Asymmetry: test 2.1.2

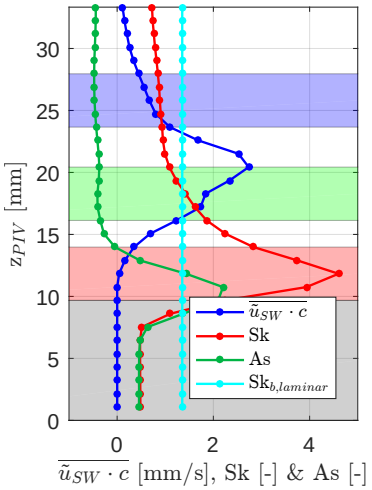


(f) Laminar near-bed skewness: test 2.1.2

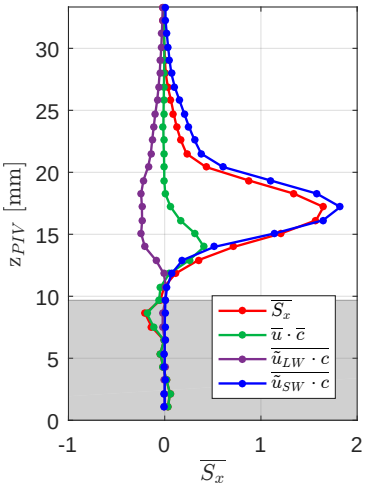


(g) Sediment transport mechanisms: test 2.1.3

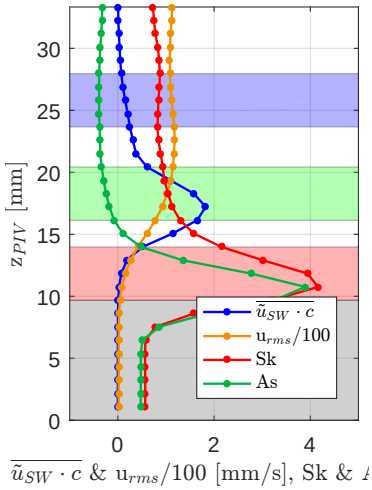


(h) Skewness and Asymmetry: test 2.1.3

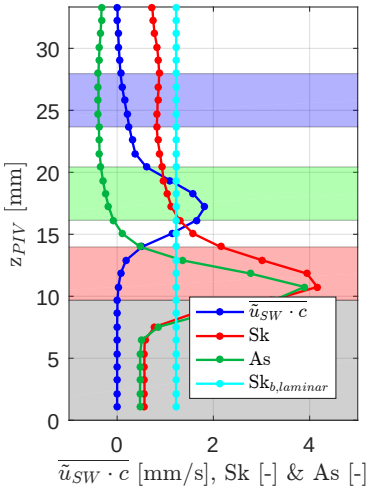


(i) Laminar near-bed skewness: test 2.1.3

Figure J.9: Vertical distribution of the different sediment transport mechanisms and wave properties per test. The still bed is displayed in grey. The coloured areas indicate the characteristics elevations: free-stream (blue), maximum sediment transport (green) and close to the bottom (red). Only the tests used to calculate the mean vertical distribution over height are displayed (Appendix G).

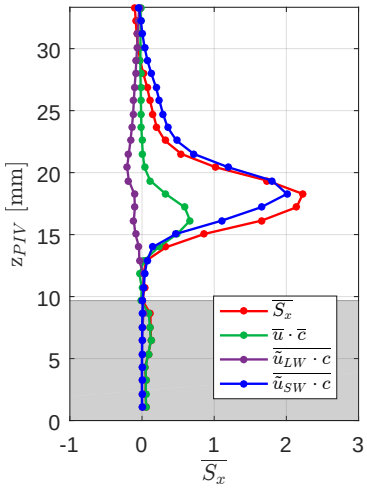


(a) Sediment transport mechanisms: test 2.2.1

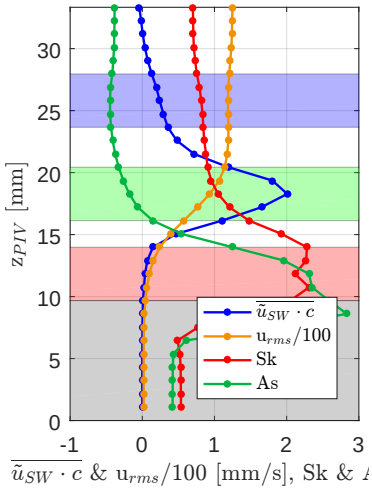


(b) Skewness and Asymmetry: test 2.2.1

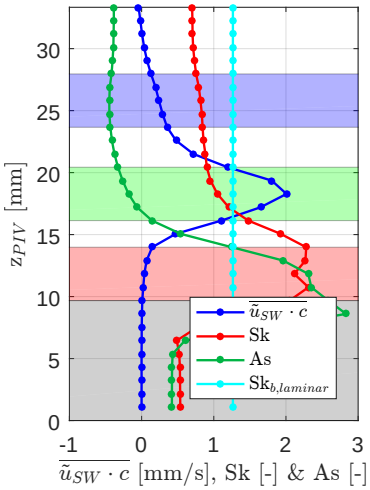


(c) Laminar near-bed skewness: test 2.2.1

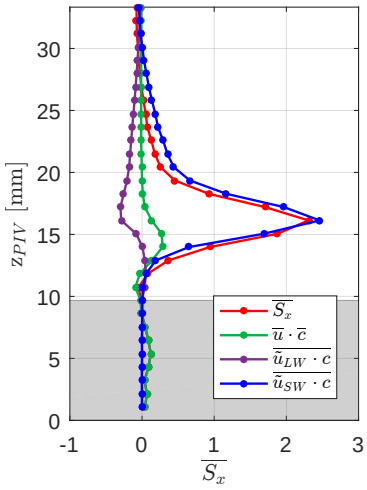


(d) Sediment transport mechanisms: test 2.2.2

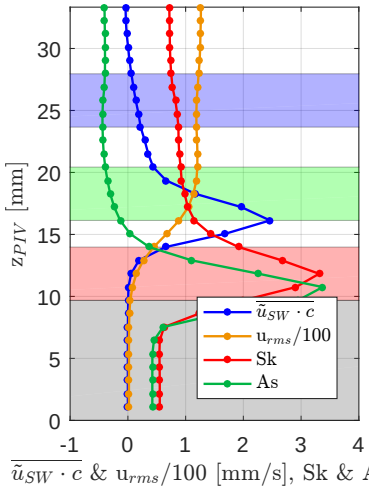


(e) Skewness and Asymmetry: test 2.2.2

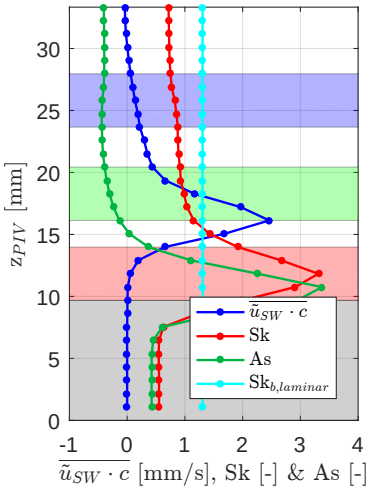


(f) Laminar near-bed skewness: test 2.2.2

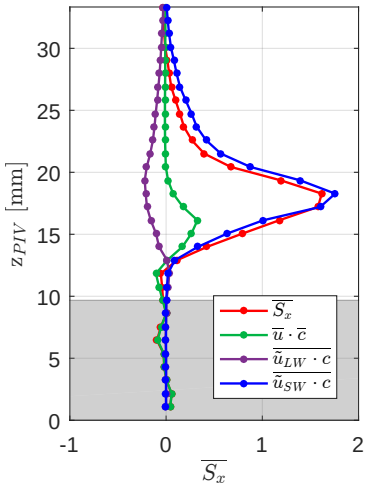


(g) Sediment transport mechanisms: test 2.2.3

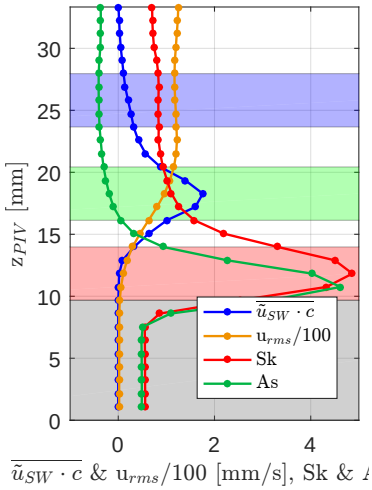


(h) Skewness and Asymmetry: test 2.2.3

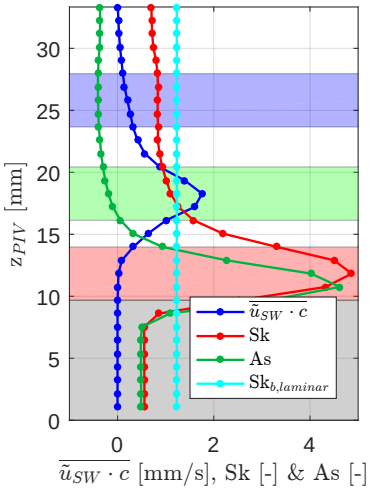


(i) Laminar near-bed skewness: test 2.2.3

Figure J.10: Vertical distribution of the different sediment transport mechanisms and wave properties per test. The still bed is displayed in grey. The coloured areas indicate the characteristics elevations: free-stream (blue), maximum sediment transport (green) and close to the bottom (red). Only the tests used to calculate the mean vertical distribution over height are displayed (Appendix G).

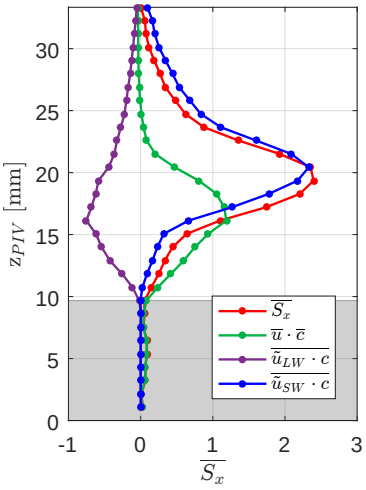


(a) Sediment transport mechanisms: test 2.3.1

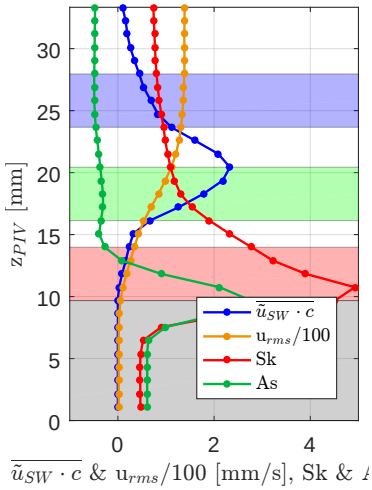


(b) Skewness and Asymmetry: test 2.3.1

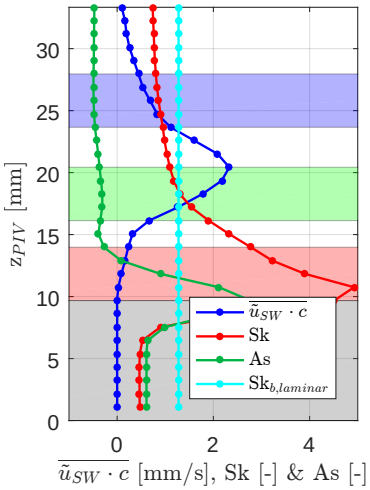


(c) Laminar near-bed skewness: test 2.3.1

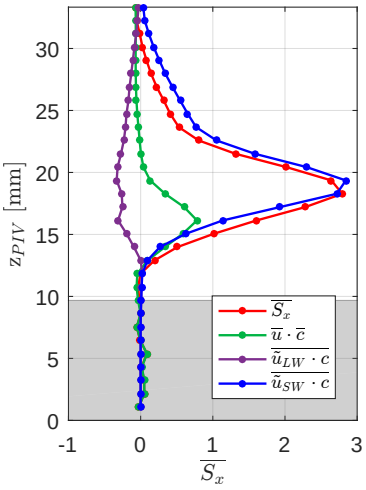


(d) Sediment transport mechanisms: test 2.3.2

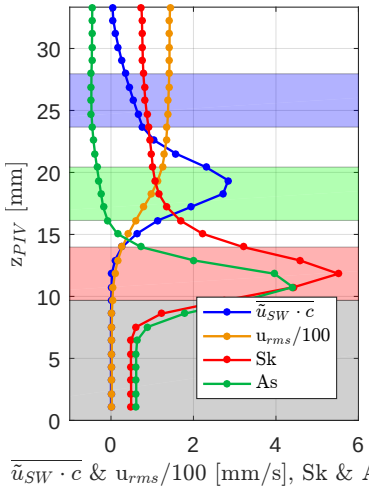


(e) Skewness and Asymmetry: test 2.3.2

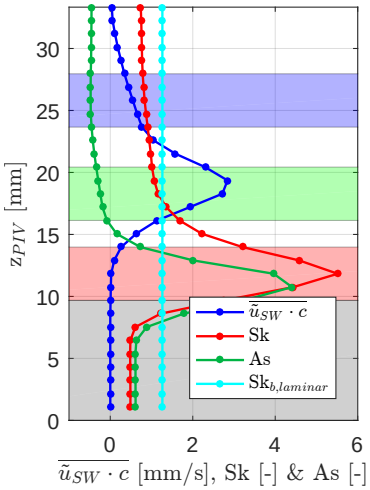


(f) Laminar near-bed skewness: test 2.3.2

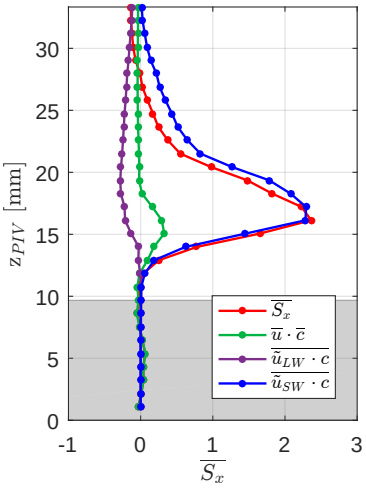


(g) Sediment transport mechanisms: test 2.3.3

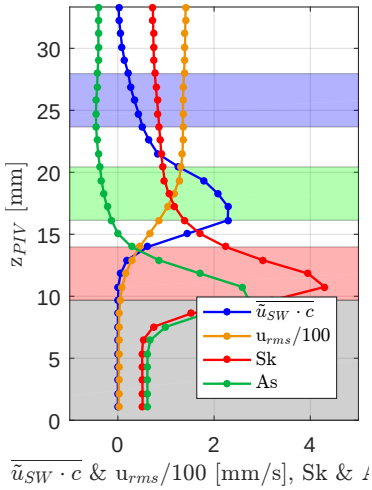


(h) Skewness and Asymmetry: test 2.3.3

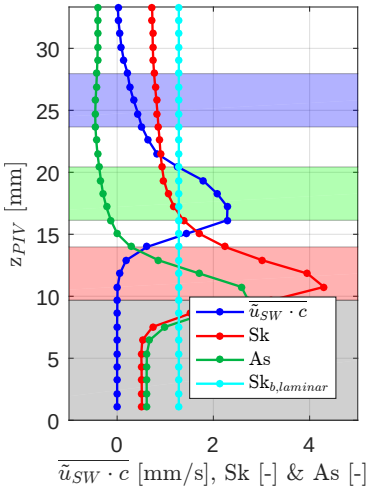


(i) Laminar near-bed skewness: test 2.3.3

Figure J.11: Vertical distribution of the different sediment transport mechanisms and wave properties per test. The still bed is displayed in grey. The coloured areas indicate the characteristics elevations: free-stream (blue), maximum sediment transport (green) and close to the bottom (red). Only the tests used to calculate the mean vertical distribution over height are displayed (Appendix G).

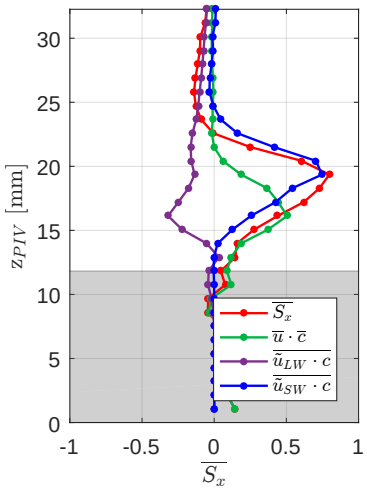


(a) Sediment transport mechanisms: test 3.1.1

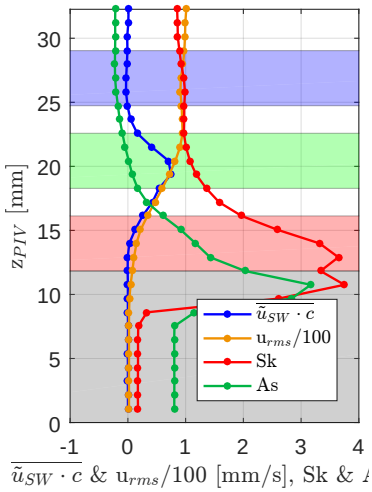


(b) Skewness and Asymmetry: test 3.1.1

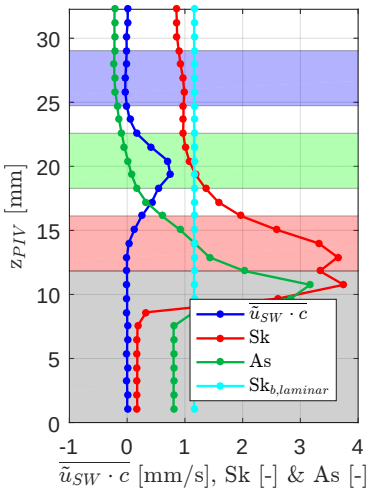


(c) Laminar near-bed skewness: test 3.1.1

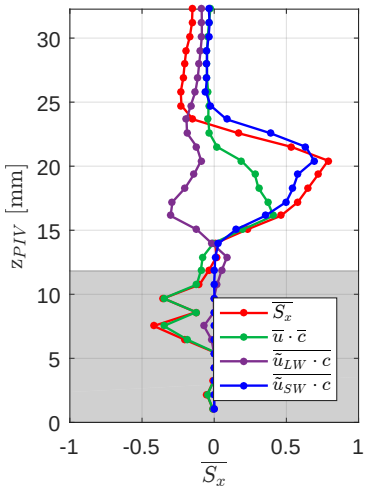


(d) Sediment transport mechanisms: test 3.1.2

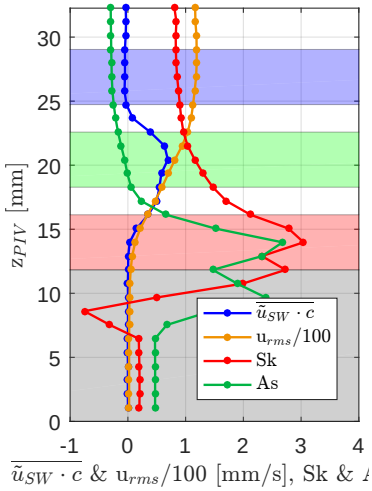


(e) Skewness and Asymmetry: test 3.1.2

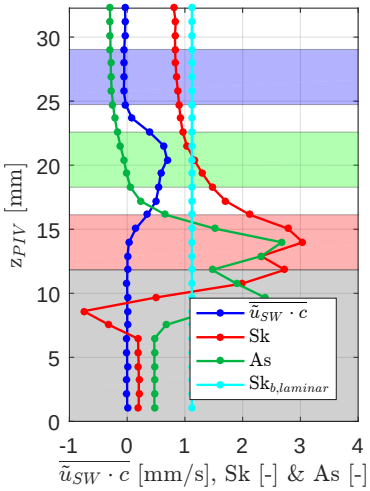


(f) Laminar near-bed skewness: test 3.1.2

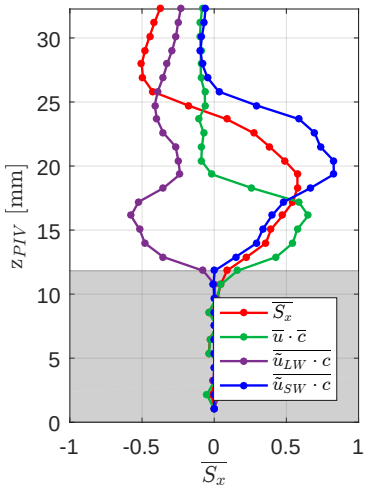


(g) Sediment transport mechanisms: test 3.2.2

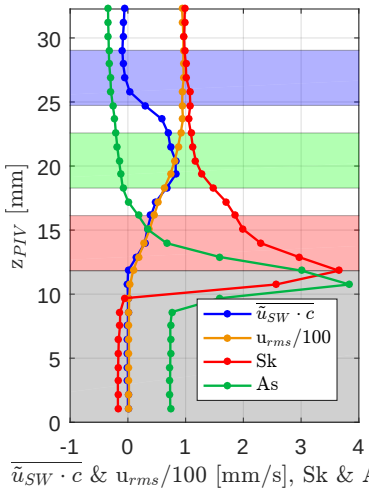


(h) Skewness and Asymmetry: test 3.2.2

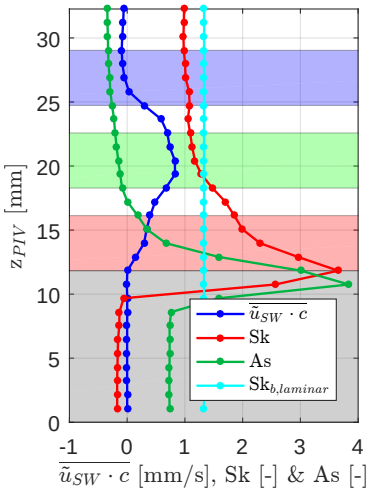


(i) Laminar near-bed skewness: test 3.2.2

Figure J.12: Vertical distribution of the different sediment transport mechanisms and wave properties per test. The still bed is displayed in grey. The coloured areas indicate the characteristics elevations: free-stream (blue), maximum sediment transport (green) and close to the bottom (red). Only the tests used to calculate the mean vertical distribution over height are displayed (Appendix G).

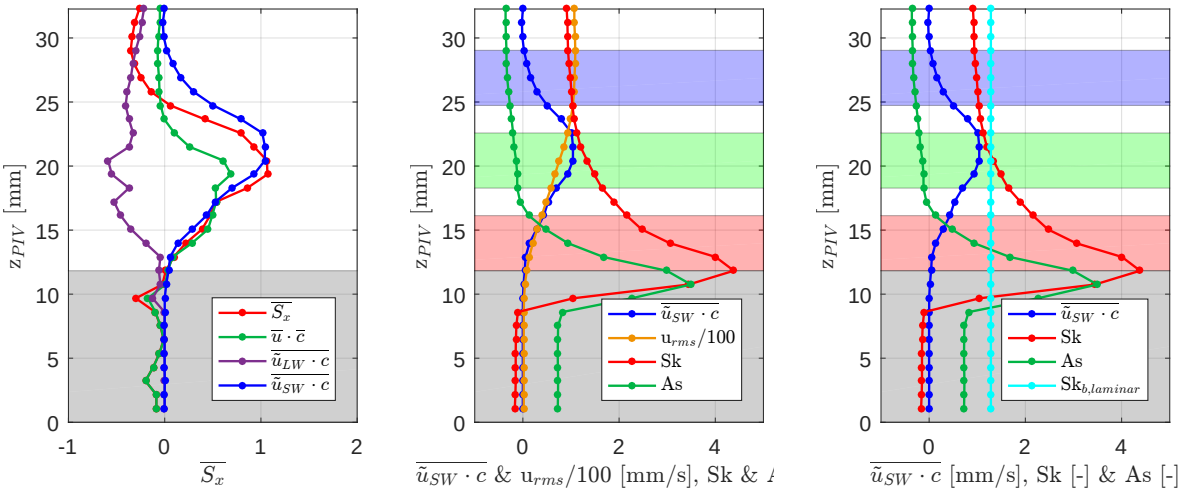


(a) Sediment transport mechanisms: test 3.2.3

(b) Skewness and Asymmetry: test 3.2.3

(c) Laminar near-bed skewness: test 3.2.3

(d) Sediment transport mechanisms: test 3.3.3

(e) Skewness and Asymmetry: test 3.3.3

(f) Laminar near-bed skewness: test 3.3.3

Figure J.13: Vertical distribution of the different sediment transport mechanisms and wave properties per test. The still bed is displayed in grey. The coloured areas indicate the characteristics elevations: free-stream (blue), maximum sediment transport (green) and close to the bottom (red). Only the tests used to calculate the mean vertical distribution over height are displayed (Appendix G).

# K

# Result of the short wave related transport analysis per wave

This chapter shows the results of the wave shape analysis per wave. In the analysis per wave, the skewness parameter, $R_u$, and the asymmetry parameter, $R_a$, are used to describe wave shape (Equation 2.7 and 2.8). The skewness and asymmetry will always be positive: values larger than 0.5 indicate positive skewness or negative asymmetry and values smaller than 0.5 mean negative skewness or positive asymmetry.

Figure K.1a shows that the correlation between velocity skewness and the total sediment transport per wave indeed increases towards the bed, while the relation between asymmetry and sediment transport decreases towards the bottom (Figure K.1c). Figure K.1d compares the asymmetry at each elevation to the sediment transport at the same elevation to study the effect of the pressure gradient. However, the relation between asymmetry per elevation and sediment transport per elevation, both includes the effect of the pressure gradient and the effect that asymmetry increases near-bed skewness and with that causes sediment transport. That at the elevation of maximum sediment transport the asymmetry relates less to the sediment transport at that elevation (Figure K.1d) than to the total sediment transport per wave (Figure K.1c), indicates that effect on near-bed skewness is more important than the asymmetric pressure gradient. However the correlations are too low to draw this kind of conclusions.

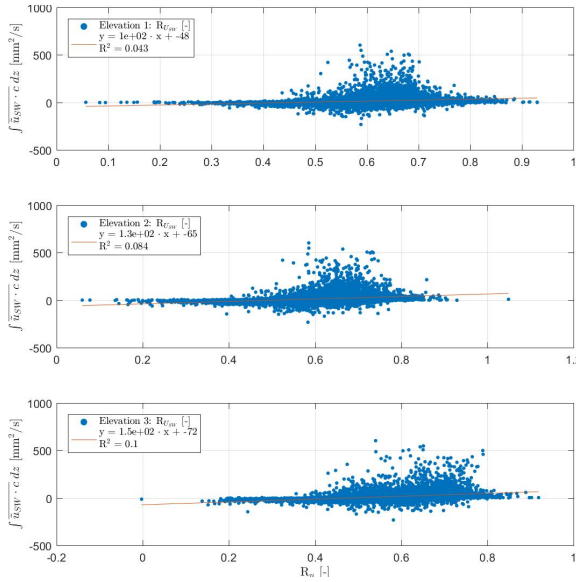


(a) Skewness of the horizontal velocities

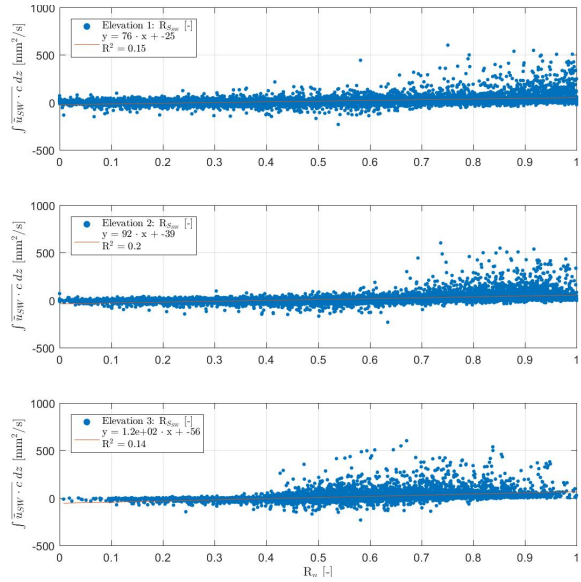


(b) Skewness of the sediment transport

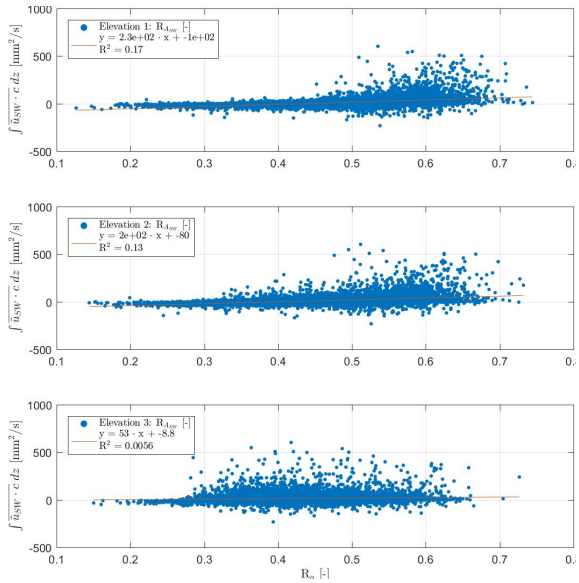


(c) Asymmetry of the horizontal velocities

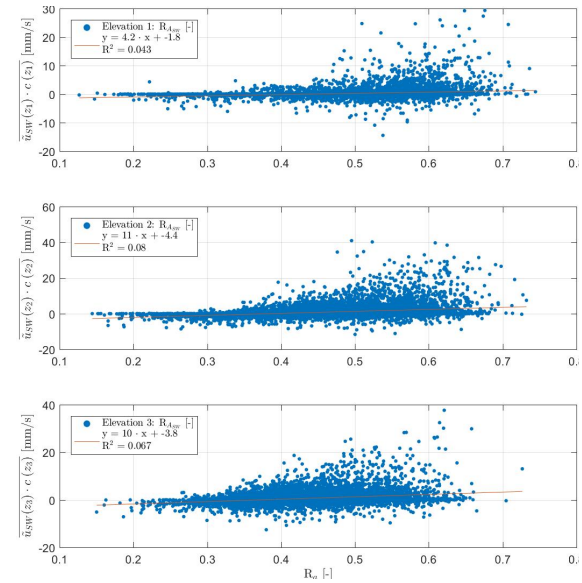


(d) Asymmetry of the horizontal velocities to mean sediment transport per elevaltion instead of total sediment transport per wave.

Figure K.1: Scatter of all waves: skewness and asymmetry comparison to total sediment transport per wave.